Magma Genesis and Mantle Sources at the Mid-Atlantic Ridge East of Ascension Island

Dissertation
zur Erlangung des Doktorgrades
der Mathematisch-Naturwissenschaftlichen Fakultät
der Christian-Albrechts-Universität zu Kiel

---

vorgelegt von
Helge Möller
2002

Danksagung

Zuallererst möchte ich mich bei Prof. Dr. P. Stoffers für die Vergabe dieser Arbeit bedanken. Prof. Dr. C.W. Devey und Dr. K. Haase sei ebenso herzlichst gedankt für ihre tatkräftige Unterstützung, durch ihre Hilfe und Anleitung ist diese Arbeit erst zu dem geworden, was sie ist. Kapitän Bülow und der Mannschaft von "FS Meteor" sei für die Unterstützung an Bord gedankt. Vielen Dank an Dr. S. Fretzdorff für ihre Hilfe bei geochemischen Problemen. Vielen Dank an Herrn O. Schneider für die Hilfe an der Mikrosonde am Geomar, Dr. D. Ackermand und Frau B. Mader für die Hilfe an der Mikrosonde am IfG. Dr. C.-D. Garbe-Schönberg, T. Arpe und Fr. H. Blaschek sei für die ICP-MS Analysen gedankt. Ich bedanke mich bei Prof. Dr. A.W. Hofmann für die Möglichkeit, Isotope am MPI für Chemie in Mainz zu messen. Für die geduldige Hilfe von Dr. W. Abouchami, Dr. S. Galer, Dr. M. Regelous am MPI möchte ich mich ganz herzlich bedanken. Der DFG sei für die dreijährige finanzielle Unterstützung gedankt.

Ein großes Dankeschön an meine beiden Brüder Olaf und Karl, die mir in knappen Zeiten Asyl in ihren Heimen in Kiel und L.A. gewährt haben und noch währen. Ein ebenso großes Dankeschön an meine Schwester Uli für die professionelle Unterstützung im Layout. Dr. B. Bader sei für das Korrekturlesen gedankt.

Bei Marc Krienitz, Gerald Maroske und Nicole Stronzik möchte ich mich für unvergessene Stunden der Netzwerkanwendungen bedanken. Bei Olaf Thiessen möchte ich mich dafür bedanken, daß er genau so wenig Fische fängt wie ich.

Vielen Dank an Dich, Anja.

Meinen Eltern gebührt der größte Dank, für alles, was sie für mich getan haben.

Abstract

Results from the Meteor 41-2 cruise to the Mid-Atlantic Ridge (MAR) between 6° and 11°S, 80 km E of Ascension Island, between the Ascension Fracture Zone (FZ) in the north and the Bode Verde FZ in the south are reported. Six spreading segments, which are bounded by non-transform offsets were discovered and numbered from north to south (Segment 1-Segment 6). Anomalously shallow segments (Segment 4 and 5) with a positive bathymetric deviation up to 1200 m occur between ~9°S and 11°S, pointing to an excess volcanism in this area. Three seamounts lie to the east of this area and seem to have no age progression with distance from the MAR. The shallowest Segment 5 does not show an axial valley, in contrast to the adjacent deeper segments. Published seismic data indicate that the thickness of the oceanic crust increases to 10 km at 9°30′ at Segment 4 (Minshull et al., 1998). For detailed geochemical and petrological investigations samples (mostly glasses) were taken every 5-10 km from north of the Ascension FZ up to the Bode Verde FZ. The results of this investigations show that:

- MELTS models and fractional crystallisation trends of major elements suggest a higher H_2O content in Segment 5 samples.
- The melting anomaly of Segment 4 and 5 consist of incompatible element enriched and radiogenic lavas.
- The enrichment of these lavas is not due to fractional crystallisation.
- Isotope ratios imply mixing between an enriched radiogenic endmember beneath Grattan seamount and an depleted unradiogenic MORB endmember beneath Segment 2 and 3.

The cause of the melting anomaly beneath Segments 4 & 5 could be either a hot mantle plume or a cold mantle heterogeneity. A mantle plume with a low excess temperature of about 50° C (Minshull et al., 1998) is unlikely because: 1) Seamounts are not aligned parallel to the motion vector of the African plate and show no age progression with distance from axis. 2) Uniform Mg# in glassy inclusions and olivine forsterite contents from all segments imply uniform mantle temperatures. Instead melting of a H_2O enriched, fertile mantle is proposed. Fertile mantle melting is confirmed by comparison with major element data from other elevated MAR areas. Higher H_2O and incompatible element concentrations are known to lower the mantle solidus significantly. The calculated H_2O mantle source concentration (Niu et al., 2001) is approx. 450 ppm beneath Segment 5 which corresponds after Wyllie (1971) and Niu et al. (2001) to a solidus temperature reduction of approx. 165°C at 3 GPa in comparison to a dry mantle solidus. HREE depletion mainly in Segment 5 lavas suggest either initial melting in the garnet peridotite stability field or melting of pyroxenite veins incorporated in spinel peridotite. An eclogitic pyroxenite source can be ruled out because of relatively high Hf/Sm ratios of the samples (van Westrenen et al., 2001) whereas melting of Ca-poor garnet pyroxenite can not be completely ruled out (although following Hirschmann and Stolper (1996) it seems unlikely). Instead melting of garnet peridotite is favored. Geochemical patterns, along axis morphology as well as a propagating rift at 8° S, which started ca. 5 Ma ago imply a northwards tending mantle flow. Partial melting of the easternmost off axis volcano E of Segment 5 seems be low (ca.1%) in comparison to Grattan seamount.

Zusammenfassung

Es werden Ergebnisse der Ausfahrt Me 41-2 vorgestellt. Ziel dieser Ausfahrt war der Mittelatlantische Rücken (MAR) im Bereich von 6° bis 11° S, 80 km E von Ascension Island, zwischen der Ascension Fracture Zone (FZ) im Norden und der Bode Verde FZ im Süden. Die Spreizungsachse ist in diesem Bereich in sechs Segmente (Segment 1-6) unterteilt, begrenzt durch non-transform offsets. Zwischen 9°S und 11°S liegen die Segmente 4 und 5 in anomal flachen Wassertiefen mit bis zu 1200 m Abweichung von der durchschnittlichen MAR-Tiefe, was auf eine Schmelzanomalie hinweist. Auf der östlichen Flanke von Segment 5 liegen drei Seamounts, die keine fortschreitende Altersentwicklung mit zunehmender Entfernung vom MAR zeigen. Außerdem ist im Gegensatz zu den tiefer gelegenen Segmenten ein axialer Graben bei Segment 5 nicht entwickelt. Seismische Daten weisen darauf hin, daß die Dicke der ozeanischen Kruste bis auf 10 km bei 9°30´ (Segment 4) zunimmt (Minshull et al., 1998). Für detailierte geochemische und petrologische Untersuchungen wurden Proben (meist vulkanische Gläser) in einem Abstand von 5-10 km im Bereich N der Ascension FZ bis zur Bode Verde FZ genommen. Die Ergebnisse dieser Untersuchungen zeigen:

- MELTS-Modellierungen und Kristallisationstrends der Hauptelemente legen einen höheren H_2O Gehalt in Segment 5 Proben nahe.
- Die Schmelzanomalie von Segment 4 und 5 besteht aus inkompatiblen Element angereicherten, radiogenen Laven,
- Diese Anreicherung kann nicht durch fraktionierte Kristallisation verursacht werden.
- Isotopenverhältnisse deuten auf eine Mischung zwischen einem angereicherten radiogenen Endglied unter Grattan Seamount und einem verarmten unradiogenen MORB Endglied unter Segment 2 und 3.

Diese Schmelzanomalie kann durch einen heißen Mantelplume oder durch eine vergleichsweise kalte Mantelheterogenität hervorgerufen werden. Ein heißer Mantelplume, der nach Minshull et al. (1998) eine Überschußtemperatur von etwa 50°C hätte, ist unwahrscheinlich aus verschiedenenGründen: 1) Die Seamounts liegen nicht parallel zur Bewegungsrichtung der afrikanischen Platte und weisen kein zunehmendes Alter mit Entfernung von der Rückenachse auf.

Einheitliche Mg# in Glaseinschlüsssen und gleichförmige Fo-Gehalte in Olivinen weisen auf einheitliche und vergleichsweise niedrige Manteltemperaturen hin. Es wird daher vermutet, daß die Ursache dieser Schmelzanomalie das Schmelzen eines H_2O angereicherten fertilen Mantels ist. Dies wird durch den Vergleich mit Hauptelementdaten anderer bathymetrischer Anomalien des MAR bestätigt. Höhere H_2O -und inkompatible Elementkonzentrationen erniedrigen den Mantelsolidus beträchtlich. Die nach Niu et al. (2001) errechneten H_2O-Gehalte des Mantels unterhalb von Segment 5 liegen bei etwa 450 ppm, was nach Wyllie (1971) und Niu et al. (2001) eine Soliduserniedrigung von etwa 165°C bei 3 Gpa im Vergleich zum trockenen Solidus verursacht. Die Verarmung an Schweren Seltenen Erdelementen (SSEE) ist entweder auf den Beginn der Schmelzbildung im Granat-Peridotitfeld zurückzuführen oder auf den Einfluß von Granat-Pyroxenitgängen, die im Spinellperidotite enthalten sind. Eklogitgänge sind aufgrund der hohen Hf/Sm Verhältnisse der Proben (van Westrenen et al., 2001) unwahrscheinlich. Allerdings kann das Vorkommen von Ca-armen Granat-Pyroxeniten im Mantel unterhalb der Anomalie nicht vollkommen ausgeschlossen werden, scheint aber nach Hirschmann and Stolper (1996) eher unwahrscheinlich. Partielles Schmelzen eines Granatperidotits wird daher bevorzugt. Geochemische Muster, achsenparallele Morphologie sowie ein propagierendes Rift bei 8° S, das vor etwa 5 Ma entstand, weisen auf einen nordwärtsgerichteten Mantelfluß. Im Vergleich zu Grattan Seamount ist der Grad der partiellen Schmelzbildung beim östlichsten Seamount gering und liegt bei etwa 1%.

TABLE OF CONTENT

CHAPTER 1

OCEAN MAGMATISM

CHAPTER 2

THE MAR BETWEEN 6° AND 11°S

CHAPTER 3

SAMPLING AND ANALYTICAL METHODS

CHAPTER 4

RESULTS

CHAPTER 5

DISCUSSION

CHAPTER 6

CHAPTER 1

INTRODUCTION – VOLCANISM IN THE OCEAN

1.1 Mid-ocean ridges

1.1.1 Introduction

The purpose of this thesis is to present new geochemical data of basaltic glasses and minerals from an abnormal part of the mid-ocean ridge near Ascension in order to provide constraints on mantle sources, melt production and fractional crystallisation. In order to clarify the causes which led to the building of this abnormal ridge it is necessary to give an introduction into current knowledge about ridge morphology, ridge segmentation, mantle models and geochemical reasoning.

Compared to continental volcanism mid-ocean ridge volcanism is a more hidden phenomenon, normally hidden under some thousand meters of seawater. Due to this, little or nothing was known about it up to the second half of the 20th century. Since that time knowledge about oceanic volcanism increased and it is clear that it has an enormous impact on the energy and material budget of the earth. Beside volcanism at mid-ocean ridges (MOR), which occurs at divergent plate boundaries, other volcanic features are present in the oceans. Back-arc spreading centers and ocean island arcs form at convergent oceanic plate boundaries but are not relevant to this work and are only mentioned here for the sake of completeness. In addition to mid-ocean ridge volcanism oceanic intraplate volcanism plays another role in this study. Ocean intraplate volcanism produces ocean island basalts (OIB) and occur within plates but also at mid-ocean ridges. This will be discussed later in more detail.

1.1.2 Morphological and tectonic variety

Fresh basaltic glasses from abyssal parts of the ocean basins were accidentally recovered for the first time in 1898 while a submarine cable was repaired in the North Atlanitic. This was the first hard evidence that active submarine volcanism occurred at “mid ocean mountains” nowadays called mid-ocean ridges (MOR). Global MOR produce 20 km^3 new ocean crust per year and present the largest, most continuous volcanic system of the earth. Figure 1.1 shows the global MOR system of the earth. These ridges are not uniform but differ significantly in terms of spreading rate, morphology, tectonics and chemical composition. In a first approach MOR can be divided into slow-, medium- and fast-spreading ridges. At slow spreading ridges like the Mid-Atlantic Ridge (MAR) the plates separate with a velocity of 10-40 mm/a, intermediate-spreading centers like the Indian Ridge show velocities of 40-80 mm/a and fast spreading center e.g. the East Pacific Rise (EPR) spread with 80–160 mm/a.

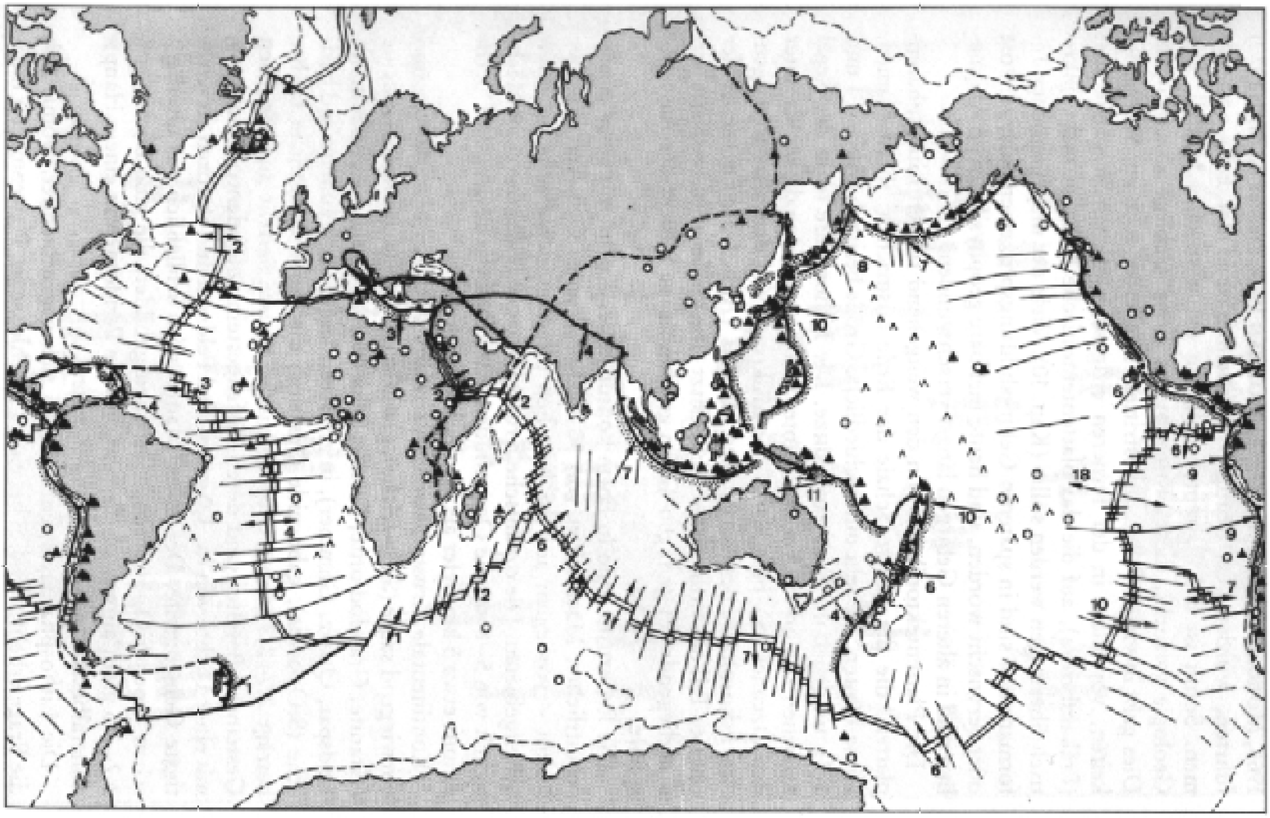

Figure 1.1: Global mid-ocean ridge system, taken from a textbook of Frisch and Loeschke 1990

This classification is supported by distinct morphologies of slow, medium and fast spreading centers both across and along axis as shown in Figure 1.2. Fast spreading ridges like the EPR show compared to the MAR a more balanced morphology. No axial valley can be found and the neovolcanic zone is very narrow, generally < 2 km. Along axis morphology is smooth. All these features imply that at fast spreading ridges magmatism dominates over tectonic stress in controlling the axial processes. In contrast, the slow-spreading MAR shows a large

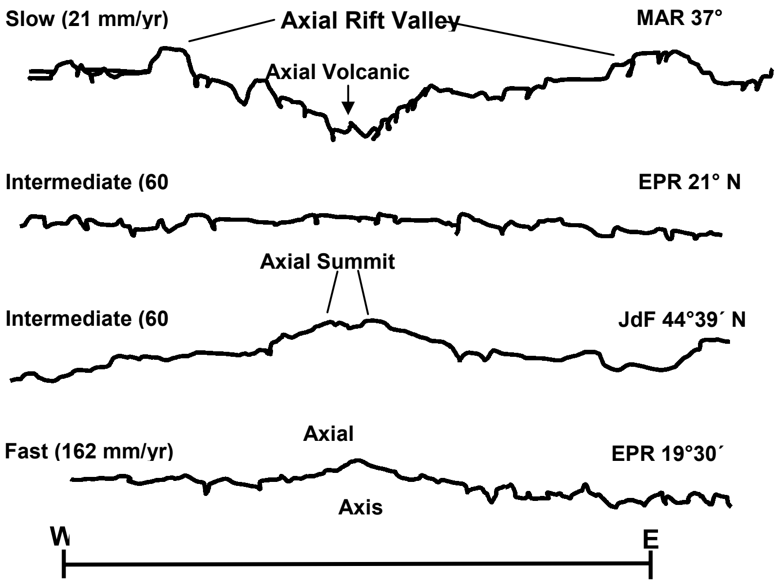

Figure 1.2: Mid-ocean ridge axial morphology, see text for discussion

axial valley (-20 km wide and 1-2 km deep) (Sigurdsson, 2000). Magmatism is not well focused and can occur across the entire axial volcanic ridge, which can be 1-5 km wide and is found in the middle of the rift valley. Small axial volcanoes are common. Rough topography both along and across axis indicates a predomination of tectonism over volcanism.

MOR are broken and offset by major faults, called Fracture Zones (FZ). These first order segments reach lengths of 400-600 km and are subdivided by non transform offsets into segments of some tens of kilometers. These 2nd order segments might overlap at fast spreading centers (Macdonald et al., 1988) but not at slow spreading centers. Geophysical observations suggests at fast spreading center relatively small but elongated magma chambers beneath the 2nd order segments even at overlapping parts (Kent et al., 2000), whereas at slow spreading center axial magma chambers (AMC) are rare and small and not easily detectable but do exist (Calvert, 1995). Modelling studies exploring buoyant mantle flow beneath MOR have indicated that at slow spreading axes a more focused mantle flow occurs, whereas fast-spreading axes are fed by a more widespread mantle flow regime (Forsyth, 1992). It should also be noted that 2nd order segments can propagate and so change their position in time. Propagating rifts are known at fast and medium spreading centers. From the South Atlantic MOR only some places are known (see Chapter 2). Moreover 2nd order segments of the MAR are variable in size and also height but generally have a length of tens of kilometres. Often these segments are displaced relative to one another through small offsets. Usually the length of 2nd order segments decreases to fracture zones and the discontinuities reflect breaks in the volcanic plumbing systems that feed the axial zone of magmatism. Thus the mantle itself seems to play an important role in the process of segmentation. This is also confirmed by Langmuir et al. (1986) who pointed out that segmentation is not only morphological but also chemical. The fact that the MAR shows a rough topography makes a definition of “normal” axial water depths at the MAR not easy but Hayes (1988) calculated a zero-age ridge crest depth of 2700 on global scale. Corresponding to this White et al. (1992) showed that away from melting anomalies and fracture zones oceanic crustal thicknesses are very similar, even at fast and slow spreading ridges with half spreading rates between 10-75 mm. He pointed out that mean crustal thickness of normal Atlantic crust younger than 30 Ma is 6.97 +/- 0.57 km. At melting anomalies ocean crustal thickness differs markedly from this value.

1.1.3 Melting anomalies at the MAR

MAR bathymetric anomalies can be divided into three main groups, these are short, medium and long wavelength anomalies. All of these bathymetric anomalies are associated with higher crustal thicknesses and shallower water depths. Long wavelength anomalies can be detected over several hundred kilometers. Medium wavelength anomalies have a size of approx. two hundred kilometers, with two or three 2nd order segments being affected. Short wavelength anomalies affect only single 2nd order segments. Figure 1.3 shows the effect on ridge morphology of selected anomalies. A long wavelength anomaly can be found N and S of Iceland, the South Kolbeinsey Ridge (SKR) and the Reykjanes Ridge respectively. Both ridges show, besides the abnormally shallow water depth, another feature which is unusual for a slow spreading ridge: the lack of a median rift valley. This feature appears when crustal thicknesses exceed a value of 9 +/- 1 km (Detrick et al., 1995) and can also be observed at short and medium wavelength anomalies. Searle et al. (1998) obtained a crustal

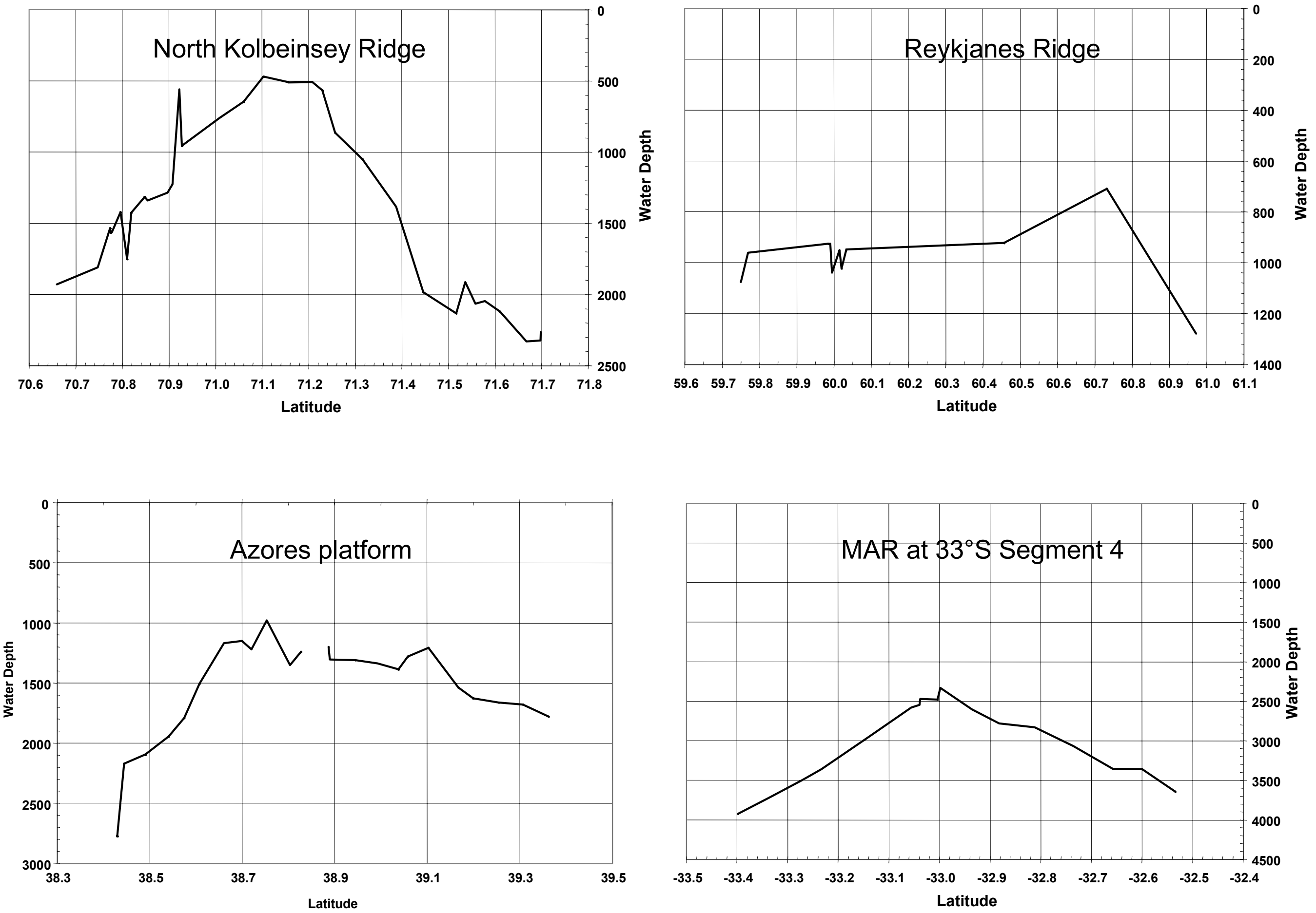

Figure 1.3: Along axis topography of melting anomalies from the MAR

thickness of 11.2 km on the ridge axis for the Reykjanes Ridge at 61°44´ with a corresponding water depth of 600 m which is quite high in comparison to the normal 6.97 km ocean crust thickness. Medium wavelength anomalies can be found in the N at the Middle Kolbeinsey Ridge (MKR). Kodaira et al. (1997) investigated the crustal structure by use of ocean bottom seismographs. They suggest a crustal thickness of 6.8 km in the South at approx. 69° 30´ N and 10 km in the North at approx 70° 20´N. The unusual crustal thickness of 10 km in the N of the profile corresponds with a water depth of ca. 1000 m. Another example for a medium wavelength anomaly is the spreading axis in the vicinity of the Azores, called the Azores Platform (Detrick et al., 1995). Following Detrick et al. (1995) five 2nd order segments, named from north to south KP-1, KP-2, KP-3, KP-4, KP-5, can be differentiated between the Pico Fracture Zone (FZ) in the S and the Kurchatov FZ in the N. Segment KP1, KP-2, KP-3 shallow continuously southwards, starting with ca. 2600 m at KP-1 to 1300 m at KP-3. Also it should be noted that this bathymetric shallowing is not symmetric, a steeper deepening can be seen on the southern end of KP-3. Associated with this bulge is a high negative Mantle Bouguer Anomaly (MBA) and the lack of a median rift valley. As ocean crust is less dense than the underlying mantle, a thicker crust will lead to a slightly lower gravity value, the negative MBA. Detrick et al. (1995) calculated a maximum crustal thickness of >8-9 km. KP-4 and KP-5 near the Azores Platform show a short wavelength topographic anomaly which means that each segment shows a pronounced topographic high (water depth ca. 1000 m) in the middle while segment ends lie in greater water depths. In addition no deep axial valley is present in the segment middles. It is surprising that no pronounced negative MBA is developed. At 35°N the MAR shows a 2nd order segment with a bathymetric anomaly which is combined with a negative MBA, the well studied segment OH-1 (e.g. Niu et al., 2001; Hooft et al., 2000; Detrick et al., 1995). Segment OH-1 has a minimum depth of 2135 m, the axial valley is shallow. Hooft et al. (2000) suggests a crustal thickness of ca. 8 km. Another small short wavelength anomaly has been reported from the South Atlantic at 33° S. Seg. 4 (Michael et al., 1994) W of Tristan da Cunha shallows to 2483 m with a corresponding crustal thickness of 8 km +/- 0.5 km (Tolstoy et al., 1993), also with a poorly defined axial valley.

1.1.4 Volcanism and excess volcanism at the MAR

Mantle melting at MOR is a result of adiabatic decompression of ascending mantle material (Figure 1.4). The upwelling mantle does not cool as fast as it is brought upwards. As a consequence the mantle solidus will be crossed at a particular depth. Three different processes may control the depth in which first melts are produced and thus the extent of melting: 1) mantle temperature, 2) composition of the mantle, 3) spreading rate. Hotter or more fertile mantle (a mantle which has not previously lost melt or has been metasomatized) will melt in greater depth than mantle which is colder or more depleted. The whole length of the mantle in which melting occurs is known as the melting column. The mantle will not melt completely, only to a certain amount, this is known as the degree of partial melting. Because the melt is less dense than the mantle, it will segregate from its source and ascend. These melts may erupt independently, mix or react with the mantle through which they pass. This collection of processes has been called dynamic melting, for details see McKenzie and O´Nions (1991; Forsyth (1992) and Devey et al. (1994). Melting experiments on mantle rocks (Kinzler, 1997; Kinzler and Grove, 1992) which have the advantage that the mantle composition is known, predict a variation in initial melting pressures from approx. 12 to 30 kbar, this is ~36 to ~90 km depth. The corresponding “normal“ MAR water depth is - as pointed out earlier - approximately 2700 m. (Klein and Langmuir, 1987; Langmuir et al., 1992; Kinzler and Grove, 1992; Niu and Batiza, 1991) used major element compositions of naturally and experimental derived MORB to infer melt proportions and melting depths in both quantitative and qualitative ways. Primary differences in major element chemistry e.g. partial melting are mostly obscured by fractional crystallisation processes which makes it necessary to eliminate different stages of crystal fractionation and recalculate major element compositions to a fixed MgO concentration (commonly to MgO 8 % wt.). Recalculated SiO_2 and FeOt (total Fe) can be used for calculating depth (and pressure) of melting. Trends of global scale suggest that low SiO_2 and high FeOt indicate higher depths of initial melting.

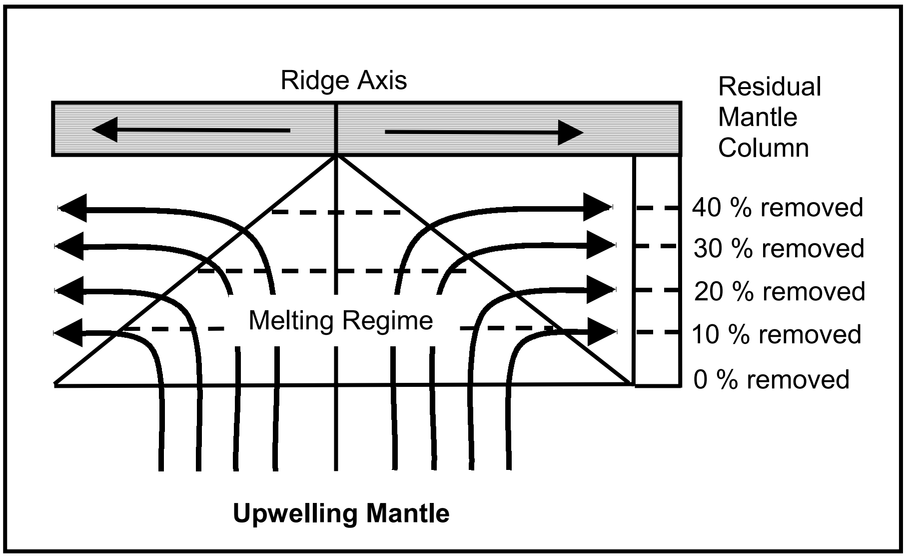

Figure 1.4: Adiabatic upwelling and decompressional melting, after Langmuir et al. (1992)

Following Klein and Langmuir (1987); Langmuir et al. (1992) this is due to the expansion of the melting column to greater depths, as a result the average depth of melting is greater. Expanded melting columns lead to higher degrees of partial melting. This is recognized by higher concentrations of mainly CaO and to a lesser extent Al_2O_3. The incompatible element Na is diluted at higher degrees of melting. The model of Klein and Langmuir (1987) and the calculations of Niu and Batiza (1991) are mainly based on the assumption that the composition of MOR magmas is due to different degrees of partial melting which in turn are the consequence of different mantle temperatures. Considering mantle temperatures Davies (1988) found that mantle temperature variations within the convecting mantle are small and within a few tens of degrees of the adiabatic gradient if areas of subduction and hot-spots are excluded. Also in the late 1980´s temperature estimates of mantle potential temperature (the potential temperature is the temperature after decompression to 1 atm.) were done. McKenzie and Bickle (1988) suggested a mantle potential temperature of 1280°C. The authors used this T to model thickness and composition of MORB and a good consistence with naturally occurring MORB was achieved. Calculated primary MgO contents were 11 % wt. Temperature calculations of Klein and Langmuir (1987) led to nearly similar results with a potential mantle temperature of slightly more than 1300°C and primary MgO contents of likewise 11 % wt. Erupting melts have commonly MgO concentrations of 7-9 % wt., which implies a reduction of the MgO concentration of 2-4 % wt. by crystal fractionation. As a result elevated mantle temperatures can only be expected in the vicinity of hotspots. In other words it was thought that bathymetric anomalies were built through the influence of hotspots. Nowadays the mantle composition e.g. the H_2O content as another cause of different degrees of partial melt is more emphasized even at hotspots (see also Chapter 6). High spreading rates (Niu and Hekinian, 1997) can also increase partial melting. Although a dependence of mantle melting and spreading rate exists, this process might not be a major reason for depth variation at the MAR due to the relatively uniform and low spreading rates at the MAR (approx. 2–4 cm/a) (Smith, 1981) and thus seems to be neglectable. In other words, the dependence of melt production on spreading rate at MOR is of global and not regional importance. In conclusion if only elevated ridge segments of the Atlantic are compared two causes should be considered: Higher mantle temperatures produced by the influence of hotspots and melting of a fertile mantle (mantle heterogeneity).

1.2 Hotspots

1.2.1 Current Models

The term hotspot was used first by Wilson (1963) in order to explain ocean-island chains. In his model hot mantle material penetrates the rigid ocean lithosphere and forms ocean-island chains like a welding torch welding on a moving plate. These linear island chains contain only a few volcanoes and sometimes just one active at any given time. Morgan (1971) proposed that hotspots are created by narrow plumes rising from the deep mantle. In addition seismic evidence was found for a discontinuity at 660 km depth (e.g., Ringwood, 1988). This led to the geochemical two layer standard model. In this two layer model the upper mantle above the 660 km discontinuity is depleted in incompatible elements due to melt segregation forming the earth´s crust. The lower mantle below 660 km was thought to be less or non depleted and chemically uniform. Material of the lower mantle forms at the 660 km discontinuity mantle plumes that rise to the earth´s surface producing radiogenic and enriched ocean-island basalts (OIB´s) in contrast to the unradiogenic and depleted MORB from the upper mantle (Hofmann, 1997). Nowadays this standard model seems to be untenable because OIB´s which form at hotspots are geochemical by highly variable (see below). This precludes their derivation from a chemically uniform primitive mantle. On the basis of radiogenic isotope ratios and trace element ratios, the following plume sources have been distinguished: HIMU, EM-1 and EM-2. HIMU stands for “high μ“, where μ is the ratio of $^{238}U/^{204}Pb$. EM-1 and-2 means enriched mantle 1 and 2 respectively. Also a component which is common to many plumes is involved and called FOZO or C. FOZO and C differ slightly in composition but both are not derived from MORB source. In different plots of isotope and trace element ratios these plume sources must not necessarily define endmembers but always build clusters regardless of their regional provenience (Hofmann, 1997). The origin of FOZO and C is thought to be the lower mantle. The sources of OIB are enriched in mantle incompatible trace elements HIMU basalts are generally depleted in Rb and Ba, this distinguishes HIMU basalts from EM-1 basalts which are not depleted in Rb and Ba. HIMU ratios of Rb/Sr are low, as ^{87}Rb decays to ^{87}Sr HIMU ratios of $^{87}Sr/^{86}Sr$ are also low. HIMU has the highest Pb ratios and the lowest $^{87}Sr/^{86}Sr$ ratio of any OIB, $^{87}Sr/^{86}Sr$ is as low as MORB, $^{143}Nd/^{144}Nd$ ratios are moderate and lie between MORB and EM-1,2. Examples of HIMU hotspots are St. Helena, Austral Islands, Balleny Islands and the Azores. EM-1 has moderate $^{87}Sr/^{86}Sr$, low $^{143}Nd/^{144}Nd$ and the $^{208}Pb/^{204}Pb$ ratio is slightly higher than MORB. Examples are Tristan and Pitcairn. EM-2 samples have the highest hotspot $^{87}Sr/^{86}Sr$, relatively high $^{207}Pb/^{206}Pb$ and $^{143}Nd/^{144}Nd$ ratios which lie between EM-1 and EM-2. Examples are Society and Samoa Islands. OIB $^{3}He/^{4}He$ ratios are not uniform but range from 5 to 30 R/R_A. Furthermore $^{3}He/^{4}He$ ratios observed in Mauna Loa show temporal trends, whereas a temporal homogeneity exists on Reunion. Clearly not all OIB are derived from primordial mantle material. High ^{3}He/^{4}He are found in the Pacific at: Hawaii, Galapagos, Easter, Juan Fernandez, Pitcairn, Samoa; in the Indian Ocean at: Reunion, Heard islands; and in the Atlantic at: Iceland and Bouvet. After Hofmann (1997) is the HIMU plume source enriched in former MORB. Loss of lead through hydrothermal ridge and subduction processes increases the U/Pb and Th/Pb ratios. The same author suggests that the source of EM-2 is a mixture of oceanic crust with a little amount of continent derived sediment. This will lead to high ^{207}Pb /^{204}Pb and ^{87}Sr/^{86}Sr isotope ratios and low Nb/U and Ce/Pb trace element ratios. The nature of EM-2 source remains after Hofmann (1997) uncertain. Low ^{206}Pb/^{204}Pb, slightly low Nb/U and high ^{208}Pb*/^{206}Pb* suggests either recycled pelagic sediment or ancient subcontinental lithosphere as a mixing partner of oceanic crust.

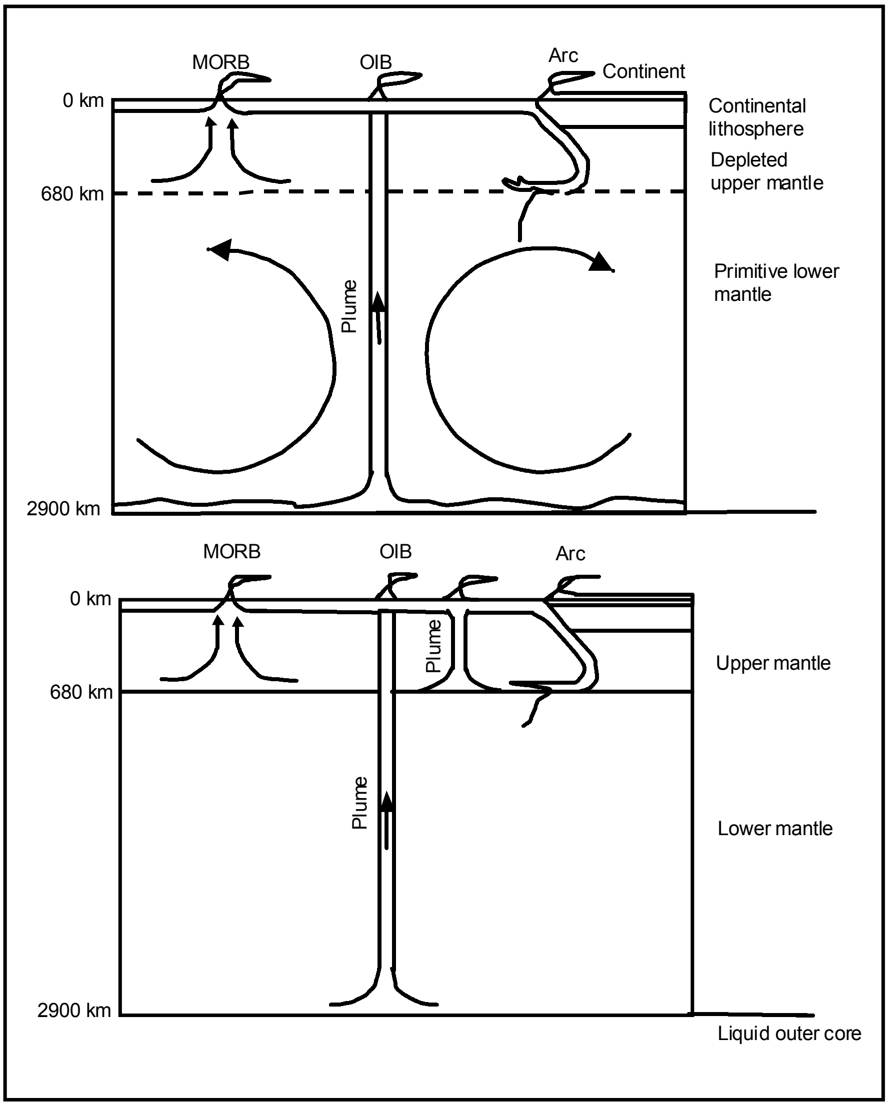

Figure 1.5: Current mantle plume models, taken from Hofmann (1997), see text for discussion

Geochemical charcterization

Isotopes: If two basalts have, for example, different $^{143}Nd/^{144}Nd$ ratios it tells us not only that their mantle sources had different initial Sm/Nd ratios, but also that these differences existed for geologically long times (10^8 years or more) as a cause of the long half live of mother isotope ^{143}Sm which will decay to ^{143}Nd.

Strontium isotopes: The important strontium isotope ratio is $^{87}Sr/^{86}Sr$. Where ^{86}Sr is the stable nonradiogenic isotope and ^{87}Sr stems from the long-lived (simplified) radioactive decay of $^{87}Rb \rightarrow ^{87}Sr$, with a half-life of $48.8*10^9$ a. Rb is more (mantle) incompatible than Sr, a depletion of Rb leads to a decrase in radiogene ^{87}Sr, a depleted source will have a low $^{87}Sr/^{86}Sr$

Neodymium isotopes: According to strontium isotopes the important neodymium isotope ratio is $^{143}Nd/^{144}Nd$. Where ^{144}Nd is the stable nonradiogenic isotope and ^{143}Nd stems from the long-lived (simplified) radioactive decay of $^{143}Sm \rightarrow ^{143}Nd$ with a half-life of $106*10^9$ a. Opposite to Sr, Nd as the daughter of Sm is more (mantle) incompatible than Sm, therefore a depleted source will have a high $^{143}Nd/^{144}Nd$ due to the enrichment of Sm relative to Nd and subsequent growt.h of ^{143}Nd.

Lead isotopes: Pb has 4 naturally occuring isotopes ^{208}Pb, ^{207}Pb, ^{206}Pb and ^{204}Pb. Only the latter, ^{204}Pb, is nonradiogenic whereas ^{208}Pb, ^{207}Pb, ^{206}Pb are of radiogenic origin. ^{204}Pb is therefore used as a stable reference isotope. The simplified long-lived decay scheme is as following:

232Th → 208Pb with a half-life of $14.01*10^9$ a.

235U → 207Pb with a half-life of $0.738*10^9$ a.

238U → 206Pb with a half-life of $4.468*10^9$ a.

Due to the higher incompatiblety of U a source depletion leads to lower U concentrations and therefore to lower radiogene Pb concentrations. This is also true for the system Th-Pb.

Helium isotopes: ^4He is a product of radiogenic decay of U and Th and is permanently and primarily produced in the earth´s crust. ^3He is a non radiogenic isotope and is considered to be a primordial component from early times of the earth. Helium is constantly degassed into the atmosphere and into space. Since ^4He is, in contrast to ^3He, continously generated, low $^3He/^4He$ R/R_A ($R/R_A=(^3He/^4He)obs / (^3He/^4He)atm$) ratio exist in degased MORB and continental crust. Continental crust $^3He/^4He$ ratios (0.01 R/R_A) are very low due to ^4He production of U and Th which is enriched in continental crust.

Nowadays mantle plumes are thought to generate 20–40 stationary hotspots (Hofmann, 1997) which is in contrast to former estimates from Burke and Wilson (1976) who supposed a number of 122 hotspots to be active during the past 10 Ma and 53 close to MOR. The geochemical characteristics lead, in the view of Hofmann (1997), to a model of layered mantle convection, in which the layers are not perfectly isolated (Figure 1.5). Plumes may arise both from the 660 km discontinuity and from the core-mantle boundary. Small, short lived plumes carrying non primordial ^{3}He are most likely to be generated at the 660 discontinuity. Large, long-lived ^{3}He-rich plumes are more likely to come from the core-mantle boundary. In turn, different ^{3}He/^{4}He ratios in plume derived material suggest that mantle plumes may sample primitive, less degassed mantle as well as recyled oceanic crust material. Seismological evidences exists that subduction slabs may reach the core-mantle boundary (van der Hilst et al., 1997) and also the 660 km discontinuity. Subducted oceanic crust is considered to be a potential plume source. Campbell and Griffiths (1990) suggests that a plume originated at the CMB may attain a diameter of about 1000 km by the time it reaches the top of the mantle. At the base of the rigid lithosphere the ascent is stopped and the plume head spreads out and flattens to a lens 2000 km wide and 180 km thick. In contrast to this, a plume originating from the 660 km discontinuity will have a diameter of 250 km before flattening and 500 km after flattening (Campbell and Griffiths, 1990; Griffiths and Campbell, 1990). Heating lowers the density of the plume and lets it rise. This leads to the question of how much hotter, in comparison to the surrounding mantle, these mantle plumes are. This is also called the excess temperature. Excess temperature estimates for mantle plumes were made by Schilling (1991) who investigated 13 plumes located near spreading centers. The mantle plumes had a geochemical influence on the composition of basalts erupted on these spreading centers. Based on the width of the geochemical anomaly and the abnormally high (excess) ridge elevation along the ridge axis, Schilling defined a simple plume source-ridge sink model and estimated the volume fluxes and temperatures of these plumes. The calculated excess temperature of these plumes fall in the range of 160-280 K, which is in reasonable agreement with other estimates made with independent methods and approaches (White, 1995). Given the uncertainty in Schilling´s temperature estimates (+/-50K) plume temperatures appear to be remarkable uniform (White, 1995). High temperatures will also lead to extrusion of high MgO lavas i.e. picrites or komatites due to higher partial melting and thus melting of high MgO mantle mineral phases like olivine. From a more experimental point of view Griffiths and Turner (1998) give a comprehensive overview of mantle - plume interaction. Their studies revealed some interesting mixing features. Subducted oceanic lithosphere descends through the lower mantle to the core-mantle boundary (CMB). As these slabs sink, surrounding mantle will be pulled down, leading to heterogeneities in the mantle if these mantle pieces are not brought to the

CMB. Additional complication comes as the subducted slab is not homogenous, consisting instead of MORB and a depleted mantle layer and maybe of some former sediments. After Davies (1990), heat is transported conductively from the hotter core into the overlying mantle leading to the formation of a thermal boundary layer, also known as the D`` layer. Plumes will rise from the boundary layer when conductive heating has lowered the density sufficiently. On their way through the mantle, plumes will develop mushroom shaped plume heads. These plume heads will, after Griffiths and Turner (1998), entrain and drag upwards large masses of mantle material. Campbell and Griffiths (1990), following computer simulations of Davies, argues that the entrained material will mostly be from the bottom of the lower mantle, entrainment of upper mantle material seems not likely. The magnitude of such transport may be one magnitude greater than the mass flux within the plume (Griffiths and Turner, 1998). Hill (1991) calculated that plume heads ascending every 20 Ma (based on geological data of the last 250 Ma) would fill a volume equal to the upper mantle every 1200 Ma. Since the same authors suggest a total mantle flushing time of 100 Ma, plume material and mantle material will be mixed. Also experiments suggest a large stirring effect that will develop when a convecting upper mantle passes around a stationary plume. Large areas of the uppermost mantle will be mixed with plume material. As pointed out before it is known that ancient oceanic crust plays an important role in plume magmatism. Experimental petrologists and mineralogists emphasise the role of eclogite in mantle plumes which is the high pressure equivalent of basaltic crust. The role of eclogite in plumes remains uncertain and is not free of petrological and geochemical problems (see Jackson, 1998). Also geochemical characteristics of mantle plumes can not be yielded with eclogite alone but needs also other material, most likely lower mantle material. Eclogite is a petrological term and has a definite mineralogical composition. Geochemical investigations of plume magmas allows us only to say that oceanic crust with or without sediments may have played a role in a specific plume. Nothing can be said about a specific petrology in the plume melting zone at ca. 100 km depth. Because of this any further considerations about possible melt sources will be based on geochemical signatures alone.

1.2.2 Hotspots and MOR

Hotspots must not always occur within plates but can also lie in the vicinity of MOR. In the case of Iceland a mantle plume appears to be seated directly beneath the ridge. This island defines the top of an approx. 20 km thick oceanic crust. This is when compared to ”normal” 7 km thick oceanic crust, a huge excess volcanism which has found much attention (White, 1988; White, 1990; White and Morton, 1995; White et al., 1995; White, 1997). Also the lateral extension of thickened crust is remarkable. Isotopic compositions of lavas suggest an influence of a more radiogenic and so more fertile or primitive Iceland plume on 2400 km (Taylor et al., 1997). Vogt (1971) proposed a hot Iceland plume to be responsible for building this anomaly. More recent seismic observations (Wolfe et al., 1997) show a narrow plume of hot upwelling mantle beneath Iceland. Data of Wolfe show a cylindrical zone of low P- and S-wave velocities that extends from 100 to at least 400 km depth beneath central Iceland with a relatively narrow radius of about 150 km. Iceland volcanic rocks show also a wide range of chemical and radiogenic isotope compositions which suggest a heterogeneous plume. Based on isotope data Mertz and Haase (1997) showed that the Iceland plume is a product of MORB asthenosphere – plume mixing.

The principle is clear, if a mid-ocean ridge is affected by a hotspot, the temperature of the mantle should be higher, partial melting will increase and thus an excess of melt will produce a thicker oceanic crust. Low normalized Na content in Icelandic MORB are interpreted as a product of dilution. For Tristan da Cunha it is known that this island is related also to a mantle plume, which lies under the eastern flank of the MAR. This hotspot produces a track of islands and seamounts trending to the east tracking the movement of the African plate (O´Connor and Duncan, 1990).

1.3 Mantle heterogeneity

Although the depleted mantle is relatively homogeneous in comparison to other mantle reservoirs, significant heterogeneity does exist within this reservoir and are permanently being produced by subduction processes and rising of mantle plumes as pointed out before. Undisputed hot mantle plumes (e.g. Hawaii, Iceland) occur and they themselves change upper mantle chemistry and its ability to melt. However hot mantle plumes may not be reponsible for all mantle heterogeneities, especially oceanic volcanic edifies at a distance from MOR. Batiza (1982) pointed out that the ocean crust exhibits thousands of small isolated volcanic seamounts littering the crust randomly which are presumably the result of melting anomalies due to mantle heterogeneities. Such heterogeneities may consist of fertile mantle which has the opportunity to segregate more melt in comparison to depleted upper mantle. These heterogeneities are not significant hotter than the surrounding mantle, in fact they need only lower temperatures to melt. Thus mantle heterogeneities including fertile mantle are, beside hotspots, an appropriate tool in genering excess volcanism at MOR. In a review of Helffrich and Wood (2001) considering the earth´s mantle the idea of a heterogenous mantle plays an important role. Advanced geophysical techniques using scattered waves give new insights into mantle structure. They revealed heterogeneities in a size smaller than 10 km, mostly < 4 km. The distribution of these heterogeneities is homogenous and extends from the base of the mantle into the MORB melting region, 40-80 km below the surface where they are destroyed via melting. This leads to the idea that MOR may act as a sink for mantle heterogeneities.

As Iceland is a good example for a hot mantle plume, the MAR in the vicinity of the Azores and the Azores archipelago itself may be an example for hot mantle heterogeneities. The Azores are not aligned in a hotspot typical island chain, which may be interpreted as a sign for a non hotspot origin. On the other hand complex tectonics (Azores triple junction) and the vicinity to the MAR may supress classic plume tracks. The Azores Platform shows a respectable elevation combined with thickened crust, due to excess volcanism. Bonatti (1990) calculated on the base of peridotite composition 20 % melt extraction for the MAR in the vicinity of the Azores which is, in comparison to other areas (as low as 8 %) of the MAR, a huge amount of partial melting. If temperature is the sole cause of this excess volcanism, an excess temperature of 250-300°C (Klein and Langmuir, 1987) has to be supposed. Bonatti compared these assumed excess mantle temperature with temperature estimates inferred from peridotite equilibration temperature using geothermometers of Wells (1977; Lindsley (1983). These calculated temperatures should, as Bonatti emphazised, be taken as relative rather than absolute values and as some reequilibration can not be ruled out, calculated temperatures may reflect cooling rates of upwelling mantle bodies rather than melting temperatures but upwelling mantle in a hot-spot region should clearly be hotter than ”normal” upwelling mantle. Estimated temperatures from the Azores MAR appear to be lower or at least not higher than those estimated from peridotites from elsewhere along the MAR. Thus the chemical composition of the mantle underlying the Azores MAR is the only factor controlling the extent of melt. MORB from this region contains 3 times more H_2O as normal MORB and tends to have lower SiO_2 contents which also points to an H_2O enriched source (Bonatti, 1990). H_2O can lower the melting temperature of a peridotite by hundreds of degrees (Bonatti, 1990). Another important feature of the mantle underlying the Azores MAR emphazied by Bonatti is the strong enrichment of LILE (Large Ion Lithophile Elements: Cs, Rb, K, Ba, Pb, Sr, Eu) relative to normal MORB as estimated and calculated by White and Schilling (1978). Such LILE enriched mantle is also known from the Zabergad peridotite complex located at the Red Sea, a mantle body from a pre-ocean rift. This peridotite complex consists of undepleted spinel lherzolite, veined by metasomatic LILE-enriched H_2O bearing amphibole peridotite, all this in a meter scale. $^3He/^4He$ ratios from samples of the Azores platform are not higher than MORB, the opposite could be expected if a strong plume from the CMB would be the cause of this melting anomaly. In fact $^3He/^4He$ tend to be lower than average MORB. Two possibilities do exist which might be the cause of such low values: incorporation of old subducted crust or He degassing from a metasomatic event, possibly a continental rift. Metasomatism seems also to play an important role in North Kolbeinsey Ridge (NKR) basalts, north of Iceland as disscused by (Haase et al., 1999). These incompatible element enriched basalts exhibit some interesting chemical pattern which hint at metasomatism. After Haase

NKR basalts are in terms of $(La/Sm)_N$, and Nb/Zr more enriched than OIB with anomalously high Nb/Zr. It is also notable that NKR basalts are heterogenous, with different degrees of enrichment in lavas spaced < 5 km. Enriched lavas of the NKR with high $(La/Sm)_N$ have, compared to depleted MORB, low $Fe_{8.0}$. This behavior of FeO is at first sight not expected. FeO acts like an incompatible element during mantle melting, similar to many trace elements like the REE, so trace element enriched magmas should have higher FeO contents. In addition FeO contents are pressure dependent with high FeO at high pressures, expected at enriched magmas with increased melting columns. In view of this NKR basalts show signs of metasomatism, a depleted source indicated throughout low FeO is metasomatized by an unusual melt or fluid with high $(La/Sm)_N$, and Nb/Zr. Haase (pers. com.) prefers an amphibole rich residual mantle because amphibole enriches Nb and Ba relative to clinopyroxene (cpx) and thus melting of such peridotite will release these elements. As a reacting component carbonatites or highly alkaline silicious melts seem to be most likely because mantle peridotite which reacted with these kind of melts have high Nb/Zr.

Short wavelength anomalies are most likely to be the result of melting of a heterogenous mantle. The latest work on these small anomalies has been done by Niu et al. (2001) who investigated the well known OH-1 segment at ca. 35° N, south of the Azores. Chemical parameters of this segment differ significantly from the one of the more normal segment OH-3 to the north, as do morphological and geophysical features. OH-1 basalts have lower MgO than OH-3 samples and they have significantly higher incompatible element abundances and ratios, including Na_2O, than OH-3 samples. Enriched lavas occur exclusively at segment centers, preferently on segment OH-1. Enrichment is due to source enrichment and cannot be explained by crystal fractionation. Depleted basalts occur along the entire length of both ridge segments. In the view of (Niu et al., 2001) this excess volcanism combined with source enrichment can only be explained by melting of a fertile mantle. In concordance with Bonatti (1990) Niu emphasizes the role of H_20 in mantle melting.

1.3.1 Hotspots vs mantle heterogeneity

After Davies (1990) thermal plumes can be expected in a cooling earth whereas there is no plausible dynamical scheme to account for the origin of long lived, slow moving wet spots and no compelling geochemical evidence for their existence. Since Klein and Langmuir (1987) revealed the global correlations of ocean ridge basalt chemistry with axial depth and crustal thickness, temperature was thought to play the dominant role in changing the extent of melt and crustal thickness. In conclusion it was not thought that increased melt production caused by melting of fertile mantle heterogeneities played an important role. During the last few years this point of view has changed (Bonatti, 1990; Niu et al., 2001; Helffrich and Wood, 2001) undisputed hot mantle material is brought upwards but also “cold” mantle heterogeneities do exist. This different point of view may have some consequences. There are calculations especially for MOR which are based on the dependence of element concentrations on mantle temperature, e.g. the extent of melt calculation from Niu and Batiza (1991). These calculation work if the upper mantle is more or less homogenous and element concentrations are only affected by the extent of melt. They may not be satisfying if the upper mantle is heterogenous and element concentrations in the melt are affected by the source in first order. This is especially true for incompatible elements which are not abundant in the source but may affect strongly the ability of the source to melt.

Conclusions

1) Slow- and fast spreading ridges show typical morphological features
2) Three different sizes of melting anomalies occur at the MAR
3) Melting anomalies have different geochemical parameter than "normal" parts of the ridge axes.
4) Hotspots and mantle heterogeneities are the causes of melting anomalies at the MAR.

Chapter 2:

The MAR between 6°-10°S

2.1 Geological setting

The MAR between 6°-10°S is an interesting part of the MAR because it offers the opportunity to study a locally restricted medium wavelength melting anomaly which is, as shown in Chapter 1, presumably produced by a hotspot or mantle heterogeneity. Two large fracture zones (FZ) characterise this area, the Ascension FZ in the north and the Bode-Verde FZ in the south. Between these fracture zones six spreading segments, bounded by non-transform offsets, have been identified (see Figure 2.1). Most of these segments have a well-developed axial rift valley as usual for the MAR, with the exception of Segments 4 and 5 which have an only poorly to not defined axial valley and morphology more reminiscent of the East Pacific Rise. In addition, Segments 4 and 5 are also anomalously shallow, with a positive deviation up to 2000 m relative to the neighbouring segments (min. water depth is 1480 m at Seg. 5, see Figure 2.2). As visible in Figure 2.3 segment 4 and 5 seem to overlap. Overlaping spreading centers are common at medium and fast spreading ridges but not at slow spreading ridges. Only from the Kolbeinsey ridge in the N-Atlantic has an overlapping spreading center been reported (Haase pers. com.). East of Segment 5 at approx. 9° 45´S three off-axis seamounts occur. From west to east these seamounts rise to depths of ca. 900 m, 72 m and 102 m below sea level (western and easternmost: pers. comm. N. Mitchell, mean seamount: Brozena (1986)). Up to present only the central of the three has been named, being known as Grattan Seamount. From W to E these three seamounts lie approx. 20, 39 and 119 km away from the spreading axis. With the recent South Atlantic half-spreading rate of 18 mm/yr^{-1} (Brozena and White, 1990) crustal ages of the seafloor underlying the seamounts can be calculated roughly. From W to E these ocean crust ages beneath the seamounts are approx. 1.1, 2.2 and 6.6 Ma. After Devey et al. (1993) Grattan Seamount has a basal diameter of 25 km and is thus bigger than typical abyssal seamounts produced off-axis near a MOR (Bourdon and Hemond, 2001). Apart from the off-axis volcanic edifices E of the MAR, a huge volcanic edifice exists some 80 km W of the MAR at approximatly 7°55´ S and 14°20´ W named Ascension Island (ocean crust age: ca. 4.4 Ma). For Tristan da Cunha it is known that this island is related to a mantle plume, which lies under the eastern flank of the MAR. This hotspot produces a track of islands and seamounts trending to the east tracking the movement of the African plate (O´Connor and Duncan, 1990). This characteristic chain building is not observed at the MAR in the vicinity of Ascension Island. South of the three seamounts the MAR changes its shape to the common Atlantic morphology and the axial valley lies in "normal" water depths (ca. 2700 m).

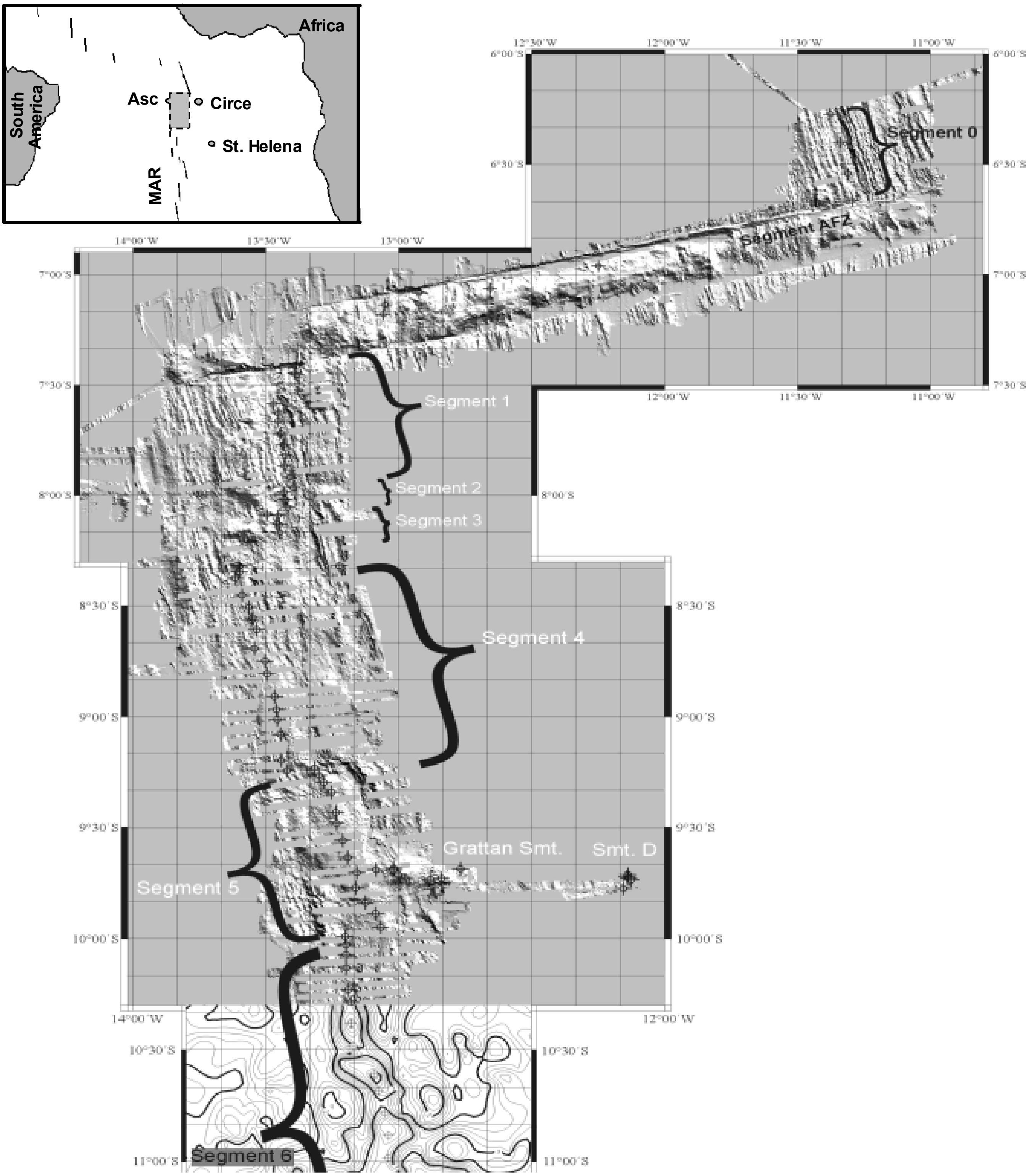

Figure 2.1: Sample and axial segment locations superimposed on seafloor bathymetry (data from Brozena and White (1990)).

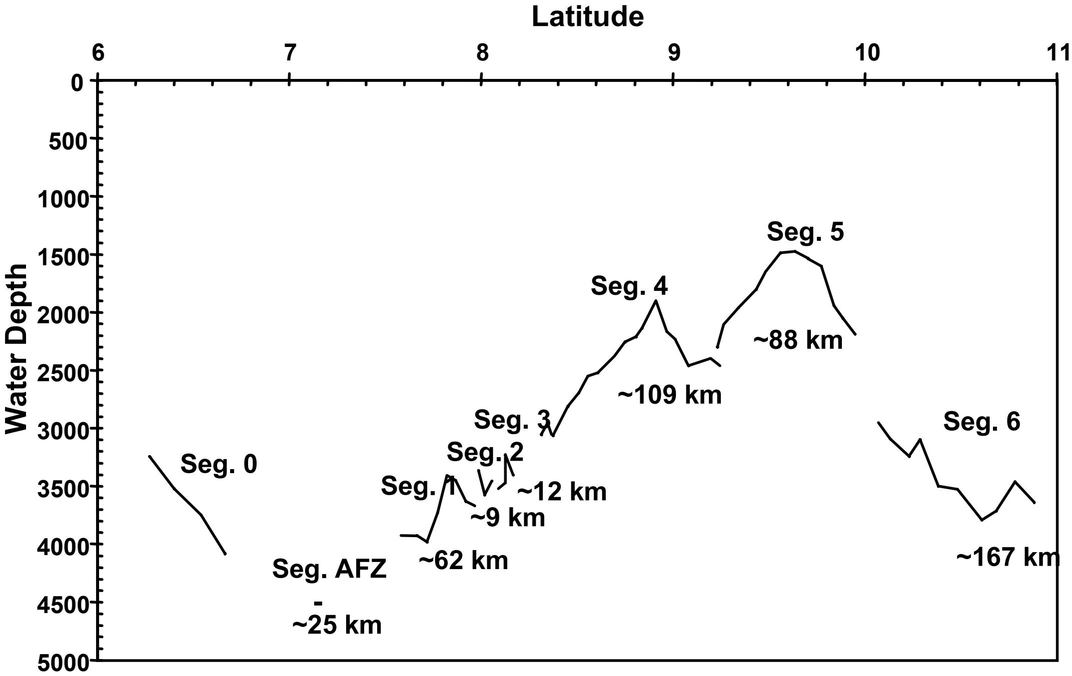

Figure 2.2: Along axis morphology of the working area

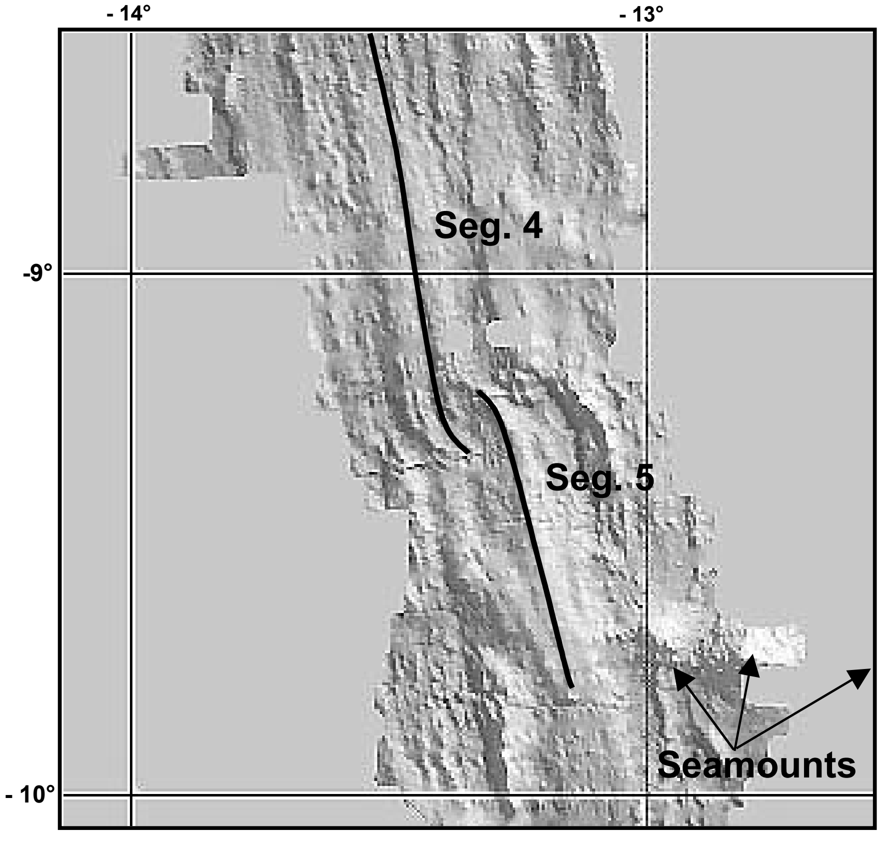

Figure 2.3: Propagating rifts at Segment 4 and 5, map downloaded from http://imager.ldeo.columbia.edu

For a detailed geochemical and petrological study, samples were taken from north of the Ascension FZ as far south as 10° 53´S on Segment 6, a distance of approximately 500 km. Dredges were taken only in the topographically-defined neovolcanic zone and 65 stations yielded fresh to slightly altered volcanic rocks. Sample localities are shown in Figure 2.4a, b, c. A high resolution sampling was performed, with an average distance between stations of 5-10 km. Coordinates and depth of recovery are given in the appendix.

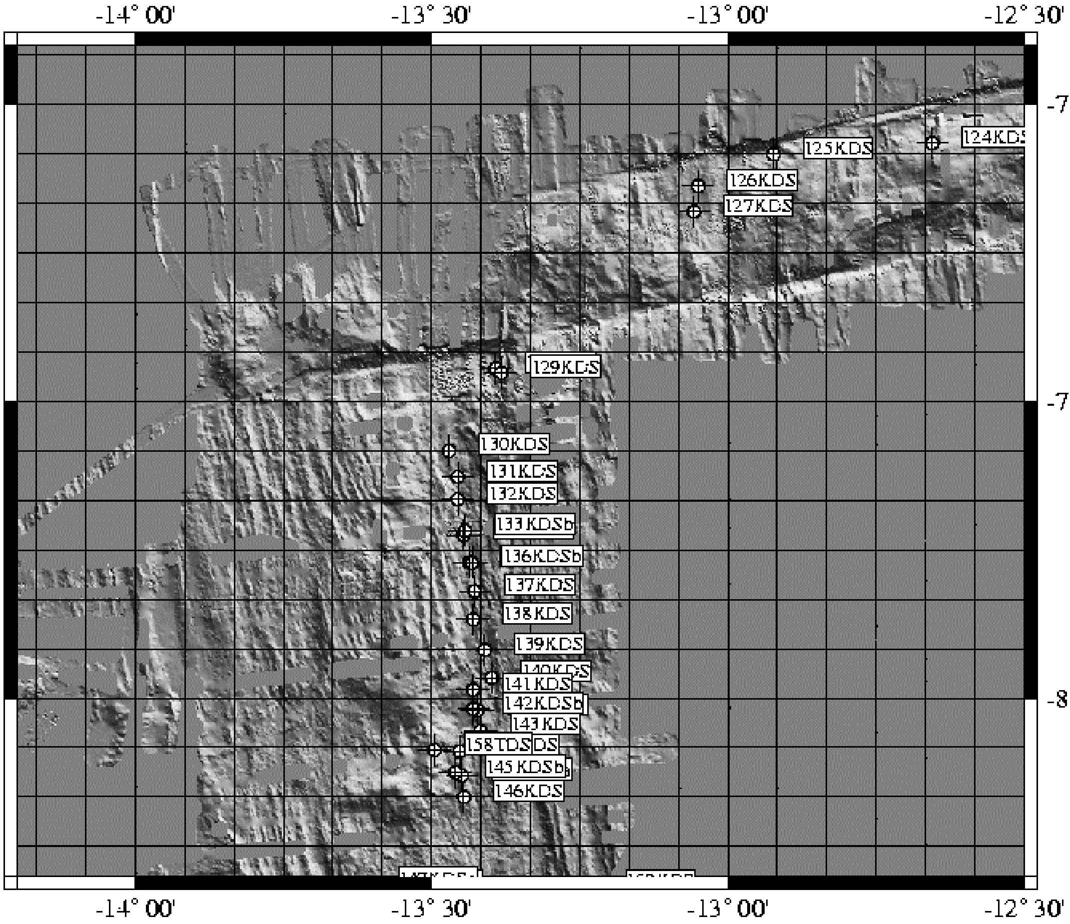

Figure 2.4a: Sample stations

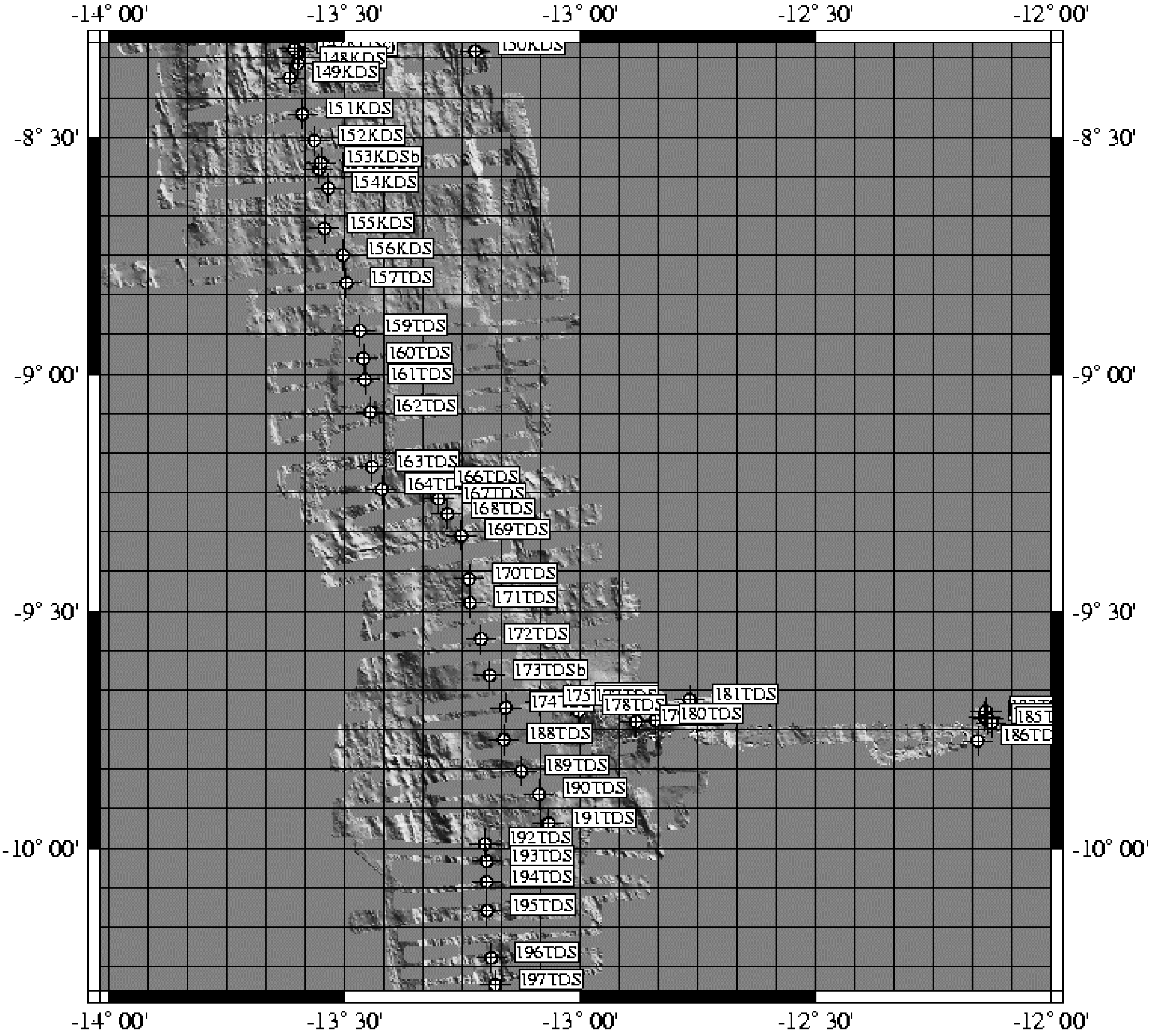

Figure 2.4b: Sample stations, continued

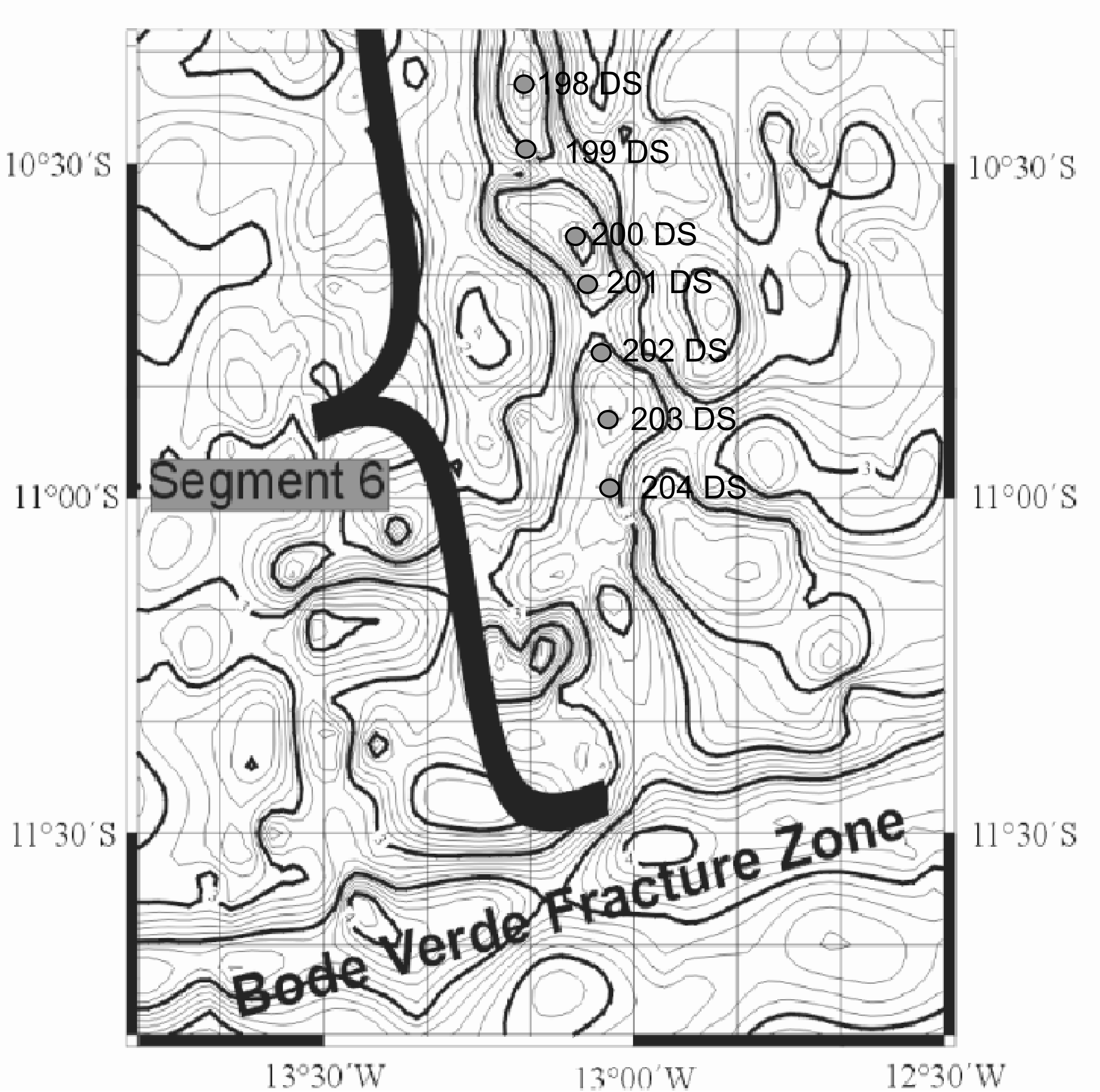

Figure 2.4c: Sample stations, continued

2.2 Previous work

First work in this area was done in 1968 by Stover (1968) who reported a gap in earthquake activity at the MAR in the vicinity of Ascension Island. Based on a profile at ca. 8°30′ S van Andel and Heath (1970) found an unusual crestal bulge which is more pronounced, as we know now, in the south. 1973 van Andel et al: confirmed the lack of seismicity S of 8° S and reported a change of strike of the MAR between 8-9° indicating a tectonically complex area. Schilling et al. (1985) combined these observations with trace element ratio data and concluded Circe Seamount 450 km east of Ascension Island to be a hotspot and responsible for the bathymetric anomaly and the production of the three seamounts. Magma channels were proposed to connect the mantle plume with the spreading axis. The plume beneath Circe Seamount was thought to have an excess temperature between 250-300° C. Further work of Hanan et al. (1986); Graham et al. (1992); Fontignie and Schilling (1996) who published Pb, He Sr and Nd isotope ratios confirmed this model. Brozena (1986) presented new results of an aeromagnetic study of the northern South Atlantic together with a better bathymetry. Beside the identification of the zero age ridge crest the bathymetry showed all volcanic edifices mentioned in the introduction including the elevated segment at 9°45′ and the seamounts on the eastern flank of the ridge. Brozena and White (1990) mapped multiple ridge jumps and propagating rifts at 8° N (South of our Segment 1) which had not been clearly identified at slow spreading ridges until then. This unusual behavior of a slow spreading ridge was attributed by Brozena and White (1990) to a hotspot at 9° S (Segment 5) on the eastern flank of the ridge 100-200 km E of the axis. This hotspot was considered to cause elevated asthenospheric mantle temperatures and lateral mantle flow, with consequent excess volcanism and disruption of the normally well focused melt delivery process at slow spreading ridges. More geophysics was done in this area by Minshull et al. (1998). Their seismic data indicate a crustal thickness of 10 km on Segment 5 which decreases to a more normal 6 km on Segment 1. These data correspond well with the bathymetric data in which the shallowest parts of the MAR possess the thickest crust. Figure 2.5 is taken from Minshull et al. (1998) (see caption for details). It is visible that own positioning of the ridge axis of Segment 4 and 5 is clearly different to estimates from Minshull. Because of the lack of fresh basalts in any other positions tried while sampling, our own positioning of the present axis seems to be more reliable. Due to this the crustal thickness estimates from Minshull et al. (1998) may be maximum estimates because they were made on older, cooler crust. Despite this, the lack of a median valley at Segment 5 suggests, as pointed out in Chapter 1, a crustal thickness of 9 +/-1 km (Detrick et al., 1995). In addition the size, height and also the asymmetry of the Ascension anomaly is strikingly similar to the Azores Platform anomaly (compare bathymetry to N of Azores from Figures 1.3 and to S of Segment 5 in Figure 2.2).

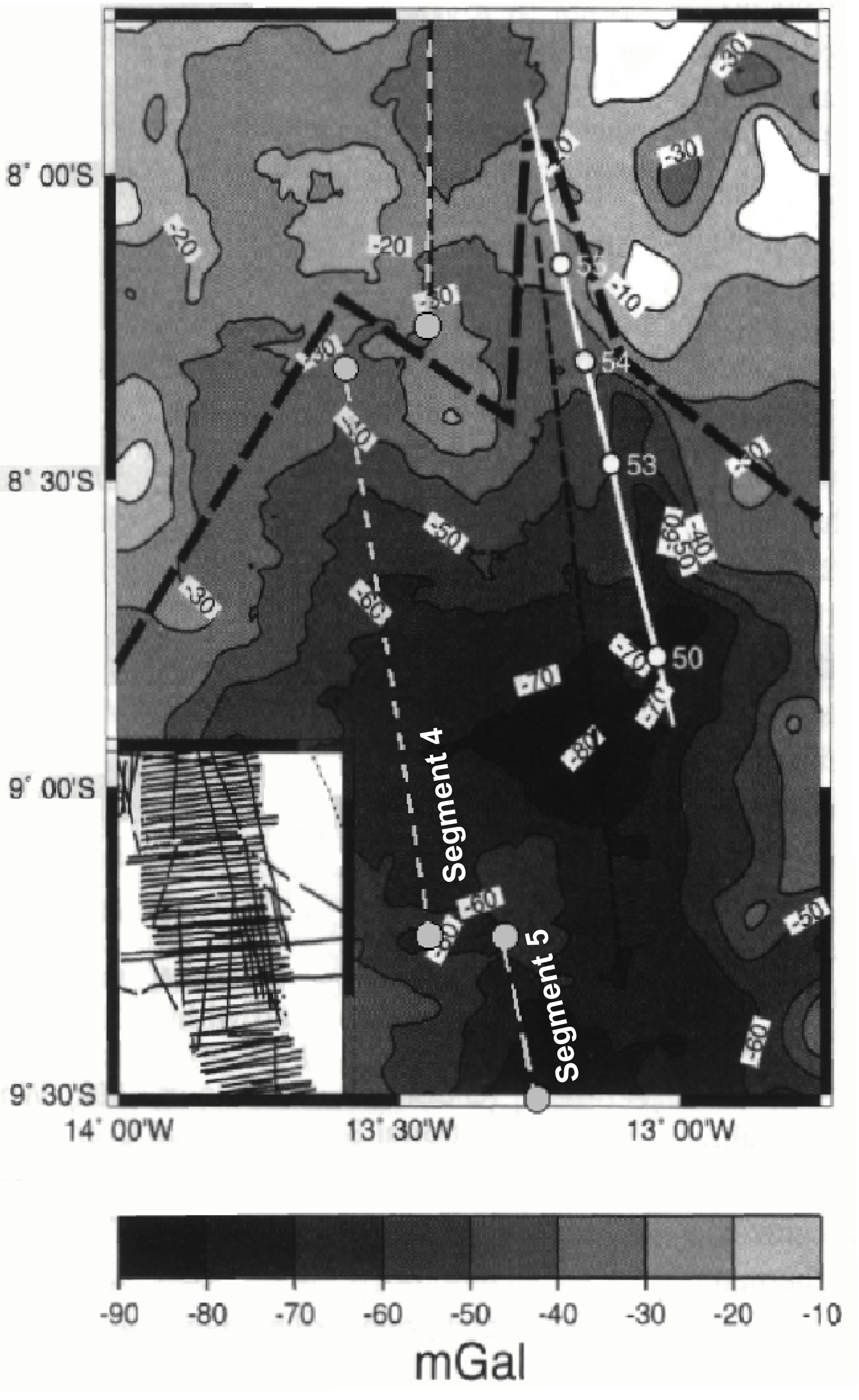

Figure 2.5: Gravity map from Minshull et al. (1998) showing negative MBA at Segment 4. The broken line indicates own suggested ridge axes based on freshness of samples, continious line corresponds to seismic profile of Minshull et al. (1998).

Therefore it is straightforward to suppose a comparable crustal thickness for the Ascension anomaly, that is >8-9 maximum crustal thickness. Based on Bown and White (1994) Minshull et al. (1998) calculated that an elevated mantle potential temperature of 50°C would be needed to produce a crustal thickness of 10 km if the mantle source is as depleted as the surrounding mantle. In view of this they suggest either the presence of a weak and intermittent plume or melting of a series of small mantle heterogeneities. Bourdon and Hemond (2001) reject the presence of mantle heterogeneities and suggest a small, weak and possibly intermittent mantle plume near Grattan Seamount.

In summary it can be concluded that the MAR near Ascension Island is unusual because

- above all Segment 5 is bulged, lies in shallower water depths and has no well defined ridge crest.
- of the presence of seamounts including Ascension Island, lying off-axis and showing no hotspot typical island chain
- of a marked lack of seismicity along the ridge axis/MAR from 8°30´S to 10°S (Brozena, 1986)
- of several ridge jumps and a propagating rift at approx. 8°15´S (Brozena and White, 1990).
- High La/Sm, Nb/Zr and high Pb, Nd, Sr and He radiogenic isotope ratios in MORB dredged at the axis.

Chapter 3

Sample preparation and analytical methods

3.1 Sample preparation

All samples were obtained by dredging. Samples were selected on board to cover the range of rock types evident in the dredge using macroscopic criteria such as grade of alteration, vesicularity, crystal content and morphology. Glassy crusts were separated from the samples and later crushed in the Institut für Geowissenschaften, Kiel to a smaller grain size. The resulting glassy sand was washed using Millipore®-Water in an ultrasonic bath in order to remove as much seawater as possible. No acids were used.

3.2 Electron microprobe

Only grains free of any visible signs of alteration were hand-picked and bedded in resin. Tablets were polished for analysis with an electron microprobe CAMECA SX 50 at GEOMAR research center, Kiel. The CAMECA SX 50 runs at an acceleration voltage of 14-15 kV with a beam current of 10 nA. For better analytical precision of alkali elements the beam was defocussed. At least two, usually three, grains from each sample were embedded. Every grain was analysed three times. Values under 97 wt% and above 103 wt% total were rejected. The accuracy of the measurements was controlled mainly with two standards using JDF D2 and CFA 47 (some measurements with ALV-Std and KN 18 Std). Always two different standards per day were used. The measurements were started with both standards. Accuracy and precision can be seen in Table 3.1. To check if any machine drift over the running time occurred these two standards were measured alternately every 50 points analysed (Figure 3.1). It is visible that elements like FeO, CaO, K_2O, Al_2O_3, MgO and SiO_2 show no significant changes over time. Na_2O (Cfa-Std.) and TiO2 (Jdf-D2-Std.) measurements show some scatter. This scatter is not time-dependent and may reflect Na_2O heterogeneities in the samples or variations in microprobe vacuum, crystal positions or beam focussing and/or intensity. Large scatter occurs for all standards for MnO and P_2O_5. This is due to the low concentration of P_2O_5 and MnO in the standards. In Figure 3.2 the percent deviation between certified standard major element values and averaged measured standard major element concentration is presented. The averages are calculated from three (ALV) to 31 (Jdf-D2) single measurements. The deviation for SiO_2, Al_2O_3, Na_2O, CaO and TiO_2 lie below 5 %. Some of the standards have higher deviations up to 10 % for the elements FeOt, K_2O, MnO and MgO. It is notable that these higher deviations occur for elements which are present in low concentrations in the standards (e.g. ALV K_2O cert. is 0,05 wt%, CFA certified FeO, MgO and MnO values are 2,65 wt%, 0,42 wt% and 0,18 wt% respectively). We attribute the high deviations therefore to the increasing influence of analytical errors at low concentrations. In Figure 3.3 deviations of duplicate measurements are presented. Deviations under 5 % occur for most elements (Na_2O, FeO, SiO_2, CaO, Al_2O_3, TiO_2 and MgO). Higher deviations (> 5%) are visible only for K_2O, MnO, P_2O_5. As was the case in Figure 3.2, these higher deviations occur for elements present in low concentrations (K_2O 0,15 – 0,28 wt%; MnO 0,18-0,22 wt%; P_2O_5 0,26 – 0,33 wt%) and are again attributable to the increasing influence of analytical uncertainties at low concentrations.

Standart	**Na_2O**	**FeO**	**SiO_2**	**CaO**	**K_2O**	**Al_2O_3**	**TiO_2**	**MgO**	**MnO**	**P_2O_5**	**Total**
ALV Std.	2.88	8.42	49.53	11.81	0.05	16.58	1.27	8.68	0.14	nn	99.36
alv mean	2.76	8.64	49.07	11.78	0.06	16.20	1.22	8.53	0.14	nn	98.41
% dev.	4.00	2.60	0.92	0.28	10.16	2.29	4.27	1.70	0.29	nn	0.95
CFA Std	5.37	2.65	61.63	1.84	7.98	18.53	0.42	0.42	0.18	nn	99.71
cfa mean	5.21	2.81	61.88	1.87	7.89	18.68	0.42	0.39	0.19	0.11	100.08
% dev.	2.89	6.17	0.40	1.63	1.07	0.83	0.89	7.04	7.52	nn	0.37
JDF Std.	2.77	12.17	50.80	10.80	0.22	13.80	1.93	6.83	0.22	0.23	99.54
jdf mean	2.78	12.04	50.54	10.82	0.20	13.77	1.94	6.73	0.23	0.35	99.59
% dev.	0.50	1.08	0.51	0.20	6.01	0.25	0.31	1.44	3.68	50.90	0.05
KN 18 Std.	5.68	3.45	74.60	0.15	4.39	10.53	0.18	nn	0.06	nn	99.04
KN 18 mean	4.73	3.42	74.54	0.17	4.42	10.55	0.17	0.03	0.09	nn	98.39
% dev.	16.75	0.86	0.07	15.22	0.73	0.16	3.70	nn	44.17	nn	0.66

Sample	**Na_2O**	**FeO**	**SiO_2**	**CaO**	**K_2O**	**Al_2O_3**	**TiO_2**	**MgO**	**MnO**	**P_2O_5**	**Total**
132 DS-6	2.45	10.14	50.29	11.27	0.16	15.35	1.33	8.53	0.18	0.33	100.31
132 DS-6	2.49	9.87	50.13	11.67	0.18	14.93	1.33	8.28	0.19	0.27	99.62
% dev.	1.31	2.68	0.31	3.56	10.26	2.77	0.08	2.90	5.99	15.93	0.69
146 DS-2	2.35	9.83	50.76	11.84	0.15	15.05	1.27	8.18	0.21	0.26	99.94
146 DS-2	2.36	9.70	50.69	11.76	0.15	15.01	1.24	8.22	0.18	0.26	99.63
% dev.	0.43	1.32	0.14	0.68	0.00	0.27	2.36	0.49	14.29	0.00	0.31
158 DS-1	2.63	10.20	50.06	11.30	0.28	14.22	1.69	6.95	0.22	0.30	97.92
158 DS-1	2.70	10.12	50.81	11.43	0.25	14.27	1.70	7.07	0.18	0.33	99.21
% dev.	2.83	0.79	1.50	1.12	8.97	0.37	0.68	1.76	16.67	10.74	1.32

Table 3.1: Accuracy and precision, see text for discussion

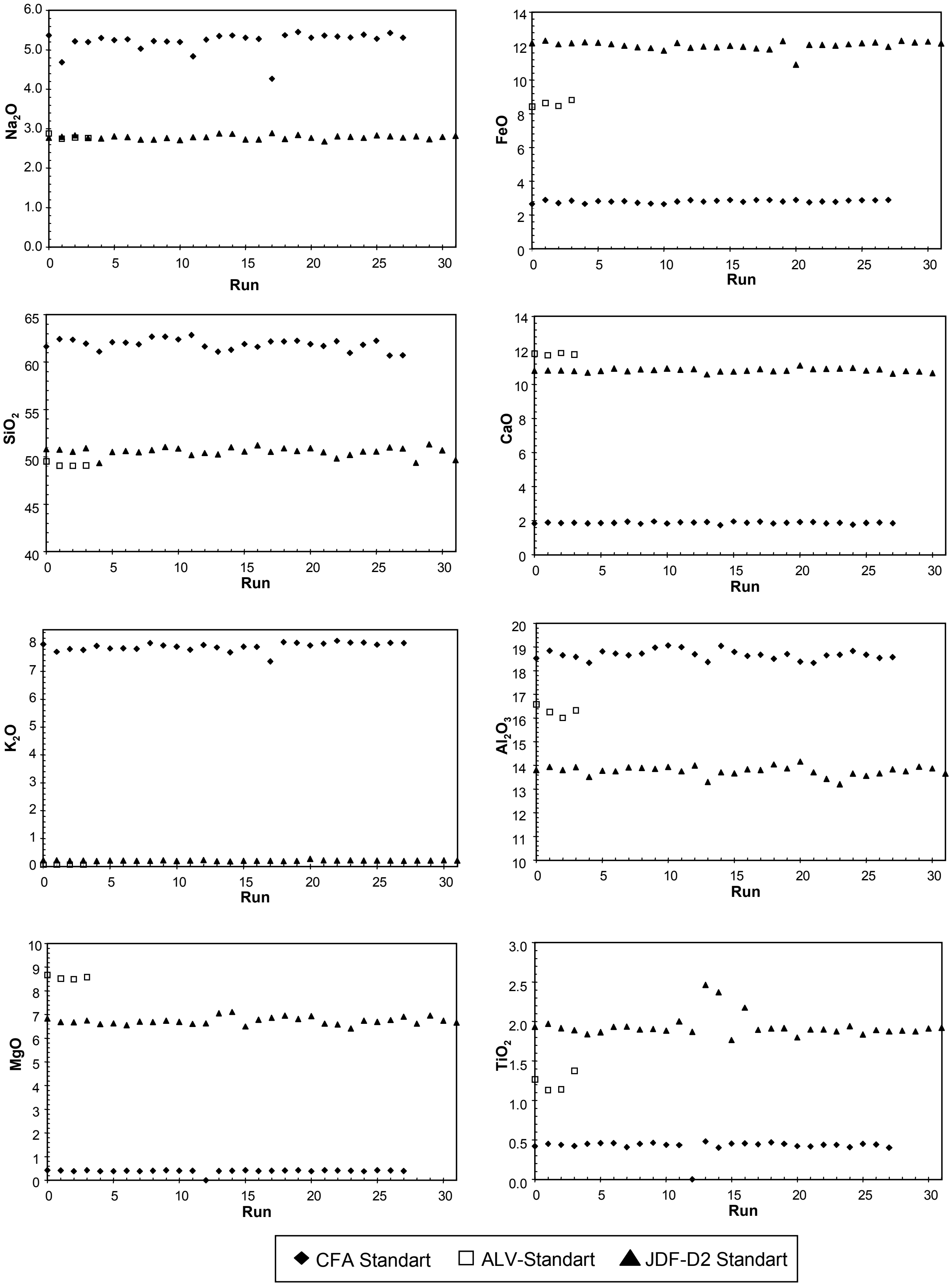

Figure 3.1: Maschine drift over time

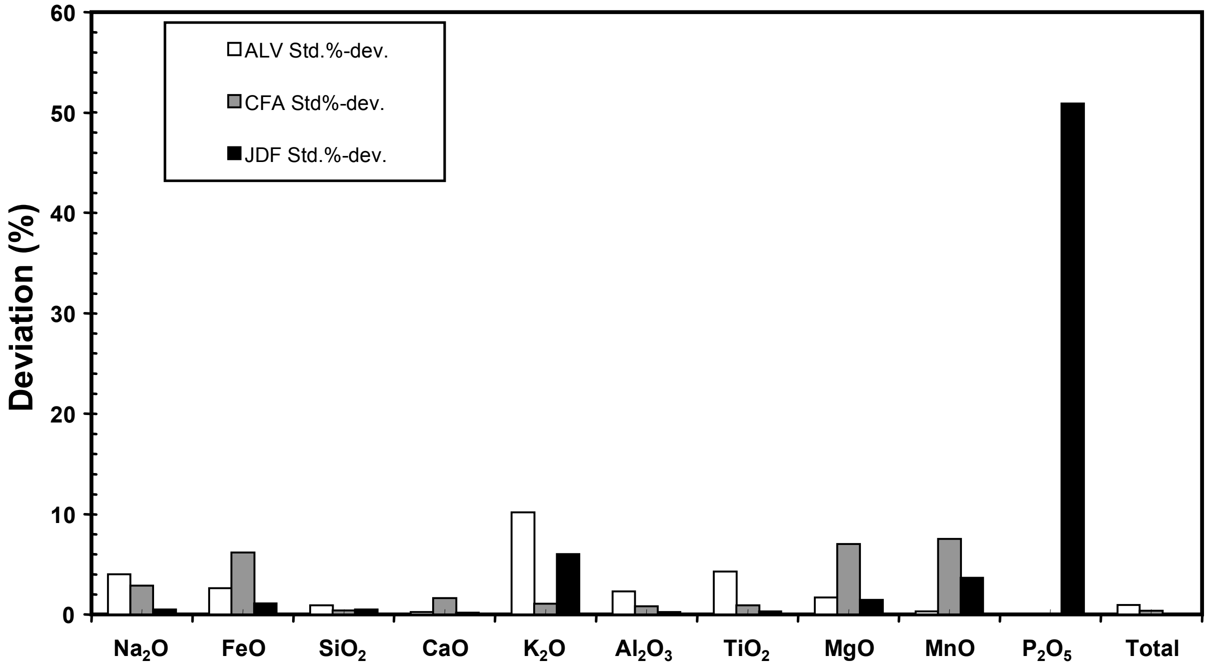

Figure 3.2: % deviations between certified and measured standard

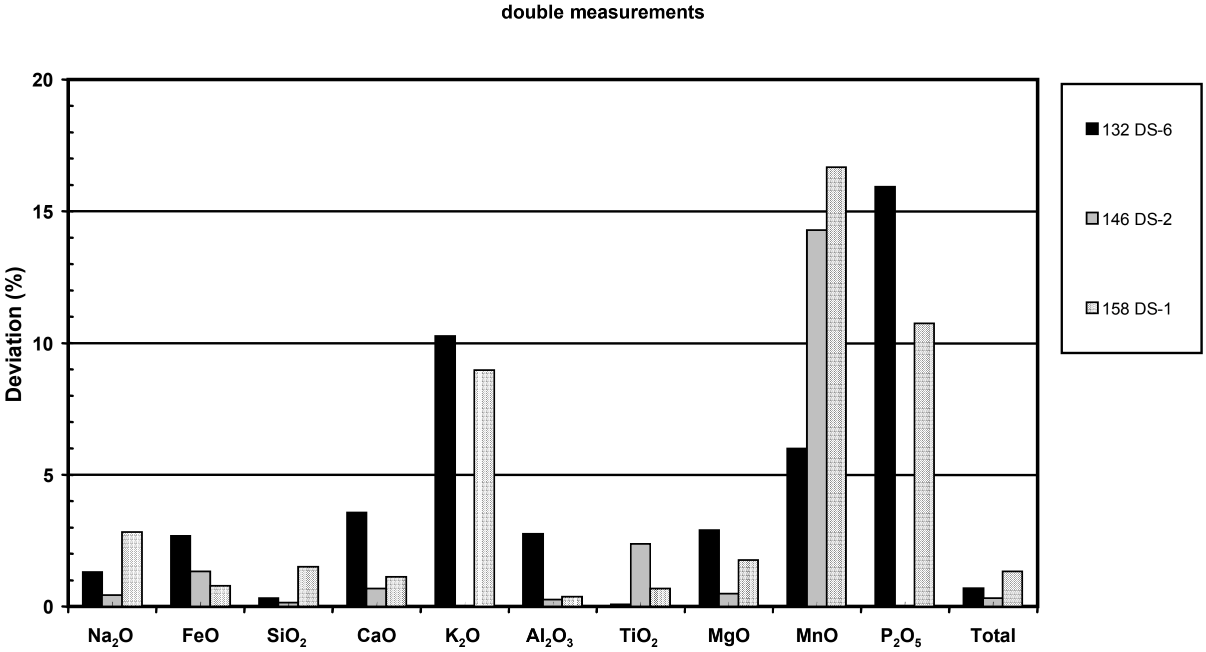

Figure 3.3: % deviations of duplicate measurements

In summary the elements P_2O_5 and MnO show much scatter in standard and duplicate measurements, so these elements will not be used for geochemical interpretation. Also due to low K_2O concentrations this element shows a higher deviation of approximately 10% when looking at duplicate measurements. This scatter is lower than natural variation in K_2O content. Natural basalts have SiO_2 concentrations of approximately 50 %. So even a small percentage relative error has a large effect (see also Klein and Langmuir, 1989). This can be seen in Figure 3.4 where a correlation between total element concentration and SiO_2 content is evident. Other elements show such no correlation. For this reason SiO_2 alone was recalculated to 100 % total element concentration by projection along the best-fit line to the data cloud (slope of line 0,5182) and is labeled SiO_2^{100}. For plots and calculations only SiO_2^{100} was used. The uncorrected data however are given in the appendix.

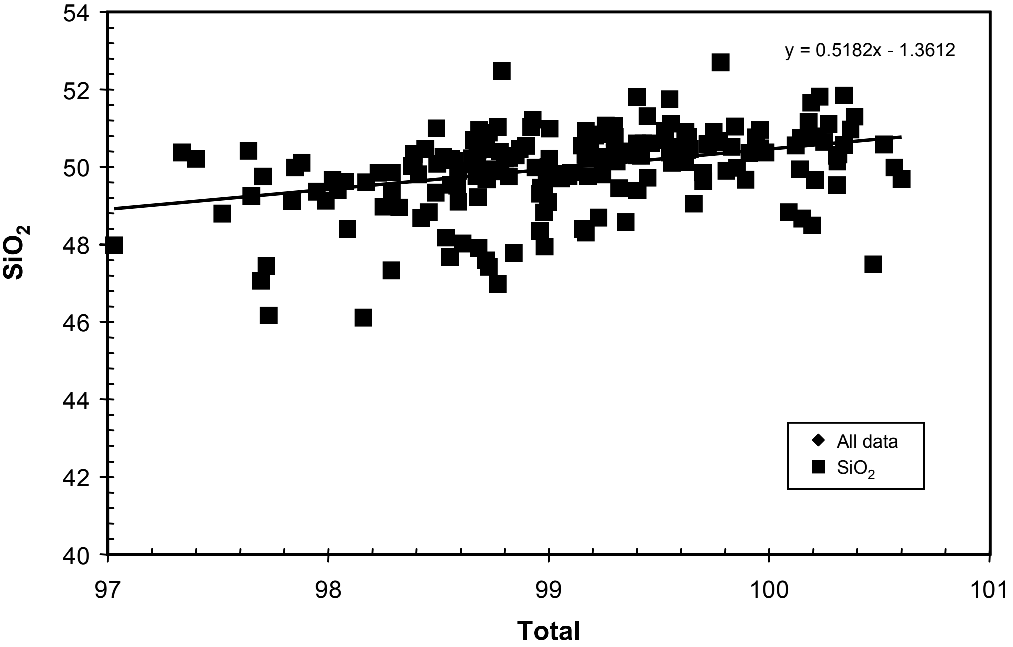

Figure 3.4: Correlation between total element concentration and SiO_2 content

Mineral chemistry measurements were carried out at the Institut für Geowissenschaften, Kiel using a CAMECA Camebax electron microprobe. In correspondence with the CAMECA SX 50, the CAMECA Camebax electron microprobe runs at an acceleration voltage of 14-15 kV with a beam current of 10 nA. For better analytical precision the beam was defocussed for plagiclase and melt inclusions. Major element data of minerals are averages of at least two measurements. Analyses outside the range of 98 and 102 wt % for olivine clinopyroxene and plagioclase were rejected. Precision was obtained by occasional measurements of internal standards. The data are presented in the appendix.

3.3 Inductively coupled plasma-mass spectrometry (ICP-MS)

Trace element concentrations were measured with an VG PlasmaQuad PQ1 ICP-MS at the Institut für Geowissenschaften Kiel. Preparation of glass chips is in concordance to microprobe analysis. Approx. 30-90 mg handpicked glass chips were weighed into screw-top Savillex® PFA beakers and dissolved using 1 ml HF and 1 ml aqua regia sealed on a hot plate at approx. 170°C for 12 hours. Afterwards 0.3 ml $HClO_4$ was added and solutions were evaporated at about 180°C to incipient dryness. Afterwards 1 ml HNO_3 and 2 ml $H_2O_{dest.}$ was added to each sample and samples were evaporated at about 180°C to incipient dryness again. Residues were taken up in 0.4 ml HNO_3 and 4 ml $H_2O_{dest.}$. $H_2O_{dest.}$ was taken from a Millipore® filter. Detailed descriptions of laboratory and machine equipment, analytical procedure, as well as the measured isotopes together with observed interferences can be found in Garbe-Schönberg (1993). Three batches of samples were analysed, the first batch contained 2 blanks, standard BHVO and BIR and duplicates of samples 119 DS-3, 148 DS-2, 164 DS-2, 173 DS-1, 190 DS-2. In batch two also BHVO and BIR standards were included, together with three blanks and duplicates of 136 DS-1, 154 DS-3, 171 DS-1 and 195 DS-2. Batch three contained only standard BIR and BHVO. Accuracy and precision can be seen in Table 3.2 and are given in %, also element concentrations (in ppm) of blank measurements are listened. In batch 1 deviations of standards and duplicates lie mostly under 10 %. Standard BHVO shows higher deviation at Pb, BIR shows higher deviations at Rb, Nb, Ta. Duplicate 148 DS-2 has higher deviations at Ba and Pb. Higher deviations are due to low element concentrations. Batch 2: Also most measured elements of standards and duplicates lie under 10 % but in comparison to batch 1 deviations effect more elements. BHVO-1 shows higher deviations than 10 % at Rb, Y, Zr, Nb, Ta, Pb; BHVO-2 at: Rb, Y, Nb, Hf, Ta; BIR-1 at: Rb, Y, Zr, Ta, Th, U; BIR-2 at: Rb, Y, Zr, Ba, La, Hf, Ta, Th, U and duplicate 171 DS-1 at Zr, Hf, U and 195 DS-2 at Pb. This can only partly be attributed to low element concentrations (Ta, Th, U). In fact blank element concentrations suggest contamination of Sr, Zr, Ba, Hf, Pb and also Y and Nb. Standards of batch 3 show higher deviations at Th and U which can also be attributed to low element concentrations. Duplicates are effected in the same way. OIB and MORB have, after Hofmann et al. (1986), Nb/U ratios of 47 +/- 10 and Ce/Pb ratios of 25 +/- 5. Thus these ratios can be used to verify measured Nb/U and Ce/Pb values. Figure 3.5a shows that most measured Nb/U ratios lie in the range of 47 +/- 10, whereas many Ce/Pb ratios (Figure 3.5b) of measured samples lie below 20. Lower Ce/Pb ratios might be due to Pb contamination while chemical pulping. It is also possible that at least some low Ce/Pb ratios are due geological processes. However Figure 3.5b shows that measured Pb concentrations should be handled with care.

Deviations		Std.-Name	Rb	Sr	Y	Zr	Nb
	%	BASALT BHVO-1	12.35	4.58	4.12	3.81	2.53
batch 1	%	BASALT BIR-1	189.96	3.22	4.66	2.99	147.72
	%	148 DS-2	5.70	4.52	5.08	2.74	7.37
	%	164 DS-1	1.13	2.01	2.62	1.22	6.99
	%	173 DS-1	1.85	3.47	3.33	4.04	2.60
	%	190 DS-2	4.63	1.36	3.63	4.55	4.18
Deviations	%	BASALT BHVO-1	21.84	3.25	20.65	32.88	18.21
batch 2	%	BASALT BHVO-1	19.93	1.91	20.96	5.31	19.98
	%	BASALT BIR-1	42.05	1.95	15.34	23.44	3.03
	%	BASALT BIR-1	2.37	2.64	14.83	295.28	1.05
	%	171 DS-1	13.55	0.62	0.42	30.77	1.98
	%	195 DS-2	4.93	1.06	2.33	1.69	0.18
Deviations	%	BHVO-1	14.85	2.93	9.16	5.23	5.32
batch 3	%	BHVO-2	13.66	5.06	7.14	3.48	3.29
	%	BIR	15.10	1.01	11.11	11.41	12.34
Deviations	ppm	Blank 1	0.00	0.00	0.00	0.00	0.00
	ppm	Blank 2	0.00	0.00	0.00	0.00	0.00
	ppm	BLANK A	0.00	0.01	0.00	0.32	0.00
	ppm	BLANK B	0.00	0.00		0.00	
	ppm	BLANK C	0.00	0.00	0.00	0.17	0.00

Deviations		Std.-Name	Ba	La	Ce	Pr	Nd
	%	BASALT BHVO-1	5.27	0.34	1.43	1.68	0.69
batch 1	%	BASALT BIR-1	1.16	0.54	4.05	2.46	7.68
	%	148 DS-2	151.95	6.03	5.06	0.88	2.44
	%	164 DS-1	1.85	0.24	1.00	1.33	1.34
	%	173 DS-1	0.40	0.28	0.72	1.96	1.36
	%	190 DS-2	4.31	4.29	4.49	3.58	4.80
Deviations	%	BASALT BHVO-1	3.15	3.38	5.80	11.44	7.53
batch 2	%	BASALT BHVO-1	7.75	2.31	5.10	9.86	9.17
	%	BASALT BIR-1	10.28	4.85	6.64	0.22	9.05
	%	BASALT BIR-1	156.47	14.71	1.48	0.70	10.40
	%	171 DS-1	28.22	3.19	2.04	1.19	2.30
	%	195 DS-2	9.09	0.43	1.57	0.02	1.95
Deviations	%	BHVO-1	3.80	2.50	4.48	4.24	2.89
batch 3	%	BHVO-2	2.84	2.17	4.03	3.31	1.88
	%	BIR	13.00	6.71	7.81	3.61	10.02
Deviations	ppm	Blank 1	0.00	0.00	0.00	0.00	0.00
	ppm	Blank 2	0.00	0.00	0.00	0.00	0.00
	ppm	BLANK A	0.10	0.00	0.00	0.00	0.00
	ppm	BLANK B	0.00	0.00	0.00	0.00	0.00
	ppm	BLANK C	0.02	0.00	0.00	0.00	0.00

Table 3.2: Accuracy and precision of trace element measurements

Deviations	%	Std.-Name	Sm	Eu	Gd	Tb	Dy
	%	BASALT BHVO-1	5.71	2.77	2.51	1.49	7.52
batch 1	%	BASALT BIR-1	3.47	4.91	4.78	2.15	1.03
	%	148 DS-2	0.24	0.97	0.81	0.89	0.77
	%	164 DS-1	2.52	2.19	1.94	1.20	3.18
	%	173 DS-1	0.82	0.88	1.54	0.11	0.42
	%	190 DS-2	3.19	3.72	1.57	3.84	3.17
Deviations	%	BASALT BHVO-1	6.87	4.25	5.23	5.15	0.61
batch 2	%	BASALT BHVO-1	7.09	2.98	4.36	4.30	0.52
	%	BASALT BIR-1	5.08	7.73	8.03	3.95	0.03
	%	BASALT BIR-1	8.38	11.11	6.92	4.61	0.52
	%	171 DS-1	0.88	0.06	4.33	1.60	0.04
	%	195 DS-2	0.73	0.20	2.30	0.79	0.71
Deviations	%	BHVO-1	0.20	0.58	1.81	0.58	3.23
batch 3	%	BHVO-2	2.12	1.77	1.19	1.10	5.05
	%	BIR	1.05	6.56	3.58	1.32	1.98
Deviations	ppm	Blank 1	0.00		0.00	0.00	0.00
	ppm	Blank 2	0.00	0.00	0.00	0.00	0.00
	ppm	BLANK A	0.00	0.00	0.00	0.00	0.00
	ppm	BLANK B	0.00	0.00	0.00		0.00
	ppm	BLANK C	0.00	0.00	0.00	0.00	0.00

Deviations		Std.-Name	Ho	Er	Tm	Yb	Lu
	%	BASALT BHVO-1	2.29	5.55	3.03	3.14	2.89
batch 1	%	BASALT BIR-1	5.59	8.35	7.70	5.89	11.04
	%	148 DS-2	0.35	0.41	2.22	0.29	1.46
	%	164 DS-1	1.77	2.56	3.61	1.21	1.15
	%	173 DS-1	1.10	0.48	0.25	0.68	0.83
	%	190 DS-2	3.09	2.30	2.19	4.49	1.96
Deviations	%	BASALT BHVO-1	2.12	1.93	3.03	1.14	8.06
batch 2	%	BASALT BHVO-1	2.24	4.93	0.24	0.66	3.27
	%	BASALT BIR-1	2.74	2.76	7.69	0.01	5.76
	%	BASALT BIR-1	2.62	1.91	3.85	1.14	1.47
	%	171 DS-1	0.26	1.75	0.61	0.26	2.99
	%	195 DS-2	2.85	3.88	0.46	0.29	0.30
Deviations	%	BHVO-1	1.76	5.13	0.52	0.24	2.90
batch 3	%	BHVO-2	2.70	7.06	2.35	2.63	0.90
	%	BIR	0.12	3.25	7.69	1.02	5.49
Deviations	ppm	Blank 1	0.00	0.00	0.00	0.00	0.00
	ppm	Blank 2	0.00	0.00	0.00	0.00	0.00
	ppm	BLANK A	0.00	0.00	0.00	0.00	0.00
	ppm	BLANK B		0.00		0.00	
	ppm	BLANK C	0.00	0.00	0.00	0.00	0.00

Table 3.2: Accuracy and precision of trace element measurements, continued

Deviations		Std.-Name	Hf	Ta	Pb	Th	U
	%	**BASALT BHVO-1**	10.34	5.29	19.65	8.70	0.09
batch 1	%	**BASALT BIR-1**	7.93	206.21	5.84	8.73	2.66
	%	**148 DS-2**	3.26	8.89	96.19	1.57	5.38
	%	**164 DS-1**	2.15	34.85	3.16	5.21	2.28
	%	**173 DS-1**	1.22	5.23	4.42	3.76	4.54
	%	**190 DS-2**	1.49	1.29	1.04	0.72	3.88
Deviations	%	**BASALT BHVO-1**	0.88	19.91	21.63	0.50	10.22
batch 2	%	**BASALT BHVO-1**	38.17	13.53	2.89	7.02	3.76
	%	**BASALT BIR-1**	1.82	48.21	5.22	17.06	23.12
	%	**BASALT BIR-1**	265.82	188.42	8.15	128.72	461.16
	%	**171 DS-1**	26.94	0.19	37.68	9.14	19.45
	%	**195 DS-2**	1.90	0.77	17.44	5.05	8.62
Deviations	%	**BHVO-1**	8.76	1.56	21.17	18.84	5.08
batch 3	%	**BHVO-2**	10.11	3.52	40.62	21.43	7.11
	%	**BIR**	0.06	7.97	5.57	5.57	2.36
Deviations	**ppm**	**Blank 1**	0.00	0.00	0.00	0.00	0.00
	ppm	**Blank 2**	0.00	0.00	0.00	0.00	0.00
	ppm	**BLANK A**	0.01	0.00	0.00	0.00	0.00
	ppm	**BLANK B**	0.00		0.00		
	ppm	**BLANK C**	0.00		0.00	0.00	0.00

Table 3.2: Accuracy and precision of trace element measurements, continued

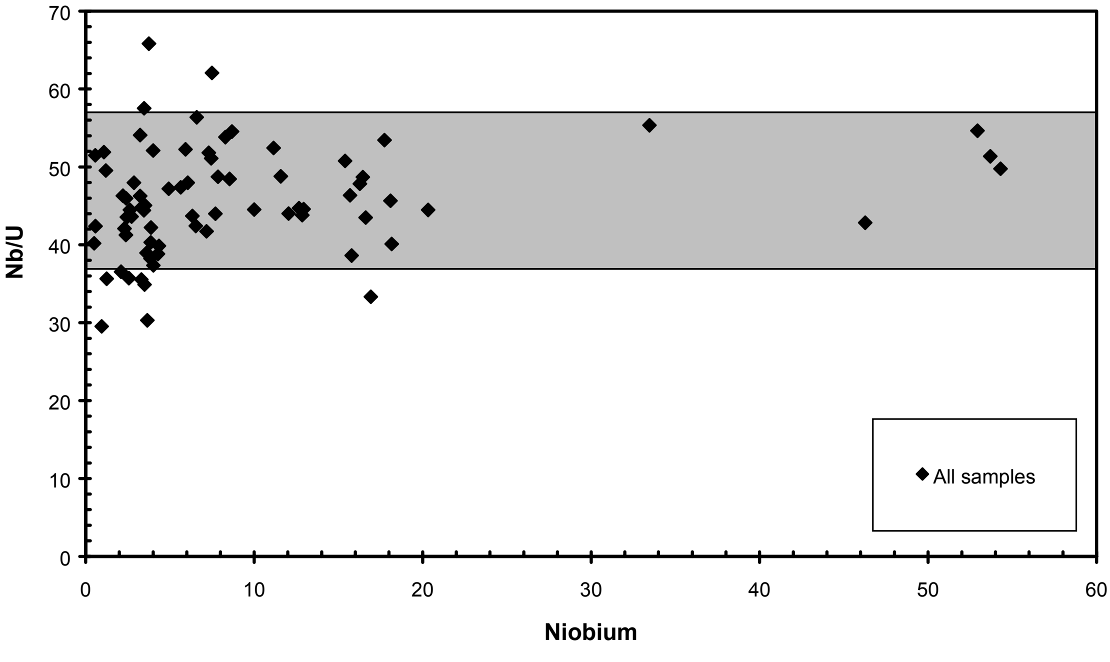

Figure 3.5a Nb/U ratios of analysed samples

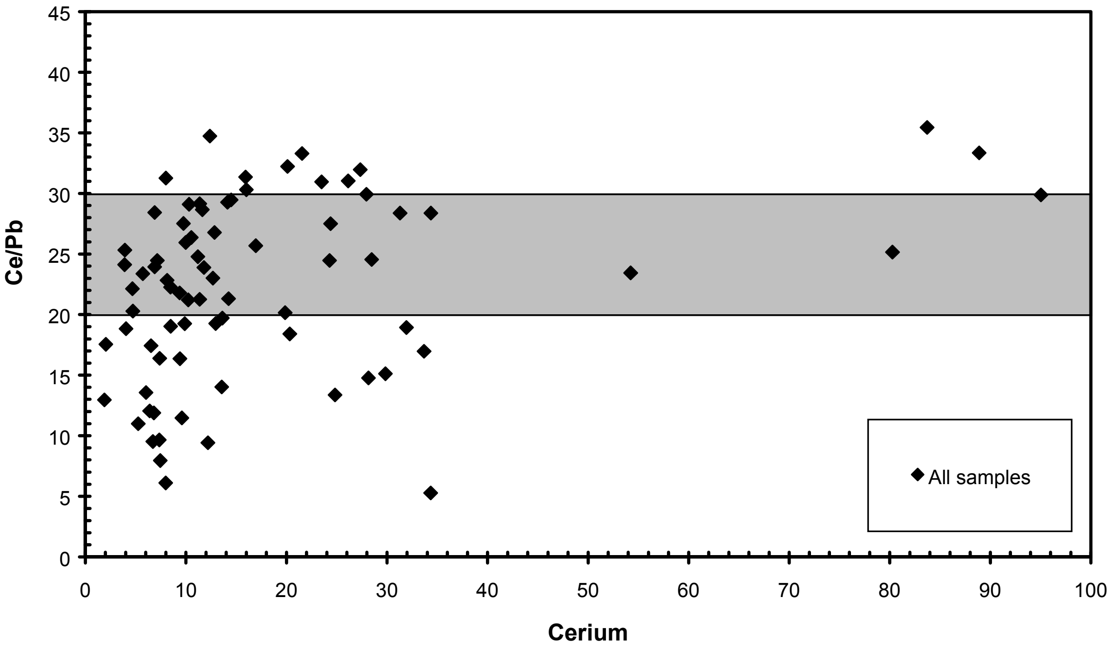

Figure 3.5b: Ce/Pb ratios of analysed samples

3.4 Therm-Ion-Mass-Spectrometry (TIMS)

Isotope ratios of Pb, Sr and Nd were measured at the Max-Planck-Institut für Chemie Mainz, using a Finnigan MAT 261 multicollector mass-spectrometer and in the Institut für Mineralogie, University of Münster (only Sr) using a VGSector54 multicollector mass spectrometer. Only handpicked glass chips were used. Cleaned glass chips (see microprobe analytical methods) were leached in 1 N HCL for 15 min. Following leaching, the samples were dissolved in a mixture of HF and HNO_3. Pb separation was done following method of Abouchami et al. (1999). The eluent from Pb chemistry was retained for Sr and Nd chemical separation. After elution of Pb, a small aliquot of the sample Pb (approx. 5%) was taken. A triple spike amount, estimated to be optimal, was then added to this aliquot and the resultant mixture homogenized by drying down. Spiked and unspiked samples were loaded separately onto Re filaments along with silica gel-H_3PO_4 activator and then measured. Procedures for combining the results from the two runs to yield the bias-corrected Pb isotopic composition have been discribed by Galer (1999) and Galer and Abouchami (1998). Lead blanks were between 15-80 pg and are negligible. Sr, Nd, Pb Isotope values, appendant 2δ standard deviations and measured standard values are given in the appendix.

Chapter 4:
Results

4.1 Petrography

All samples are of submarine origin and where obtained by dredging. Three different types of rocks, based on morphology, can be distinguished. Pillows are most common, although pieces of sheet flows and lava tubes were also dredged. Glass rims occur on most samples and reach a thickness of 30 mm, but in an average of about 3 to 5 mm. Most of the samples are fresh or only slightly altered. Altered samples can be covered with brown to dark-grey coloured Mn and Fe coatings. Alteration reduces the thickness of glass rims and leads to a brown coloured alteration product. The vesicularity of the samples is very variable. The basalts differ from vesicle free, solid basalts to highly (50%) vesicular. Generally speaking, samples from elevated ridge segments show more vesicles than samples from „normal“ ridge segments. Also the size of the vesicles tends to be higher in samples from the shallow ridges and can reach 8 mm. On the other hand, even samples from deep segments show a remarkable vesicle content. The average diameter of the vesicles is however less than 1 mm. The samples show a wide range of textures from aphyric to highly porphyritic basalts. The main phenocrysts mineral phases are plagioclase, olivine and clinopyroxene. Plagioclase is the most abundant mineral phase followed by olivine and to a small extent clinopyroxene, spinel is an accessory phase. Most thin sections show a glomerophyric texture with clusters of olivine and plagioclase. The matrix is glassy to microlithic, containing thin plagioclase needles forming an intersertal texture. In most samples two generations of plagioclase phenocryts could be observed, large plagioclase megacrysts and small plagioclase needles. The plagioclase megacrysts are sometimes rounded and resorbed, smaller plagioclase phenocrysts are euhedral or subhedral. Olivine also appears quite often in two generations as small anhedral microcrysts and in the form of bigger phenocrysts. These phenocrysts often show skeletal growth indicating rapid cooling of the sample. Clinopyroxene is rare, as an exception thin sections 149 DS-1 contains some rounded clinopyroxene phenocrysts which do not appear in textural equilibrium with the host melt. These types of basalts fit well into the well described petrography of the MAR. It should also be mentioned that in the vicinity of the seamounts, basalts from the elevated ridge segment show an aphyric or near aphyric texture. Ridge segment boundaries seem not to have any influence on the petrography of the samples.

4.2 Major elements

4.2.1 Mineral chemistry

Feldspars

As shown in the triangular system Anorthite – Albite - Potassium-feldspar (An-Ab-Or, Figure 4.1), feldspars have low K_2O concentrations (≤ 2.21 %) and are thus plagioclase. The anorthite content of the plagioclase ranges from An_{56} to An_{90} with smaller phenocrysts tending to be more sodic than larger plagioclase phenocrysts. Figure 4.2 shows a clear positive correlation between plagioclase composition in small phenocrysts and MgO content of the glass, as has previously been observed for the East Pacific Rise by Batiza and Niu (1996). The larger plagioclase phenocrysts do not show such a clear correlation. Normal zoning with An-rich cores and Ab-rich rims implying a growth from a primitive to more evolved melt is common, although inverse zoning with Ab-rich cores and An-rich rims, implying a change from evolved to more primitive magma, does occur. Figures 4.3a & b show the anorthite contents of rims and cores respectively of plagioclase phenocrysts (all sizes) plotted against latitude on the ridge. Analyses from off-ridge seamounts are distinguished. The An component in plagioclase phenocrysts decreases in some samples towards the Ascension FZ in the north and towards the end of Segment 5 in the south. Plagioclase phenocrysts from seamounts have higher An-contents than plagioclase phenocrysts from Segment 5.

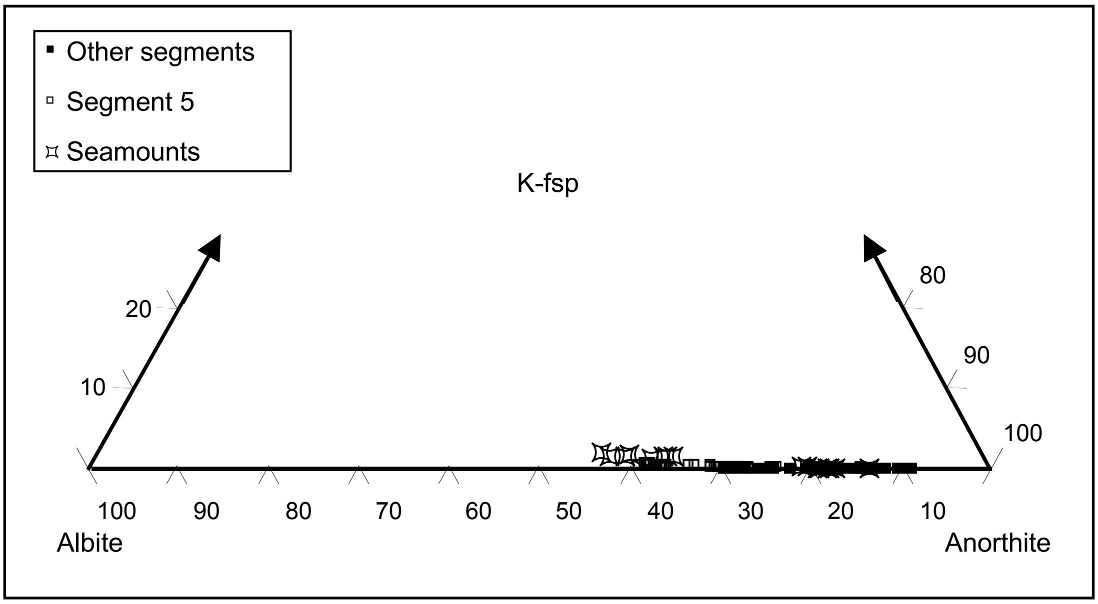

Figure 4.1: Triangular system of Anorhtite - Albite - Potassium-feldspar (An-Ab-Or)

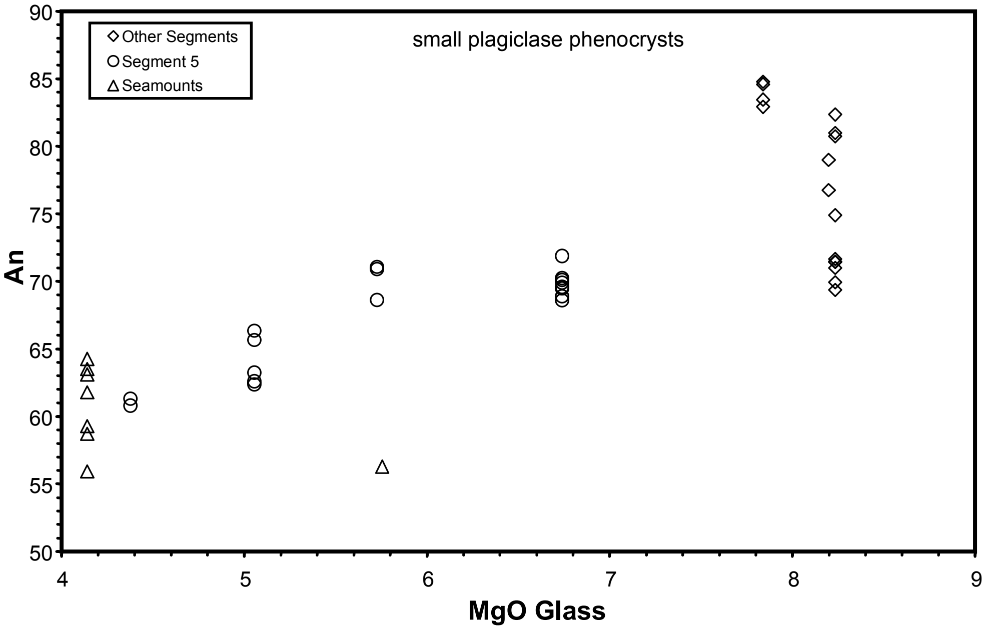

Figure 4.2: Correlation of MgO concentration of host glass with An content of small plagioclase phenocrysts

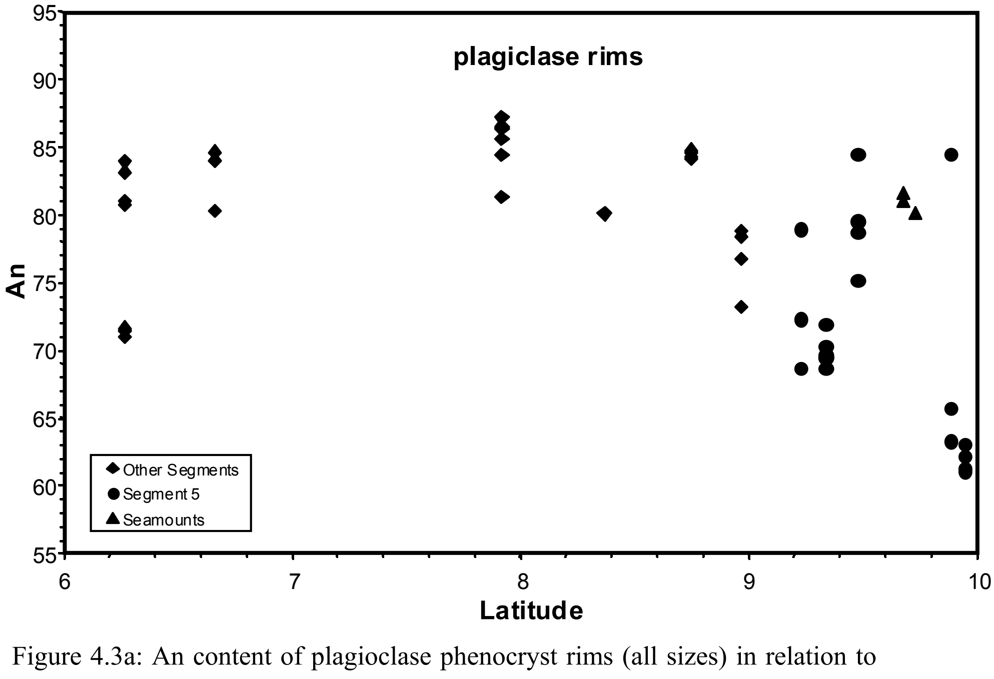

Figure 4.3a: An content of plagioclase phenocryst rims (all sizes) in relation to latitude

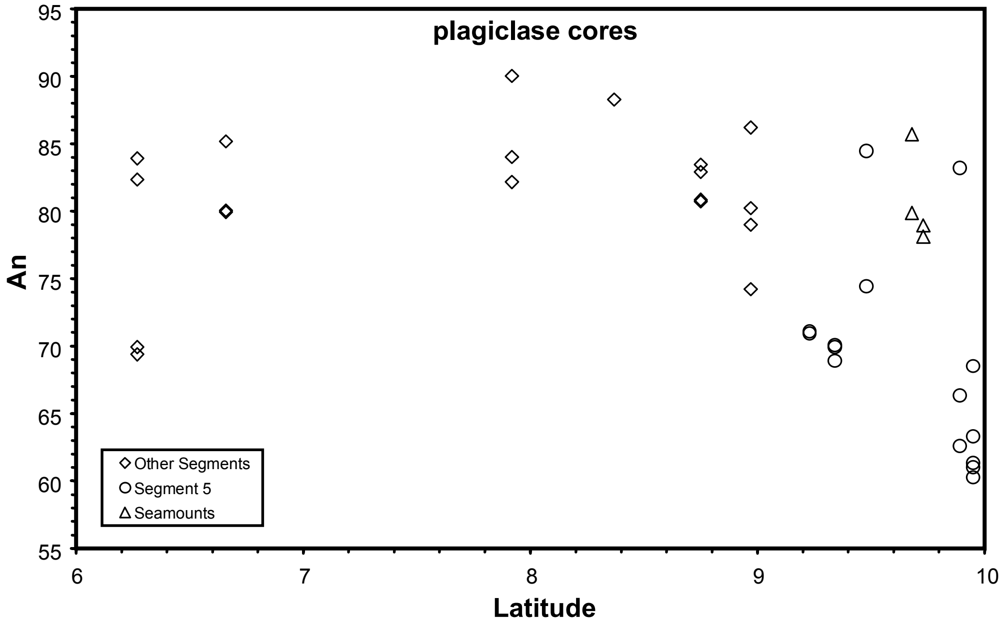

Figure 4.3b: An content of plagioclase phenocryst cores (all sizes) in relation to latitude

Olivine

Measured olivines vary in composition between Fo_{76} to $Fo_{90.}$ The Mg rich olivines, which are as primitive as mantle olivines, occur on Segment 1 in sample 139 DS-2 in the vicinity of Ascension island. Rim / core measurements of olivine show chemical zoning with commonly Fo rich cores and Fo depleted rims. Inverse zoning also occurs as shown in Figure 4.4. Differences in Fo contents of cores and rims are generally small but can reach approx. 4 % Fo. In Figure 4.5 the Fo-content of olivine phenocrysts is plotted versus the Mg-number of their host lava. These different divisions of measured olivines lead to following conclusions:

- Olivine composition does vary with liquid composition, with high Fo-olivines in MgO rich liquids.
- Based on the experimental Mg/Fe partitoning between ol and melt (Roeder and Emslie, 1970) most of the analysed olivines are not in equilibrium with their host melt. Smaller olivines tend to be closer to equilibrium than larger ones but are nevertheless not fully equilibrated. This implies rapid ascent and cooling of the magmas.
- Although it is apparent from Figure 4.5 that olivines from segment 5 and from the seamouts show lower Mg contents than olivine phenocrysts from other segments and so a dependence of Fo content and latitude does exists, there is no sign of geographical influence on the state of olivine / melt equilibrium.

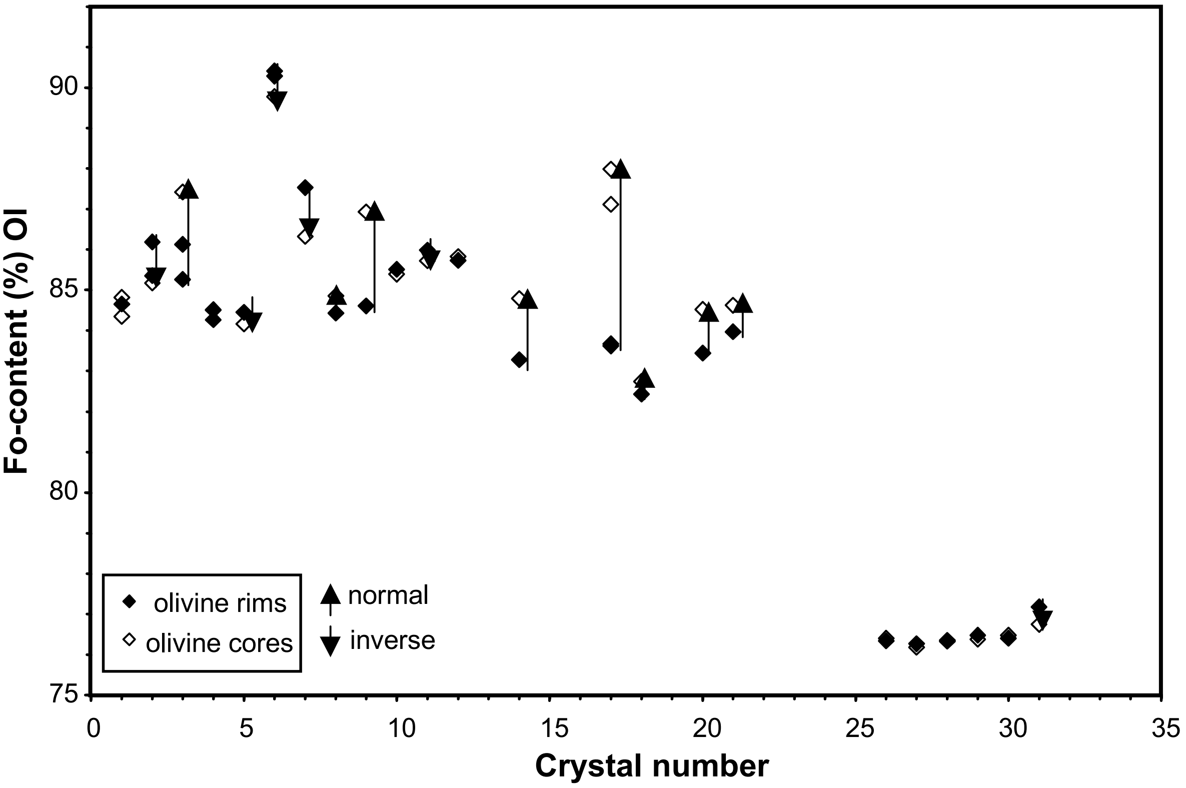

Figure 4.4: Zoning of olivine phenocrysts

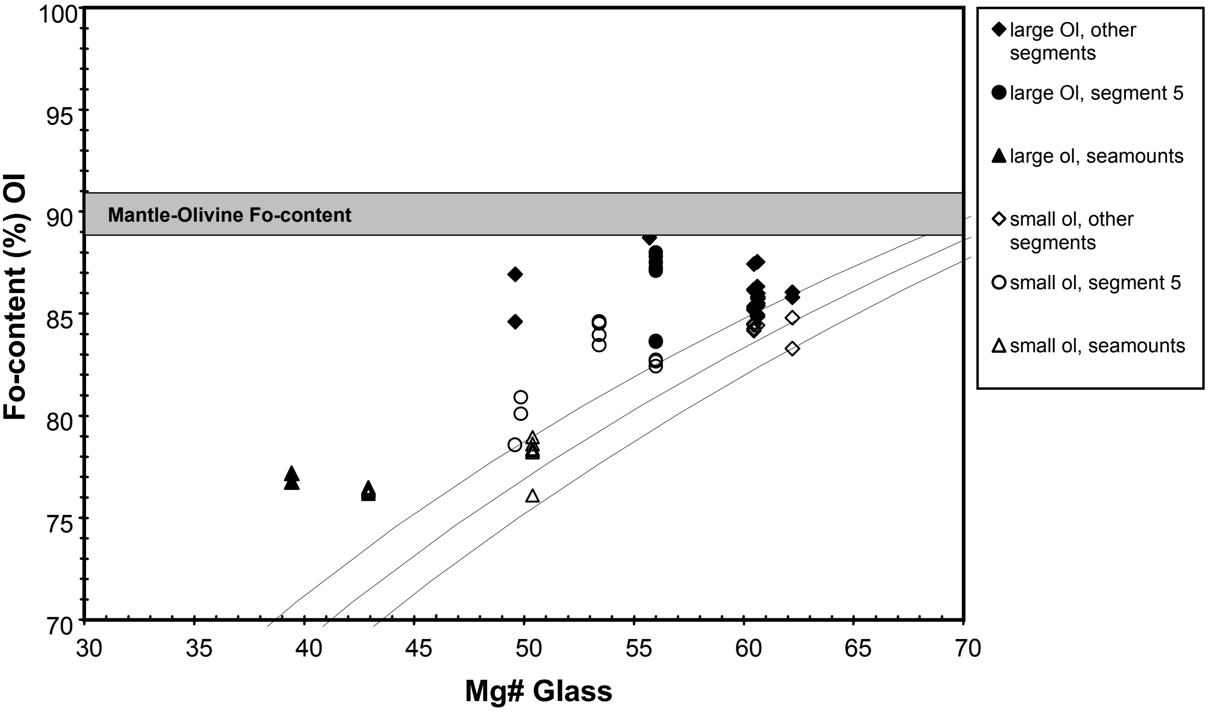

Figure 4.5: Mg# of host glasses vs. forsterite content of olivine phenocrysts, solid lines represent, from bottom to top, olivine-liquid equilibrium with K_D values of 0.27, 0.30, 0.33

Pyroxene

Pyroxene phenocrysts are rare in the investigated thin sections. Only solitary phenocryts were observed and measured, no cpx were found in the seamount samples. The measurements are plotted in Figure 4.6. All measured phenocrysts are clinopyroxene (cpx) and can be mostly defined as augites. The augites show a relatively wide compositional range with $Wo_{34\text{-}45}$, $En_{43\text{-}53}$, $Fs_{7\text{-}15}$. Cpx from Segment 5 tend to be more Fe rich than cpx phenocrysts from other segments.

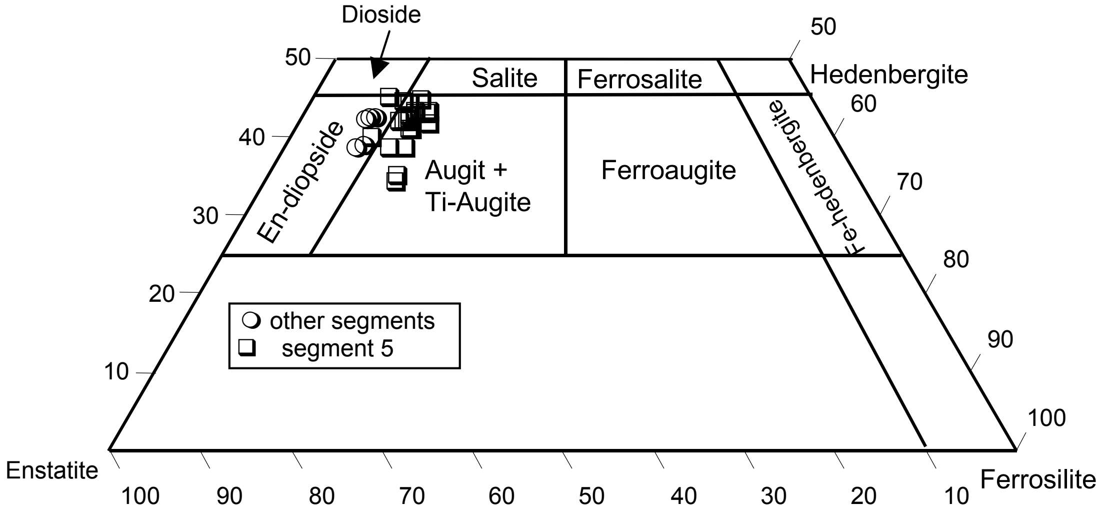

Figure 4.6: Pyroxene tetrahedron, see text for discussion

Spinel

Spinel occurs as inclusions in olivine and plagioclase. Two spinel minerals which were hosted in plagioclase phenocrysts were analysed (see Appendix). These spinels contain Cr_2O_3, FeO, Al_2O_3, MgO and to a minor amount TiO_2 and are thus picotite.

Melt Inclusions

Glassy melt inclusions represent portions of the melt which were isolated during host mineral growth. As melt moves through the crust and changes its composition by crystal fractionation and mixing, melt inclusions may be less affected by these processes and so give insights into earlier stages of melt formation. Melt inclusions in the study area occur mainly in plagioclase and to a smaller extent in olivine phenocrysts. Intensive work on plagioclase-hosted melt inclusions were made by Nielsen (1995) who investigated plagioclase phenocrysts from the Gorda Ridge, Pacific Ocean. He pointed out that chemical data from melt inclusions show distinct scatter in terms of major and minor elements if the inclusions are not reheated and quenched before measurement. This he attributed to the effects of crystallisation processes in the glassy inclusions following their entrapment. Since such reheating was not performed during the present study, our measurements show the mentioned scatter (Figure 4.7) in major elements although only total glassy inclusions were taken into account. In view of these difficulties, melt inclusion data should be treated with caution. Nevertheless investigations of elements in melt inclusions which are unlikely to be incorporated into the plagioclase host crystal during eruption and cooling are presented in Figure 4.7. It shows K/Ti ratios of glassy inclusions in dependence to MgO. An initial observation is that, despite the fact that Segment 5 has lower MgO contents in its erupted lavas than the other segments, all segments have similar MgO contents in their inclusions. Furthermore we see no signs of any differences in K/Ti between the segments.

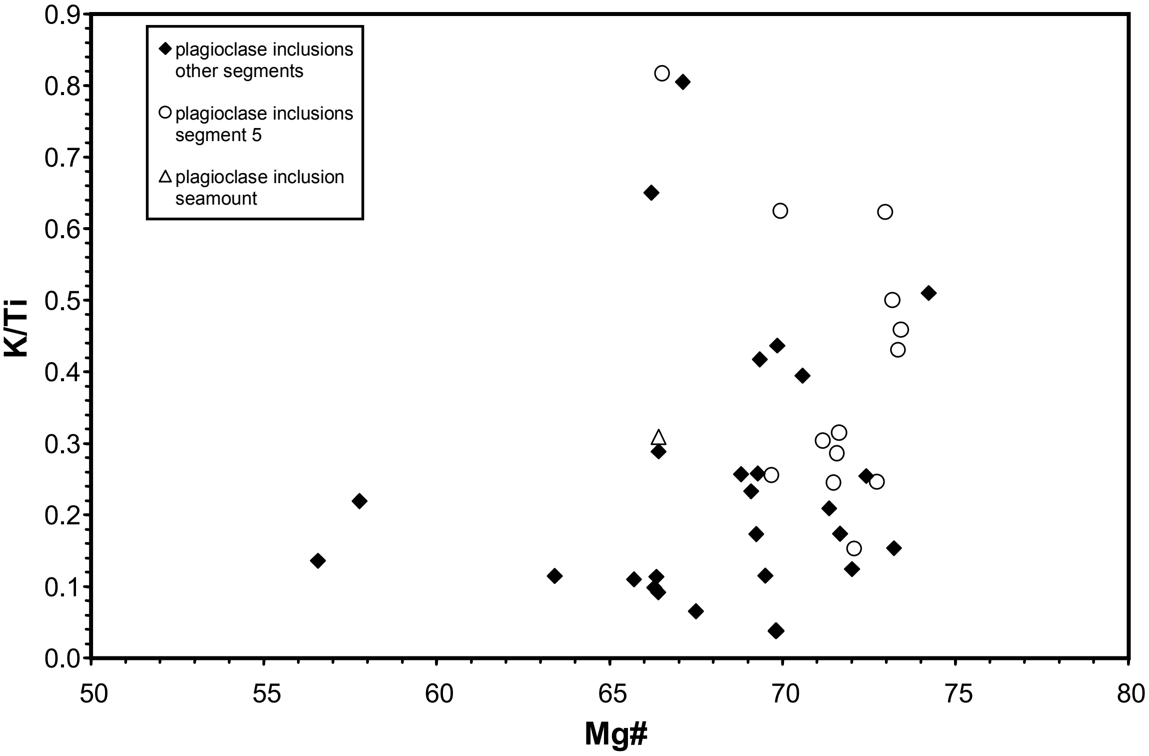

Figure 4.7: K/Ti vs MgO for the inclusions in plagioclase

4.2.2 Basalt glass chemistry

For classification the $Na_2O + K_2O$ diagramm (Le Bas and Streckeisen, 1991) (Figure 4.8) is used. Three groups can be distinguished. Most ridge samples are typical basalts, whereas the majority of the seamount samples are trachybasalts. The samples from Segment 5 lie in an intermediate position between the trachybasalts from the seamounts and the basalts of the remaining segments. The diagramm K_2O versus SiO_2 (Figure 4.9) shows that most of the basalts of the investigated ridge-segments are poor in K_2O and thus low-K sub alkalic basalts or tholeiites. Segment 5 samples are sub-alkalic basalts and most of the seamount samples are alkalic basalts.

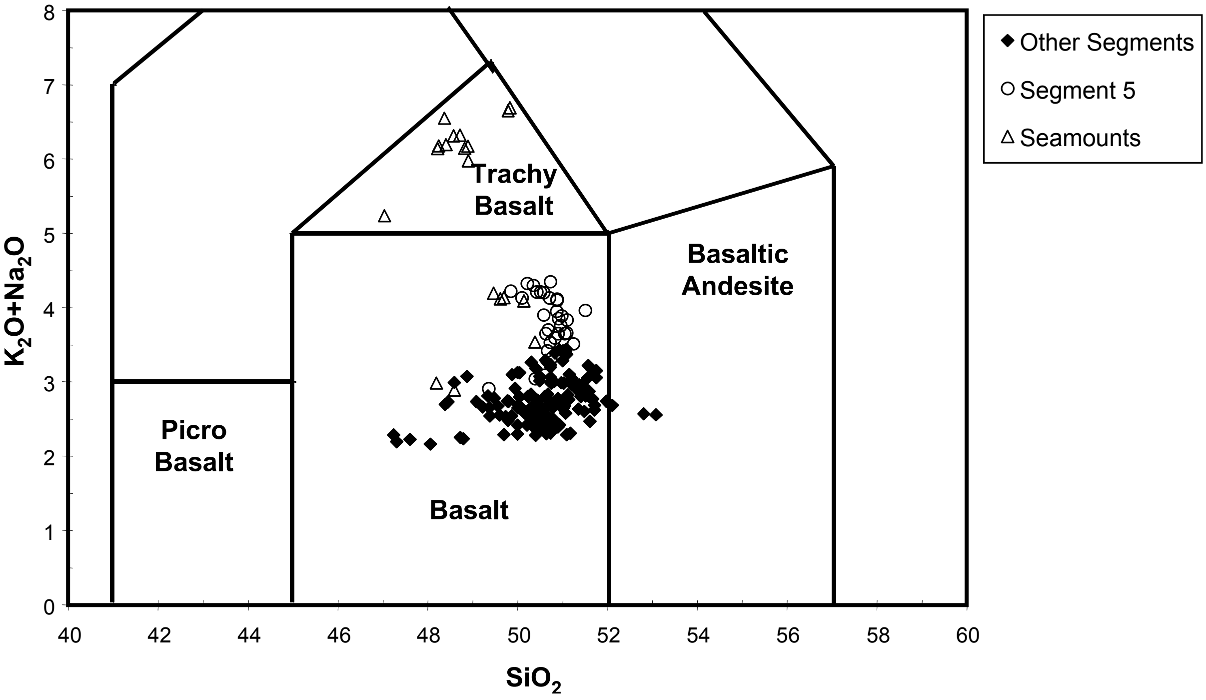

Figure 4.8: $Na_2O + K_2O$ diagramm of Le Bas and Streckeisen (1991)

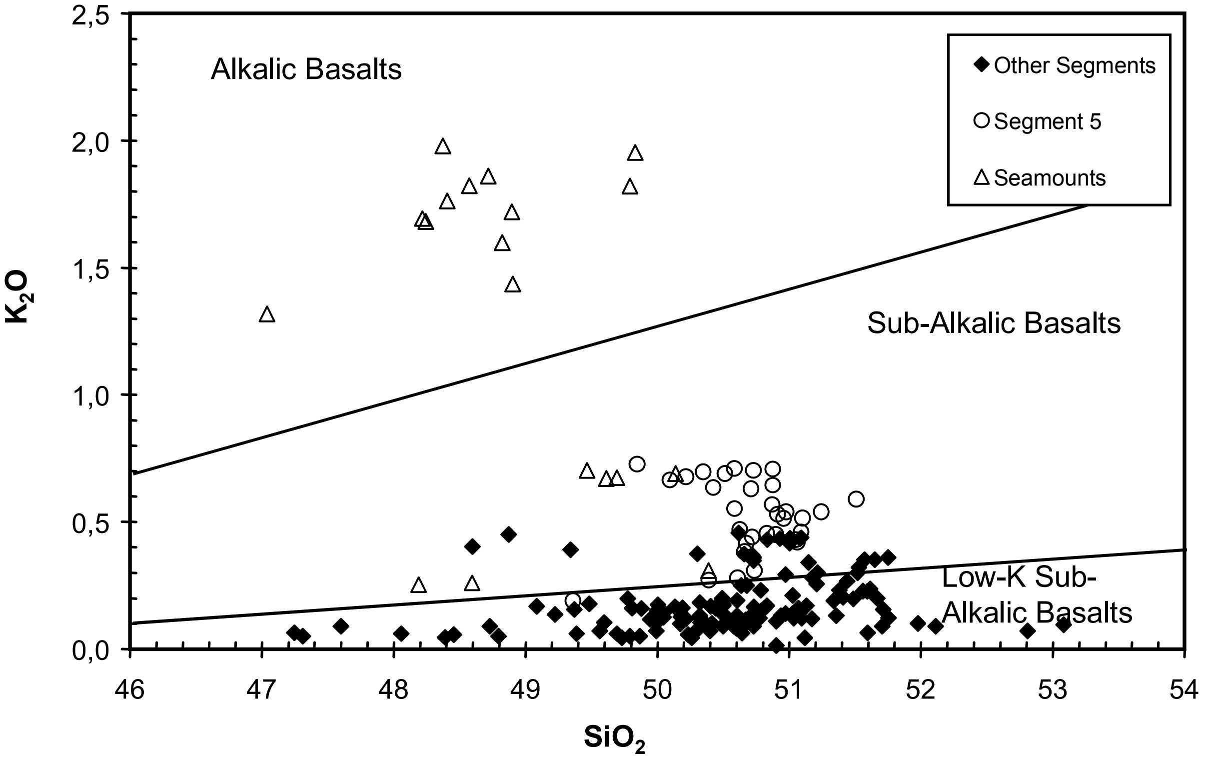

Figure 4.9: K_2O vs. SiO_2 showing that most of the basalts are tholeiites

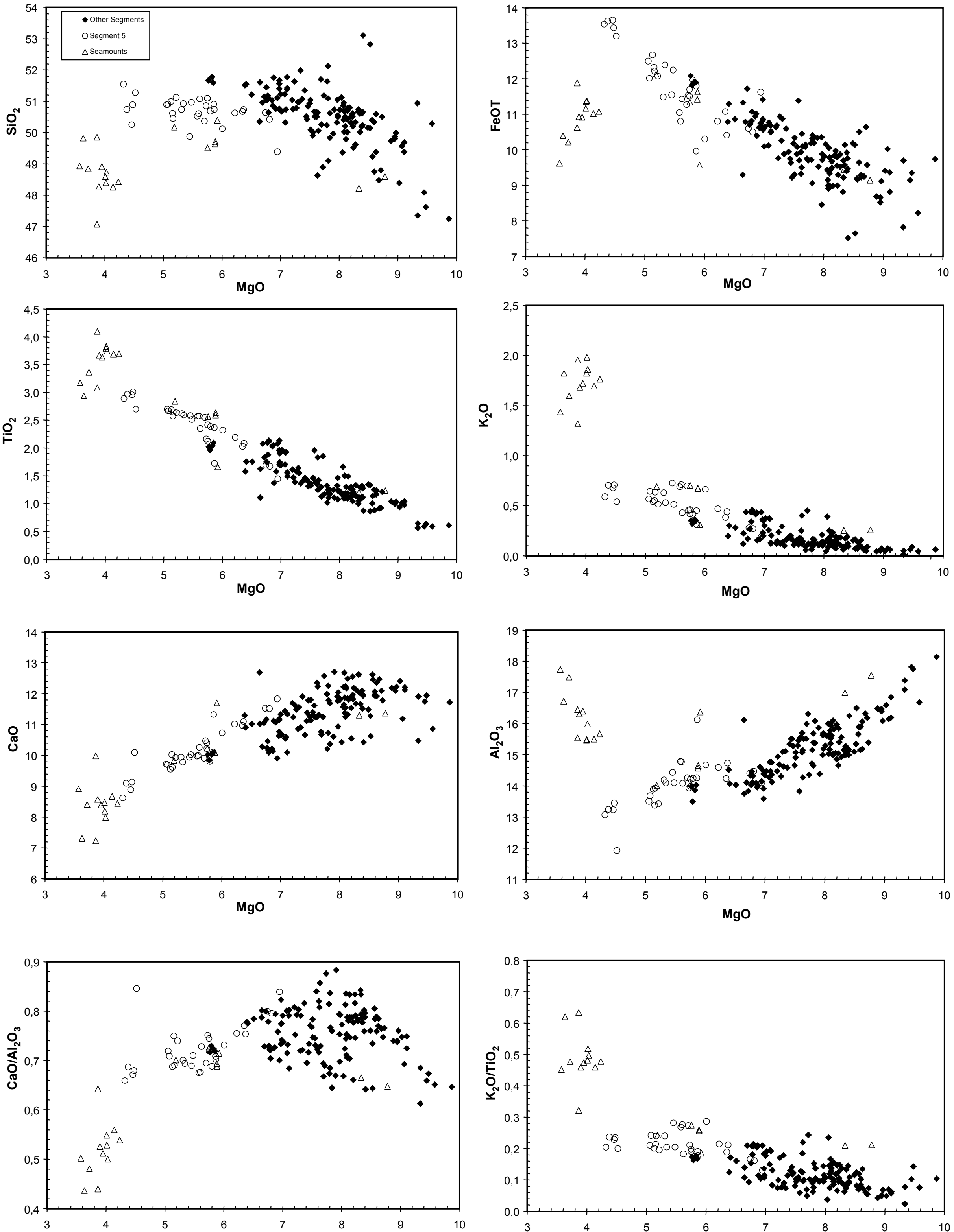

Figure 4.10: MgO vs. major element concentrations and ratios

In Figure 4.10 major element concentrations and ratios are plotted against the MgO content. All major element analyses are given in the appendix. For ease of description samples are divided into groups. MgO contents lie in a wide range of 9.87 and 3.57 wt.%. Beside some samples with high MgO concentrations, three main groups can be distinguished: Most samples have typical MORB MgO contents between 8.7 and 6.6 wt.%. The majority of all sampled segments except Segment 5 lie within this range. Most samples of Segment 5 show intermediate MgO contents between 6 and 5 wt.%. Finally mainly the samples from the seamounts but also some samples from Segment 5 show low MgO contents between 4.4 and 3.5 wt.%. The SiO_2 contents are significantly scattered both for the seamount and for the ridge axis samples. The Segment 5 and seamount fields are progressively displaced towards lower MgO and SiO_2 relative to the field for the other segments. FeOt, TiO_2 and K_2O show negative correlations with MgO contents for the ridge segments as previously shown by Klein and Langmuir (1987), the samples from Segment 5 showing slightly lower FeOt at a given MgO content. The seamount samples lie on a continuation of this trend in the TiO_2 vs MgO diagramm but are significantly displaced from the axial basalt trends in terms of FeOt and K_2O. Thus the most MgO depleted seamount samples have lower FeOt concentrations than the high FeOt segment 5 samples building a kink at approx. 4.4 wt.% MgO and 13.6 wt.% FeOt respectively. CaO and Al_2O_3 are positively correlated with MgO for the spreading ridge magmas as also previously outlined by Klein and Langmuir (1987). Although the CaO content shows significant scatter for MgO concentrations higher than 6.8 wt.%, CaO contents are well correlated with MgO contents less than 6.8 wt.% MgO. Al_2O_3 shows a similar but opposite behavior to FeOt, the seamount samples having higher Al_2O_3 at a given MgO than the spreading axis basalts and Segment 5 being somewhat displaced to higher Al_2O_3 relative to the trend for the other segments. On both the CaO/Al_2O_3 and K_2O/TiO_2 vs. MgO plots the seamount samples are clearly distinguished from the axial samples. The few seamount samples which fall within the field for the axial samples come from the seamount closest to the present spreading centre.

4.2.3 Along axis chemical variation

Along axis major element concentrations and ratios show significant trends. As shown in Figure 4.11 the MgO content is strongly correlated with water depth, with the most MgO poor lavas being found on the shallow Segment 5. As we have seen from Figure 4.10 that MgO depletion is systematically related to enrichment or depletion of other major elements e.g. FeO, CaO, Na_2O (for details see previous section) presumably via crystal fractionation, we will only plot elements with independent or nearly independent systematics here. The ratio of K_2O/TiO_2 is higher in Segment 5 samples (Figure 4.10, 4.11). Also one dredge at approx. 8° S shows higher values than the

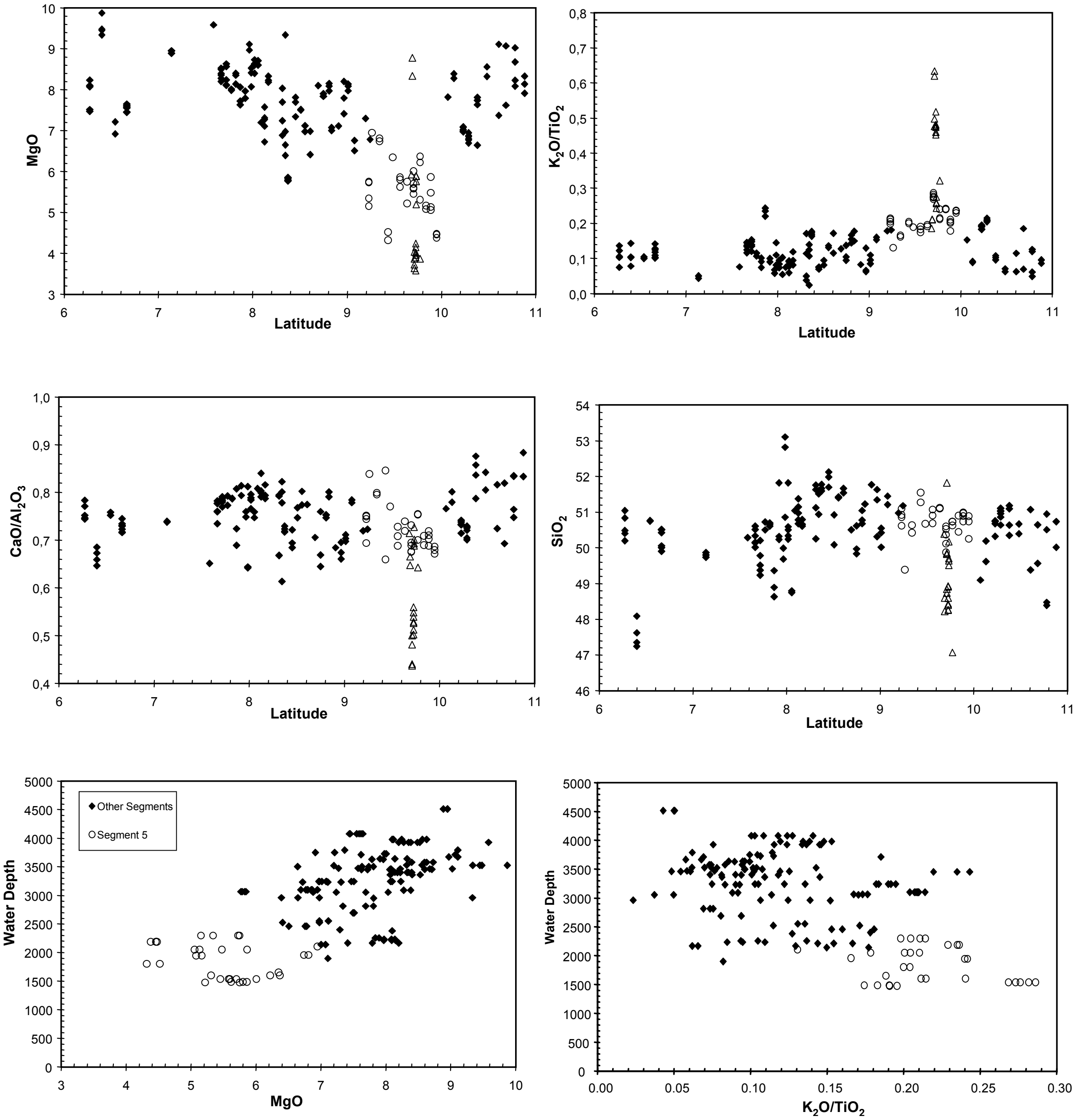

Figure 4.11: Along axis major element concentrations

surrounding samples. This ratio is also well correlated with water depth (Figure 4.11). Interestingly the CaO/Al_2O_3 ratios show a gradual increase at Segment 6. The SiO_2 concentrations of Segment 5 show no conspicuous trend and fall within the scatter of the other segments. One dredge haul north of the AFZ contained samples with high MgO and low SiO2 similar to the seamount samples. The high MgO and low K_2O/TiO_2 in this dredge distinguishes it however from the seamount samples.

To summarize these observations it can be said that taking all the segments together, the MgO concentration is well correlated with water depth with low MgO lavas in shallow water. This relationship does not always hold for the segments taken individually. The concentrations of incompatible major elements is highest in segment 5 and seamount lavas. These lavas also show some of the lowest CaO and Al_2O_3 contents.

4.3 Trace elements

Selected samples were analysed for trace element compositions, element abundances are given in the Appendix. Generally mantle-incompatible trace elements mirror the trends of incompatible major elements. Ratios of highly/moderately incompatible trace elements like La/Sm are well correlated with K_2O/TiO_2 (Figure 4.12). In concordance to K_2O/TiO_2, La/Sm ratios show a correlation with water depths, with enriched lavas occurring in shallow water depths (see discussion). Figure 4.13 shows chondrite normalized trace element ratios arranged in decreasing incompatibility from left to right (spider diagram). Plotted are means of each MAR segment. Segment O and AFZ are very depleted in highly incompatible elements. Segment 1 is more enriched as both enriched and depleted lavas occur. Segment 2 and 3 are also depleted in incompatible elements but also not as much as samples from Segment 0 and AFZ. The enrichment increases in samples from Segment 4 and 5 and in the Seamount lavas. Also notable is the negative slope in heavy rare earth elements (HREE) which is increasing from Segment 4 over Segment 5 to the Seamounts. Segment 6 samples are heterogenous, incompatible element depleted and enriched lavas occur.

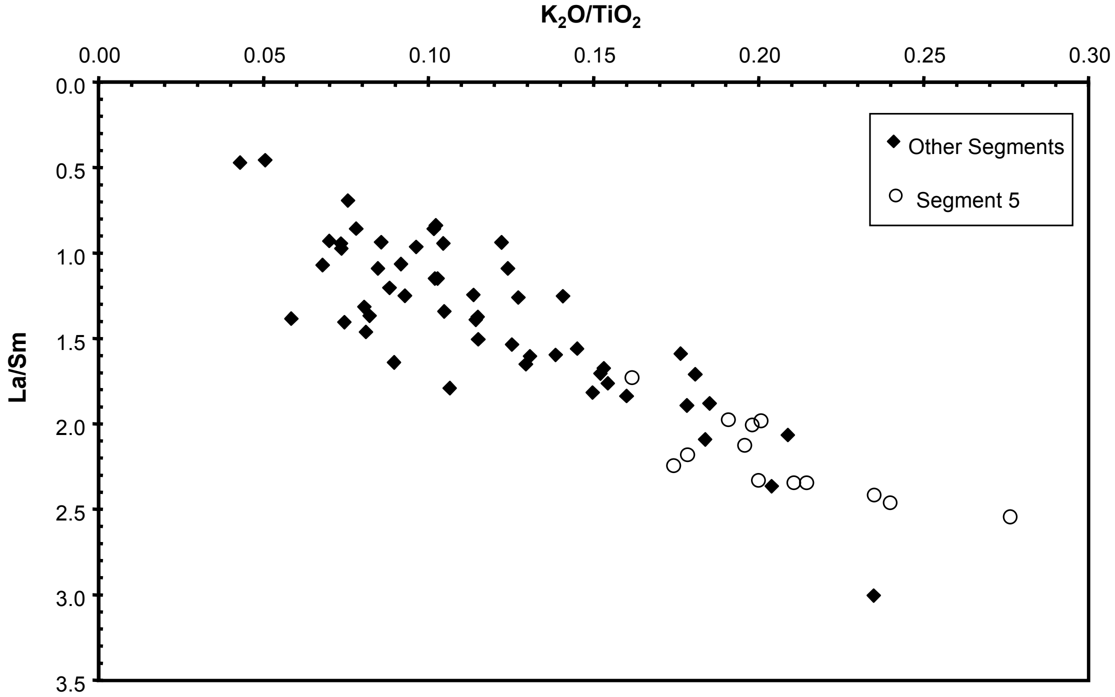

Figure 4.12: Correlation of La/Sm with K_2O/TiO_2

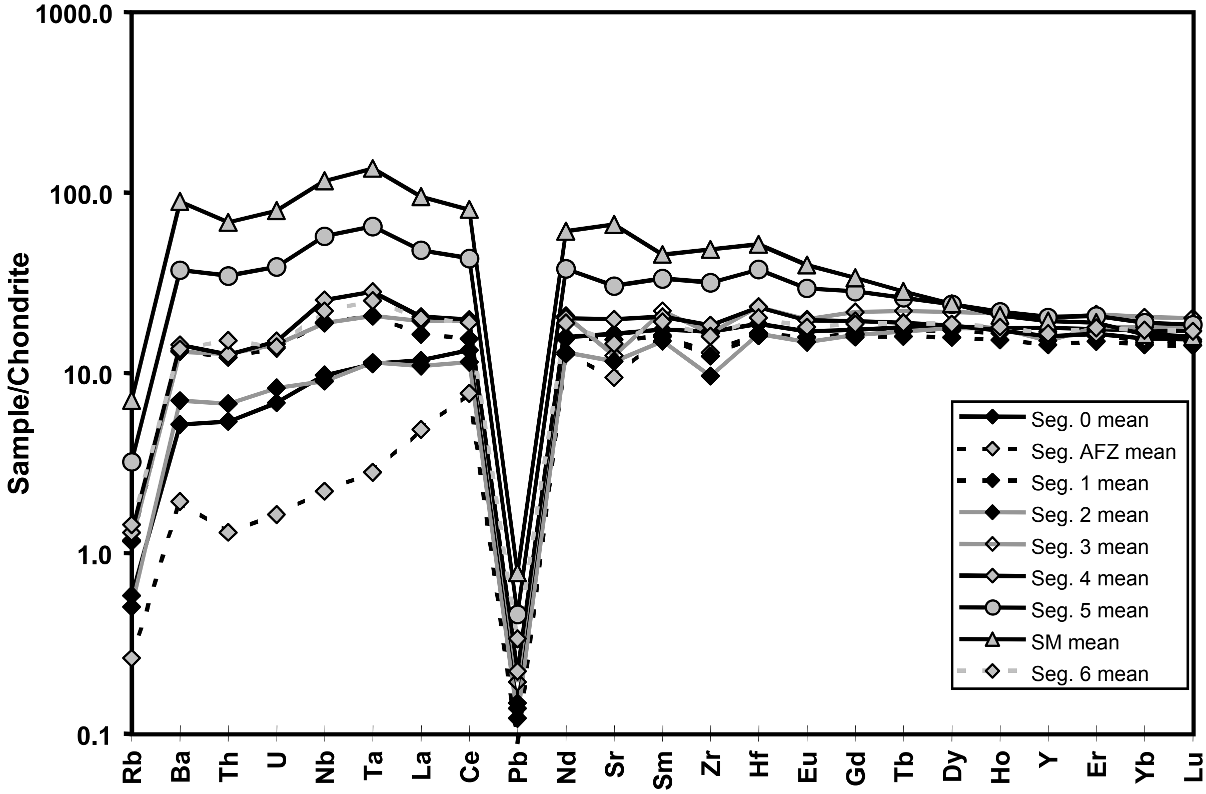

Figure 4.13: Spider diagram, chondrite from (Sun and McDonough, 1989)

4.4 Radiogenic isotopes ratios

Figure 4.14 shows that samples define a linear array with positive correlation in a plot of $^{206}Pb/^{204}Pb$ vs $^{207}Pb/^{204}Pb$. The range of $^{206}Pb/^{204}Pb$ ratios is between 17.71 and 19.42. Positive correlation also exists between $^{87}Sr/^{86}Sr$ and $^{206}Pb/^{204}Pb$ (Figure 4.15), although it is significantly more scattered. $^{87}Sr/^{86}Sr$ ratios lie between 0.7021 and 0.7028. Seamount samples which have the highest $^{206}Pb/^{204}Pb$ do not have highest $^{87}Sr/^{86}Sr$, highest $^{87}Sr/^{86}Sr$ are found in Segment 5 samples.

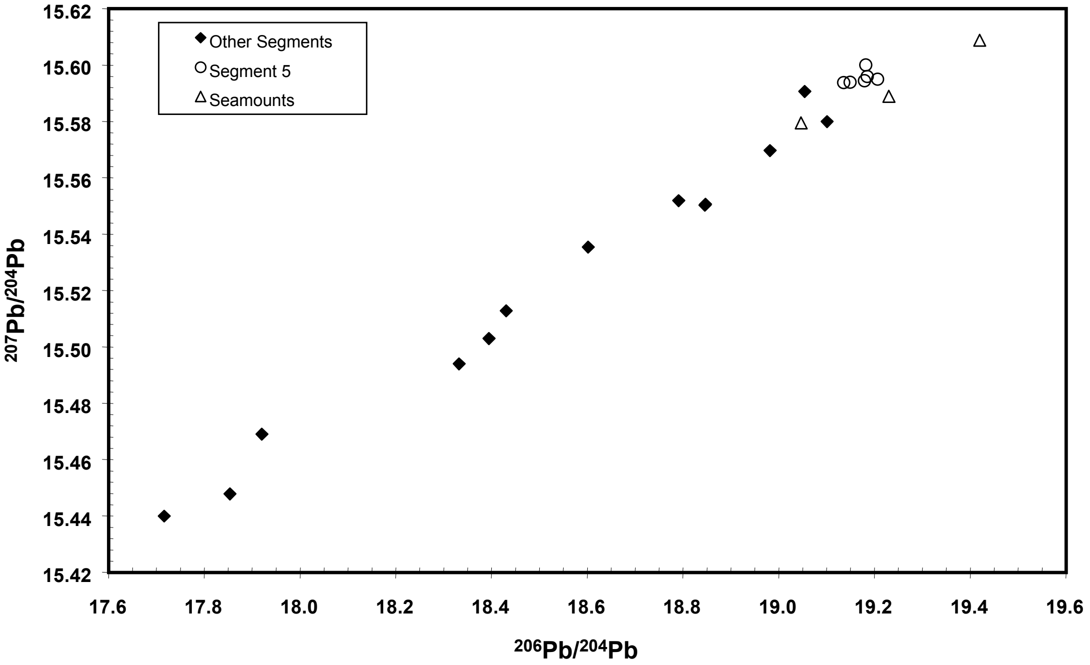

Figure 4.14: Plot of $^{206}Pb/^{204}Pb$ vs $^{207}Pb/^{204}Pb$

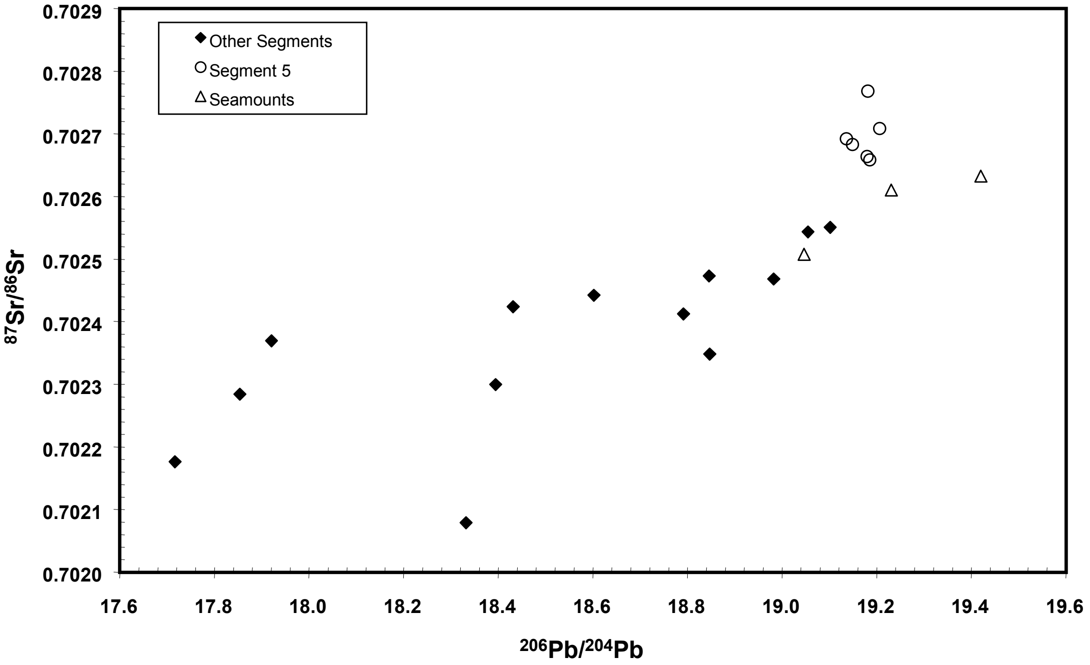

Figure 4.15: Plot of $^{87}Sr/^{86}Sr$ and $^{206}Pb/^{204}Pb$

CHAPTER 5

DISCUSSION

5.1 Major element variation

Figure 4.10 shows that the major element composition of analysed samples is highly variable. These variations can be due to crystal fractionation or magma mixing. Considering magma mixing we have to think about a very evolved (low MgO), enriched melt and a very primitive (high MgO), depleted melt in order to produce the wide range of major element compositions presented in this work. Major element variations due to magma mixing can be ruled out for the following reason: Curved trends on some of the major element binary plots for the Segment 5 samples (especially Al_2O_3 and K_2O vs. MgO, see Figure 4.10) allow us to exclude the possibility that magma mixing is an important process for generating the major element variation in the magmas because mixing products should lie on a straight line. Based on trace element and isotope ratios, deep level mixing in the mantle can not be ruled out and will be discussed later.

5.2 Fractional crystallisation

5.2.1 Introduction

After a melt separates from its source due to its lower density it will ascend. While ascending into cooler mantle regions the melt cools. The lowering of melt temperature causes mineral phases to solidify from the melt due to the passing of their liquidus temperature. Major element variations in the melt can result from these crystallisation processes. Basically two different modes of crystallisation processes occur: fractional or equilibrium crystallisation. The main difference between these two crystallisation modes is that in the case of fractional crystallisation the solid is removed from the melt and so minerals and melt can not equilibrate. Considering fractional crystallisation, mineral – liquid separation can occur by gravitational separation, crystallisation on the wall rock, flow differentiation, in situ crystallisation (Langmuir, 1989) and by filterpressing in which melt is separated from a crystal mush through pressure. Continuous extraction of one or more mineral phases will progressively change the composition of the melt. In terms of their mineralogy and compared to other magmatic rocks MORB are not very variable. Typical MORB contain mainly plagioclase and olivine and to a lesser extent clinopyroxene phenocrysts. The percentage of fractionating mineral phases depends on the initial composition of the melt, the temperature (T) of the magma and on the depth of crystallisation i.e. the pressure (P). As indicated above most magmas that reach the earth´s surface are not aphyric but contain abundant mineral phenocrysts. This indicates relatively low magma temperatures below the liquidus. Such “cold” phenocryst-rich melts should show a different composition than their starting composition. As pointed out in the chapter “Oceanic Magmatism” MORB parental magmas should have MgO contents of ca. 11 % MgO wt and should crystallize olivine exclusively down to 9 % MgO wt.

5.2.2 Low pressure fractionation

In order to determine the pressure of fractional crystallisation for the MORB of the working area Figure 5.1 shows the ternary ol–cpx-qtz sytem. The normative mineral assemblage was calculated from the major element concentrations of the analysed volcanic glasses according to Walker et al. (1979). Also plotted is the 1 atm phase boundary from Walker et al. (1979) and three high pressure phase boundaries from Stolper (1980). Most samples of the investigated area and even from the elevated Segment 5 plot near the 1 atm ol – cpx cotectic but some samples from the other Segments plot between the 1 atm cotectic and the 10 kbar ol – cpx – qtz eutectic point. Seamount samples are undersaturated in SiO_2 and lie outside of the ternary diagram. It can be stated that high pressure crystal fractionation seems not to play an important role in samples of the investigated area.

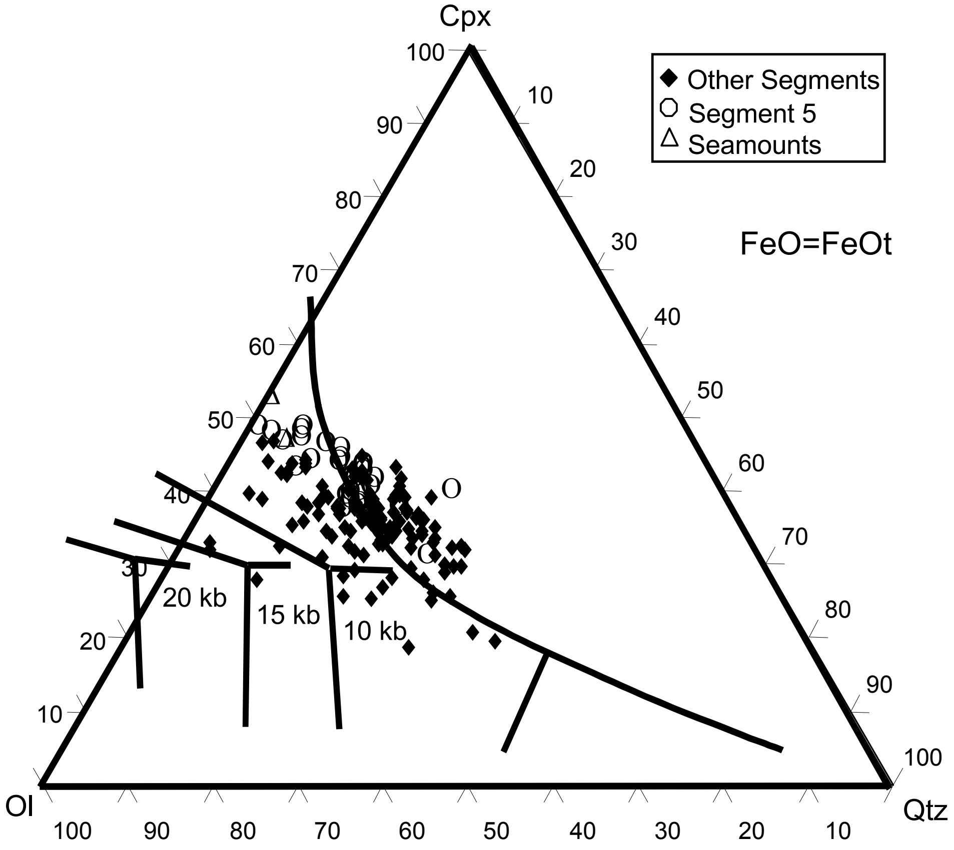

Figure 5.1: Ol-Cpx-Qtz ternary system, plotted is the normative mineral assemblage, see text for discussion and references

5.2.3 Crystallizing phases

Different volumes of crystallizing mineral phases will produce slightly different trends in the major element diagrams (Figure 4.10). In general, fractional crystallisation of MORB leads to MgO depletion which is combined with an increase of FeOt, Na_2O, K_2O and TiO_2, and a decrease in CaO and Al_2O_3 content. Due to the relatively low CaO/Al_2O_3 ratio of plagioclase (ca. 0.5) and the relatively high CaO/Al_2O_3 ratio of clinopyroxene (ca. 7.5) major element variations imply at high MgO values an olivine – plagioclase crystallisation which increases the CaO/Al_2O_3 ratio (Figure 5.2). At high MgO concentrations CaO/Al_2O_3 ratios appear to fall onto two trends, a low CaO/Al_2O_3 and a high CaO/Al_2O_3 trend. This points either to two different parent magmas with different MgO contents or stronger olivine fractionation in the lavas with lower MgO. The lavas with higher CaO/Al_2O_3 show earlier onset of cpx crystallisation at ca. 8 % MgO compared to the low CaO/Al_2O_3 lavas at ca. 7 % MgO. At lower MgO concentrations fractional crystallisation of clinopyroxene and plagioclase (+/- ol) does occur which lowers the CaO/Al_2O_3 ratio significantly.

Although the fractional crystallisation paths will be examined in detail in the next section it should be mentioned now that there is a discrepancy between the observed cpx fractionation in major element diagrams and the lack of modal appearance of cpx (except rare crystals) in MORB thin sections. This feature is common in MORB (Walker et al., 1979), and called the clinopyroxene paradox. An explanation could be that melts do not equilibrate well with cpx at shallow depths and may have crystallized cpx at greater depths (Kinzler and Grove, 1992), suggesting a more rapid extrusion without the cpx. Langmuir (1989) explained this paradox with in situ crystallisation. This process combines magma mixing and crystallisation. Cooler evolved melt from the walls of a magma chamber that crystallized cpx mixes with more primitive and hotter melt from the interior of the chamber. This produces a cpx signature in the melt without requiring cpx phenocrysts present in the erupted magma. Because magma chambers beneath the MAR are absent or at least very rare, in situ crystallisation may not play an important role at the MAR and the cpx paradox may have a different origin.

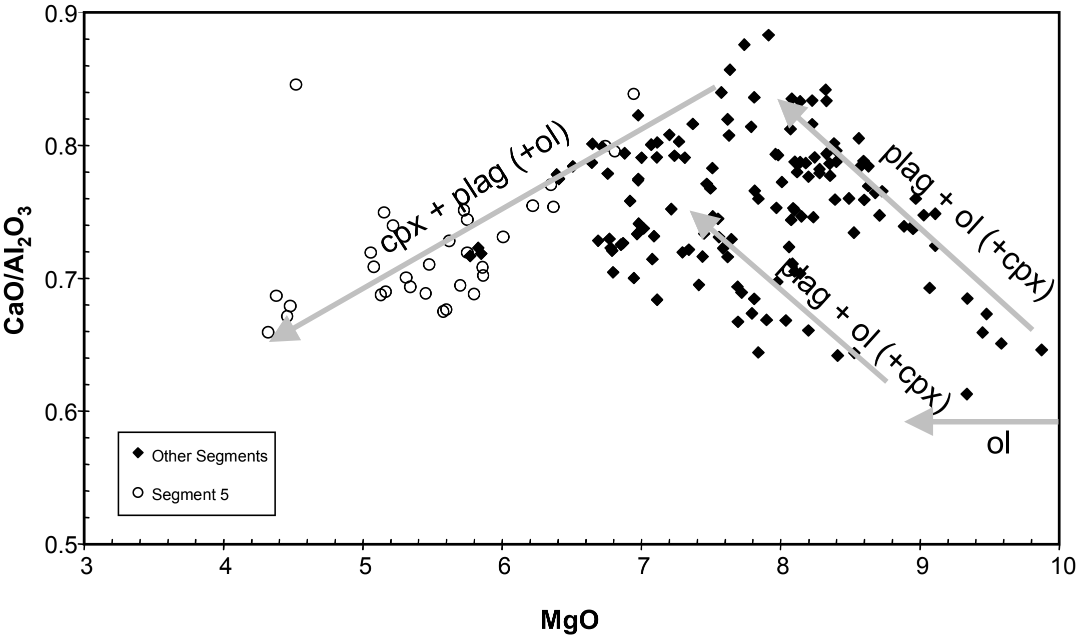

Figure 5.2: A Diagram of MgO vs. CaO/Al_2O_3. The arrows indicate the way a melt takes while different mineral phases fractionate from the liquid

5.2.4 Modelling of fractionation with MELTS

Introduction

In this section calculations of fractional crystallisation processes are presented using the MELTS software of Ghiorso (1993) in a public release version from 1995. The calculations are done as follows: First a starting composition is needed. Preferable are MgO rich, primitive glass compositions. With these starting compositions mineral crystallisation can be computed by using the MELTS software. It is possible to change the amount of crystallizing mineral phases, the mode of crystallisation (equilibrium or fractional crystallisation) and the crystallizing pressure (bar) in order to optimize the crystallisation path. This path is compared with crystallisation paths of the samples from the MAR. To do so it is possible to make constraints on crystallisation modes, pressures and participating phases that controlled crystallisation processes of the samples of the investigated area. The following Table shows the starting compositions that were taken for the calculations.

Sample	**Morb-melt 1**	**126 DS-1**
SiO_2	48.68	49.45
TiO_2	1.01	0.99
Al_2O_3	17.64	16.40
Fe_2O_3	0.89	
FeO	7.59	
FeOt		8.52
MnO		0.18
MgO	9.1	8.95
CaO	12.45	12.09
Na_2O	2.65	2.43
K_2O	0.03	0.05
P_2O_5	0.08	0.21
H_2O	0.2	

Table 5.1: Major element concentrations of starting compositions. Morb-melt 1 is a MORB composition for testing MELTS from Ghiorso with already defined FeO/Fe_2O_3 ratio. FeO/Fe_2O_3 ratio of 126 DS-1 is depending on fO_2 buffer and therefore varies. Also different H_2O concentrations and crystallisation pressures were used, see text for discussion

It should be noted that the redox state of the melt has to be comprised into modeling. Based on magnesiochromite phenocrysts Ballhaus (1993) found that MORB cover a range of –1 to +0.5 log units below/above QFM buffer (QFM: Quartz-Fayalite-Magnetite). Therefore all model runs used the QFM-buffer.

Results

Figure 5.3 shows the crystallisation path of Morb-melt 1 with 0.2 % H_2O at 500 bar given as an example from Ghiorso and Sack for testing MELTS. This MORB composition fits well into our major element concentration and should serve as an example if our samples show a comparable crystallisation path because P and H_2O contents have to be determined by the model. Although derivation especially for SiO_2 and FeOt exist, modeled crystallisation paths resemble the real liquid lines of descent. Fractional crystallisation seems to be the major reason for changing major element composition and thus this modeled path gives a rough idea about pressure and H_2O content needed for fractional crystallisation modelling.

Dependence on P and H_2O

Sample 126 DS-1 shows a suitable major element composition for modeling fractional crystallisation processes. While modelling, it turned out that pressure and H_2O content are the main factors that control the crystallisation path of a specific composition. The pressure dependence of fractionation trends is shown in Figure 5.4a. Variable crystallisation pressures are combined with a fixed H_2O content. Higher pressures up to 3 kbar lead to significantly lower SiO_2 and CaO and higher Al_2O_3 concentrations than observed. Figure 5.4a suggests low pressure fractionation at <0.5 kbar even for Segment 5 magmas in concordance to Figure 5.1.

The water content of a magma has a strong effect on the crystallisation path. Michael and Chase (1987) pointed out that H_2O enriched primary magmas undergo less plagioclase crystallisation than H_2O poor primary magmas, in fact the interval of plagioclase + olivine crystallisation is shorter to the advantage of clinopyroxene. As a result H_2O enriched differentiates have higher Al_2O_3 and lower FeOt than dry MORB at a given MgO content. This can be seen in Figure 4.10 and 5.4b. Most Segment 5 samples have lower FeOt and higher Al_2O_3 than samples from the other segments. This suggests a H_2O enriched source. In addition, Segment 5 samples define distinct trends in terms of SiO_2, and CaO. Unfortunately all samples from Segment 5 are relatively evolved so that a primitive magma from which calculations could start are not available. Michael and Chase (1987) found that their H_2O enriched primary magmas are similar in major element chemistry to the depleted primary magmas with exception of Al_2O_3 which is lower in the H_2O enriched magmas. Although depleted in Al_2O_3 these enriched primary magmas show higher Al_2O_3 concentration when they crystallize. In Figure 5.4b the isobaric low pressure (500 bar) fractionation trends of parental magma 126 DS-1 are shown with variable H_2O contents of 0.1, 0.35 and 0.60 % wt H_2O. Figure 5.4b shows that water contents of 0.1 % wt are too low even for the other segments. Better results especially for the other segments were obtained with a water content of 0.35 % water. The diagrams MgO vs. FeO resp. Al_2O_3 show that Segment 5 crystallisation trends suggest higher water contents between 0.35 to 0.6 % wt H_2O. Primitive magmas with more than 0.4 % wt H_2O are not hypothetical but were reported from the South Atlantic by Michael (1995). In addition data from Michael (1995) suggest that high H_2O contents are more common in the North Atlantic. Furthermore modeled crystallisation trends suggest strong K_2O enrichment which cannot be attributed to crystallisation processes. K_2O enriched lavas occur not only at Segment 5, also many samples of the other segments and not only in the direct vicinity of Segment 5 show a K_2O enrichment.

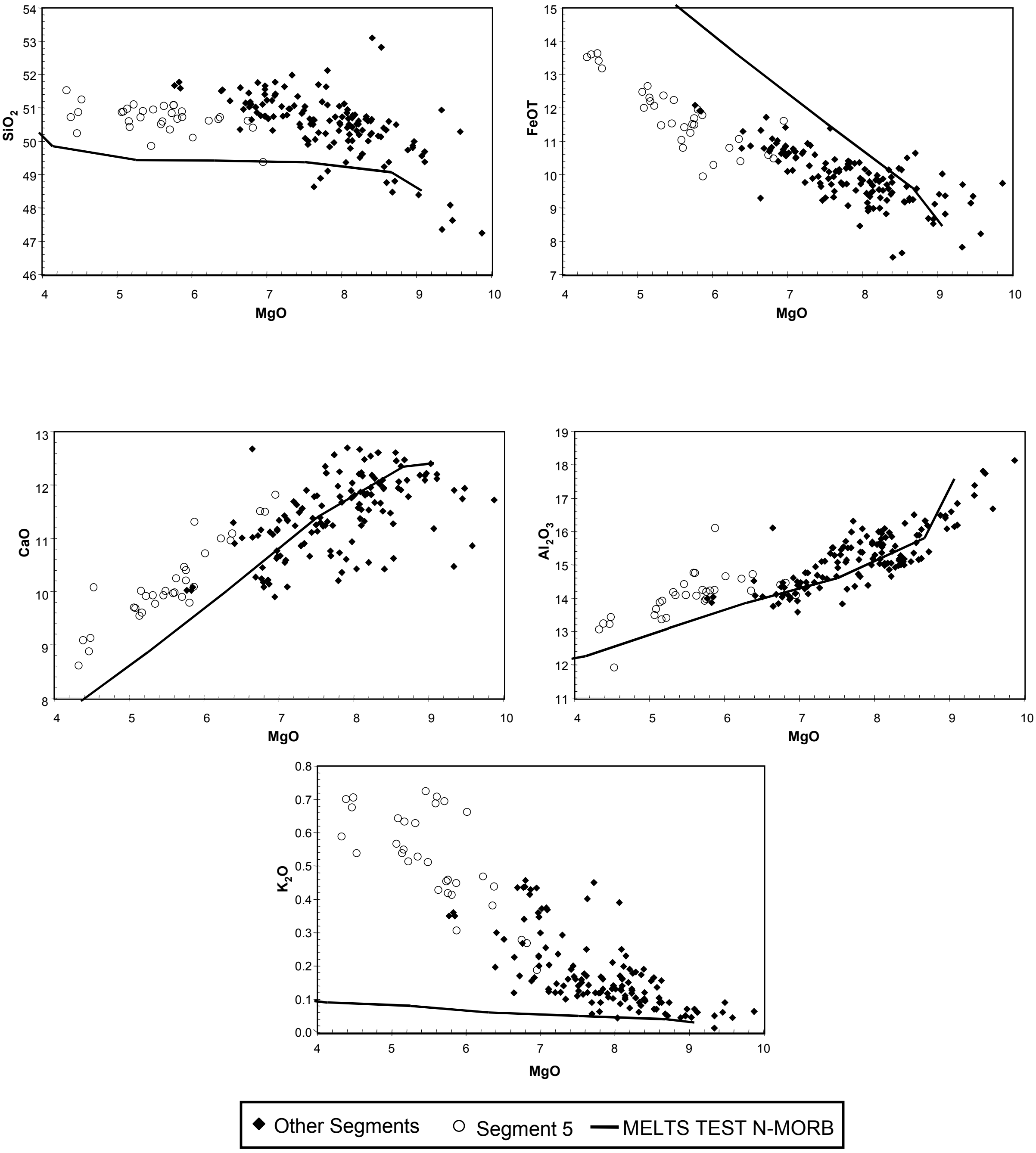

Figure 5.3: Crystal fractionation paths of MELTS N-MORB in comparison to own samples, see text for discussion

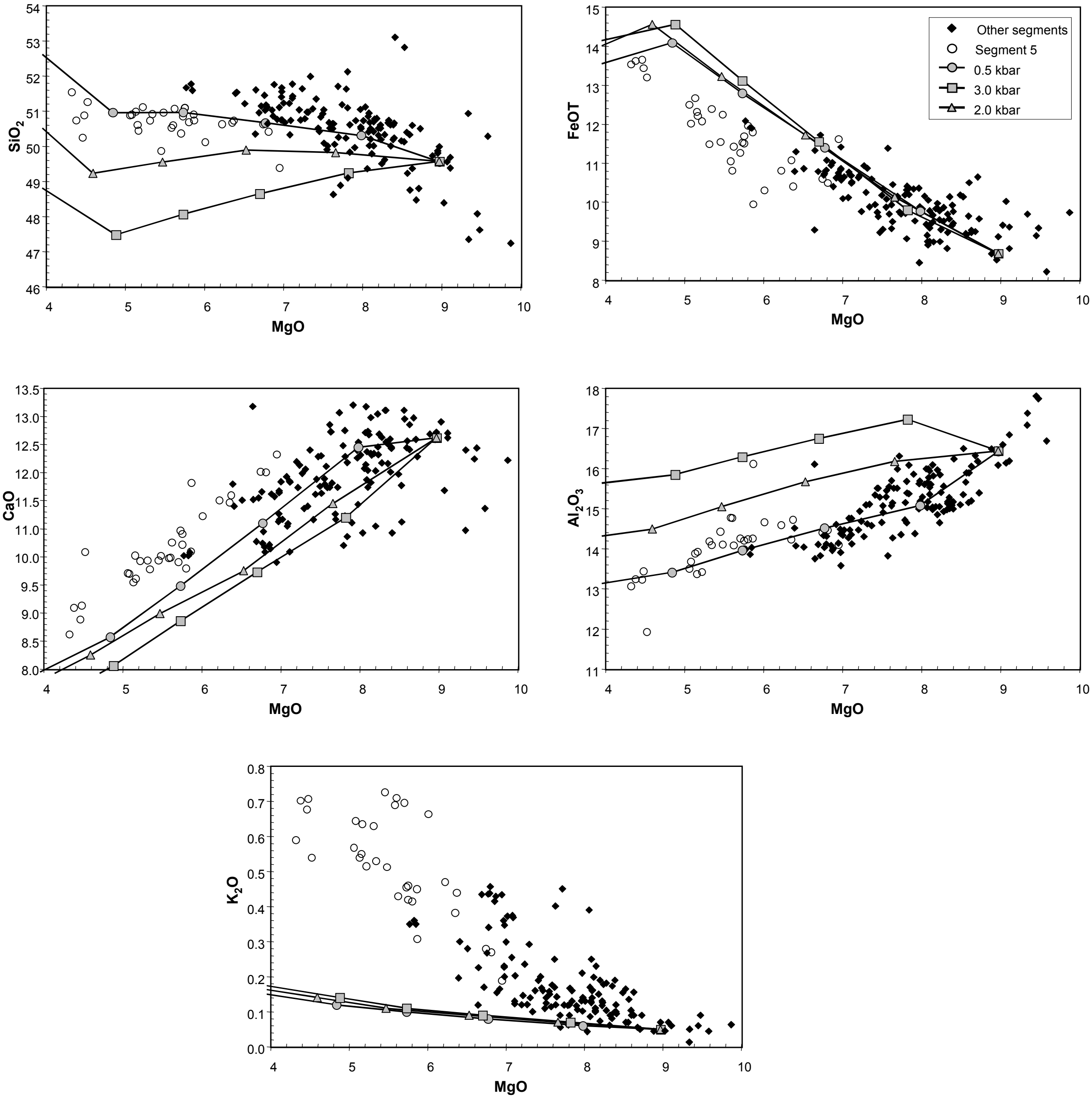

Figure 5.4a: Calculated fractionation paths with fixed H_2O content (0.35 % wt) and variable crystallisation pressure

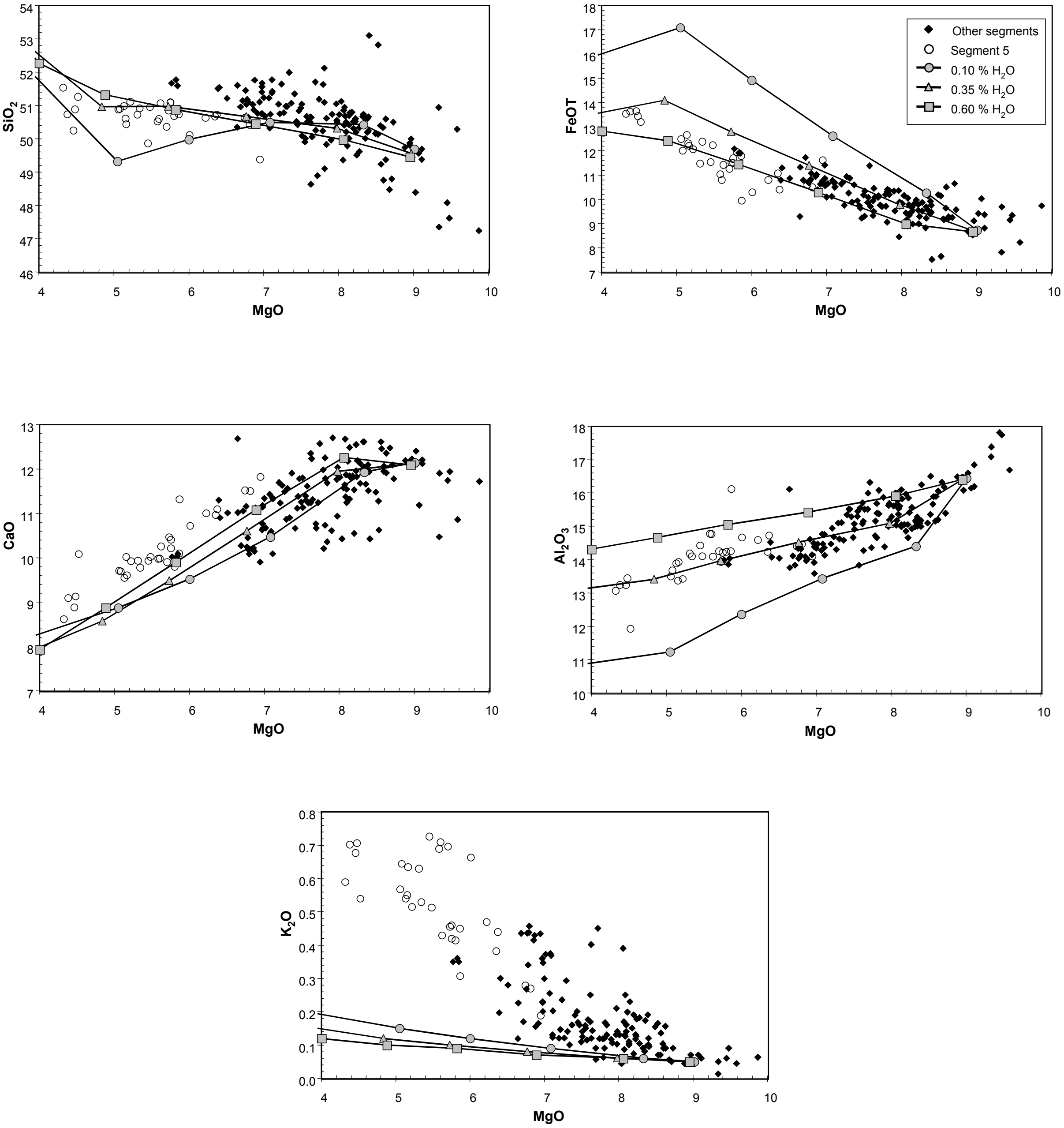

Figure 5.4b: Calculated fractionation paths with fixed pressure (0.5 kbar) and variable H_2O content

Quantitative results

Figures 5.5 shows quantitative results of the fractional crystallisation models. It is visible that higher water contents lead also in the MELTS models to a delayed plagioclase crystallisation whereby the absolute percentages of crystallized mineral phases in both MELTS runs are roughly the same. Considering the MELTS run with 0.35 % water at 0.5 kbar, MgO contents of 3.67 % wt are reached after 70.5 % of the melt crystallized. These MgO contents are reached at ca. 1079°C. At ca. 7 % wt MgO the mass of crystallising phases decreases. At high MgO concentrations plag and ol are the major crystallizing phases. From 7 % wt MgO cpx plays an important role during crystallisation and precipitates in approx. equal amounts to plagioclase. Segment 5 samples should contain high amounts of cpx which is not observed (the cpx paradox as pointed out earlier). Thin sections show only rare, rounded cpx phenocrysts. This leads to considerations of melt and mineral densities values of melt and precipitating phases in order to find out if gravitational processes may play a role during magma evolution. The modeled crystallisation process suggests for a comparatively evolved magma with MgO of 4.84 % wt a liquid density of 2.63 g/cm^3 with mineral densities of 3.41 for olivine, 3.29 for cpx and 2.65 for plag. This implies that ol and cpx might be extracted from the melt via gravitational processes. Plagioclase densities correspond approximately to liquid densities and so they should be transported much easier in the liquid.

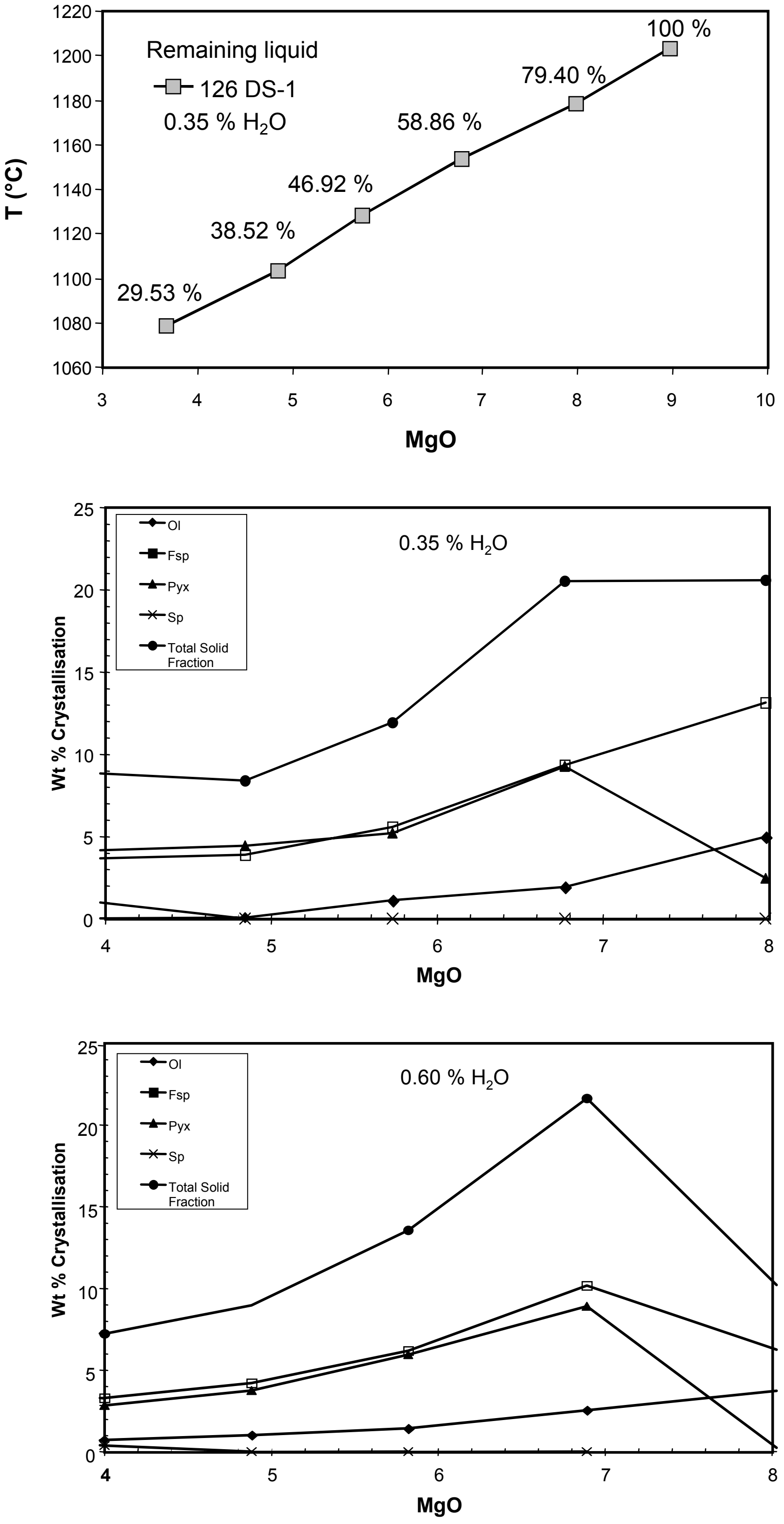

Figure 5.5: Qualitative results of MELTS models, see text for discussion

5.2.5 Trace element fractionation

The mentioned results of calculations with MELTS can be used to model the reaction of trace element abundances and ratios during fractional crystallization (Rayleigh Fractionation: $C_l/C_o=F^{(D-1)}$): In Figure 5.6 selected trace element abundances and ratios are plotted. Rb and K are highly incompatible trace element, La/Sm, K/Ti and Tb/Yb incompatible element ratios, partition coefficients are taken from the compilation of Rollinson (1993). Paths of trace element enrichment due to fractional crystallisation are shown as arrows. The used MELTS calculations are low pressure calculations. High pressure fractionation and also varying volatile contents may have varying liquid lines of descent but should not change the ratios of La/Sm, K/Ti and Tb/Yb significantly (Niu et al., 2001). Therefore it is not possible to attribute the enrichment of incompatible element ratios and abundances with decreasing MgO to crystal fractionation. They must have an origin in partial melt and/or source enrichment processes. In summary it can be stated that:

- Major element variations are due to fractional crystallisation
- Data suggest low pressure fractionation
- MELTS models and fractional crystallisation trends of major elements suggest a higher H_2O content at Segment 5 samples
- Trace element enrichment is not due to fractional crystallisation

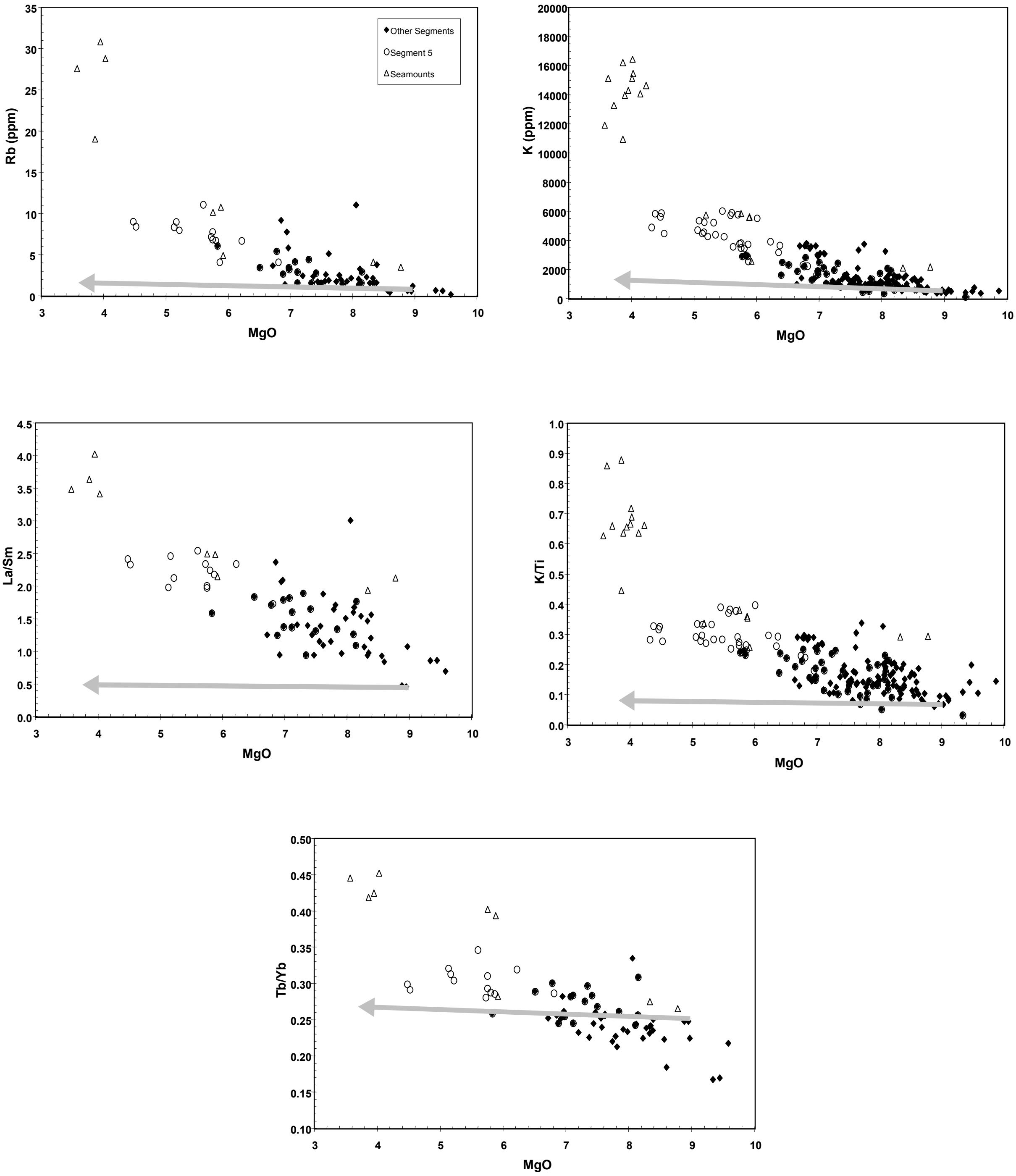

Figure 5.6: Trace element fractionation indicated by arrows, trace element ratios and abundances canot be produced with fractional crystallisation.

5.3 Origin of the melting anomaly

5.3.1 Melting of an enriched source

Figure 5.7a and b shows selected incompatible element abundances and ratios of more-to-less incompatible elements as well as radiogenic isotope ratios as a function of water depth. Although often scattered, correlations do exist. Topographic highs combined with higher crustal thicknesses are associated with enriched lavas. (Seamount samples lie off the trend in terms of trace element abundances and ratios which points to another process involved here.) As it was shown before, fractional crystallisation cannot account for the incompatible element enrichment of lavas from topographic highs at the MAR. In addition very small degrees of partial melt may enrich incompatible element abundances and incompatible element ratios but a low degree of melting is in contrast to the observed thickened crust. Therefore melting of an enriched source can be supposed. Variation of the mantle source is also confirmed by correlations of water depth with isotope ratios like ^{206}Pb/^{204}Pb and ^{87}Sr/^{86}Sr, which are not affected by partial melting and fractional crystallisation. Concerning the bathymetric and geochemical anomaly at Ascension island it was shown in Chapter 2 that hot spots are mostly enriched (with exceptions in the NE Pacific) but vice versa enriched sources do not have to be necessarily hot. Therefore the question arises if an excess mantle temperature (a mantle plume) plays a role in producing this melting anomaly.

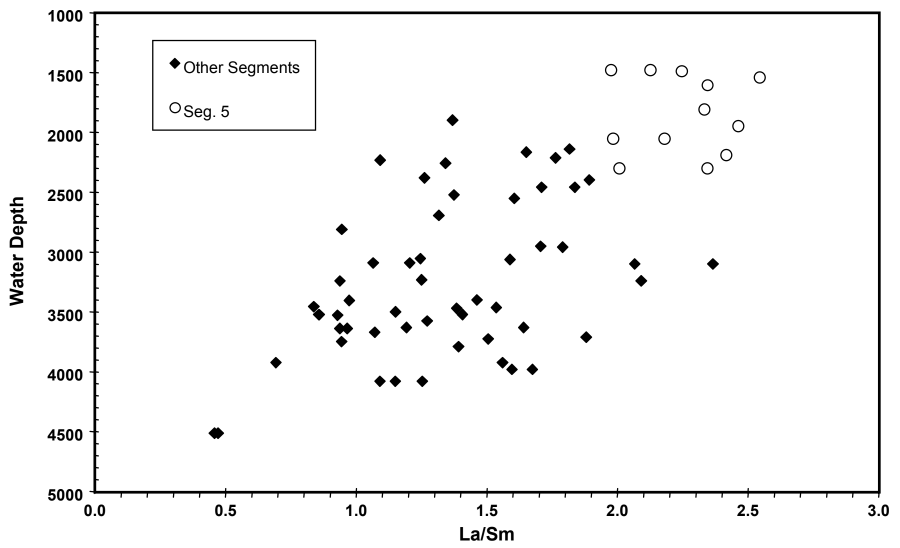

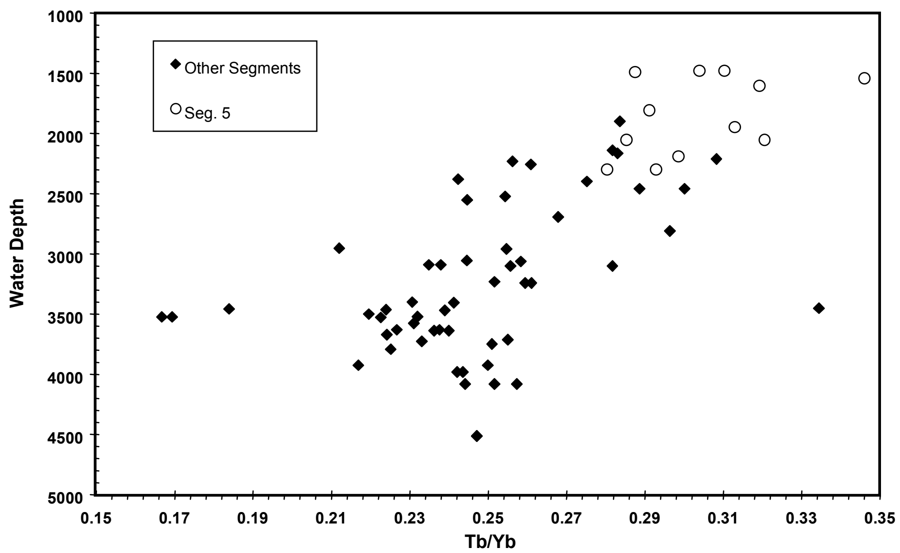

Figure 5.7a: Variation of trace element ratios with waterdepth

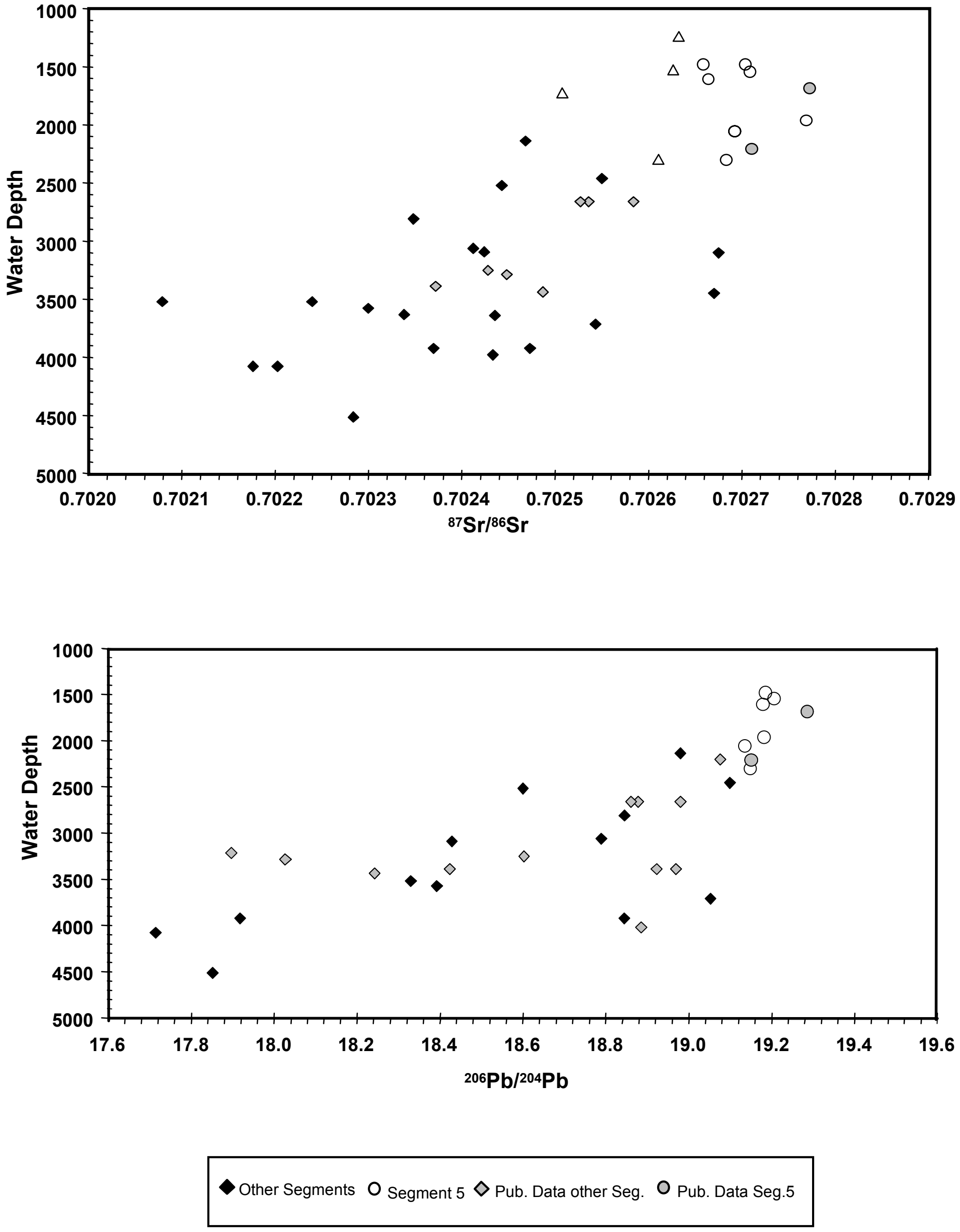

Figure 5.7b: Variation of isotope ratios with waterdepth, pub. data were taken from Fontignie and Schilling (1996)

5.3.2 Hot spot vs. wet spot

Schilling et al. (1985) argued that the Circe hotspot is responsible for a melting anomaly at Ascension MAR (see Chapter 2). This can be ruled out because isotope ratios of $^{206}Pb/^{204}Pb$ vs. $^{207}Pb/^{204}Pb$ show that Circe is not a mixing endmember (Figure 5.11a & b) which would be expected if a MOR is affected by a hotspot. Furthermore O´Connor et al. (1999) found that Circe seamount is inactive and approx. 6 Ma old. A hotspot in the vicinity of the MAR as supposed by Brozena and White (1990) is another and more likely possibility. Based on the passive-upwelling model of Bown and White (1994) a crustal thickness of 10 km corresponds to an asthenospheric potential temperature of 1360° C. This is approx. 50° C higher than the temperature required to generate a 7 km thick crust (Minshull et al., 1998). The estimated excess temperature of 50° C is significantly smaller than the temperature normally inferred for mantle plumes of 160-280°C +/- 50°C (see Chapter 1). Marquart and Schmeling (2000) pointed out that plumes with excess temperatures of 50°-600°C will founder at the top of the lower mantle if their head radii are less than ~100 km. Since the Ascension MAR bulge has a larger diameter than 100 km and affects two large segments and may be in steady state, a mantle plume with a low excess temperature cannot be ruled out. On the other hand, no seamount chain, which would be expected for a near ridge hotspot, exists. In fact the seamounts E of segment 5 do not lie parallel to the motion vector of the African plate (Minshull et al., 1998). In addition, alteration does not progress from W to E which would be the direction of progressive altering. K-Ar datings which were made on plagioclase minerals and glass rims from each of these seamounts failed to find any significant quantities of radiogenic ^{40}Ar, suggesting the same young age for all of these seamounts. As pointed out by Niu et al. (2001) and Jochum et al. (1983), incompatible element enriched magma sources contain higher concentrations of heat producing elements like K, U and Th. Due to the very long half-lives, heat production is slow and thus not relevant, e.g. too low to create an excess temperature of about 50°C. Glassy inclusions in phenocrysts from Segment 5 (see Chapter 4) show similar Mg# as inclusions from other segments. This hints at similar mantle temperatures as higher mantle temperatures would lead to higher Mg# in the magmas. Green et al. (2001) calculated anhydrous liquidus temperatures beneath all segments, of primary melts using primitive olivine phenocrysts. The highest Fo content of olivines from Segment 5 is 88 %. A comparison to the data of Green et al: (2001) suggests that the mantle temperature of the enriched MORB of Segment 5 is not significantly higher than the normally inferred mantle temperature. In fact, based on the olivine thermometer Green et al. (2001) find that temperature contrasts of primitive hotspot and MOR magmas is ≤20°C. They conclude that mantle plumes e.g. Hawaii are not hotter than normal MORB and that hot spots do not exist. They argue that melting anomalies are mainly driven by source compositional heterogeneities. This point of view may be exaggerated but it shows that temperature must not play a dominant role. Therefore it can be suggested that mainly mantle composition controls mantle melting in our investigated area. This can also be shown by using major element data.

5.3.3 Major element evidence for mantle composition and temperature, MAR 5-11°S

To try and take into account crystal fractionation effects, major element concentrations were recalculated to a constant MgO content of 8 % wt (see caption of Figure 5.8 for details). Differences in recalculated major element concentrations can be due to different degrees of partial melting and / or source composition. Figure 5.8 reveals that Segment 5 lavas differ from the segments to the north in Si8, Al8 and Ti8. Any enriched mantle source which may be feeding Segment 5 may consist of fertile mantle. In case of a higher fertility the mantle should show a higher CaO and a lower Al_2O_3 content due to higher cpx content which should be reflected in the magmatic compositions. This is not observed. A possible explanation for higher Al8 values is the influence of water on crystal fractionation as pointed out by Michael and Chase (1987) and discussed earlier (crystal fractionation). Higher average pressures of melting due to an taller melting column lead to lower concentrations of SiO_2 but also to higher FeOt. As only higher nomalized Si8 values are observed, the effects of a longer melting column, although not completely excluded, seems unlikely. Bonatti (1990) emphazised that higher amounts of H_2O lower the SiO_2 content of a magma during partial melting. This seems to be the best explanation of lower Si8 values at Segment 5 because it is consistent with higher Al8 values. TiO_2 is known to be moderately incompatible. Therefore a TiO_2 enriched source (also true for K2O) beneath Segment 5 can be suggest. It should be noted that the Ti8 calculation is based on the regression line of the fractional crystallisation path of 126 DS-1 (see caption of Figure 5.8 for details) due to the fact that observed sample trend and fractional crystallisation trend are different. Depth and degree of melting calculations (Kinzler and Grove, 1992; Niu and Batiza, 1991) are based on the assumption that different degrees of melting (and thus also magma composition) are caused by different mantle temperatures. Such calculations (not shown) did not lead to acceptable results, implying that temperature variations play no significant role in the working area.

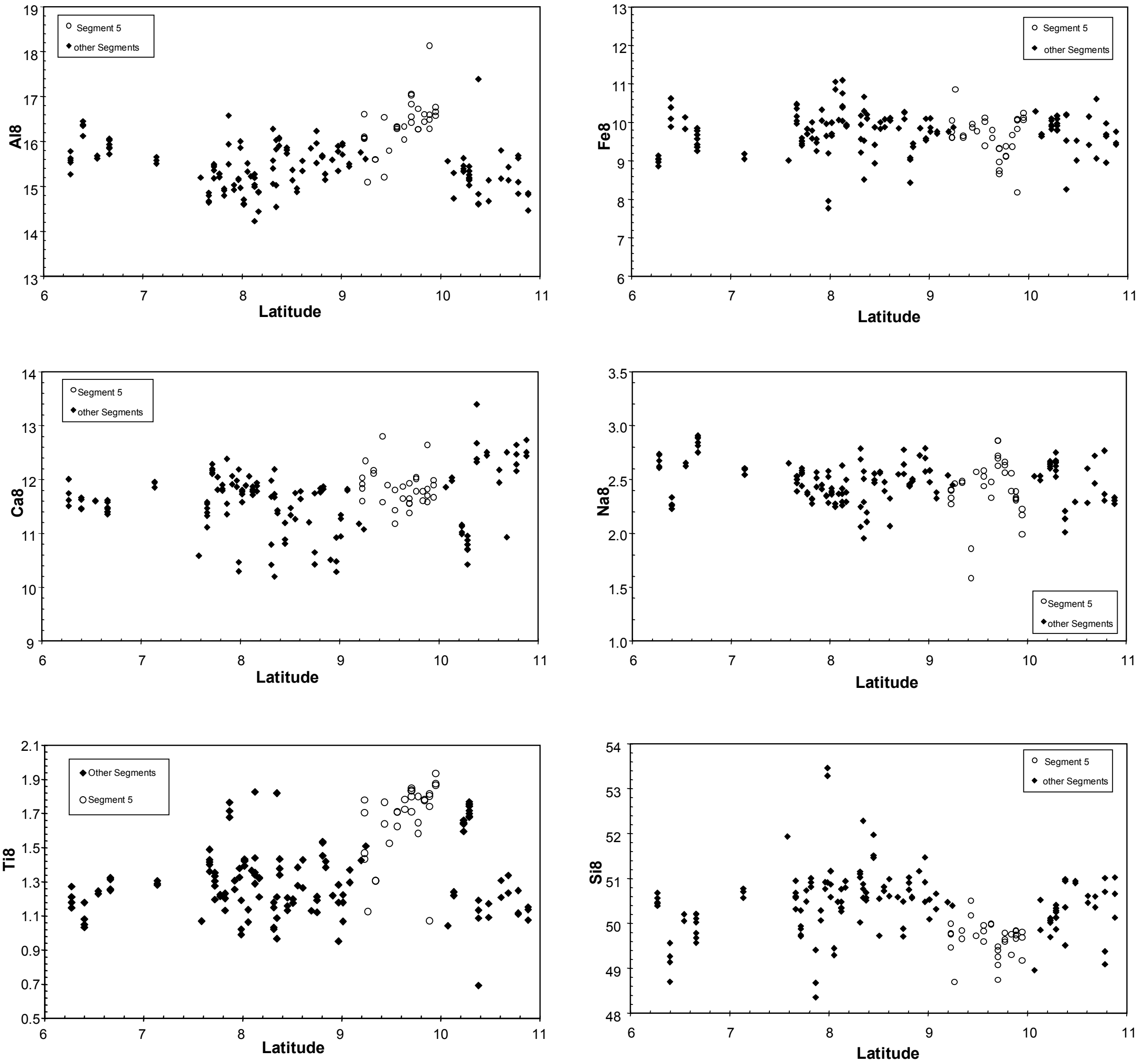

Figure 5.8: Recalculated major element concentrations, recalculated to a fixed MgO content of 8 % wt, calculations were done using linear and polynomic regression lines. Linear calculation: El8 = El + (8 – MgO) * m, polynominal calculation: El8 = El – x_1 * MgO^2 + x_2* MgO + x_1* 8^2- x_2* 8, El = element, x_{1}, $_{2}$ = gradient. Observed sample trends and modeled MELTS fractional crystallisation trends correspond for SiO_2, FeOt, Al_2O_3, Na_2O and CaO. Therefore regression lines of observed sample trends can be used. TiO_2 fractional crystallisation trend differs from the sample trend. To avoid the influence of possible magma mixing on calculation, Ti8 calculations are based on the fractional crystallisation trend of 126 DS-1 with 0.35 wt % water at 0.5 kbar.

5.3.4 Major element information on melting: MAR information

Figure 5.9 shows the average chemistry of selected samples of “normal” (Mohns Ridge, Segment OH-3) and elevated ridge segments of the MAR (Middle Kolbeinsey Ridge = MKR, Reykjanes Ridge, Azores Platform, own elevated area of Segment 4 and Segment 4 at 33° S) against crustal thickness. Chosen are only relative primitive samples with Mg# of 65-60 in order to minimize fractional crystallisation effects. Because of this, only Segment 4 samples could be taken from the investigated Ascension Area, Segment 5 samples are too evolved and seismic data for the crustal thickness are also not available. Nevertheless effects of fractional crystallisation exist for FeOT in the range of Mg# 65-60 and are visible in Figure 5.10 and were not corrected. Standard deviations are shown in Figure 5.9. In this Figure of Na_2O vs. crustal thickness two different trends can be seen. Thin ocean crust of the MAR seems to be combined with intermediate concentrations of Na_2O, while large crustal thicknesses can be either combined with low or high Na_2O concentrations. Low Na_2O concentrations of MKR and Reykjanes Ridge samples combined with thick crust may be attributed to high degrees of partial melting of a depleted source. This negative correlation between Na_2O and crustal thickness is called the global trend (Klein and Langmuir, 1987) (left arrow in Figure 5.9) and was confirmed by experiments of Kinzler and Grove (1992) on a depleted source with involvement of excess temperature. In contrast the Ascension Segment 4, segment OH-1 and the Azores Platform are products of large degrees of partial melting of an enriched source. The discussion presented here indicates that no excess temperature is needed. As FeOt concentrations are pressure dependent, higher degrees of partial melting will lead to higher amounts of FeOt due to an enlarged melting column. This can be seen in Figure 5.9, where areas with large crustal thicknesses are combined with high FeO concentrations. In summary, high Na_2O contents combined with high crustal thicknesses point to excess mantle melting due to the fertility of the source. Deeper increased melting can be seen in higher FeOt concentrations.

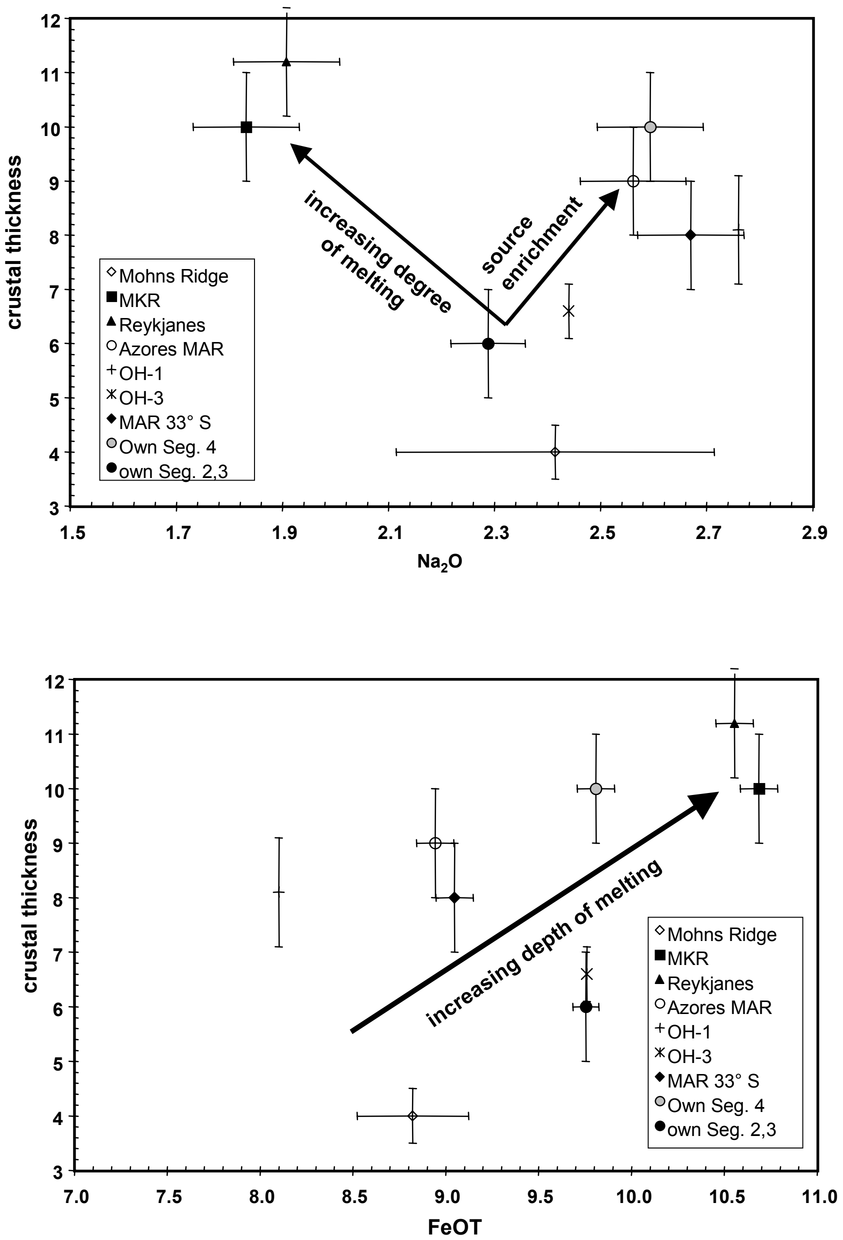

Figure 5.9: Plot of FeO and Na_2O vs. crustal thickness of selected MAR areas. Only samples were taken with a Mg# range of 65-60 to avoid crystal fractionation effects. Mg# calculated with =MgO/40.3/(MgO/40.3+FeO/71.8)*100, assuming FeO= FeOt*0.89. Data from PETDB; Mohns Ridge: (Neumann and Schilling, 1984; Waggoner, 1989; Melson and O'Hearn, 1986; NKR: Wieneke, 1998); Reykjanes: (Schilling et al., 1983; (Schilling, 1973; (Hermes and Schilling, 1976); Azores Platform: (Bourdon et al., 1996; (Sigurdsson, 1981; Langmuir,1998 pers. com. to PETDB, OH-1, OH-3 (Niu et al., 2001); MAR at 33°S, (Michael et al., 1994). Arrows indicate results of melting experiments made by (Kinzler and Grove, 1992) using depleted source composition. CaO of MKR and own Segment 4 were recalculated to most primitive Mg# of the respective area, see text for discussion. Crustal thicknesses: Mohns Ridge: (Klingelhoefer et al., 2000); MKR: (Kodaira et al., 1997); Reykjanes: (Searle et al., 1998) and (Smallwood and White, 1998); Azores platform: (Detrick et al., 1995); OH-1, 3: (Hooft et al., 2000); MAR 33°S: (Tolstoy et al., 1993).

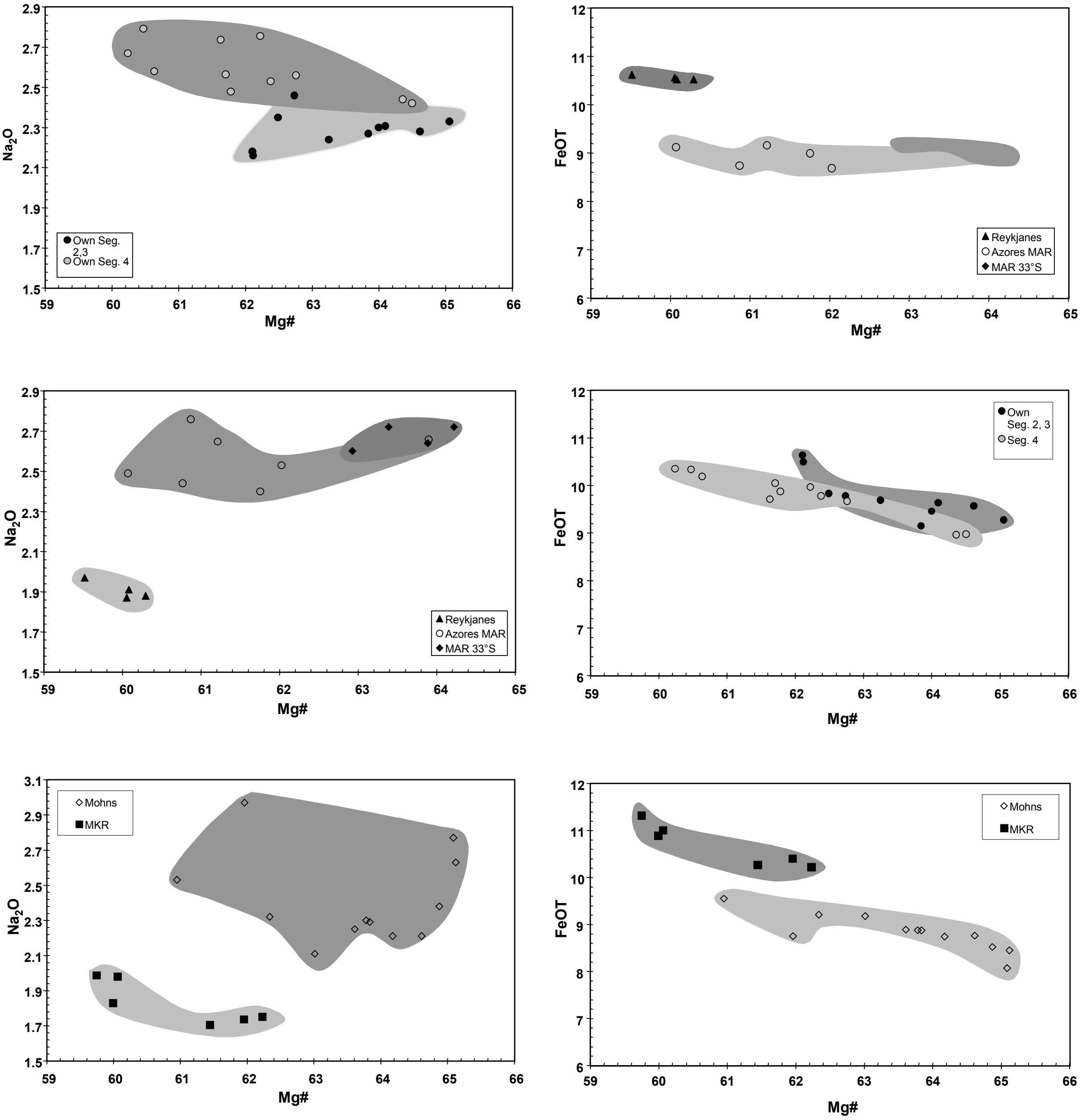

Figure 5.10: Dependence of FeOt and Na_2O on Mg# of different MAR areas, see text for discussion.

5.3.5 Trace elements and radiogenic isotopes: mixing processes

It was shown that excess temperature plays a minor role in increasing the degree of partial melting in our investigated elevated MAR area. In fact, the source enrichment itself seems to have a primary influence on partial melting processes. Source enrichment can be examined using radiogenic isotopes, Figures 5.11a, b suggest that binary mixing of a depleted and an enriched source is occuring beneath the MAR near Ascension. 122 DS-4 north of Ascension Fracture Zone (FZ) is unradiogenic, with Pb ratio values similar to very depleted MORB from Garrett FZ (Wendt et al., 1999). In a diagram of $^{206}Pb/^{204}Pb$ vs. $^{87}Sr/^{86}Sr$ (Figure 5.11c) two trends of MAR MORB can be observed, indicating binary mixing between an enriched source beneath Segment 5 and seamounts and a depleted source beneath Segment 2, 3. Furthermore K_2O/TiO_2 and La/Sm ratios indicate that Segment 2 and 3 erupt suitable depleted MORB´s. Therefore sample 142 DS-2 from Segment 2 was taken as the depleted endmember, while the radiogenic endmember is represented by 179 DS-2, the most radiogenic sample from the off-ridge seamounts. Segment 5 $^{206}Pb/^{204}Pb$ vs. $^{207}Pb/^{204}Pb$ ratios can be produced by magma mixing of 20 % 142 DS-2 and 80 % 179 DS-2. Figure 5.11 a, b shows that Ascension Island samples lie slightly off the mixing line but are even more radiogenic than sample 179 DS-2 suggesting a different source and/or genesis. Isotope/trace element plots (Figure 5.12) reveal positive correlation of $^{206}Pb/^{204}Pb$ ratios and incompatible element ratios. These trace element ratios support the idea of binary mixing.

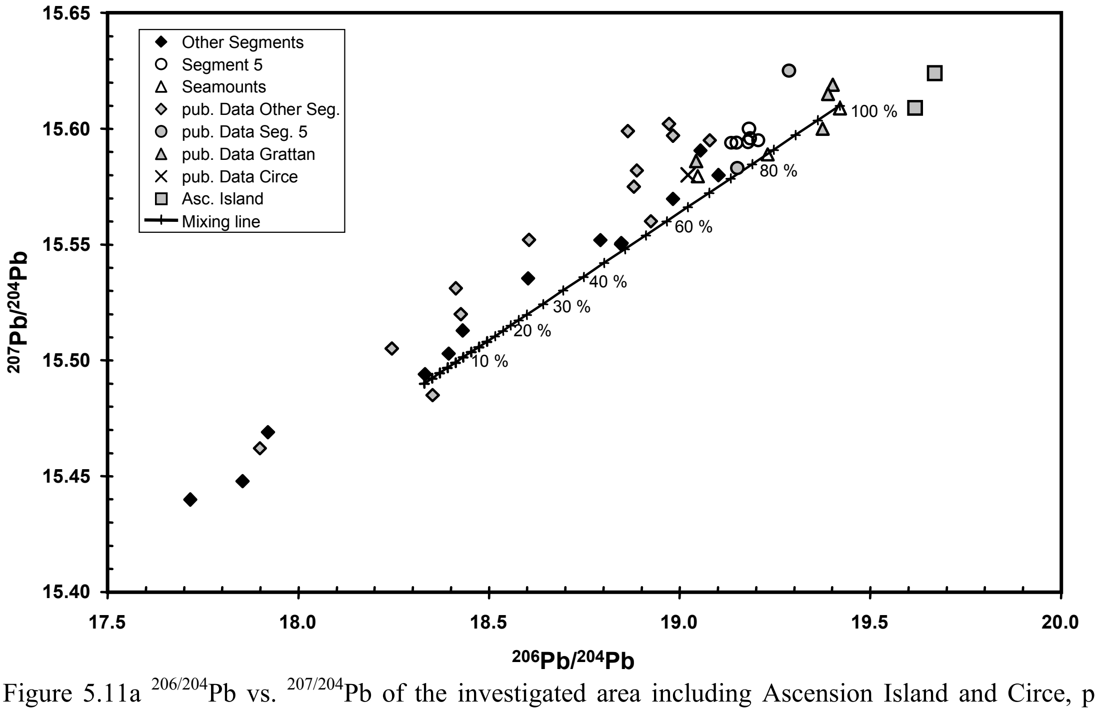

Figure 5.11a $^{206/204}Pb$ vs. $^{207/204}Pb$ of the investigated area including Ascension Island and Circe, pub. data are from (Fontignie and Schilling, 1996; Bourdon and Hemond, 2001 and (Kar et al., 1998)

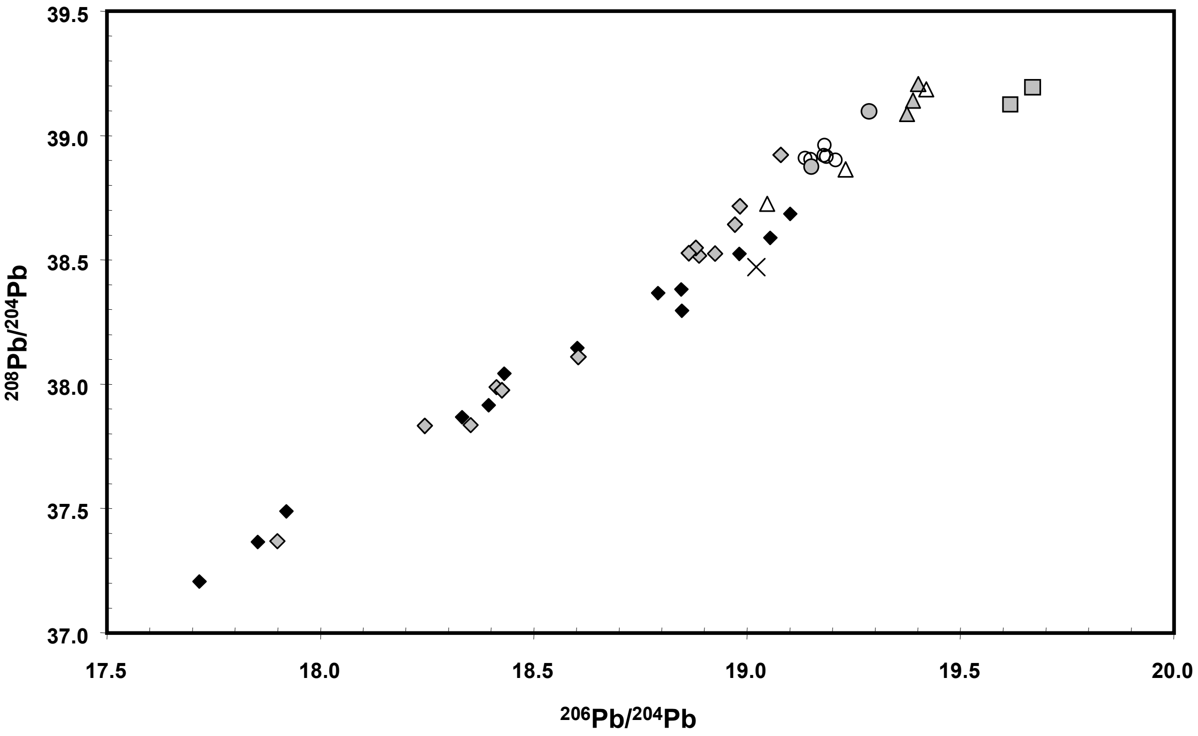

Figure 5.11b: $^{206/204}$Pb vs. $^{208/204}$Pb pub data same like Figure 5.12a

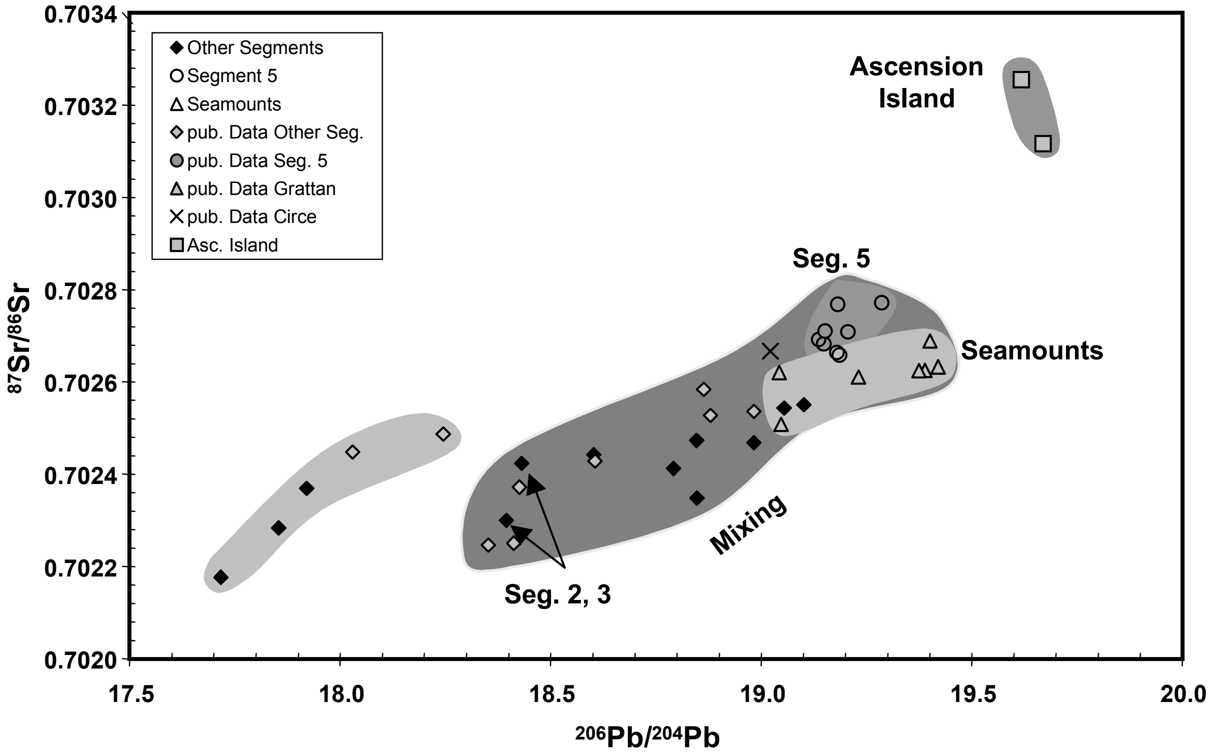

Figure 5.11c: $^{206/204}$Pb vs. $^{87/86}$Sr, data source see Figure 12, see text for details

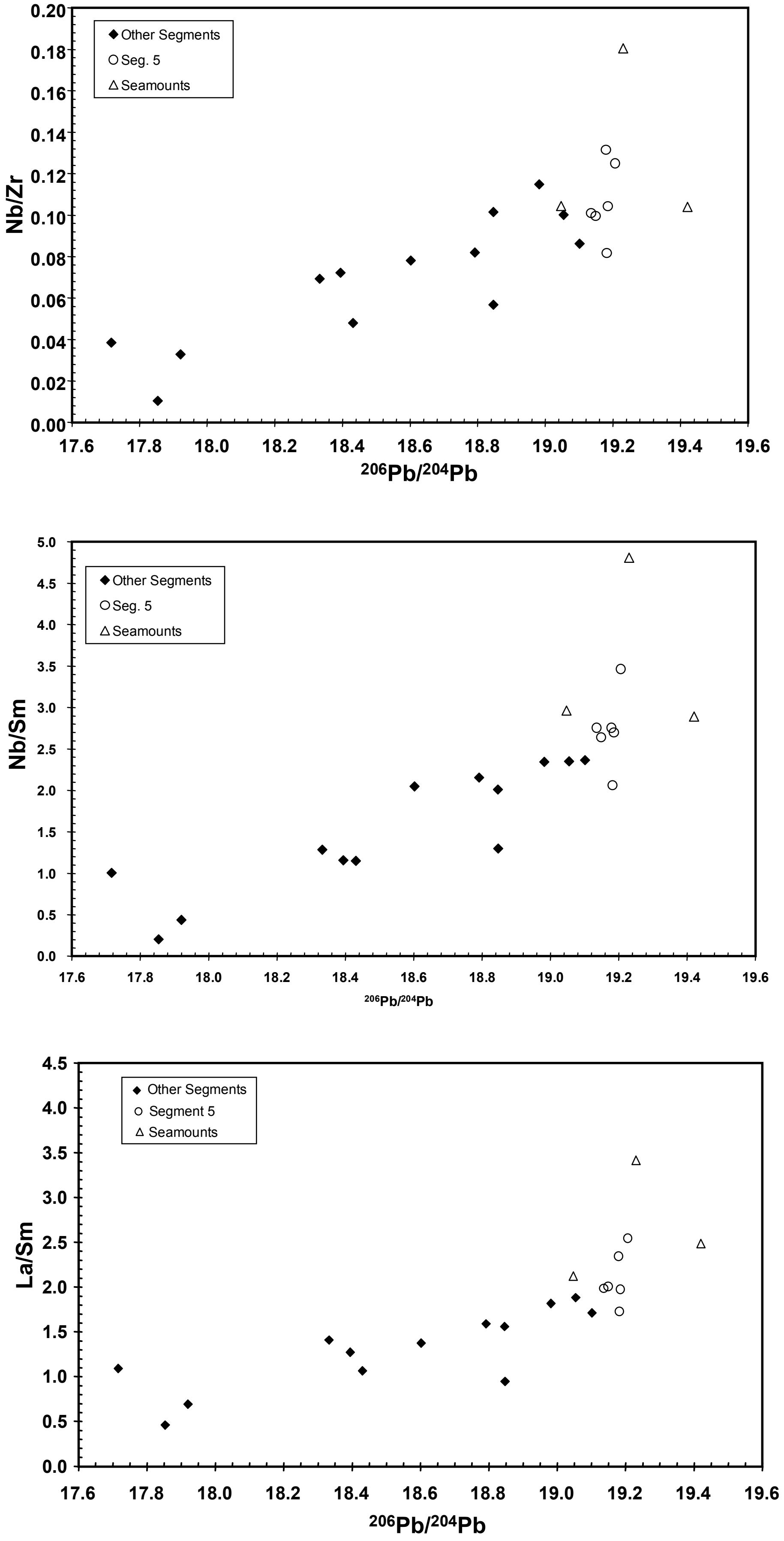

Figure 5.12: Correlation of $^{206/204}$Pb isotope ratios with selected trace element ratios, see text for details

5.3.6 Incompatible elements and H_2O: Effect on partial melting

In the following, the effect of mantle composition on the extent of partial melting is discussed. As shown in Figure 5.13, samples of Segment 4 are predominantly and Segment 5 exclusively enriched MORB (E-MORB) with (La/Sm) ratios > 1. An enriched source has a lower solidus and thus begins to melt deeper and produces more melt than a depleted source (Green and Falloon, 1998). The lowering of solidus temperatures of fertile mantle sources has two causes. Firstly, alkalis and other incompatible elements lower the solidus significantly (Green and Falloon, 1998; Takahashi, 1986; Niu et al., 2001). The relative enrichment of Segment 5 is plotted in Figure 5.14. Shown are trace element ratios of Segment 5 and Seamount samples divided by a mean of Segment 2 & 3 N-MORB (see Table 5.2).

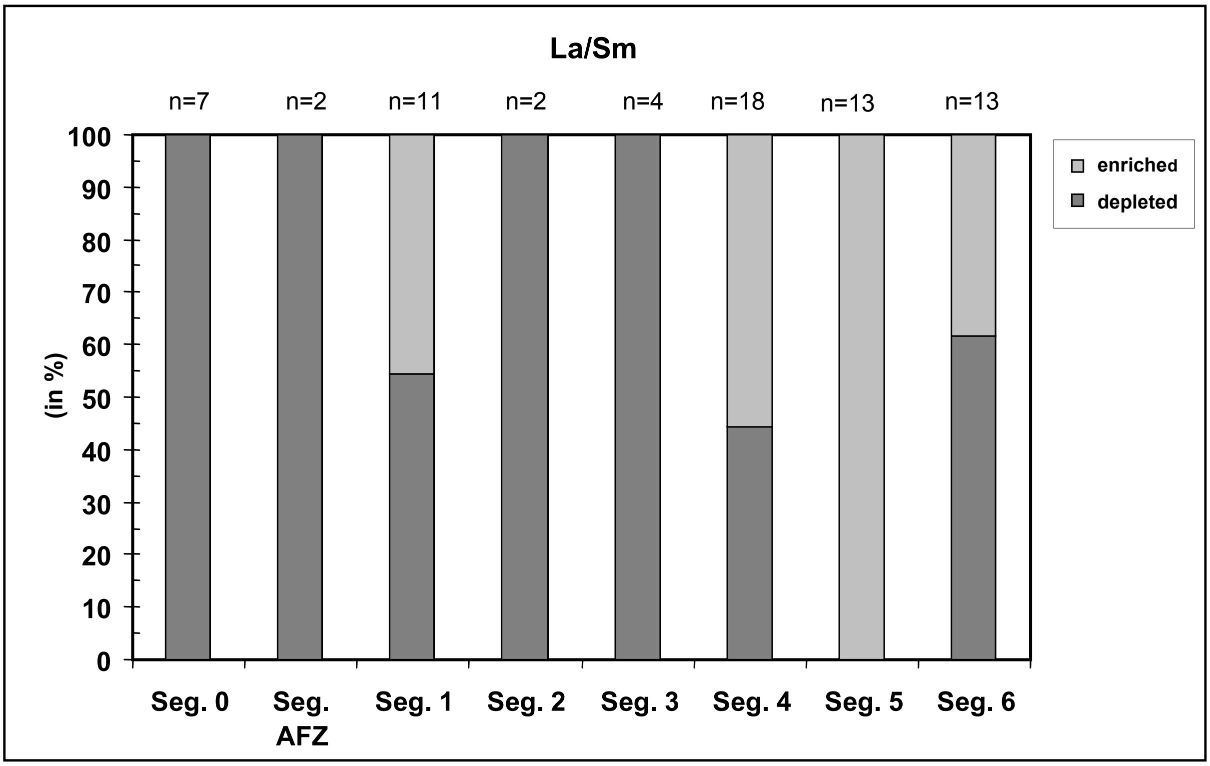

Figure 5.13: Percentage of enriched samples per spreading ridge segment. The boundary enriched/depleted is taken as La/Sm = 1

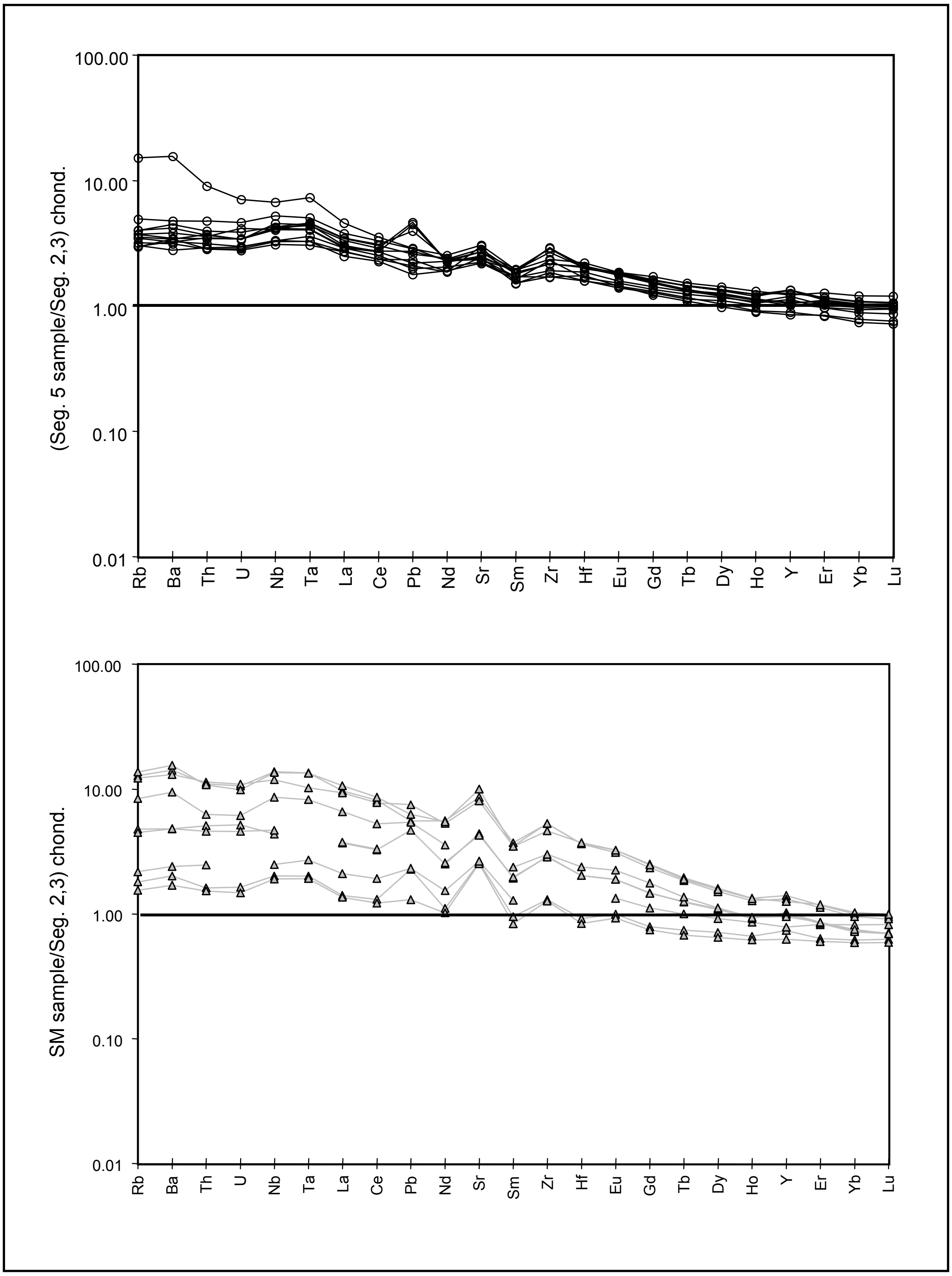

Figure 5.14: Relative enrichment of Segment 5 and Seamount samples to N-MORB of Segment 2 and 3.

Sample	mean conc. (ppm)	Sample	mean conc. (ppm)
Rb	2.19	**Zr**	55.05
Ba	26.75	**Hf**	2.24
Th	0.31	**Eu**	1.05
U	0.10	**Gd**	4.08
Nb	3.83	**Tb**	0.76
Ta	0.25	**Dy**	5.18
La	3.93	**Ho**	1.14
Ce	10.29	**Y**	28.71
Pb	0.42	**Er**	3.32
Nd	8.47	**Yb**	3.32
Sr	88.46	**Lu**	0.49
Sm	3.02		

Table 5.2: mean trace element concentrations (ppm) of Segment 2 and 3

Highly incompatible elements are more enriched than moderately incompatible elements in samples of Segment 5, pointing to a significant enrichment of these elements in the mantle beneath Segment 5. Secondly, the water content of a source has a strong influence on mantle solidus temperature. High water contents lead to a significant lowering of the mantle solidus. Niu et al. (2001) argues that 0.05 % H_2O in the mantle lowers the solidus temperature in excess of 200°C at ~100 km depth. The effect of water on the extent of partial melting is emphazised by Hirose and Kawamoto (1995). They found that the addition of 0.2 wt % water to a natural lherzolite (KLB-1) causes an 18 wt % higher extent of melting at 1350°C during batch melting. The role of water during partial melting is also confirmed by Stolper and Newman (1994) who investigated the petrogenesis of Mariana trough magmas. They showed that the degree of melting is higher in a H_2O enriched source. H_2O acts like an incompatible element during MORB genesis (Michael, 1995). Enriched sources, with their higher alkalis and other incompatible elements, also have higher water contents. H_2O concentrations were calculated using the equation of Michael (1995) ($H_2O = 259.22X\ Ce+172.14$; r= 0.969, in ppm). Using this formula it has to be kept in mind that H_2O behaves like an incompatible element and is strongly affected by crystal fractionation processes.

Segment		**H_2O calc.**	**H_2O calc. Ce8**
0	Mean	0.22	0.23
	Std. dev.	0.08	0.11
AFZ	Mean	0.14	0.29
	Std. dev.	0.00	0.01
1	Mean	0.29	0.35
	Std. dev.	0.18	0.15
3	Mean	0.33	0.24
	Std. dev.	0.05	0.07
4	Mean	0.33	0.20
	Std. dev.	0.12	0.08
5	Mean	0.70	0.31
	Std. dev.	0.14	0.10
6	Mean	0.32	0.28
	Std. dev.	0.19	0.11

Table 5.3 means and standard deviation of calculated H_2O contents, see text for details

Because of this H_2O concentrations were recalculated using Ce8 (Cerium recalculated to 8 % wt MgO). Table 5.3 shows means and standard deviations. Segment 5 samples have higher water contents than Segment 4 and 6. We recovered enriched lavas on one position (138 DS, Segment 1) with high incompatible element abundances which affects the mean considerably. Seamount samples lie off the regression line used to calculate Ce8 values suggesting a different melting regime (which will be discussed later). Thus these H_2O conc. are not comparable to MAR segments and therefore are not shown. These H_2O estimates of 0.31 wt % especially for Segment 5 are slightly lower than H_2O contents suggested by MELTS fractional crystallisation models (0.35-0.60 wt % H_2O) but would also lead to reliable results in MELT calculations.

5.3.7 Modelling mantle compositions and partial melting processes

Calculations of mantle sources and degrees of partial melting were made following Niu et al. (2001) (for details see Appendix). In contrast to Niu et al. (2001) who took Ba/element ratios, Rb/element ratios were taken here. This lead to better results, visible in REE patterns which showed smoother curves. Analytical problems are probably the cause for the calculation problems with Ba. As Rb is comparable to Ba in terms of incompatibility the calculations should not be affected. Partition coefficients were taken from Kennedy et al. (1993) and Hart and Dunn (1993). As shown above, the chemical pattern of Seg, 2 & 3 are suitable for calculating a depleted source. Segment 5 samples represent the enriched endmember and were used to calculate the enriched source. Results of source composition calculations are given in Figure 5.15. We find that the source of Segment 5 is significantly more enriched than the depleted source of Segment 2,3. Highly incompatible elements are more enriched than less incompatible elements, the HREE are depleted. Since Michael (1995) argues that the partition coefficient of H_2O is comparable to that of Ce, the H_2O content of the source can be calculated as for the REE. Mean values of H_2O are ca. 90 and 450 ppm for the depleted and the enriched source respectively (enriched source approx. 5 times higher).

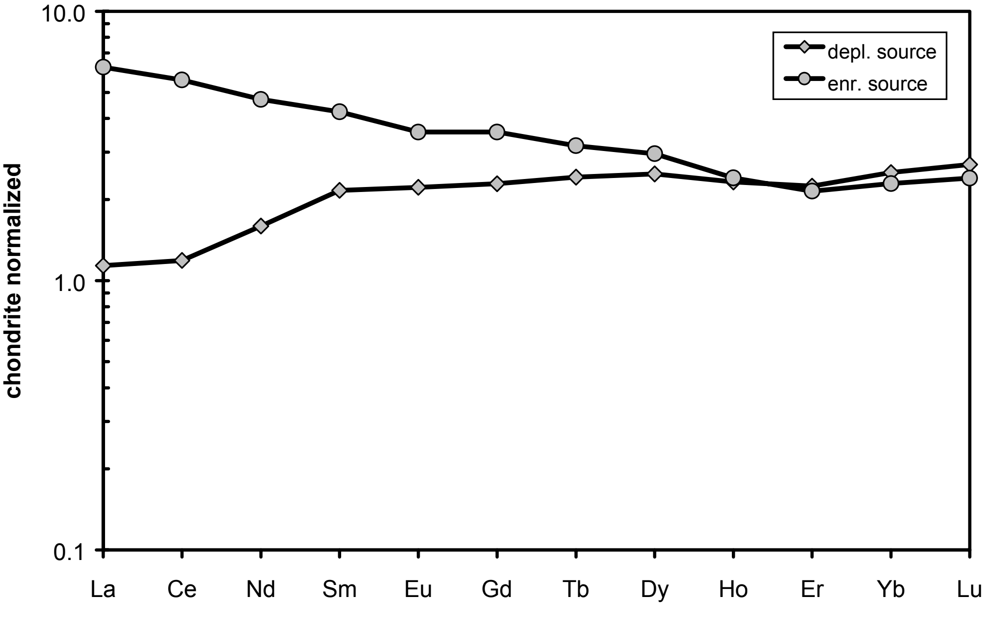

Figure 5.15: REE pattern of calculated enriched source of Segment 5 and depleted source of Segment 2 and 3

The degree of melting was calculated. Segment 2,3 shows an approx. constant degree of melting of ca. 5 % (+/- 1). In contrast to this, the Segment 5 source shows a decreasing value for the extent of melting from La to Lu from 11 to 3 %. This variation can be explained by melting in the garnet stability field leading to higher whole rock partition coefficients for HREE. (D^i_o and P^i, see Appendix for details). Since garnet was not considered in source calculations, estimates of F are too low for HREE. 11 – 10 % partial melting seem to be realistic due to the fact that crustal thickness is about 2 times higher at Segment 4 than at Segment 2,3 (Minshull et al., 1998) and water depths suggest a comparable crustal thickness at Segment 5. Heavy rare earth elements (HREE) seem to be slightly depleted in Segment 5 samples indicated by a slightly negative slope (Figure 5.14). This points to an involvement of garnet in the source because HREE are compatible in garnet. This involvement increases in the seamount samples which can be seen from the steeper slope of their (HREE). The presence of residual garnet in partial melting processes can also be seen in Figure 5.7a. High Tb/Yb ratios are combined with shallow water depths and large crustal thicknesses. Most enriched samples mainly from Segment 5 and also from Seamounts with high $^{206}Pb/^{204}Pb$ ratios show signs of Tb/Yb fractionation (not shown).

5.3.8 Influence of source enrichment on depth and degree of melting

Figure 5.16 shows that a source water content of approximately 450 ppm beneath Segment 5 corresponds to a solidus temperature reduction of approx. 165°C at 3 GPa (ca. 100 km depth) and

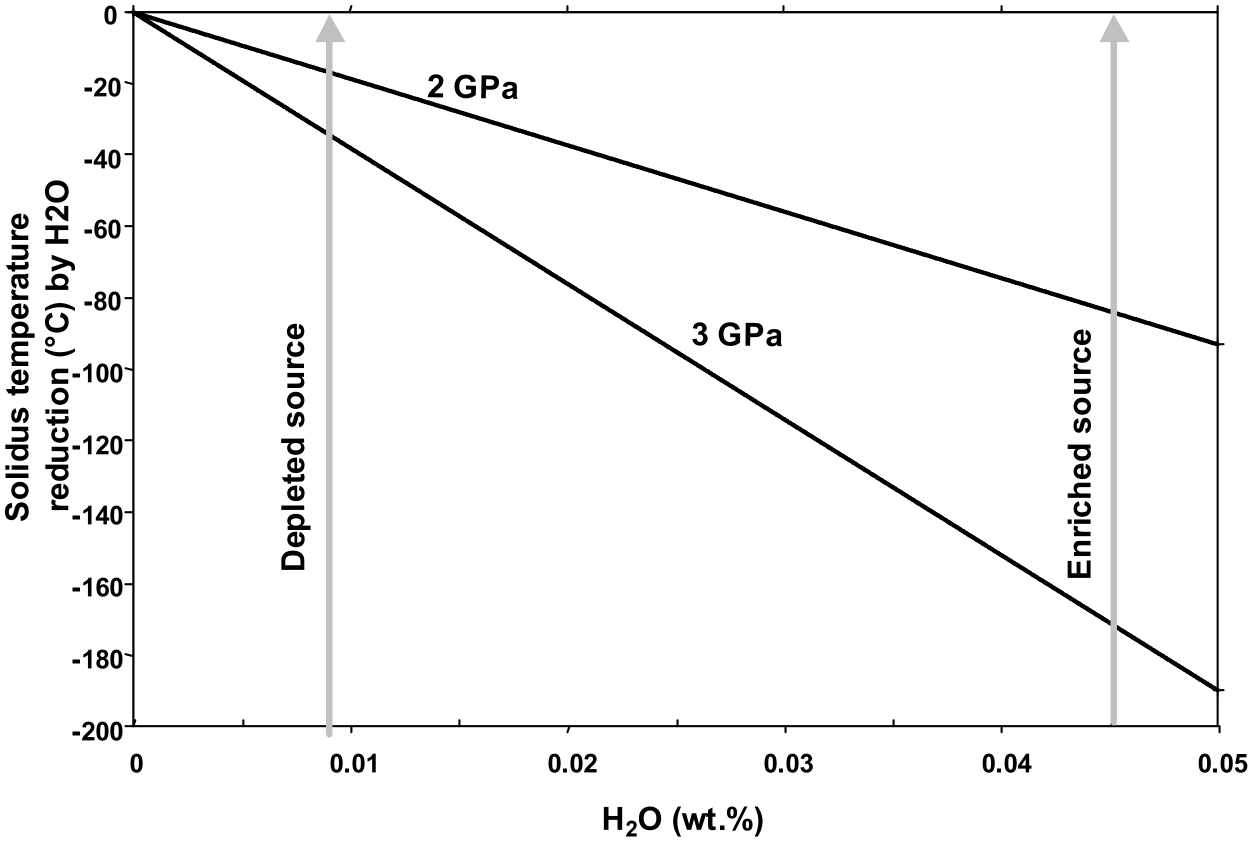

Figure 5.16 Solidus temperature reduction of wet peridotite lineary interpolated by (Niu et al., 2001) using solidus of wet peridotite with 0.1 % H2O by (Wyllie, 1971). Calculated mean source water contents are 91 ppm and 455 ppm for Segment 2,3 and Segment 5 respectively

85°C at 2 Gpa (ca. 60 km depth, see caption for details). These estimates can be combined with P,T data of a wet solidus with 0.2 % H_2O and a dry solidus of fertile peridotite (details see caption of Figure 5.17). Considering Segment 2,3 the solidus of this source should be reached at lower pressures as this source is fairly depleted. On the other hand, even this depleted source contains nearly 100 ppm water which has the effect of lowering the solidus. In summary, the solidus of the depleted source is lik ely to be the same as the dry solidus plotted or maybe slightly moved to lower pressures. In contrast, the solidus of the Segment 5 source is clearly crossede at higher pressures compared to the dry solidus. Thus melting starts in the garnet stability field (Figure 5.17). The melting column of the mantle peridotite beneath Segment 5 is larger, thus produces more melt and might also produce more melt per unit pressure release than the Segment 2,3 source due to the water content and enrichment. Thus more melt reaches the MAR and builds a thicker crust.

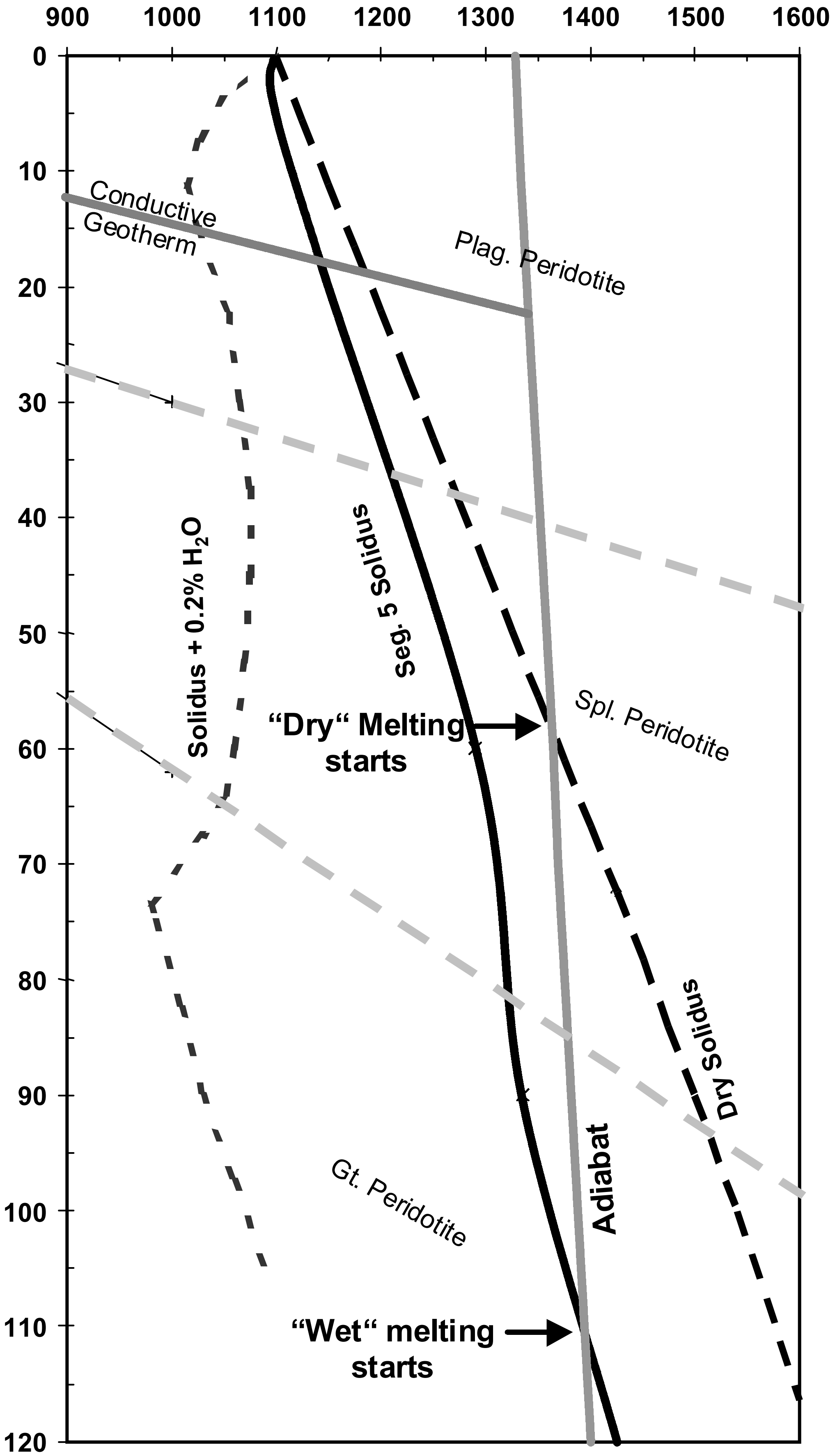
900
1000
1100
1200
1300
1400
1500
1600
0
10
20
30
40
50
60
70
80
90
100
110
120
Conductive Geotherm
Plag. Peridotite
Solidus + 0.2% H$_2$O
Seg. 5 Solidus
"Dry" Melting starts
Spl. Peridotite
Dry Solidus
Adiabat
Gt. Peridotite
"Wet" melting starts

5.4 Pyroxenite – another cause of enriched lavas

Hirschmann and Stolper (1996) investigated the role of garnet pyroxenite in mantle composition and during partial melting. Their ideas are founded on the conflict that the garnet signature of MORB in HREE links to melting in the garnet stability field while mean ocean thickness is too low for such a large melting column. The role of pyroxenite in mantle petrography is verified by pyroxenite veins and layers in ophiolites and alpine massif outcrops as well as pyroxenite mantle xenoliths. These pyroxenites consist of cpx, opx and gt. After Hirschmann and Stolper (1996) pyroxenite has a lower solidus compared to peridotite. Furthermore it melts much more than peridotite per unit pressure release. The pyroxenite of a source made of 5 % pyroxenite and 95 % peridotite contributes 15 – 20 % of the whole melting amount. Typical HREE depletion in the lavas ("garnet signature") must not be directly associated with melting in the garnet peridotite stability field as garnet is stable in pyroxenite also in the spinel peridotite field. In view of the investigated area it seems possible that pyroxenite veins and layers produce this melting anomaly. However Hirschmann and Stolper (1996) pointed out that melting of a spinel peridotite / garnet pyroxenite source would be expected to yield stronger garnet signatures in regions of thinner crust. Weaker signatures can be expected in regions of thicker crust where pyroxenite melts are diluted by peridotite melts. In this case the garnet signature is due to garnet peridotite. Thicker crust and thus a higher degree of melting is after Hirschmann and Stolper (1996) caused by a hotter mantle which leads to melting in greater depths i.e in the garnet stability field. A hot mantle can probably be ruled out in our investigated area, therefore a lowering of the peridotite solidus due to a higher water content is suggested. Two scenarios are possible: 1. As shown before a H_2O rich, fertile source melts in the garnet peridotite stability field due to its lower solidus. 2. The mantle beneath Segment 5 contains more than the supposed normal 5 % garnet pyroxenite. As the Sm/Yb ratio of Segment 5 is approx. 2.3 times higher than normal MORB (MORB taken from the GERM homepage) approx. 12 % of the source has to be garnet pyroxenite which contributes, after Hirschmann and Stolper (1996), at least 36 % to the total melt. Figure 5.18 shows the basic difference between these two models. In model A the solidus is lowered into the garnet peridotite stability field. In model B the depth at which garnet is stable is also changed. Melting starts in greater depths due to the melting of the pyroxenite and the garnet stability field is shifted to lower depths because of the enhanced stability field of garnet in pyroxenite. The geochemical fingerprints of these two processes are not easy to decipher as Hirschmann and Stolper (1996) pointed out that the pyroxenites data which are available show a high variability in major and trace elements. In addition, radiogenic isotopes show no significant trend. However pyroxenites may have eclogitic composition as they might be remnants of subducted lithosphere. van Westrenen et al. (2001) found that Ca rich eclogitic garnet

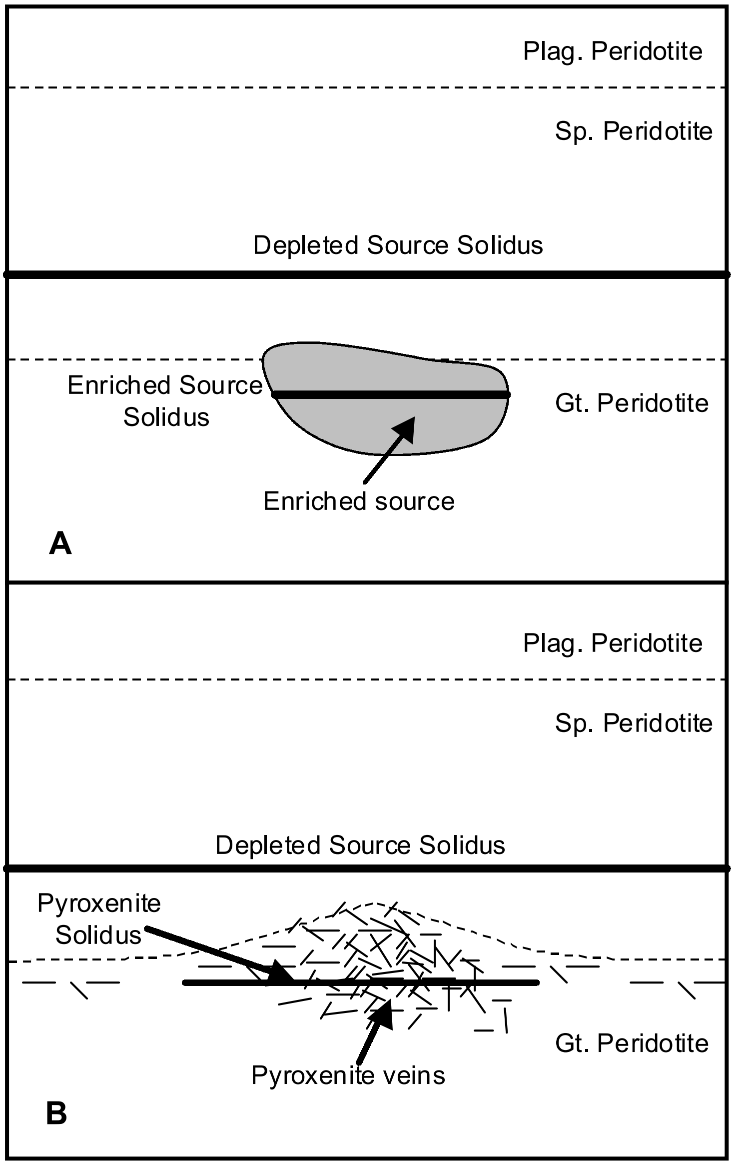

Figure 5.18: Possible causes of "garnet signature", Plag.: Plagioclase, Sp.: Spinel, Gt.: Garnet, see text for details

has different partition coefficients for certain elements than Ca poor peridotitic garnet. They found that Zr, Hf and Ti are incompatibe in Ca poor garnet, while at higher Ca levels Zr, Hf and Ti become more compatible. Thus these authors suggest that a combination of low Hf/Sm ratios and Zr/HREE and Hf/HREE (e.g. Yb) can be indicative for the involvement of eclogitic rocks. Because they are independent of the melt fraction and HREE show no different partition coefficients in garnet. In Figure 5.19 Hf/Yb and Hf/Sm ratios of samples from the working area as well as non modal batch melting calculations are shown. The calculations include Hf/Yb and Hf/Sm ratios of primitive mantle (see caption of Figure 5.19) and Segment 5 source. Hf is estimated for Segment 5 source from Eu and Sm concentrations. Hf, Sm and Yb partition coefficients of garnet eclogite and garnet peridotite are taken from van Westrenen et al. (2001). In conformity to these authors, calculations show that Hf/Sm is low in melts from garnet eclogite but higher in garnet peridotite melts. Moreover Hf/Yb vary with degree of partial melting only in garnet peridotite melts whereas Hf/Yb is approx. constant in garnet eclogite melts. Thinner crust of the other segments seems to be more affected by eclogitic pyroxenite as it was also supposed from Hirschmann and Stolper (1996) for pyroxenites generally. Hf/Yb ratios of Seamount samples is high (most samples >1.5) which is consistent with decreasing partial melting of garnet peridotite. Based on these observations it seems that a model of mantle without the involvement of pyroxenites has to be favored.

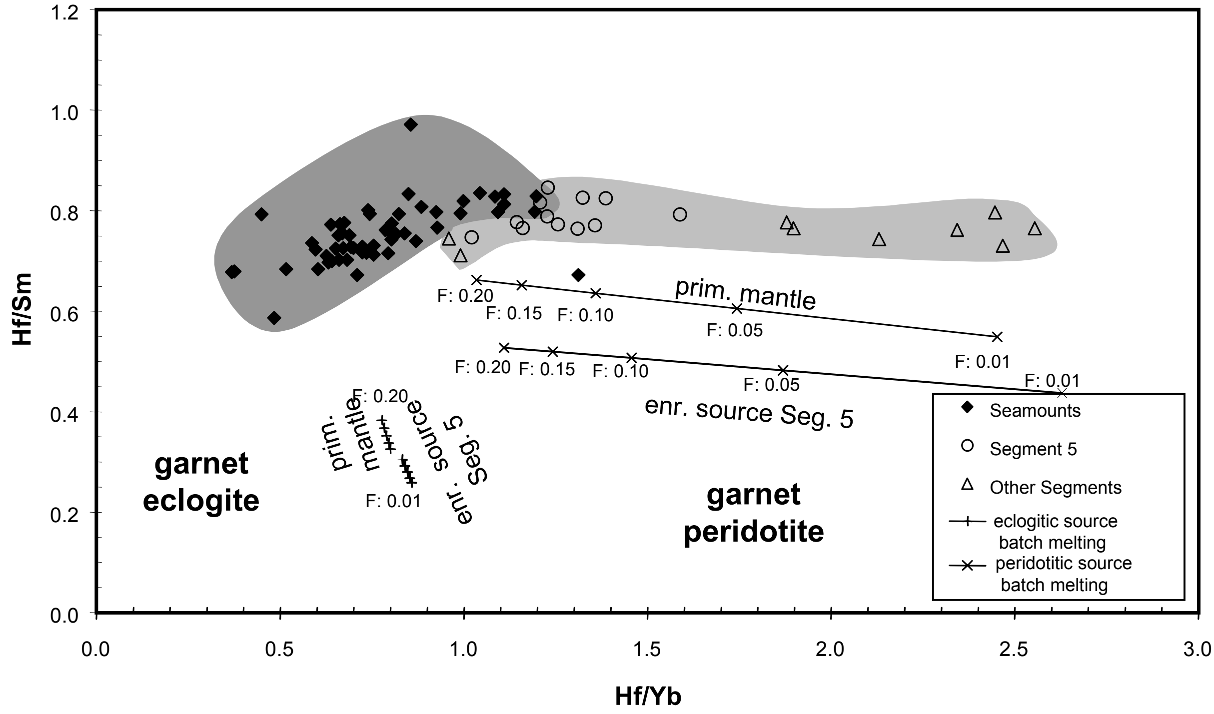

Figure 5.19: Diagram of Hf/Yb vs. Hf/Sm which may help to investigate the role of eclogitic pyroxenite especially Segment 5 samples, partition coefficients from van Westrenen et al. (2001), chosen Hf/Yb and Hf/Sm ratios are taken from the prim. mantle composition of Hofmann (1988).

5.5 Variation with latitude - a link to mantle flow

In Figure 5.20 several geochemical parameters as well as water depth are plotted against latitude. Besides the obvious enrichment of Segment 5, it is visible that the Ascension anomaly is not symmetric. From Segment 5 water depth increases rapidly in southerly direction. This morphological asymmetry is particulary confirmed by MgO concentrations and La/Sm and Tb/Yb ratios. A gentle gradient to the N but a steep change to depleted lavas to the S can be observed. The morphological and geochemical asymmetry suggests a mainly northwards trending ridge-parallel mantle flow. A possible model is that enriched melts produced by upwelling enriched mantle are deflected to the N and mix with depleted melts from upwelling depleted mantle. This flow may contribute to the formation of the propagating rift at 8° S which was discovered by Brozena and

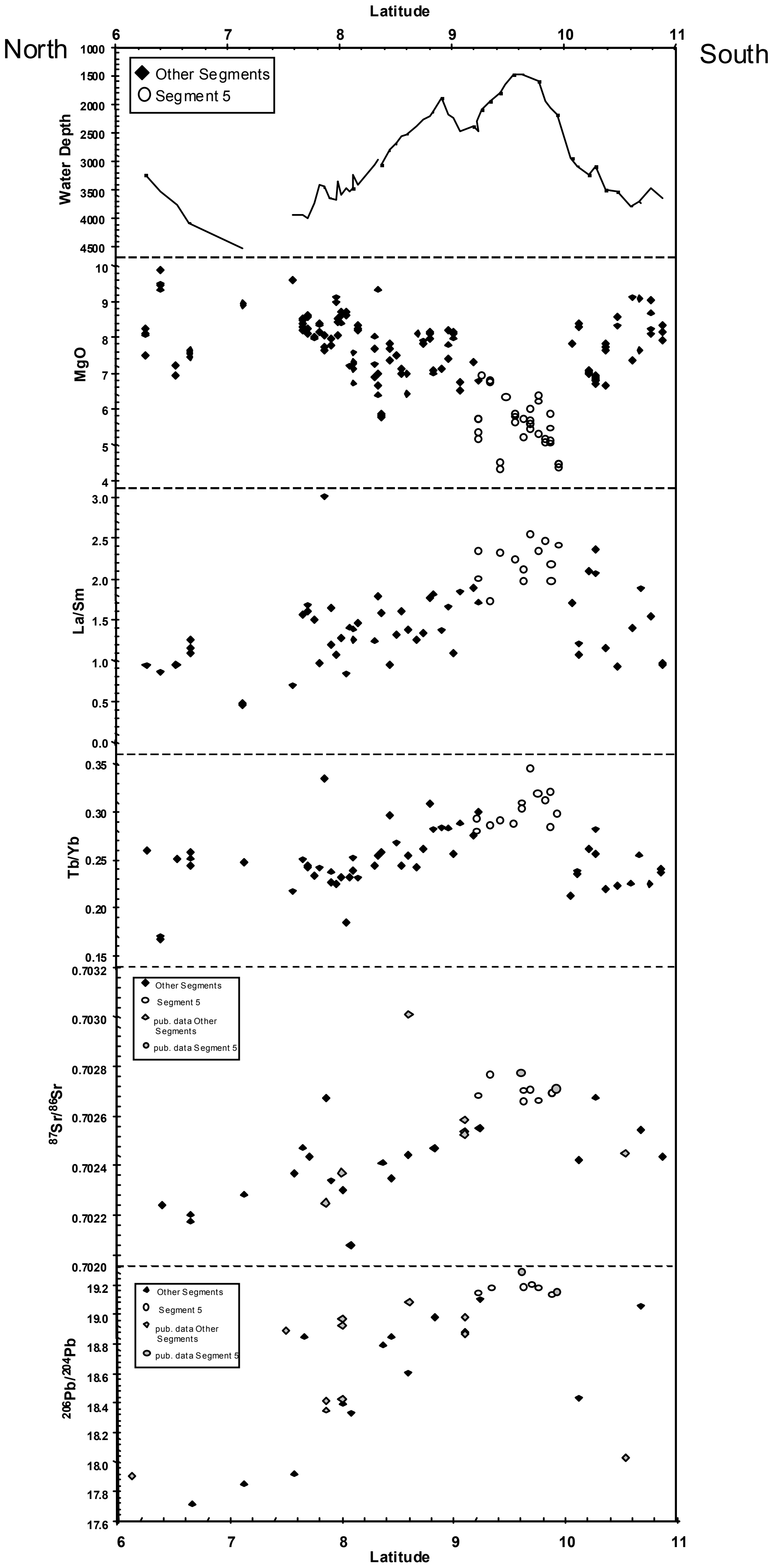

Figure 5.20: Several geochemical parameters plotted against latitude, see text for details

White (1990) and combined with several ridge jumps. As visible in Figure 5.21 the southern rift is growing at the expense of the northern rift implying a more robust magma plumbing in the south. As pointed out in Chapter 2, propagating rifts and ridge jumps are unusual at slow spreading ridges and are often connected with excess volcanism, whereby Brozena and White (1990) preferred a ridge - hot spot interaction (Chapter 2). The authors pointed out that the propagating rift started ca. 5 Ma ago. This age marks the beginning of abnormal volcanism at 8° S and may give a minimum age of the melting anomaly itself. It is also notable that the Azores platform also shows an asymmetric morphology but with a steeper slope to the N, opposite to the Ascension anomaly, implying a ridge parallel mantle transport to the S. Moreover asymmetric mantle flow can be seen at Iceland and Easter Island.

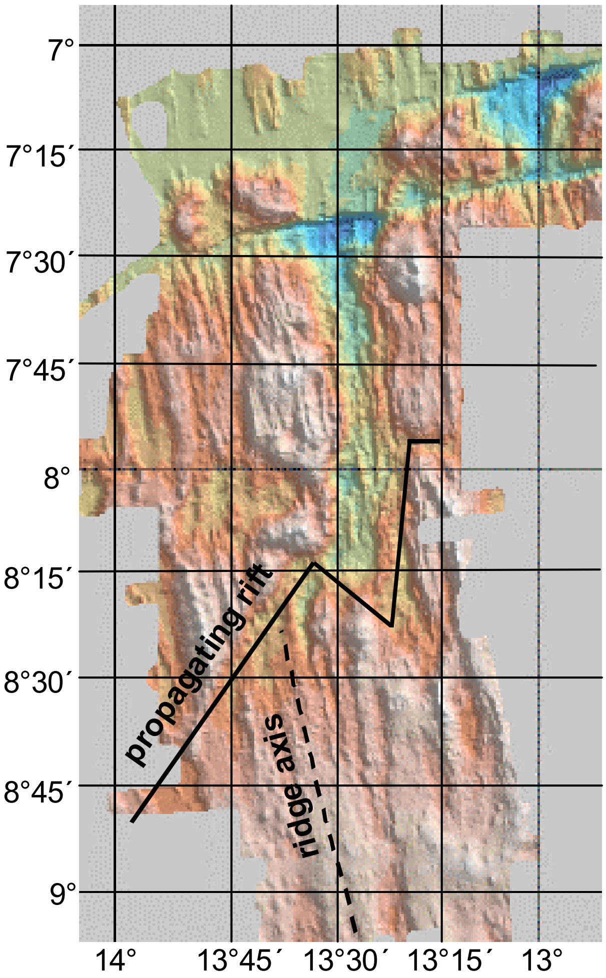

Figure 5.21: Propagating rift as supposed by Brozena and White (1990)

5.6 Off axis volcanism and partial melting

A plot of longitude vs. Tb/Yb (Figure 5.22) reveals an interesting feature. Comparable tectonic settings including a spreading axis with seamounts perpendicular to the ridge axis normally show increasing Tb/Yb ratios with increasing distance to the axis (Haase et al. (1996). This behavior can be attributed to a shift of the melting column to greater depths as a consequence of increasing thickness of the cold and rigid lithosphere which inhibits shallow level melting. As a consequence the degree of partial melting and the average melting depth decreases. This is not the case in the investigated area. Tb/Yb ratios show no simple correlation with distance from the axis. Tb/Yb ratios are relatively high at the axis, E of the MAR the ratio decreases and then increases again. Supported by slightly lower La/Sm and Sr and Pb isotope ratios, a possible explanation is the entrainment of less enriched material which leads to delayed and shallower melting. The slight increase of Tb/Yb from Grattan to the easternmost Seamount may be due to the influence of an increased lithospheric thickness (Figure 5.22) combined with a lower degree of partial melting. In addition it is also possible that previous melting lead to the observed eastward Tb/Yb increase. Moreover seamount

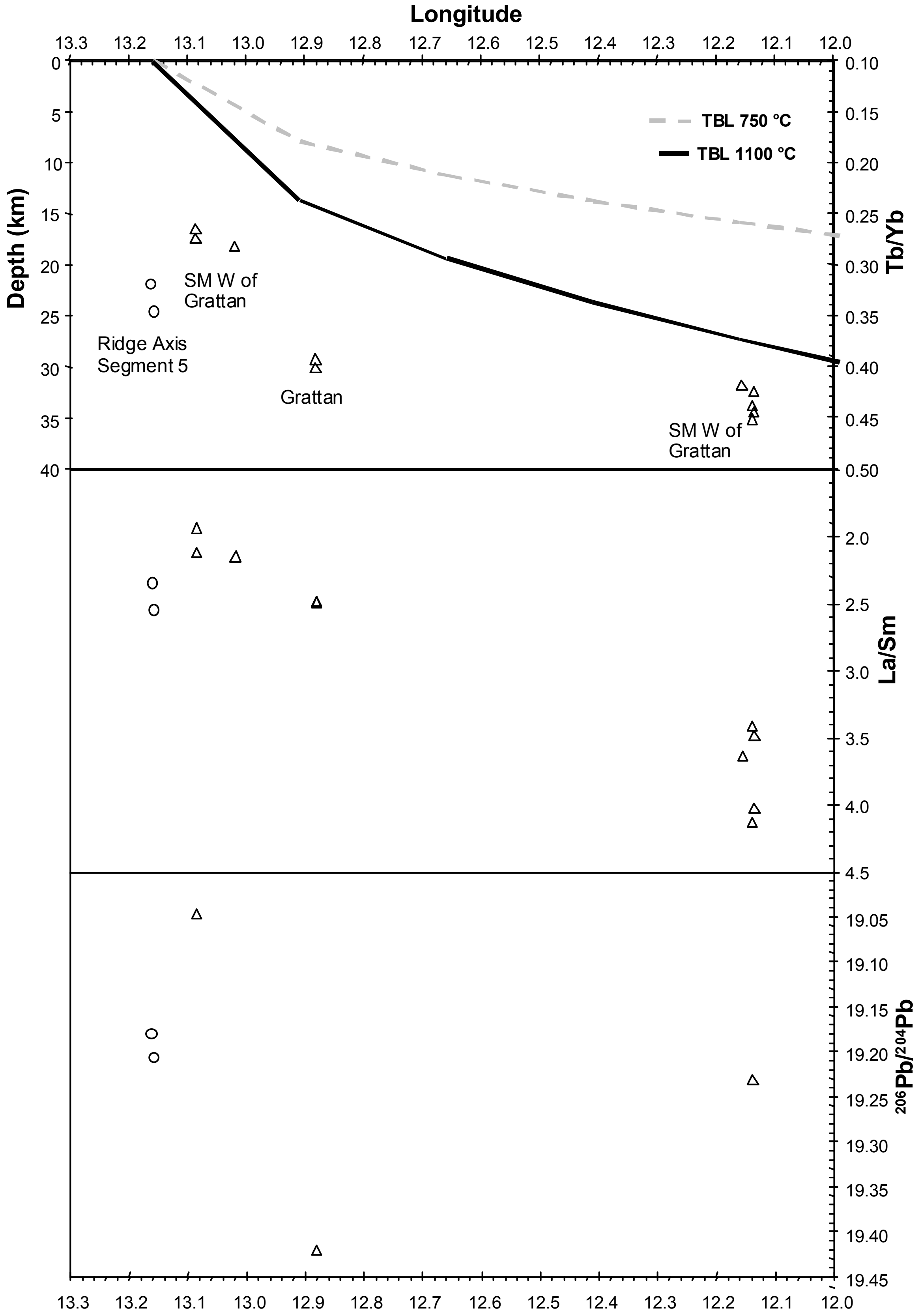

Figure 5.22: E-W profile of Segment 5 cutting through the off-axis seamounts, TBL is thermal boundary layer, lithosphere colder than 750°C is believed to behave rigidly rigid. Melting is stopped

samples show different grades of enrichment, this can be seen in a plot of longitude vs. La/Sm. The most enriched samples come from the easternmost seamount whereas Pb^{206}/Pb^{204} ratios suggest the most radiogenic source beneath Grattan and not east of it. Figure 5.23 reveals that fractional crystallisation accounts for La/Sm differences of the westernmost Seamount and Grattan but cannot account for the higher La/Sm ratios of the easternmost Seamount. The decoupling of isotopic and incompatible element signature implies that the signature is not due to variable degrees of mantle depletion (Phipps et al., 1995; Phipps, 1999 and Niu et al., 1996). Therefore a lower degree of partial melting can be supposed for this seamount because low degrees of partial melting can fractionate incompatible elements efficiently. As it was supposed before, approx. 10 % melting were calculated to produce the thickened crust of Segment 5. If a comparable source enrichment and a modal batch melting modus is supposed, a degree of approx. 1 % partial melting can produce the observed La/Sm (calculated value is 3.96) ratios at the seamount furthest E. With this low degree of partial melting also the Tb/Yb ratio is raised to values of ca. 0.38 which is slightly lower than the observed values, suggesting that garnet may play an enhanced role in Tb/Yb fractionation.

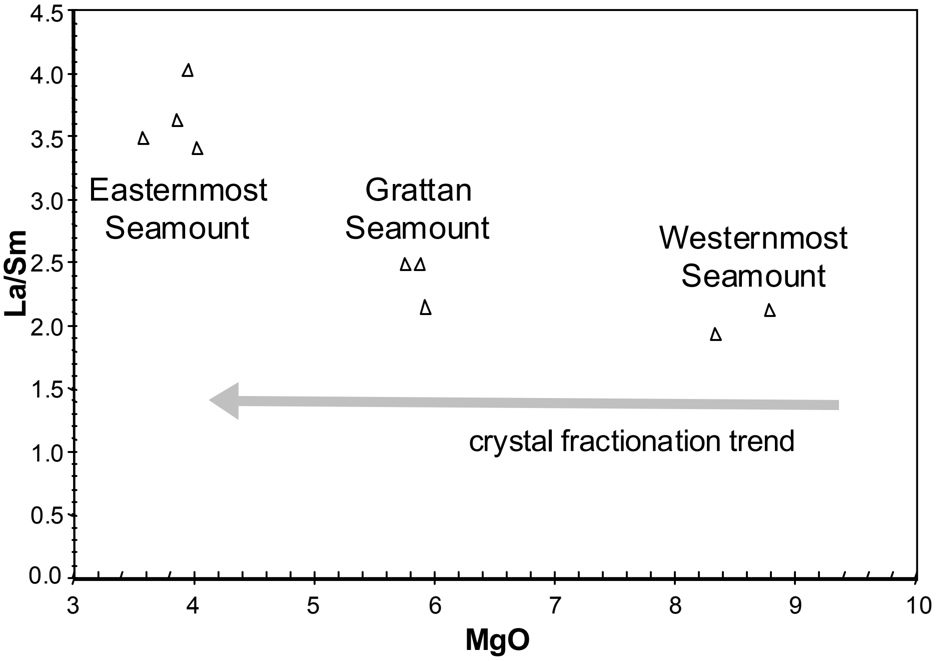

Figure 5.23: La/Sm ratios of seamounts, arrow indicates La/Sm enrichment due to crystal fractionation

5.7 Prefered mantle model

Figure 5.24 shows the prefered simplified mantle model of the Ascension melting anomaly. Fertile mantle rises on the eastern flank of Segment 5 following the MOR mantle flow. Due to its lower solidus, the first melts are formed in the garnet peridotite stability field. In accordance with Zou et al. (2002) most melts are entrained into the spreading axis but they also rise off-axis building three seamounts. Enriched radiogenic melts mix with unradiogenic depleted melts beneath the spreading axis. A northwards tending mantle flow deflects mixed magma from the vertical ascent. Magmas beneath Segment 5 must penetrate an approx. 2 times thicker ocean crust. This leads to longer cooling times. Due to their high H_2O concentrations these magmas have a lower solidus temperature which protects the melts from solidification and allows MgO poor lavas to extrude.

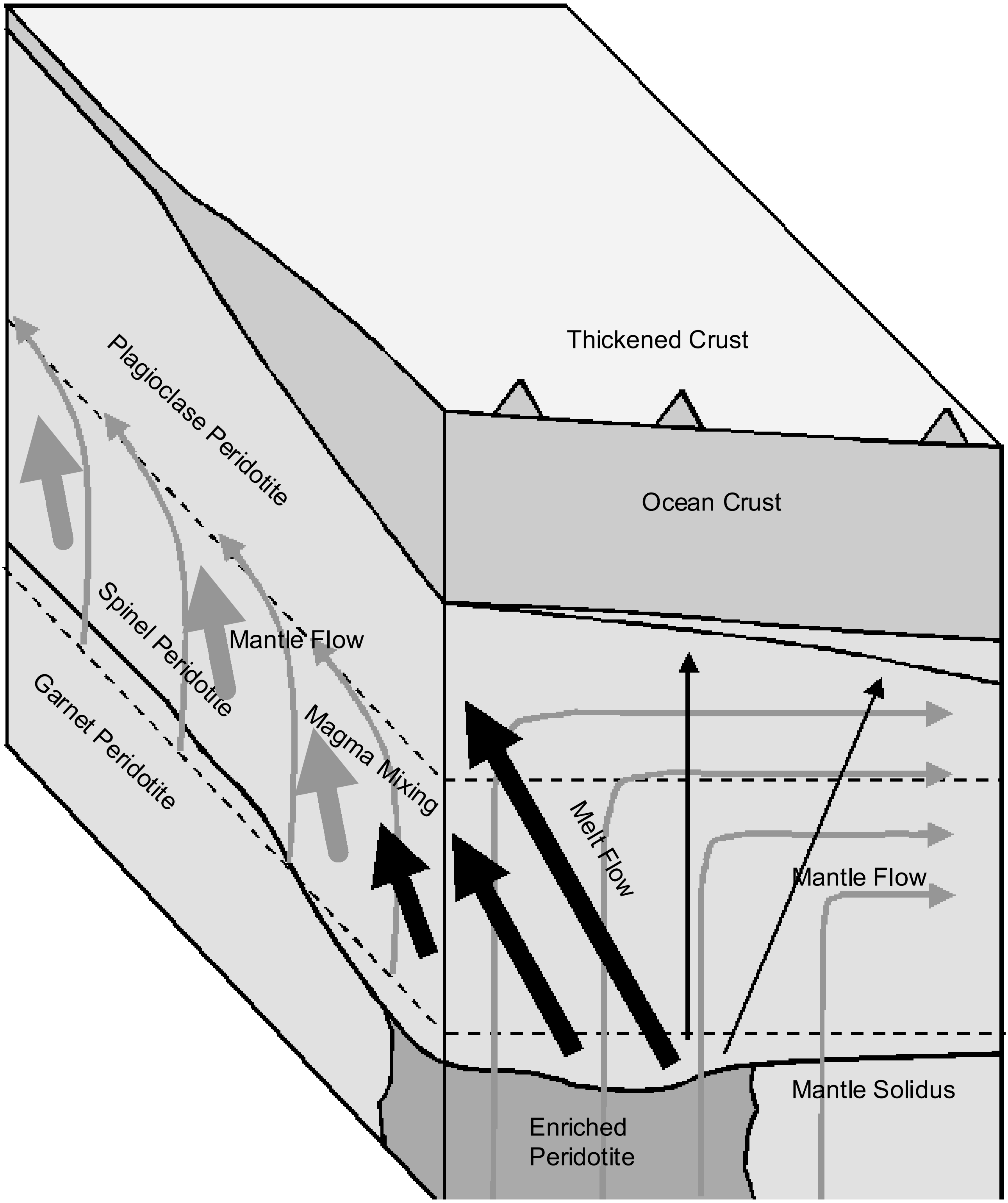

Figure 5.24: Supposed mantle model of the investigated area near Ascension island

Conclusions

1) MELTS models and fractional crystallisation trends of major elements suggest a higher H_2O content in Segment 5 samples.

2) The melting anomaly of Segment 4 and 5 consist of incompatible element enriched and radiogenic lavas whereby fractional crystallisation can not account for this enrichment.

3) Isotope ratios imply mixing between an enriched radiogenic endmember beneath Grattan seamount and an depleted unradiogenic MORB endmember beneath Segment 2 and 3.

4) A mantle plume with a low excess temperature of about 50° C (Minshull et al., 1998) is unlikely because seamounts are not aligned parallel to the motion vector of the African plate and show no age progression with distance from axis. Furthermore uniform Mg# in glassy inclusions and olivine forsterite contents from all segments imply uniform mantle temperatures.

5) Melting of a H_2O enriched, fertile mantle is proposed. Fertile mantle melting is confirmed by comparison with major element data from other elevated MAR areas. The calculated H_2O mantle source concentration (Niu et al., 2001) is approx. 450 ppm beneath Segment 5 which corresponds after Wyllie (1971) and Niu et al. (2001) to a solidus temperature reduction of approx. 165°C at 3 GPa in comparison to a dry mantle solidus.

6) HREE depletion mainly in Segment 5 lavas suggest either initial melting in the garnet peridotite stability field or melting of pyroxenite veins incorporated in spinel peridotite. An eclogitic pyroxenite source can be ruled out because of relatively high Hf/Sm ratios of the samples (van Westrenen et al., 2001) whereas melting of Ca-poor garnet pyroxenite can not be completely ruled out (although following (Hirschmann and Stolper, 1996) it seems unlikely). Instead melting of garnet peridotite is favored.

7) Geochemical patterns, along axis morphology as well as a propagating rift at 8° S, which started ca. 5 Ma ago imply a northwards tending mantle flow.

8) Partial melting of the easternmost off axis volcano E of Segment 5 seems be low (ca.1%) in comparison to Grattan seamount.

References

Abouchami, W., Galer, S.J.G., and Koschinsky, A., 1999, Pb and Nd isotopes in NE Atlantic Fe-Mn crusts; proxies for trace metal paleosources and paleocean circulation: Geochimica et Cosmochimica Acta, v. 63, p. 1489-1505.

Ballhaus, C., 1993, Redox states of lithospheric and asthenospheric upper mantle: Contributions to Mineralogy and Petrology, v. 114, p. 331-348.

Batiza, R., 1982, Abundances, distribution and sizes of volcanoes in the Pacific Ocean and implications for the origin of non-hotspot volcanoes: Earth Planetary Science Letters, v. 60, p. 195-206.

Bonatti, E., 1990, Not so hot "hot spots" in the oceanic mantle: Science, v. 250, p. 107-111.

Bourdon, B., Langmuir, C.H., and Zindler, A., 1996, Ridge-hotspot interaction along the Mid-Atlantic Ridge between 37°30' and 40°30'N: the U-Th disequilibrium evidence: Earth and Planetary Science Letters, v. 142, p. 175-189.

Bourdon, E., and Hemond, C., 2001, Looking for the "missing endmember" in South Atlantic Ocean mantle around Ascension Island: Mineralogy and Petrology, v. 71, p. 127-138.

Bown, J.W., and White, R.S., 1994, Variation with spreading rate of oceanic crustal thickness and geochemistry: Earth and Planetary Science Letters, v. 121, p. 435-449.

Brozena, J.M., 1986, Temporal and spatial variability of seafloor spreading processes in the northern South Atlantic: Journal of Geophysical Research, v. 91, p. 497-510.

Brozena, J.M., and White, R.S., 1990, Ridge jumps and propagations in the South Atlantic Ocean: Nature, v. 348, p. 149-152.

Burke, K.C., and Wilson, J.T., 1976, Hot spots on the Earth's surface: Scientific American, v. 235, p. 46-57.

Calvert, A.J., 1995, Seismic evidence for a magma chamber beneath the slow-spreading Mid-Atlantic Ridge: Nature, v. 377, p. 410-414.

Campbell, I.H., and Griffiths, R.W., 1990, Implications of mantle plume structure for the evolution of flood basalts: Earth and Planetary Science Letters, v. 99, p. 79-93.

Davies, G.F., 1988, Ocean bathymetry and mantle convection 1. Large-scale flow and hotspots: Journal of Geophysical Research, v. 93, p. 10467-10480.

Davies, G.F., 1990, Mantle plumes, mantle stirring and hotspot chemistry: Earth and Planetary Science Letters, v. 99, p. 94-109.

Detrick, R.S., Needham, H.D., and Renard, V., 1995, Gravity anomalies and crustal thickness variations along the Mid-Atlantic Ridge between 33 degrees N and 40 degrees N: Journal of Geophysical Research, B, Solid Earth and Planets, v. 100, p. 3767-3787.

Devey, C.W., Garbe-Schönberg, C.-D., Stoffers, P., Chauvel, C., and Mertz, D.F., 1994, Geochemical effects of dynamic melting beneath ridges: Reconciling major and trace element variations in Kolbeinsey (and global) mid-ocean ridge basalt: Journal of Geophysical Research, v. 99, p. 9077-9095.

Devey, C.W., and Party, S., 1993, SO-84 Cruise report: The St Helena Hotspot.: Berichte-Reports, Geol. Paläont. Inst. Univ. Kiel, v. 64.

Fontignie, D., and Schilling, J.-G., 1996, Mantle heterogeneities beneath the South Atlantic: a Nd-Sr-Pb isotope study along the Mid-Atlantic Ridge (3°S-46°S): Earth and Planetary Science Letters, v. 142, p. 209-221.

Forsyth, D.W., 1992, Geophysical constraints on mantle flow and melt generation beneath Mid-ocean Ridges, in Phipps Morgan, J., Blackman, D.K., and Sinton, J.M., eds., Mantle flow and melt generation at mid-ocean ridges, Volume Geophys. Mon. 71: Washington, D.C., Am. Geophys. Union, p. 1-65.

Galer, S.J.G., 1999, Optimal double and triple spiking for high precision lead isotopic measurement: Chemical Geology, v. 157, p. 255-274.

Galer, S.J.G., and Abouchami, W., 1998, Practical application of lead triple spiking for correction of instrumental mass discrimination, in Anonymous, ed., V. M. Goldschmidt conference; extended abstracts., Volume 62a: Mineralogical Magazine: London, United Kingdom, Mineralogical Society, p. 491-492.

Garbe-Schönberg, C.-D., 1993, Simultaneous determination of thirty-seven trace elements in twenty-eight international rock standards by ICP-MS: Geostandards Newsletters, v. 17, p. 81-97.

Ghiorso, M.S., and Sack, R.O., 1993, MELTS; software for the thermodynamic analysis of phase equilibria in magmatic systems, in Anonymous, ed., Geological Society of America, 1993 annual meeting., Volume 25: Abstracts with Programs - Geological Society of America: Boulder, CO, United States, Geological Society of America (GSA), p. 96.

Graham, D.W., Jenkins, W.J., Schilling, J.-G., Thompson, G., Kurz, M.D., and Humphris, S.E., 1992, Helium isotope geochemistry of mid-ocean ridge basalts from the South Atlantic: Earth and Planetary Science Letters, v. 110, p. 133-147.

Green, D.H., and Falloon, T.J., 1998, Pyrolite: A Ringwood concept and its current expression: in: I. Jackson (ed.), The Earth´s Mantle, Composition, Structure and Evolution. Cambridge University Press, p. 311-380.

Green, D.H., Falloon, T.J., Eggins, S.M., and Yaxley, G.M., 2001, Primary magmas and mantle temperatures: European Journal of Mineralogy, v. 13, p. 437-451.

Griffiths, R.W., and Campbell, I.H., 1990, Stirring and structure in mantle starting plumes: Earth and Planetary Science Letters, v. 99, p. 66-78.

Griffiths, R.W., and Turner, J.S., 1998, Understanding Mantle Dynamics through Mathematical Models and Labratory Experiments: The Earth´s Mantle, p. 191-227.

Haase, K.M., Devey, C.W., and Goldstein, S.L., 1996, Two-way exchange between the Easter mantle plume and the Easter microplate spreading axis: Nature, v. 382, p. 344-346.

Haase, K.M., Goldstein, S.L., Devey, C.W., and Wieneke, M., 1999, Geochemistry of Kolbeinsey Ridge MORB; implications for mantle sources and mixing processes, in Anonymous, ed., AGU 1999 fall meeting., Volume 80: Eos, Transactions, American Geophysical Union: Washington, DC, United States, American Geophysical Union, p. 1085-1086.

Hanan, B.B., Kingsley, R.H., and Schilling, J.-G., 1986, Pb isotope evidence in the South Atlantic for migrating ridge-hotspot interactions: Nature, v. 322, p. 137-144.

Hart, S.R., and Dunn, T., 1993, Experimental cpx/melt partitioning of 24 trace elements: Contributions to Mineralogy and Petrology, v. 113, p. 1-8.

Hayes, D.E., 1988, Age-depth relationships and depth anomalies in the southeast Indian Ocean and South Atlantic Ocean: Journal of Geophysical Research, v. 93, p. 2937-2954.

Helffrich, G.R., and Wood, B.J., 2001, The Earth´s mantle: Nature, v. 412, p. 501-507.

Hermes, O.D., and Schilling, J.G., 1976, Olivine from Reykjanes Ridge and Iceland tholeiites, and its significance to the two-mantle source model: Earth and Planetary Science Letters, v. 28, p. 345-355.

Hill, R.I., 1991, Starting plumes and continental break-up: Earth and Planetary Science Letters, v. 104, p. 398-416.

Hirose, K., and Kawamoto, T., 1995, Hydrous partial melting of lherzolite at 1 GPa; the effect of H (sub 2) O on the genesis of basaltic magmas: Earth and Planetary Science Letters, v. 133, p. 463-473.

Hirschmann, M.M., and Stolper, E.M., 1996, A possible role for garnet pyroxenite in the origin of the "garnet signature" in MORB: Contributions to Mineralogy and Petrology, v. 124, p. 185-208.

Hofmann, A.W., 1988, Chemical differentiation of the Earth: the relationship between mantle, continental crust, and oceanic crust: Earth and Planetary Science Letters, v. 90, p. 297-314.

Hofmann, A.W., 1997, Mantle geochemistry: The message from oceanic volcanism: Nature, v. 385, p. 219-229.

Hofmann, A.W., Jochum, K.P., Seufert, M., and White, W.M., 1986, Nb and Pb in oceanic basalts; new constraints on mantle evolution: Earth and Planetary Science Letters, v. 79, p. 33-45.

Hooft, E.E.E., Detrick, R.S., Toomey, D.R., Collins, J.A., and Lin, J., 2000, Crustal thickness and structure along three contrasting spreading segments of the Mid-Atlantic Ridge, 33.5°-35°N: Journal of Geophysical Research, v. 105, p. 8205-8226.

Jackson, I.e., 1998, The earth´s mantle; composition, structure and evolution: Cambridge University Press.

Jochum, K.P., Hofmann, A.W., Ito, E., Seufert, H.M., and White, W.M., 1983, K, U and Th in mid-ocean ridge basalt glasses and heat production, K/U and K/Rb in the mantle: Nature, v. 306, p. 431-436.

Kar, A., Weaver, B., Davidson, J., and Colucci, M., 1998, Origin of differentiated volcanic and plutonic rocks from Ascension Island, South Atlantic Ocean, in Davidson, J.P., and Bohrson, W.A., eds., Shallow-level processes in ocean-island magmatism., Volume 39: Journal of Petrology: Oxford, United Kingdom, Clarendon Press, p. 1009-1024.

Kennedy, A.K., Lofgren, G.E., and Wasserburg, G.J., 1993, An experimental study of trace element partitioning between olivine, orthopyroxene and melt in chondrules: equilibrium values and kinetic effects: Earth and Planetary Science Letters, v. 115, p. 177-195.

Kent, G.M., Singh, S.C., Harding, A.J., Sinha, M.C., Orcutt, J.A., Barton, P.J., White, R.S., Bazin, S., Hobbs, R.W., Tong, C.H., and Pye, J.W., 2000, Evidence from three-dimensional seismic reflectivity images for enhanced melt supply beneath mid-ocean-ridge discontinuities: Nature (London), v. 406, p. 614-618.

Kinzler, R.J., 1997, Melting of mantle peridotite at pressures approaching the spinel to garnet transition; application to mid-ocean ridge basalt petrogenesis: Journal of Geophysical Research, B, Solid Earth and Planets, v. 102, p. 853-874.

Kinzler, R.J., and Grove, T.L., 1992, Primary magmas of Mid-Ocean Ridge basalts, 2. Applications: Journal of Geophysical Research, v. 97, p. 6907-6926.

Klein, E.M., and Langmuir, C.H., 1987, Global correlations of ocean ridge basalt chemistry with axial depth and crustal thickness: Journal of Geophysical Research, B, Solid Earth and Planets, v. 92, p. 8089-8115.

Klein, E.M., and Langmuir, C.H., 1989, Local versus global variations in ocean ridge basalt composition; reply: Journal of Geophysical Research, B, Solid Earth and Planets, v. 94, p. 4241-4252.

Klingelhoefer, F., Geli, L., and White, R.S., 2000, Geophysical and geochemical constraints on crustal accretion at the very-slow spreading Mohns Ridge: Geophysical Research Letters, v. 27, p. 1547-1550.

Kodaira, S., Mjelde, R., Gunnarsson, K., Shiobara, H., and Shimamura, H., 1997, Crustal structure of the Kolbeinsey Ridge, North Atlantic, obtained by use of ocean bottom seismographs: Journal of Geophysical Research, v. 102, p. 3131-3151.

Langmuir, C.H., 1989, Geochemical consequences of in situ crystallization: Nature, v. 340, p. 199-205.

Langmuir, C.H., Bender, J.F., and Batiza, R., 1986, Petrological and tectonic segmentation of the East Pacific Rise, 5 degrees 30'-14 degrees 30'N: Nature (London), v. 322, p. 422-429.

Langmuir, C.H., Klein, E.M., and Plank, T., 1992, Petrological Systematics of Mid-Ocean Ridge Basalts: Constraints on Melt Generation Beneath Ocean Ridges: Geophysical Monograph, v. 71, p. 183-280.

Le Bas, M.J., and Streckeisen, A.L., 1991, The IUGS systematics of igneous rocks: Journal of the Geological Society of London, v. 148, p. 825-833.

Lindsley, D.H., 1983, Pyroxene thermometry: American Mineralogist, v. 68, p. 477-493.

Macdonald, K.C., Fox, P.J., Perram, L.J., Eisen, M.F., Haymon, R.M., Miller, S.P., Carbotte, S.M., Cormier, M.-H., and Shor, A.N., 1988, A new view of the mid-ocean ridge from the behaviour of ridge-axis discontinuities: Nature, v. 335, p. 217-225.

Marquart, G., and Schmeling, H., 2000, Conditions for plumes to penetrate the mantle phase boundaries: Journal of Geophysical Research, v. 105, p. 5679-5693.

McKenzie, D., and Bickle, M.J., 1988, The volume and composition of melt generated by extension of the lithosphere: Journal of Petrology, v. 29, p. 625-679.

McKenzie, D., and O, N.R.K., 1991, Partial melt distributions from inversion of rare earth element concentrations: Journal of Petrology, v. 32, p. 1021-1091.

Melson, W.G., and O'Hearn, T., 1986, "Zero-age" variations in the composition of abyssal volcanic rocks along the axial zone of the Mid-Atlantic Ridge, in Vogt, P.R., and Tucholke, B.E., eds., The Geology of North America: The Western North Atlantic Region, Volume Vol. M, Geol. Soc. America, p. 117-136.

Mertz, D.F., and Haase, K., 1997, The radiogenic isotope composition of the high-latitude North Atlantic mantle: Geology, v. 25, p. 411-414.

Michael, P., 1995, Regionally distinctive sources of depleted MORB: Evidence from trace elements and H2O: Earth and Planetary Science Letters, v. 131, p. 301-320.

Michael, P.J., and Chase, R.L., 1987, The influence of primary magma composition, H2O and pressure on Mid-Ocean Ridge basalt differentiation: Contributions to Mineralogy and Petrology, v. 96, p. 245-263.

Michael, P.J., Forsyth, D.W., Blackman, D.K., Fox, P.J., Hanan, B.B., Harding, A.J., Macdonald, K.C., Neumann, G.A., Orcutt, J.A., Tolstoy, M., and Weiland, C.M., 1994, Mantle control of a dynamically evolving spreading center: Mid-Atlantic Ridge 31-34°S: Earth and Planetary Science Letters, v. 121, p. 451-468.

Millhollen, G.L., Irving, A.J., and Wyllie, P.J., 1974, Melting interval of peridotite with 5.7 per cent water to 30 kilobars: Journal of Geology, v. 82, p. 575-586.

Minshull, T.A., Bruguier, N.J., and Brozena, J.M., 1998, Ridge-plume interactions or mantle heterogeneity near Ascension Island?: Geology, v. 26, p. 115-118.

Morgan, W.J., 1971, Convection plumes in the lower mantle: Nature (London), v. 230, p. 42-43.

Neumann, E.R., and Schilling, J.G., 1984, Petrology of basalts from the Mohns-Knipovich Ridge; the Norwegian-Greenland Sea: Contributions to Mineralogy and Petrology, v. 85, p. 209-223.

Nielsen, R.L., Crum, J., Bourgeois, R., Hascall, K., Forsythe, L.M., Fisk, M.R., and Christie, D.M., 1995, Melt inclusions in high-An plagioclase from the Gorda Ridge; an example of the local diversity of MORB parent magmas: Contributions to Mineralogy and Petrology, v. 122, p. 34-50.

Niu, Y., and Batiza, R., 1991, An empirical method for calculating melt compositions produced beneath mid-ocean ridges: applicaion for axis and off-axis (seamounts) melting: Journal of Geophysical Research, v. 96, p. 21753-21777.

Niu, Y., Waggoner, D.G., Sinton, J.M., and Mahoney, J.J., 1996, Mantle source heterogeneity and melting processes beneath seafloor spreading centers: The East Pacific Rise, 18°-19°S: Journal of Geophysical Research, v. 101, p. 27711-27733.

Niu, Y., Bideau, D., Hekinian, R., and Batiza, R., 2001, Mantle compositional control on the extent of mantle melting, crust production, gravity anomaly, ridge morphology, and ridge segmentation; a case study at the Mid-Atlantic Ridge 33-35 degrees N: Earth and Planetary Science Letters, v. 186, p. 383-399.

Niu, Y., and Hekinian, R., 1997, Spreading-rate dependence of the extent of mantle melting beneath ocean ridges: Nature, v. 385, p. 326-329.

Niu, Y., and Hékinian, R., 1997, Basaltic liquids and harzburgitic residues in the Garrett Transform: a case study at fast-spreading ridges: Earth and Planetary Science Letters, v. 146, p. 243-258.

Niu, Y., Waggoner, D.G., Sinton, J.M., and Mahoney, J.J., 1996, Mantle source heterogeneity and melting processes beneath seafloor spreading centers: The East Pacific Rise, 18°-19°S: Journal of Geophysical Research, v. 101, p. 27711-27733.

O´Connor, J.M., and Duncan, R.A., 1990, Evolution of the Walvis Ridge-Rio Grande Rise hot spot system; implications for African and South American Plate motions over plumes: Journal of Geophysical Research, B, Solid Earth and Planets, v. 95, p. 17,475-17,502.

O´Connor, J.M., Stoffers, P., van, d.B.P., and McWilliams, M., 1999, First seamount age evidence for significantly slower African Plate motion since 19 to 30 Ma: Earth and Planetary Science Letters, v. 171, p. 575-589.

Phipps, M.J., 1999, Isotope topology of individual hotspot basalt arrays; mixing curves or melt extraction trajectories?: Geochemistry, Geophysics, Geosystems - G 3, v. 1, p. ; 5,802 words.

Phipps, M.J., Morgan, W.J., Zhang, Y.S., and Smith, W.H.F., 1995, Observational hints for a plume-fed, suboceanic asthenosphere and its role in mantle convection: Journal of Geophysical Research, B, Solid Earth and Planets, v. 100, p. 12,753-12,767.

Ringwood, A.E., 1988, Nature of the 650 km seismic discontinuity; implications for mantle dynamics and differentiation: Nature, v. 331, p. 131-136.

Roeder, P.L., and Emslie, R.F., 1970, Olivine-liquid equilibrium: Contributions to Mineralogy and Petrology, v. 29, p. 275-289.

Rollinson, 1993, using geochemical data:evaluation, presentation, interpretation: .

Schilling, J.-G., 1991, Fluxes and excess temperatures of mantle plumes inferred from their interaction with migrating mid-ocean ridges: Nature, v. 352, p. 397-403.

Schilling, J.G., 1973, Iceland Mantle Plume; Geochemical Study of Reykjanes Ridge: Nature (London), v. 242, p. 565-571.

Schilling, J.-G., Thompson, G., Kingsley, R., and Humphris, S., 1985, Hotspot-migrating ridge interaction in the South Atlantic: Nature, v. 313, p. 187-191.

Schilling, J.-G., Zajac, M., Evans, R., Johnston, T., White, W., Devine, J.D., and Kingsley, R., 1983, Petrologic and geochemical variations along the Mid-Atlantic Ridge from 29°N to 73°N: American Journal of Science, v. 283, p. 510-586.

Searle, R.C., Keeton, J.A., Owens, R.B., White, R.S., Mecklenburgh, R., Parsons, B., and Lee, S.M., 1998, The Reykjanes Ridge; structure and tectonics of a hot-spot-influenced, slow-spreading ridge, from multibeam bathymetry, gravity and magnetic investigations: Earth and Planetary Science Letters, v. 160, p. 463-478.

Sigurdsson, H., 1981, First-order major element variation in basalt glasses from the Mid-Atlantic Ridge; 29 degrees N to 73 degrees N: JGR. Journal of Geophysical Research. B, v. 86, p. 9483-9502.

Sigurdsson, H.e., 2000, Encyclopedia of Volcanoes: .

Smallwood, J.R., and White, R.S., 1998, Crustal accretion at the Reykjanes Ridge, 61 degrees -62 degrees N: Journal of Geophysical Research, B, Solid Earth and Planets, v. 103, p. 5185-5201.

Smith, D.G.e., 1981, The Cambridge encyclopedia of earth sciences: Cambridge Unuversity Press.

Stolper, E., 1980, A phase diagram for mid-ocean ridge basalts: preliminary results and implications for petrogenesis: Contribuions to Mineralogy and Petrology, v. 74, p. 13-27.

Stolper, E., and Newman, S., 1994, The role of water in the petrogenesis of Mariana trough magmas: Earth and Planetary Science Letters, v. 121, p. 293-325.

Stover, C.W., 1968, Seismicity of the south Atlantic Ocean: Journal of Geophysical Research, v. 73, p. 3807-3820.

Sun, S.-S., and McDonough, W.F., 1989, Chemical and isotopic systematics of oceanic basalts: implications for mantle composition and processes, in Saunders, A.D., and Norry, M.J., eds., Magmatism in the ocean basins, Volume 42: London, Geological Society Special Publications, p. 313-345.

Takahashi, E., 1986, Melting of a dry peridotite KLB-1 up to 14 GPa; implications on the origin of peridotitic upper mantle, in Waff, H.S., and Kumazawa, M., eds., Special section; Partial melting phenomena in the Earth and planetary evolution., Volume 91: JGR. Journal of Geophysical Research. B: Washington, DC, United States, American Geophysical Union, p. 9367-9382.

Taylor, R.N., Thirlwall, M.F., Murton, B.J., Hilton, D.R., and Gee, M.A.M., 1997, Isotopic constraints on the influence of the Icelandic plume: Earth and Planetary Science Letters, v. 148, p. E1-E8.

Tolstoy, M., Harding, A.J., and Orcutt, J.A., 1993, Crustal thickness on the Mid-Atlantic-Ridge: Bull´s-eye gravity anomalies and focused accretion: Science, v. 262, p. 726-729.

van Andel, T.H., and Heath, G.R., 1970, Tectonics of the Mid Atlantic Ridge, 6-8° south latitude: Marine Geophysical Research, v. 1, p. 5-36.

van Andel, T.H., Rea, D.K., von Herzen, R.P., and Hoskins, H., 1973, Ascension Fracture Zone, Ascension Island, and the Mid-Atlantic Ridge: Geological Society of America Bulletin, v. 84, p. 1527-1546.

van der Hilst, R.D., Widiyantoro, S., and Engdahl, E.R., 1997, Evidence for deep mantle circulation from global tomography: Nature, v. 386, p. 578-584.

van Westrenen, W., Blundy, J.D., and Wood, B.J., 2001, High field strength element/rare earth element fractionation during partial melting in the presence of garnet: Implications for identification of mantle heterogeneities: Geochemistry, Geophysics, Geosystems, v. 2.

Vogt, P.R., 1971, Asthenosphere motion recorded by the ocean floor south of Iceland: Earth and Planetary Science Letters, v. 13, p. 153-160.

Waggoner, D.G., 1989, An isotopic and trace element study of mantle heterogeneity beneath the Norwegian-Greenland Sea.

Walker, D., Shibata, T., and Long, S.E., 1979, Abyssal tholeiites from the Oceanographer Fracture Zone II. Phase equilibria and mixing: Contributions to Mineralogy and Petrology, v. 70, p. 111-135.

Wells, P.R.A., 1977, Pyroxene thermometry in simple and complex systems: Contributions to Mineralogy and Petrology, v. 62, p. 129-139.

Wendt, J.I., Regelous, M., Niu, Y., Hekinian, R., and Collerson, K.D., 1999, Geochemistry of lavas from the Garrett transform fault; insights into mantle heterogeneity beneath the eastern Pacific: Earth and Planetary Science Letters, v. 173, p. 271-284.

White, R.S., 1988, A hot-spot model for the early Tertiary volcanism in the N Atlantic, in Morton, A.C., and Parson, L.M., eds., Early Tertiary Volcanism and the Opening of the NE Atlantic, Volume 39, Geol. Soc. Spec. Publ., p. 3-13.

White, R.S., 1990, Initiation of the Iceland plume and the opening of the North Atlantic, in Tankard, A.J., and Balkwill, H.R., eds., Extensional tectonics and stratigraphy of the North Atlantic margins, Volume 46, Am. Ass. Petrol. Geol. Mem., p. 149-154.

White, R.S., 1997, Rift-plume interaction in the North Atlantic: Philosophical Transactions of the Royal Society of London, v. A355, p. 319-339.

White, R.S., Bown, J.W., and Smallwood, J.R., 1995, The temperature of the Iceland plume and origin of outward-propagating V-shaped ridges: Journal of the Geological Society London, v. 152, p. 1039-1045.

White, R.S., McKenzie, D., and O´Nions, R.K., 1992, Oceanic crustal thickness from seismic measurements and rare earth element inversions: Journal of Geophysical Research, v. 97, p. 19683-19715.

White, R.S., and Morton, A.C., 1995, The Iceland plume and its influence on the evolution of the Atlantic: Journal of the Geological Society London, v. 152, p. 933.

White, W.M., 1995, Geochemical tracers of mantle processes: Reviews of Geophysics Supplement, v. 33.

White, W.M., and Schilling, J.G., 1978, The nature and origin of geochemical variation in Mid-Atlantic Ridge basalts from the central North Atlantic: Geochimica et Cosmochimica Acta, v. 42, p. 1501-1516.

Wieneke, M., 1998, Geochemical variations along the Kolbeinsey Ridge: The behaviour of the sub-axial magmatic system on a slow-spreading ridge: phD thesis.

Wilson, J.T., 1963, Hypothesis of Earth's behaviour: Nature (London), v. 198, p. 925-929.

Wolfe, C.J., Bjarnason, I.T., VanDecar, J.C., and Solomon, S.C., 1997, Seismic structure of the Iceland mantle plume: Nature, v. 385, p. 245-247.

Wyllie, P.J., 1971, Role of water in magma generation and initiation of diapiric uprise in the mantle: Journal of Geophysical Research, v. 76, p. 1328-1338.

Zou, H., Zindler, A., and Niu, Y., 2002, Constraints on Melt Movement Beneath the East Pacific Rise From 230Th-238U Disequilibrium: Science, v. 295, p. 107-110.

APPENDIX

Table A 1: List of stations occupied during the cruise Me 41/2. Stations are in latitudal order. DS: dredge station

Station	Location	Latitude °	Latitude ´	Longitude °	Longitude ´	water depth
119 DS	on axis	6	16.35	11	22.53	3242
120 DS	on axis	6	23.96	11	20.30	3523
121 DS	on axis	6	32.51	11	18.58	3749
122 DS	on axis	6	39.83	11	17.59	4080
126 DS	on axis	7	8.28	13	3.01	4514
130 DS	on axis	7	35.01	13	28.22	3925
132 DS	on axis	7	39.95	13	27.36	3925
133 DS	on axis	7	43.08	13	26.64	3980
136 DS	on axis	7	46.35	13	25.89	3727
137 DS	on axis	7	49.21	13	25.63	3405
138 DS	on axis	7	52.03	13	25.83	3451
139 DS	on axis	7	55.13	13	24.63	3631
140 DS	on axis	7	57.90	13	23.93	3670
141 DS	on axis	7	59.14	13	25.83	3364
142 DS	on axis	8	1.12	13	25.80	3576
143 DS	on axis	8	3.29	13	25.03	3457
144 DS	on axis	8	5.37	13	27.17	3522
145 DS	on axis	8	7.49	13	24.63	3470
146 DS	on axis	8	10.00	13	26.73	3401
147 DS	on axis	8	18.81	13	36.39	3055
148 DS	on axis	8	20.67	13	36.00	2959
149 DS	on axis	8	22.45	13	36.97	3063
151 DS	on axis	8	27.07	13	35.39	2811
152 DS	on axis	8	30.49	13	33.84	2693
153 DS	on axis	8	33.29	13	33.02	2552
154 DS	on axis	8	36.47	13	32.08	2523
155 DS	on axis	8	41.60	13	32.59	2380
156 DS	on axis	8	44.96	13	30.18	2257
157 DS	on axis	8	48.46	13	29.77	2212
158 DS	on axis	8	50.27	13	29.72	2139
159 DS	on axis	8	54.56	13	28.07	1899
160 DS	on axis	8	58.05	13	27.62	2166
161 DS	on axis	9	0.75	13	27.40	2232
162 DS	on axis	9	4.80	13	26.71	2460
163 DS	on axis	9	11.76	13	26.53	2398
164 DS	on axis	9	14.65	13	25.27	2460
166 DS	on axis	9	13.80	13	18.96	2299
167 DS	on axis	9	15.87	13	18.02	2107
169 DS	on axis	9	20.51	13	15.12	1958
170 DS	on axis	9	26.01	13	14.13	1805
171 DS	on axis	9	28.96	13	13.99	1652
172 DS	on axis	9	33.59	13	12.62	1488
173 DS	on axis	9	38.19	13	11.49	1477
174 DS	on axis	9	42.24	13	9.44	1539

Table A 1: (continued) List of stations occupied during the cruise Me 41/2.

Station	Location	Latitude °	Latitude ´	Longitude °	Longitude ´	water depth
176 DS	off axis	9	41.01	13	1.14	1543
179 DS	off axis	9	44.05	12	52.86	1241
183 DS	off axis	9	42.72	12	8.27	2297
184 DS	off axis	9	43.70	12	8.08	1529
185 DS	off axis	9	44.12	12	7.51	1370
186 DS	off axis	9	46.46	12	9.29	918
188 DS	on axis	9	46.32	13	9.70	1603
189 DS	on axis	9	50.27	13	5.23	1945
190 DS	on axis	9	53.19	13	5.23	2052
191 DS	on axis	9	56.90	13	4.01	2188
194 DS	on axis	10	4.26	13	11.88	2953
195 DS	on axis	10	7.89	13	11.84	3091
196 DS	on axis	10	13.84	13	11.31	3241
197 DS	on axis	10	17.33	13	10.80	3100
198 DS	on axis	10	22.89	13	10.70	3500
199 DS	on axis	10	29.01	13	10.19	3528
200 DS	on axis	10	36.52	13	5.53	3791
201 DS	on axis	10	41.01	13	4.47	3712
202 DS	on axis	10	46.91	13	3.03	3463
203 DS	on axis	10	52.94	13	2.26	3639

Table A 2: Petrography and mineralogy of rock samples

Station Area	**Sample descriptions and samples taken (M = microprobe slide, GC = Geochemistry, Gl = Glass)**
119DS North of Ascension FZ	-1: 15x15x10, pillow, some pl phenos, some vesics <1mm, 3mm glass (M, GC, Gl) -2: 15x10x10, pillow, flow structure, some pl phenos, vesics to 2mm, 2mm glass (M, GC, Gl) -3: 30x20x17, pillow, some pl phenos (2mm), thin old glass rim (1mm), some vesics (ca. 1mm) (M, GC, Gl) -4: 15x10x5, sheet flow, rare pl (< 5mm), very fresh (M, Gl) -5: Pillow bud, Pl to 5mm, 1-2mm glass, Mn coating on broken surface (M, Gl)
120DS North of Ascension FZ	-1: 20x10x10, pillow, rare pl (0,5-2mm) non-vesic, 2 glass rinds 3-4mm thick -2: 10x6x6, pillow bud, some pl (<2mm), 1-2mm glass, non-vesic -3: 14x8x6, pillow, rare pl to 2mm, non-vesic, 2mm glass, fresh -4: 4x4x2,5, glass buds (2 pieces) some ol 3mm, rare pl
121DS North of Ascension FZ	-1: 5x5x3. pillow bud, many micro-vesics, rare large plag (to 3mm) on rim. 1mm glass -2: 7x4,5x3, glass crust, 2mm plag
122DS Inside corner N of Ascension FZ	-1: 20x20x3, sheet flow, 6mm glass, rare pl (M, Gl) -2: 15x10x5, pillow, ol 3-4mm, pl 5-6mm, few vesics, 2-3mm glass (M, GC, Gl) -3: 30x20x10, pillow, ca. aphyric, rare ol 1-2mm, 3mm glass (M, GC, Gl) -4: 40x30x20, pillow, like –3 but more altered (M, GC, Gl) -5: ?x?x?, pillow, like –3 and –4 nut more and larger vesics, some pl (2-3mm) near glass rim (M, GC, Gl) -6: ?x?x?, like –3, -4, -5 but with double glass rim (M, GC, Gl) -7: 5cm diameter, lava tube, abundant pl 1-5mm, glass, Mn caoting on broken surface (M, Gl)
126DS Axis(?) between the faults	-1: 10x10x8, pillow, pl 2-3mm, banded vesics, 7mm glass (M, GC, Gl) -2: 10x10x8, pillow, as –1(M, GC, Gl) -3: 10x6x6, pillow, 2-3mm glass, pl phenos xenomorph(M, GC, Gl)
130DS Segment ASC1, north	-1: 15x10x4, sheet flow, 25mm glass, aphyric, few vesics -2: 20x14x8, sheet flow, 2mm glass -3: 10x8x4, sheet flow, 15mm glass, similar to –1 -4: 4x4x4, glass piece
131DS Segment ASC1	-1: 5x3x3, pillow, altered, no glass, aphyric
132DS Segment ASC1	-1: 30x20x10, sheet flow, vesics 1-3mm, 5mm glass, pl 10mm (M, GC, Gl) -2: 30x20x20, pillow, 5% vesics (<2mm), 10mm glass, 10mm pl, fresh (M, GC, Gl) -3: 15x10x19, pillow, 2-4mm pl, vesics 2-8mm ca. 5% (M) -4: ?x?x?, pillow, altered, some sed. coating, 1-2mm glass (altered) -5: ?x?x?, pillow, 2-4mm glass, pl, 10% vesics (1-4mm) (M, GC, Gl) -6: 30x30x20, pillow, some pl to 2mm, 4mm glass, fresh (M, GC, Gl)
133DSb Segment ASC1	-1: 15x15x8, sheet flow, mn dusting, 1-6mm pl, <0,5mm cpx? (M, GC) -2: 20x15x15, pillow, old, mn caoting, pl to 2mm (M, GC) -3: 20x10x10, pillow, 1mm glass, rare rounded pl megaxst (M, GC, Gl) -4: 20x15x15, pillow, 2mm glass, non-vesic, Mn coating, rare 10mm rounded pl megaxst ((M, GC, Gl) -5: 15x15x12, pillow, 3mm glass, 1-10mm pl (M, GC, Gl) -6: 5x5x5, pillow, 1mm glass, Mn coating, Pl (3mm) in glass (M, GC) -7: 15x10x12, pillow, 2mm glass, pl to 3mm (M, GC) -8: 20x20x13, pillow, 3mm glass, pl 1mm rounded, flow banding at rim (M, GC, Gl) -9: 30x30x25, pillow, 4mm glass, rare rounded pl (1-4mm). Vesics up to cm with FeOH coatings (M, GC, Gl) -10:10x8x4, pillow, Mn dusting, 3mm glass (M, Gl) -11: as 7, more vesicular (M, GC, Gl)
136DSb Segment ASC1	-1: 10x5x5, Sheet flow, 15mm glass, 15mm pl megaxst (M, Gl) -2: 100x100x100, pillow, 7mm glass, pl megaxst >5mm (M, GC, Gl) -3: 100x100x100, pillow, 5mm glass, 3mm pl, some vesics (M, GC, Gl)
137DS Segment ASC1	-1: 28x12x17, hydroth. altered pillow, dark green (M, GC, Gl) -2: 23x14x8, pillow, 10mm glass, 10-15mm pl megaxst some rounded (M, GC, Gl) -3: 50x33x35, pillow, 5mm glass, pl megaxst to 12mm, vesics with FeOH (M, GC, Gl) -4: 18x12x?, pillow, 2mm glass, pl megaxst to 21mm conc. at rim (M, GC, Gl)
138DS Segment ASC1	-1: 32x22x24, tube lava, 2mm glas, hydroth. Mn coating, 1-3mm vesics at rim (M, GC, Gl) -2: ?x?x?, pillow, 5mm glass, vesic (at rim up to 20mm) (M, GC, Gl) -3: 20x16x11, pillow, 3mm glass, mn coating, some pl megaxst to 10mm (M, GC, Gl)
139DS Segment ASC 1	-1: 15x18x16, pillow, 4mm glass, Mn caoting, rounded pl to 10mm (M, GC, Gl) -2: 18x15x11, tube, 6mm glass, rounded Pl to 10mm esp. at rim (M, GC, Gl) -3: 14x10x4,5, sheet flow, 8mm and 4mm glass rim, abundant rounded pl to 7mm (M, GC, Gl)
140DS	-1: 12x6x4, sheet flow, 3mm glass, few vesics, pl to 20mm, ol to 2mm (M, Gl) -2: 15x12x3, as –1 with different surface structures (M, Gl)

Segment ASC1	
141DS Segment ASC2	-1: 30x20x8, pillow, 5mm glass, pl phenos 3-5mm + rounded megaxsts to 10mm, vesics 1-2mm in centre (M, GC, Gl) -2: ?x?x?, pillow, rare pl to 5mm, some vesics to 1mm, glass max 5mm (M, GC, Gl) -3: 20x20x7, pillow, like 1 but fewer vesics (M, GC, Gl)
142DSb Segment ASC2	-1: ?x?x?, Sheet flow, altered, no glass, some vesics (M) -2: 18x18x4, sheet flow, 2-10mm glass, Mn dusting, large vesics (M, Gl) -3:?x?x?, pillow, 2mm glass, some small vesics., mn dusting (M, GC, Gl) -4: 18x20x8, sheet flow, 2-7mm glass, 1mm vesics, some animal traces (M, GC, Gl) -5: ?x?x?, pillow, vesics to 7mm (M, GC) -6: 10x15x7, pillow, no glass, minute vesics (M,GC) -7: 30x20x10, sheet flow, to 5mm glass, ca. 10% vesics 1-2mm, pl phenos (M, GC, Gl) -8: 30x10x10, lava tablet, homog., vesics 3mm, no glass (M, GC) -9: 20x10x15, pillow, vesics 1-2mm, pl phenos (M, GC) -10: 30x20x20, pillow, glass to 10mm, Mn dusting (M, GC, Gl)
143DS Segment ASC2	-1: 40x20x20, pillow, 10mm glass, idiomorph pl to 15mm, ol idio. to 2mm, 5% vesics 2mm (M, GC, Gl) -2: 30x20x20, pillow, 10-20mm pl, 5mm glass, few vesics 1mm (M, GC, Gl)
144DS Segment ASC3	-1: 14x12x7, sheet flow, 6-30mm glass
145DSb Segment ASC3	-1: 30x30x30, pillow, altered, 1mm glass, few pl to 1mm, few vesics (M, GC, Gl). -2: 15x20x10, pillow, 1-2mm pl, 2-3mm glass, one pl megaxst 13mm, few vesics 1mm (M, GC, Gl) -3:10x10x6, pillow, as –2 but with more glass (5mm) and less Mn (M, GC, Gl) -4: 25x10x15, pillow, as 2 plus some Pl to 5mm (M, GC, Gl)
146DS Segment ASC3	-1: 25x25x25, pillow, glass, rare pl to 5mm (M, GC, Gl) -2: 25x14x7, sheet flow, 10mm glass, pl to 10mm (M, GC, Gl) -3: 30x20x14, pillow, 2mm glass, altered, aphyric (M, GC, Gl)
147DSc Segment ASC3	-1: 20x20x10, pillow, 3mm altered glass, some pl 2mm, FeOx coatings (M, GC, Gl) -2: 10x10x4, sheet flow, glass to 10mm, pl to 5mm (M, GC, Gl) -3: 10x7x7, tube, 2-3mm glass, pl megaxst to 10mm (M, GC, Gl) -4: 15x10x10, pillow, 3mm altered glass, rare pl to 3mm (M, Gl)
148DS Segment ASC4	-1: 16x8x8, pillow, up to 6mm glass, abundant pl <3mm, vesics to 1mm (M, GC, Gl) -2: 18x17x17, pillow, 2mm glass, Ol to 1mm (M, GC, Gl) -3: 20x18x15, pillow, 1mm glass, altered, Mn coating (M, GC) -4: 22x25x18, pillow, 1mm glass, thcik Mn coating -5: 24x29x24, pillow, thick Mn (Gl) -6: 45x40x40, pillow, 1-2mm glass, abundant pl to 1mm some to 5mm, vesics to 2mm
149DS Segment ASC4	-1: 15x13x14, tube, 8-10mm glass, 1mm vesics, many Pl to 3mm -2: 12x15x13, pillow, 1-2mm vesics, 6mm glass, Pl to 4mm, Mn coating -3: 12x13x11, pillow, 3mm glass, Pl to 6mm, Mn coating -4: 16x16x17, pillow, 3mm glass, Pl to 5mm, vesics 2mm, Ol? + 1x Extra piece
151DS Segment ASC4	-1: 15x13x10, tube, rounded Pl 2-3mm, vesics 1-2mm (M, GC) -2: 15x10x8, pillow, some Mn coating (M, GC, Gl) -3: 18x14x10, pillow, as –1 and –2 with Pl 3-4mm, glass to 10mm (M, GC, Gl)
152DS Segment ASC4	-1: 10x10x10, tube, 5mm glass, rare Pl to 2mm (M, GC) -2: ?x?x?, pillow, altered 2mm glass, no vesics, altered (M, GC)
153DSb Segment ASC4	-1: 10x10x4, sheet flow, glass to 10mm, abundant Pl to 5mm, some cpx? (M, Gl) -2: 8x8x8, tube, glass 3mm, Pl to 10mm, rare vesics to 2mm (M, Gl) -3: 10x10x10, pillow, abundant Pl to 5mm, vesics to 4mm, 3mm glass, some cpx? (M, GC, Gl) + 3x extra pieces
154DS Segment ASC4	-1: 10x7x6, pillow, 8mm glass, rare pl to 3mm, many vesics 1-2mm (M, GC, Gl) -2: 8x7x2, sheet flow, Pl < 2mm, many vesics 1mm
155DS Segment ASC4	-1: 12x8x7, sheet flow, Pl to 15mm, glass 5mm, no vesics (M, GC, Gl)
156DS Segment ASC4	-1: 25x22x12, pillow, 1mm glass, pl to 6mm, Mn coating (M, GC, Gl) -2: 17x13x17, pillow, 5-10mm glass, 2mm vesics abundant, some pl to 4mm (M, GC, Gl) -3: 11x11x7, pillow, 6mm glass, 1-2mm vesics, pl to 8mm, some ol 1mm (M, GC, Gl) -4: 9x9x7, tube, 3mm glass, some vesics 2mm (M, GC, Gl)
157DS Segment ASC4	-1: 15x5x5, sheet flow, few vesics, 15mm glass, aphyric (M, Gl) -2: 10x5x5, sheet flow, like –1 but glass somewhat altered (M, Gl) -3: 12x7x7, sheet flow, like –1 but vesicular (1-2mm) + 3 extra pieces
158DS	-1: 25x20x10, sheet flow, fresh, 10mm glass, aphyric, vesics to 2mm (M, GC, Gl) -2: 20x20x20, pillow, less fresh than –1, glass <2mm, aphyric, few vesics (M, GC, Gl)

Segment ASC4	+ 2 extra pieces
159DS Segment ASC4	-1: 10x15x10, pillow, no glass, pl 2-3mm, few vesics 2mm (M, GC) -2: 10x10x10, pillow, 3-5mm glass, aphyric, rare vesics (M, GC, Gl)
160DS Segment ASC4	-1: 20x15x10, sheet flow, 2-5mm glass, fresh, nonvesic (M, GC, Gl) -2: 30x20x25, sheet flow, 2-5mm glass, <5%vesics 1-2mm (M, GC, Gl) -3: 40x35x30, pillow, pl to 8mm, few vesics to 1mm, 3-5mm glass, some cpx (M, GC, Gl) + 3 extra pieces
161DS Segment ASC4	-1: 15x10x10, pillow, glass to 10mm, <10% vesics 2mm, rare pl 3mm (M, GC, Gl) -2: 15x10x10, pillow, glass to 5mm, <10% vesics to 2mm (M, GC, Gl) -3: 20x15x10, pillow, 5 mm glass, >10% vesics (2mm), cpx 1mm, pl 2-4mm, carbonate mud impregnated (M, GC, Gl) -4: 10x10x10, pillow, no glass, rare pl 2mm, few vesics 2mm (M, GC)
162DS Segment ASC4	-1: 22x15x14, pillow, glass to 12mm, few pl to 5mm, abundant vesics 1-3mm (M, GC, Gl) -2: 15x17x10, pillow, 3mm glass, some vesics 1-2mm, pl to 10mm, some ol 1-2mm (M, GC, Gl)
163DS Segment ASC4	-1: 14x7x1, sheet flow, glass, 3mm pl (M, GC, Gl)
164DS Segment ASC4	-1: 18x13x15, pillow, 4mm glass, some pl to 5mm, few vesics (1-2mm) (M, GC, Gl) -2: 14x10x6, pillow, 3mm glass, some 6mm pl, abundant vesics (1.-2mm), FeOx (M, GC, Gl)
166DS Segment ASC5	-1: 10x15x10, pillow, pl 2-5mm, 1-3mm glass, some sed. in cracks (M, GC, Gl) -2: 15x15x10, sheet flow, 5mm glass, few vesics 4mm, rare pl 3mm (M, GC, Gl) -3: 10x10x6, pillow, altered glass 5mm, some pl 2-3mm -4: 5x5x2, just glass, some vesics 2mm (Gl) -5: 10x5x5, pillow, >10% pl 3-5mm, >10% vesics 3-5mm, 3-5mm glass, some cpx? (M, GC, Gl)
167DS Segment ASC5	-1: ?x?x?, pillow, glass to 7mm, >10% pl 3mm, <10% vesics 2mm, rare cpx (M, GC, Gl)
168DS Segment ASC5, small cone in axis	-1: 20x20x18, pillow, to 3mm vesic glass, abundant pl 2-10mm, some ol 2mm (M, GC, Gl)
169DS Segment ASC5	-1: 9x7x6, pillow, glass to 14mm, abundant pl 6mm (M, GC, Gl) -2: 11x9x6, pillow, 1-12mm glass, pl 4mm, few vesics 2mm (M, GC, Gl) + 1 extra piece like –1
170DS Segment ASC5	-1: 15x12x9, 3mm glass, zoned vesics, Mn coating (M, GC, Gl) -2: 23x17x18, pillow, 4mm glass, 2-6mm vesics (M, GC, Gl) + 1 extra piece like –1
171DS Segment ASC5	-1: 20x15x7, sheet flow, Mn coat, 8mm vesics, many pl to 10mm, some ol, 10mm glass (M, GC, Gl) -2: 15x15x5, sheet flow, as –1 + 1 extra piece
172DS Segment ASC5	-1: 30x20x10, sheet flow, 8mm glass, aphyric, Mn coating (M, GC, Gl) -2: 20x10x10, sheet flow, as –1 with white alteration patches (M, GC, Gl) -3: 10x8x6, sheet flow, fresh, aphyric (M,Gl) + 8 extra pieces
173DSb Segment ASC5	-1: 30x15x15, pillow, aphyric, abundant vesics 1-3mm, 2-4mm glass (M, GC, Gl) -2: 10x5x3, pillow, as –1 with less glass (M, GC, Gl)
174DS Segment ASC5	-1: 15x30x8, sheet flow, aphyric, 30% long vesics to 30mm, 5mm glass (M, GC, Gl) -2: 30x30x15, sheet flow, aphyric, vesics as –1, 10mm glass (M, GC, Gl) -3: 10x10x15, sheet flow, aphyric, 40% stretched vesics up to 10mm, 10mm glass (M, GC, Gl)
175DS Small smt between ASC5 and Grattan	-1: 8x8x8, tube, 5mm glass, 10% vesics 1mm, pl to 1mm (M, GC, Gl) -2: 10x10x10, pillow, 3mm altered glass, >10% vesics 1-2mm, abundant pl <1mm (M, GC, Gl)
176DS Small smt. between ASC5 and Grattan	-1: 25x10x12, pillow, vesic to 4mm, no glass, some FeOx (M, GC) -2: 13x20x10, pillow, altered glass 1-2mm, >10% vesics 5-15mm sed filled (M, Gl) -3: 5x5x5, pillow, much FeOx and Mn, many vesics 2mm (M, GC)

177DS Small smt between ASC5 and Grattan	-1: 13x9x8, vesic-rich (to 4mm) (M, GC) -2: 19x22x15, pillow, FeOx, Mn coating, vesicular (to 8mm) -3: 10x10x10, pillow, 3mm vesics with sediment, FeOx
178DS Small smt between ASC5 and Grattan	-1: 23x20x11, pillow, altered, FeOx -2: 14x11x6, pillow, abundant pl to 5mm, vesics <1mm -3: 9x10x7.5, pillow, FeOx, some Mn, many vesics to 2mm -4: 20x15x3, breccia, sed.-cemented
179DS Grattan Smt	-1: 33x24x14, pillow, 8mm altered glass, Mn + FeOx, 2mm vesics (M, GC, Gl) -2: 30x22x14, pillow, 3mm altered glass, vesics to 6mm some elongated (M, GC,Gl) -3: 22x14x9, pillow, 2mm altered glass, vesics 2-8mm (M, GC,Gl) -4: 12x17x14, pillow, vesicular (M, GC,Gl)
180DS Grattan Smt	-1: 26x18x10, foamy lava, some FeOx, vesics 1-10mm (M, GC) -2: 19x12x12, pillow, altered, FeOx coating -3: 21x16x15, pillow (M, GC)
183DS Smt D	-1: 10x10x5, pillow, abundant vesics to 5mm, Pl to 10mm (M, GC,Gl) -2: 25x18x10, pillow, >10% vesics to 7mm, 10mm glass, <10% Pl to 2mm (M, GC,Gl) -3: 10x15x4, sheet flow, 5mm glass, <10% vesics to 10mm, some Pl to 3mm (M, GC,Gl) -4: 25x10x10, pillow, Pl to 5mm, 20% vesics to 10mm, 2mm glass (M, GC,Gl) -5: 10x10x10, pillow, 10mm glass, 25% vesics to 5mm, rare Pl to 2mm (M, GC,Gl) -6: 20x20x15, pillow, 15% vesics 1-2mm, some Pl 2mm, 5mm glass (M, GC,Gl)
184DS Smt D	-1: 20x20x10, pillow, 10% Pl 15mm, 40% vesics to 5mm, 5mm glass (M, GC, Gl) -2: 20x20x20, 20%Pl 15mm idiomorph, 40%vesics to 5mm, 10mm glass (M, GC, Gl) -3: 10x8x4, sheet flow, 10% Pl to 10mm, 40% vesics, 5mm glass (M, GC, Gl) -4: 20x20x20, pillow, 5% Pl to 10mm, 1% cpx? <1mm, 30% vesics, 5mm glass (M, GC, Gl) -5: 10x10x5, pillow, 30% vesics 1mm, Pl to 2mm, glass 3mm -6: 15x20x15, pillow, Pl <10%, vesics 2-4mm (M, GC, Gl) -7: 10x12x10, pillow, Pl 2-3mm aligned, very vesicular (M,GC) -8: ?x?x?, pillow, vesic 1-2mm, Pl <10%, altered glass 1-3mm (M, GC, Gl)
185DS Smt D	-1: 10x13x7, altered pillow, , vesics 1-2mm, Pl to 3mm (M, GC) -2: 22x12x11, pillow, few Pl 2mm, vesic 1-2mm (M, GC) -3: 13x13x10, pillow, altered, highly vesicular 2-6mm, Pl 1-10mm (M, GC, Gl) -4: 12x9x13, pillow, 20mm glass, Pl 4mm (M, GC) -5: 12x14x9, pillow, vesicular 1-2mm, altered (M, GC)
186DS Smt D	-1: 15x15x10, pillow, 2mm altered glass, vesicular (M, GC, Gl) -2: 11x8x6, pillow, vesicular 1mm, Pl 3mm (M,GC) -3: 50x50x50, pillow, altered, vesicular, some sed. in vesics (M, GC) -4: 13x9x6, pillow, dense, vesicular 1-4mm (M, GC) -5: 14x14x14, pillow, like-1, vesics < 6mm (M) -6: 16x14x14, pillow, like –1 but larger vesics (M) -7: 24x18x5, sheet flow, vesic 1-25mm, Pl to 2mm (M, Gl) -8: 11x12x10, pillow, like –1 but no vesic > 10mm (M)
188DS Segment ASC5	-1: 13x10x7, sheet flow, glass 3-5mm, few vesics, aphyric (M, GC, Gl) -2: 20x20x20, pillow, 5mm glass, aphyric, slightly more altered than –3 (M, GC, Gl) -3: 30x20x20, pillow, fresh glass, 1-2mm vesics (M, GC, Gl)
189DS Segment ASC5	-1: 40x30x35, pillow, some vesics 2-3mm, <5% Pl (M, Gl) -2: 20x20x15, pillow, like –1 with sed. traces (M, Gl)
190DS Segment ASC5	-1: 20x20x14, pillow, 10% vesics 1-3mm, <10% Pl 2mm, 3-5mm glass (M, GC, Gl) -2: 7x7x4, pillow, <10% vesics 2mm, 10% Pl 2mm, 5mm glass, few cpx, FeOx coating (M, Gl) -3: 10x10x10, pillow, vesics 2mm, <10% Pl 4mm, 5mm glass (M, GC, Gl) -4: 30x38x30, <10% vesics 2-4mm, Pl (GC, Gl)
191DS Segment ASC5	-1: 10x10x8, pillow, 2mm glass, Pl 1-6mm (larger rarer), few vesics, thick Mn caoting (M, GC, Gl) -2: 24x19x13, pillow, 30mm glass, few vesics 2-4mm, abundant Pl 1-2mm (M, GC, Gl) -3: 7x4x6, pillow, like –1 with less Mn (M, GC, Gl)
192DS Segment ASC6	Empty, sed. traces on dredge
193DS Segment ASC6	Empty, sed. traces on dredge
194DS Segment ASC6	-1: 5x4x3, glass piece with Mn coating (Gl)
195DS	-1: 10x7x5, pillow, aphyric, 2mm glass (M, GC, Gl) -2: 10x8x6, pillow, 3mm glass, aphyric, some vesics 1mm (M, GC, Gl)

Segment ASC6	+ 2 extra pieces like –1
196DS Segment ASC6	-1: 3x3x3, all glass, Pl 2mm (Gl) -2: 2x3x3, pillow, glass 2mm, <10% vesics von 1mm, 5% Pl 1-2mm (M, Gl) -3: 5x5x5, pillow, 10% vesics 1mm, 10% Pl 5mm, cpx 1-3mm (M, GC, Gl) -4: 15x10x5, sheet flow, glass 3mm, 10% vesics 5mm, few Pl 2-4mm (M, Gl) -5: 10x15x10, pillow, <10% Pl 3mm, few vesics 1mm, 3mm glass (M, Gl)
197DS Segment ASC6	-1: 20x15x10, pillow, 5% vesics 1mm, 5% Pl 1-2mm, 2mm glass (M, GC, Gl) -2: 20x30x10, pillow, 2mm glass, <10% vesics 1mm, rare Pl 1mm (M, GC, Gl) -3: 15x10x10, pillow, <10% vesics 1mm, rare Pl 1mm, glass 1-2mm (M, Gl) -4: 15x20x10, pillow, <5%Pl 1mm, 2-3mm glass (M, Gl) -5: 10x10x3, sheet flow, few Pl to 5mm idiomorph, few vesics 1mm, 5mm glass (M, GC, Gl) -6: 20x10x10, pillow, few Pl to 5mm, few vesics 1mm, 10mm glass (M, Gl) -7: 10x8x5, pillow, few Pl 3mm, nonvesic., 10mm glass (M, Gl)
198DSb	-1: 11x5x1, pillow glass rim, Pl 3mm (Gl) -2: 7x6x12, pillow glass rim, Pl 5mm (Gl) -3: 8x4x3, pillow, 10-20mm glass, Pl 5mm, vesics 1mm (Gl) -4: 4x4x4, no glass, Pl to 7mm (GC) -5: 6x5x4, like –2 but less altered (Gl)
199DS Segment ASC6	-1: 16x12x10, pillow, Pl 2-5mm, 1-2mm glass, Mn coating (Gl) -2: 20x15x12, pillow, like –1 but more Mn (2-3mm) (Gl) -3: 7x3x3, glass fragment, abundant Pl 3-5mm
200DS Segment ASC6	-1: 7x7x5, pillow, some Pl 3-5mm, vesics 1-2mm, 3-5mm glass (Gl) -2: 8x7x5, pillow, as –1 but less Pl and vesics rare (Gl) -3: 8x7x5, pillow, less Pl than –1, some Mn coatin, 3-5mm glass altered (Gl) + 6 extra pieces in one bag
201DS Segment ASC6	-1: 20x15x10, pillow, 5mm glass, 10% Pl -2: 20x15x15, pillow, 5mm glass, few vesics 1mm, some Pl 1-2mm (Gl) -3: 10x10x5, pillow, Mn coating, <10% vesics 1mm, <10% Pl 1mm -4:15x10x10, pillow, few Pl to 5mm 3mm glass, 10% vesics 1mm -5: 10x5x5, 10% Pl 2mm, 2mm glass, some cpx, vesics 1mm (Gl) -6: 5x3x3, no glass
202DS Segment ASC6	-1: 19x8x7, 3mm glass, 2mm Plag, 5mm Ol (Gl) -2: 12x11x6, pillow, 2mm glass, Pl 10mm, Ol 2mm (Gl) -3: 14x15x8, pillow, 4mm glass (Gl) -4: 30x30x30, pillow, 6mm glass, Pl 4mm, no Ol (Gl)
203DS Segment ASC6	-1: 14x16x12, pillow, 2mm glass, Pl to 4mm (Gl) -2: 14x14x3, sheet flow, vesics 2mm, rare Pl 6mm (Gl) -3: 8x6x6x, pillow, Pl to8mm, Mn coating (Gl)

Table A 3a: Microprobe analyses (in wt. %) of feldspar crystals, feldspar cores

Sample	119-1 plag 1	119-1 plag 2	119-1 plag 3	119-1 plag 4	122-1plag 1
Size	s. plag.	s. plag.	l. plag.	s. plag.	l. plag.
NaO	3.26	1.89	1.70	3.33	1.60
MgO	0.29	0.21	0.22	0.29	0.17
Al2O3	30.58	33.16	33.38	30.57	33.61
SiO2	51.46	47.80	47.29	51.62	47.40
K2O	0.02	0.02	0.02	0.04	0.01
CaO	14.48	17.06	17.41	14.42	17.77
TiO2	0.06	0.02	0.02	0.04	0.03
Cr2O3	0.00	0.01	0.01	0.02	0.02
MnO	0.04	0.01	0.00	0.01	0.01
FeOT	0.48	0.29	0.33	0.45	0.40
Total	100.67	100.46	100.38	100.79	101.02
An	69.92	82.34	83.91	69.37	85.17
Ab	28.89	16.66	15.02	29.41	14.00
Or	0.13	0.10	0.10	0.20	0.06

Sample	122-1plag 2	122-1plag 2	139-2 plag 1	139-2 plag 2	139-2 plag 3
Size	l. plag.	l. plag.	l. plag.	l. plag.	l. plag.
NaO	2.19	2.20	1.70	1.89	1.03
MgO	0.20	0.21	0.24	0.28	0.18
Al2O3	32.29	32.37	33.32	32.86	34.65
SiO2	48.36	48.54	47.72	48.08	45.64
K2O	0.03	0.01	0.01	0.01	0.01
CaO	16.85	16.83	17.64	17.25	18.68
TiO2	0.04	0.02	0.03	0.03	0.01
Cr2O3	0.03	0.00	0.03	0.00	0.00
MnO	0.00	0.01	0.02	0.00	0.03
FeOT	0.37	0.38	0.33	0.37	0.27
Total	100.36	100.57	101.04	100.77	100.49
An	80.06	79.93	84.02	82.16	90.02
Ab	19.01	19.12	14.86	16.53	9.06
Or	0.17	0.06	0.03	0.04	0.05

Table A 3a: (continued) Microprobe analyses (in wt. %) of feldspar crystals, feldspar cores

Sample	149-1plag 2	156-3 plag 1	156-3 plag 2	156-3 plag 3	156-3 plag 4
Size	l. plag.	l. plag.	s. plag.	s. plag.	l. plag.
NaO	1.21	2.05	1.75	1.79	2.06
MgO	0.22	0.23	0.23	0.24	0.22
Al2O3	33.52	32.59	33.18	33.03	32.89
SiO2	46.40	48.37	47.56	48.10	48.76
K2O	0.01	0.02	0.01	0.01	0.02
CaO	18.40	16.81	17.35	17.07	16.71
TiO2	0.01	0.03	0.04	0.01	0.03
Cr2O3	0.00	0.01	0.01	0.00	0.01
MnO	0.01	0.00	0.02	0.01	0.00
FeOT	0.32	0.38	0.46	0.43	0.44
Total	100.12	100.49	100.60	100.70	101.15
An	88.26	80.85	83.45	82.91	80.71
Ab	10.62	18.06	15.45	15.94	18.25
Or	0.06	0.09	0.04	0.06	0.10

Sample	160-1plag 1	160-1plag	160-1plag 4	160-1plag 5	166-1 plag 1
Size	l. plag.	s. plag.	l. plag.	l. plag.	l. plag.
NaO	2.81	2.26	2.14	1.47	3.10
MgO	0.25	0.22	0.22	0.19	0.23
Al2O3	31.42	32.22	32.65	33.61	30.51
SiO2	50.80	49.29	48.94	47.50	50.33
K2O	0.03	0.03	0.02	0.03	0.05
CaO	15.48	16.35	16.70	17.99	14.43
TiO2	0.04	0.01	0.06	0.04	0.03
Cr2O3	0.00	0.00	0.00	0.04	0.06
MnO	0.01	0.00	0.00	0.03	0.00
FeOT	0.39	0.37	0.35	0.37	0.51
Total	101.22	100.74	101.07	101.26	99.24
An	74.22	78.99	80.21	86.19	71.07
Ab	24.66	19.97	18.78	12.87	27.90
Or	0.18	0.16	0.11	0.14	0.31

Table A 3a: (continued) Microprobe analyses (in wt. %) of feldspar crystals, feldspar cores

Sample	**166-1 plag 2**	**169-1plag3**	**169-1plag1**	**169-1plag2**	**171-2plag 1**
Size	s. plag.	s. plag.	s. plag.	s. plag.	l. plag.
NaO	3.15	3.40	3.27	3.26	1.65
MgO	0.25	0.26	0.24	0.22	0.19
Al2O3	30.59	30.25	30.16	30.34	32.92
SiO2	50.38	51.93	51.28	51.56	47.27
K2O	0.06	0.06	0.06	0.06	0.03
CaO	14.60	14.30	14.43	14.44	17.43
TiO2	0.05	0.06	0.07	0.05	0.02
Cr2O3	0.01	0.00	0.01	0.00	0.01
MnO	0.04	0.05	0.10	0.04	0.00
FeOT	0.52	0.59	0.71	0.61	0.47
Total	99.64	100.90	100.34	100.60	100.00
An	70.93	68.90	69.92	70.09	84.47
Ab	27.96	29.98	29.01	28.92	14.59
Or	0.35	0.34	0.33	0.35	0.20

Sample	**171-2plag2**	**176 DS-7 plag 3**	**176-7 plag 2**	**179-4 plag 1**	**179-4 plag 1**
Size	l. plag.	l. plag.	l. plag.	l. plag.	l. plag.
NaO	2.78	1.52	2.17	2.30	2.38
MgO	0.22	0.15	0.21	0.15	0.17
Al2O3	31.01	33.70	32.68	31.41	30.87
SiO2	50.32	47.36	48.91	48.10	48.06
K2O	0.06	0.02	0.03	0.06	0.08
CaO	15.40	17.56	16.55	16.25	16.07
TiO2	0.06	0.01	0.05	0.06	0.06
Cr2O3	0.04	0.01	0.03	0.00	0.00
MnO	0.01	0.01	0.00	0.00	0.00
FeOT	0.54	0.38	0.41	0.51	0.40
Total	100.46	100.74	101.05	98.83	98.09
An	74.43	85.70	79.87	78.95	78.11
Ab	24.53	13.54	19.16	20.30	21.05
Or	0.36	0.13	0.19	0.37	0.44

Table A 3a: (continued) Microprobe analyses (in wt. %) of feldspar crystals, feldspar cores

Sample	**190-1plag 1**	**190-1plag**	**190-1plag**	**191-1 plag 1**	**191-1 plag 1**
Size	s. plag.	l. plag.	s. plag.	l. plag.	l. plag.
NaO	4.06	1.80	3.65	4.46	4.52
MgO	0.23	0.20	0.18	0.17	0.16
Al2O3	28.88	32.92	29.61	29.21	29.30
SiO2	53.46	47.98	52.26	55.02	55.37
K2O	0.12	0.04	0.08	0.11	0.13
CaO	12.74	17.30	13.42	12.95	12.69
TiO2	0.11	0.02	0.08	0.09	0.08
Cr2O3	0.00	0.02	0.00	0.03	0.00
MnO	0.01	0.02	0.03	0.03	0.00
FeOT	0.70	0.40	0.68	0.65	0.63
Total	100.31	100.69	99.99	102.73	102.89
An	62.60	83.21	66.33	61.01	60.27
Ab	36.31	15.81	32.80	38.17	38.91
Or	0.71	0.20	0.49	0.60	0.73

Sample	**191-1 plag 1**	**191-1 plag 2**	**191-1 plag 5**
Size	l. plag.	l. plag.	l. plag.
NaO	4.42	4.17	3.54
MgO	0.19	0.19	0.18
Al2O3	29.13	29.25	30.42
SiO2	54.68	53.81	52.36
K2O	0.14	0.12	0.08
CaO	13.06	13.41	14.41
TiO2	0.11	0.12	0.04
Cr2O3	0.04	0.01	0.00
MnO	0.00	0.01	0.03
FeOT	0.56	0.80	0.57
Total	102.33	101.90	101.63
An	61.36	63.30	68.52
Ab	37.71	35.79	30.66
Or	0.77	0.66	0.44

Table A 3b: Microprobe analyses (in wt. %) of feldspar crystals, feldspar rims

Sample	119-1 plag 1	119-1 plag 1	119-1 plag 2	119-1 plag 2	119-1 plag 3
Size	s. plag.	s. plag.	s. plag.	s. plag.	l. plag.
NaO	3.08	3.17	2.05	2.07	1.72
MgO	0.29	0.28	0.22	0.22	0.20
Al_2O_3	30.70	30.75	32.91	32.78	33.31
SiO_2	51.15	51.27	48.35	48.45	47.39
K_2O	0.03	0.02	0.01	0.01	0.03
CaO	14.81	14.84	16.88	16.82	17.47
TiO_2	0.02	0.04	0.03	0.01	0.02
Cr_2O_3	0.00	0.01	0.01	0.01	0.01
MnO	0.00	0.00	0.00	0.03	0.00
FeOT	0.42	0.46	0.42	0.36	0.41
Total	100.52	100.82	100.90	100.78	100.57
An	71.47	71.00	80.97	80.75	83.92
Ab	27.30	27.84	18.02	18.23	15.11
Or	0.17	0.12	0.08	0.07	0.19

Sample	119-1 plag 3	119-1 plag 4	119-1 plag 4	122-1plag 1	122-1plag 1
Size	l. plag.	s. plag.	s. plag.	l. plag.	l. plag.
NaO	1.81	3.06	3.12	1.71	1.72
MgO	0.21	0.28	0.27	0.21	0.19
Al_2O_3	33.30	30.93	30.90	33.52	33.24
SiO_2	47.56	50.98	50.88	47.84	47.70
K_2O	0.01	0.03	0.02	0.01	0.02
CaO	17.39	14.80	14.90	17.50	17.58
TiO_2	0.03	0.05	0.05	0.03	0.02
Cr_2O_3	0.01	0.01	0.00	0.02	0.02
MnO	0.01	0.04	0.01	0.02	0.04
FeOT	0.36	0.51	0.48	0.41	0.40
Total	100.69	100.68	100.63	101.27	100.93
An	83.16	71.65	71.44	83.97	84.06
Ab	15.83	27.17	27.45	15.02	15.03
Or	0.03	0.14	0.09	0.06	0.11

Table A 3b: (continued) Microprobe analyses (in wt. %) of feldspar crystals, feldspar rims

Sample	122-1plag 2	122-1plag 2	139-2 plag 1	139-2 plag 1	139-2 plag 2
Size	l. plag.	l. plag.	l. plag.	l. plag.	l. plag.
NaO	2.14	1.66	1.52	1.65	1.99
MgO	0.22	0.17	0.17	0.24	0.23
Al_2O_3	32.65	33.36	33.66	33.45	32.73
SiO_2	48.48	47.34	46.97	47.53	48.28
K_2O	0.02	0.02	0.00	0.01	0.01
CaO	16.80	17.66	17.48	17.71	16.90
TiO_2	0.01	0.03	0.03	0.02	0.02
Cr_2O_3	0.00	0.01	0.00	0.01	0.02
MnO	0.03	0.02	0.01	0.02	0.01
FeOT	0.40	0.43	0.44	0.42	0.45
Total	100.75	100.70	100.27	101.07	100.64
An	80.27	84.65	85.59	84.43	81.33
Ab	18.71	14.52	13.57	14.43	17.59
Or	0.11	0.11	0.01	0.07	0.04

Sample	139-2 plag 2	139-2 plag 3	139-2 plag 3	149-1plag 2	156-3 plag 1
Size	l. plag.	l. plag.	l. plag.	l. plag.	l. plag.
NaO	1.45	1.41	1.35	2.07	1.67
MgO	0.20	0.20	0.19	0.30	0.20
Al_2O_3	33.66	33.72	33.73	32.06	33.33
SiO_2	46.95	46.81	46.15	48.27	47.39
K_2O	0.01	0.01	0.01	0.01	0.01
CaO	18.02	17.95	18.18	16.51	17.56
TiO_2	0.01	0.03	0.01	0.05	0.01
Cr_2O_3	0.00	0.04	0.01	0.00	0.04
MnO	0.03	0.00	0.01	0.00	0.00
FeOT	0.49	0.42	0.44	0.56	0.46
Total	100.82	100.61	100.10	99.84	100.68
An	86.30	86.54	87.17	80.08	84.35
Ab	12.73	12.45	11.86	18.50	14.68
Or	0.05	0.07	0.07	0.08	0.04

Table A 3b: (continued) Microprobe analyses (in wt. %) of feldspar crystals, feldspar rims

Sample	**156-3 plag 2**	**156-3 plag 3**	**156-3 plag 4**	**160-1plag 1**	**160-1plag 2**
Size	s. plag.	s. plag.	l. plag.	l. plag.	s. plag.
NaO	1.61	1.64	1.68	2.90	2.50
MgO	0.23	0.21	0.17	0.25	0.23
Al_2O_3	33.38	33.55	33.60	31.17	31.89
SiO_2	47.45	47.51	47.93	51.00	49.94
K_2O	0.02	0.01	0.01	0.02	0.02
CaO	17.65	17.67	17.24	15.09	15.80
TiO_2	0.03	0.01	0.01	0.05	0.03
Cr_2O_3	0.00	0.01	0.01	0.01	0.01
MnO	0.01	0.03	0.01	0.00	0.02
FeOT	0.47	0.44	0.43	0.43	0.41
Total	100.84	101.07	101.11	100.92	100.85
An	84.78	84.60	84.15	73.15	76.74
Ab	14.12	14.37	15.00	25.78	22.23
Or	0.10	0.05	0.04	0.13	0.13

Sample	**160-1plag 4**	**160-1plag 5**	**166-1 plag 1**	**166-1 plag 2**	**166-1 plag 2**
Size	l. plag.	l. plag.	l. plag.	l. plag.	s. plag.
NaO	2.33	2.28	3.03	2.27	3.42
MgO	0.22	0.22	0.21	0.20	0.25
Al_2O_3	32.19	32.38	30.89	32.36	30.25
SiO_2	49.28	49.44	50.85	48.18	50.91
K_2O	0.03	0.01	0.06	0.04	0.07
CaO	16.25	16.34	14.93	16.22	14.17
TiO_2	0.04	0.03	0.05	0.06	0.07
Cr_2O_3	0.03	0.00	0.00	0.04	0.03
MnO	0.01	0.01	0.00	0.02	0.00
FeOT	0.44	0.38	0.65	0.51	0.63
Total	100.83	101.10	100.67	99.90	99.79
An	78.43	78.84	72.26	78.91	68.62
Ab	20.56	20.17	26.80	20.14	30.26
Or	0.18	0.08	0.31	0.22	0.38

Table A 3b: (continued) Microprobe analyses (in wt. %) of feldspar crystals, feldspar rims

Sample	169 DS-1plg3	169 DS-1plg3	169-1plg1	169-1plg1	169-1plg1
Size	s. plag.	s. plag.	s. plag.	s. plag.	s. plag.
NaO	3.32	3.39	3.25	3.32	3.32
MgO	0.26	0.28	0.24	0.26	0.26
Al_2O_3	30.24	30.34	30.37	30.28	30.28
SiO_2	51.52	51.88	51.42	51.79	51.79
K_2O	0.05	0.04	0.02	0.03	0.03
CaO	14.38	14.10	14.56	14.38	14.38
TiO_2	0.05	0.03	0.07	0.08	0.08
Cr_2O_3	0.00	0.00	0.00	0.02	0.02
MnO	0.00	0.06	0.01	0.12	0.12
FeOT	0.57	0.77	0.55	0.63	0.63
Total	100.39	100.89	100.49	100.93	100.93
An	69.48	68.62	70.25	69.49	69.49
Ab	29.42	30.22	28.74	29.40	29.40
Or	0.29	0.24	0.11	0.19	0.19

Sample	169-1plg2	169-1plg2	171-2plag 1	171-2plag 1	171-2plg2
Size	s. plag.	s. plag.	l. plag.	l. plag.	l. plag.
NaO	3.03	3.36	2.71	1.67	2.32
MgO	0.28	0.26	0.20	0.17	0.19
Al_2O_3	30.58	30.31	31.11	33.02	32.28
SiO_2	51.33	51.54	50.09	47.43	48.97
K_2O	0.04	0.05	0.08	0.05	0.06
CaO	14.85	14.60	15.56	17.46	16.31
TiO_2	0.07	0.10	0.06	0.02	0.06
Cr_2O_3	0.06	0.05	0.00	0.01	0.03
MnO	0.02	0.00	0.00	0.01	0.01
FeOT	0.70	0.70	0.61	0.51	0.48
Total	100.96	100.97	100.42	100.35	100.70
An	71.89	69.59	75.14	84.45	78.69
Ab	26.88	29.29	23.87	14.69	20.39
Or	0.22	0.27	0.47	0.26	0.34

Table A 3b: (continued) Microprobe analyses (in wt. %) of feldspar crystals, feldspar rims

Sample	171-2plg2	190-1plag 1	190-1plag 2	190-1plag 3	191-1 plag 1
Size	l. plag.	s. plag.	l. plag.	s. plag.	l. plag.
NaO	2.23	3.76	1.67	4.00	4.43
MgO	0.19	0.18	0.18	0.19	0.16
Al_2O_3	31.71	29.60	33.16	28.97	29.11
SiO_2	48.21	52.96	47.31	53.10	54.30
K_2O	0.06	0.10	0.03	0.10	0.12
CaO	16.51	13.41	17.48	12.82	12.86
TiO_2	0.04	0.11	0.05	0.11	0.08
Cr_2O_3	0.04	0.00	0.02	0.01	0.00
MnO	0.03	0.00	0.01	0.00	0.24
FeOT	0.51	0.75	0.46	0.87	0.66
Total	99.53	100.87	100.36	100.17	101.96
An	79.48	65.65	84.42	63.24	61.01
Ab	19.60	33.47	14.69	35.85	38.18
Or	0.35	0.55	0.18	0.60	0.65

Sample	191-1 plag 1	191-1 plag 2	191-1 plag 5	176-7 plag 2	176-7 plag 3
Size	l. plag.	l. plag.	l. plag.	l. plag.	l. plag.
NaO	4.44	4.29	4.19	1.94	2.04
MgO	0.16	0.20	0.17	0.20	0.17
Al_2O_3	29.00	29.20	29.60	32.82	32.78
SiO_2	54.82	54.03	53.93	48.32	48.47
K_2O	0.14	0.12	0.10	0.03	0.02
CaO	13.00	13.14	13.31	16.69	16.71
TiO_2	0.04	0.06	0.06	0.06	0.05
Cr_2O_3	0.00	0.00	0.02	0.00	0.01
MnO	0.00	0.04	0.00	0.01	0.02
FeOT	0.65	0.73	0.78	0.45	0.44
Total	102.27	101.80	102.16	100.53	100.73
An	61.28	62.19	63.09	81.66	81.06
Ab	37.88	36.88	36.11	17.35	18.10
Or	0.77	0.67	0.55	0.19	0.14

Table A 3b: (continued) Microprobe analyses (in wt. %) of feldspar crystals, feldspar rims

Sample	**179-4 plag 1**
Size	l. plag.
NaO	2.17
MgO	0.15
Al_2O_3	31.80
SiO_2	47.75
K_2O	0.04
CaO	16.57
TiO_2	0.05
Cr_2O_3	0.00
MnO	0.01
FeOT	0.51
Total	99.05
An	80.17
Ab	19.11
Or	0.22

Table A 4a: Microprobe analyses (in wt. %) of olivine crystals, olivine rims

Sample	**122-1 3ol1**	**122-1 5ol-1**	**122-1 5ol-3**	**122-1 7ol-1**	**122-1 7ol-3**	**122-1 ol3**	**122-1 ol3**
Size	large ol	large ol	large ol	large ol	large ol	small ol	small ol
Latitude	6.66	6.66	6.66	6.66	6.66	6.66	6.66
NaO	0.01	0.02	0.01	0.03	0.03	0.02	0.01
MgO	45.02	46.23	45.42	45.45	46.06	44.95	45.21
Al_2O_3	0.06	0.04	0.04	0.05	0.05	0.05	0.05
SiO_2	40.35	40.46	40.41	40.27	40.57	40.10	40.32
K_2O	0.00	0.01	0.01	0.01	0.00	0.01	0.00
CaO	0.31	0.32	0.30	0.32	0.30	0.33	0.31
TiO_2	0.02	0.00	0.02	0.00	0.02	0.01	0.00
Cr_2O_3	0.05	0.06	0.05	0.05	0.05	0.05	0.04
MnO	0.20	0.20	0.22	0.16	0.19	0.26	0.24
FeOT	14.55	13.21	13.89	14.01	13.22	14.96	14.78
Total	100.57	100.55	100.37	100.35	100.49	100.74	100.96
Fo	84.65	86.19	85.36	85.26	86.13	84.27	84.50
Fay	15.35	13.81	14.64	14.74	13.87	15.73	15.50

Table A 4a: (continued) Microprobe analyses (in wt. %) of olivine crystals, olivine rims

Sample	**122-1 ol4**	**139-2 ol 1**	**139-2 ol 1**	**139-2 ol 2**	**139-2ol 3**	**149-1ol3**	**156-3 ol1**
Size	small ol	large ol	large ol	large ol	small ol	large ol	small ol
Latitude	6.66	7.92	7.92	7.92	7.92	8.37	8.75
NaO	0.02	0.02	0.01	0.01	0.02	0.02	0.01
MgO	44.36	49.80	49.62	47.17	44.44	44.68	46.36
Al_2O_3	0.08	0.04	0.06	0.05	0.04	0.04	0.06
SiO_2	39.98	41.51	41.52	40.81	39.99	40.61	40.73
K_2O	0.02	0.00	0.00	0.00	0.00	0.00	0.01
CaO	0.32	0.32	0.31	0.33	0.33	0.34	0.30
TiO_2	0.03	0.01	0.00	0.02	0.01	0.01	0.03
Cr_2O_3	0.04	0.09	0.05	0.05	0.05	0.05	0.04
MnO	0.24	0.15	0.15	0.17	0.19	0.20	0.20
FeOT	14.57	9.41	9.52	11.98	14.61	14.49	14.00
Total	99.65	101.34	101.22	100.59	99.68	100.45	101.74
Fo	84.45	90.42	90.29	87.53	84.43	84.61	85.52
Fay	15.55	9.58	9.71	12.47	15.57	15.39	14.48

Sample	**156-3 ol2**	**156-3 ol3**	**160-1ol2**	**169-1 ol1**	**169-1 ol1**	**169-1 ol2**	**171-2ol2**
Size	large ol	large ol	small ol	large ol	large ol	small ol	small ol
Latitude	8.75	8.75	8.97	9.34	9.34	9.34	9.48
NaO	0.02	0.00	0.01	0.03	0.02	0.02	0.04
MgO	46.38	46.34	44.50	45.21	44.59	43.72	43.87
Al_2O_3	0.05	0.05	0.03	0.04	0.03	0.04	0.04
SiO_2	40.74	40.92	40.33	40.28	39.82	39.26	40.15
K_2O	0.00	0.03	0.00	0.01	0.01	0.00	0.01
CaO	0.29	0.31	0.24	0.31	0.33	0.31	0.34
TiO_2	0.01	0.01	0.01	0.01	0.02	0.01	0.02
Cr_2O_3	0.05	0.04	0.05	0.04	0.01	0.02	0.03
MnO	0.19	0.27	0.20	0.23	0.24	0.25	0.24
FeOT	13.48	13.74	15.93	15.79	15.50	16.61	15.51
Total	101.21	101.71	101.32	101.94	100.58	100.24	100.25
Fo	85.98	85.74	83.28	83.62	83.68	82.43	83.45
Fay	14.02	14.26	16.72	16.38	16.32	17.57	16.55

Table A 4a: (continued) Microprobe analyses (in wt. %) of olivine crystals, olivine rims

Sample	171-2ol3	184-1 ol1	184-1 ol2	184-1 ol3	184-1 ol4	184-1 ol5	186-2 ol1
Size	small ol	small ol	small ol	small ol	small ol	small ol	large ol
Latitude	9.48	9.73	9.73	9.73	9.73	9.73	9.77
NaO	0.05	0.01	0.00	0.02	0.01	0.01	0.01
MgO	44.22	39.56	39.68	39.46	38.90	39.17	39.25
Al_2O_3	0.02	0.04	0.04	0.02	0.04	0.05	0.03
SiO_2	40.08	39.15	39.14	39.12	39.02	39.21	38.85
K_2O	0.02	0.01	0.00	0.00	0.00	0.01	0.00
CaO	0.35	0.23	0.23	0.24	0.22	0.23	0.23
TiO_2	0.02	0.03	0.05	0.06	0.00	0.04	0.04
Cr_2O_3	0.08	0.03	0.00	0.02	0.02	0.04	0.02
MnO	0.19	0.33	0.34	0.30	0.26	0.34	0.28
FeOT	15.05	21.86	22.02	21.82	21.33	21.57	20.69
Total	100.08	101.25	101.50	101.05	99.81	100.68	99.41
Fo	83.97	76.34	76.26	76.33	76.48	76.40	77.18
Fay	16.03	23.66	23.74	23.67	23.52	23.60	22.82

Table A 4b: Microprobe analyses (in wt. %) of olivine crystals, olivine cores

Sample	122-1 3ol-2	122-1 3ol-3	122-1 5ol-2	122-1 7ol-2	122-1 ol3	122-1 ol4	139-2 ol 1
Size	large ol	large ol	large ol	large ol	large ol	large ol	large ol
Latitude	6.66	6.66	6.66	6.66	6.66	6.66	7.92
NaO	0.02	0.02	0.03	0.02	0.01	0.02	0.02
MgO	45.27	45.02	45.50	47.22	45.12	44.85	49.06
Al_2O_3	0.05	0.04	0.13	0.05	0.06	0.04	0.04
SiO_2	40.38	40.46	40.46	40.82	40.32	40.16	41.45
K_2O	0.01	0.01	0.01	0.00	0.01	0.01	0.01
CaO	0.26	0.30	0.31	0.30	0.31	0.32	0.32
TiO_2	0.02	0.01	0.01	0.03	0.02	0.02	0.00
Cr_2O_3	0.07	0.05	0.02	0.04	0.06	0.05	0.07
MnO	0.23	0.21	0.22	0.18	0.24	0.26	0.16
FeOT	14.45	14.89	14.12	12.11	14.74	15.04	9.96
Total	100.76	101.01	100.81	100.77	100.89	100.76	101.10
Fo	84.82	84.35	85.17	87.42	84.51	84.17	89.77
Fay	15.18	15.65	14.83	12.58	15.49	15.83	10.23

Table A 4b: (continued) Microprobe analyses (in wt. %) of olivine crystals, olivine cores

Sample	**139-2 ol 2**	**139-2ol 3**	**149-1ol3**	**156-3 ol1**	**156-3 ol2**	**156-3 ol3**	**160-1ol2**
Size	large ol	small ol	large ol	large ol	large ol	large ol	small ol
Latitude	7.92	7.92	8.37	8.75	8.75	8.75	8.97
NaO	0.02	0.03	0.00	0.01	0.02	0.01	0.00
MgO	46.41	45.05	46.32	46.33	46.42	46.66	45.61
Al_2O_3	0.06	0.04	0.07	0.06	0.07	0.04	0.07
SiO_2	40.79	40.42	41.03	40.32	40.78	40.88	40.79
K_2O	0.01	0.00	0.01	0.00	0.00	0.00	0.01
CaO	0.32	0.29	0.32	0.30	0.29	0.30	0.23
TiO_2	0.02	0.00	0.01	0.00	0.02	0.01	0.01
Cr_2O_3	0.07	0.03	0.06	0.07	0.04	0.06	0.03
MnO	0.17	0.20	0.19	0.24	0.20	0.18	0.21
FeOT	13.11	14.34	12.42	14.13	13.78	13.74	14.59
Total	100.99	100.38	100.42	101.46	101.62	101.87	101.56
Fo	86.32	84.85	86.93	85.39	85.72	85.83	84.79
Fay	13.68	15.15	13.07	14.61	14.28	14.17	15.21

Sample	**169-1 ol1**	**169-1 ol1**	**169-1 ol2**	**171-2ol2**	**171-2ol3**	**184-1 ol1**	**184-1 ol2**
Size	large ol	large ol	small ol	small ol	small ol	small ol	small ol
Latitude	9.34	9.34	9.34	9.48	9.48	9.73	9.73
NaO	0.00	0.01	0.01	0.02	0.02	0.01	0.01
MgO	47.61	47.76	43.69	44.92	45.04	39.80	39.67
Al_2O_3	0.06	0.03	0.03	0.05	0.04	0.06	0.04
SiO_2	40.94	40.37	39.18	40.53	40.38	39.42	39.42
K_2O	0.00	0.00	0.00	0.01	0.00	0.02	0.01
CaO	0.30	0.31	0.28	0.33	0.31	0.22	0.21
TiO_2	0.02	0.00	0.03	0.01	0.02	0.03	0.05
Cr_2O_3	0.02	0.04	0.04	0.06	0.07	0.00	0.02
MnO	0.22	0.18	0.26	0.25	0.26	0.28	0.23
FeOT	12.55	11.63	16.24	14.66	14.59	21.92	22.11
Total	101.71	100.33	99.76	100.84	100.72	101.75	101.77
Fo	87.12	87.99	82.74	84.53	84.62	76.40	76.18
Fay	12.88	12.01	17.26	15.47	15.38	23.60	23.82

Table A 4b: Microprobe analyses (in wt. %) of olivine crystals, olivine cores

Sample	**184-1 ol3**	**184-1 ol4**	**184-1 ol5**	**186-2 ol1**
Size	small ol	small ol	small ol	large ol
Latitude	9.73	9.73	9.73	9.77
NaO	0.01	0.01	0.00	0.01
MgO	38.92	38.97	39.23	39.16
Al_2O_3	0.05	0.04	0.04	0.04
SiO_2	39.17	39.33	39.08	39.12
K_2O	0.00	0.00	0.01	0.00
CaO	0.25	0.23	0.23	0.24
TiO_2	0.03	0.03	0.03	0.05
Cr_2O_3	0.00	0.00	0.15	0.01
MnO	0.36	0.37	0.24	0.27
FeOT	21.50	21.49	21.51	21.16
Total	100.28	100.47	100.51	100.06
Fo	76.34	76.38	76.47	76.74
Fay	23.66	23.62	23.53	23.26

Table A 5: Microprobe analyses (in wt. %) of clinopyroxene crystals

Sample	**149-1cpx1**	**149-1cpx1**	**149-1cpx2**	**149-1cpx2**	**188-1 cpx1**	**149-1cpx1**
coment	large cpx, core	large cpx, rim	large cpx, core	large cpx, rim	large cpx, core	large cpx, rim
NaO	0.22	0.23	0.21	0.28	0.26	0.18
MgO	18.03	17.55	19.01	17.14	16.30	18.68
Al_2O_3	2.34	3.04	1.98	3.59	2.93	2.02
SiO_2	53.72	53.16	54.18	52.54	51.84	53.86
K_2O	0.00	0.01	0.01	0.00	0.00	0.01
CaO	20.89	20.74	19.09	20.59	21.96	19.36
TiO_2	0.26	0.34	0.23	0.44	0.73	0.32
Cr_2O_3	0.83	0.90	0.67	0.95	0.32	0.67
MnO	0.16	0.15	0.16	0.13	0.14	0.17
FeOT	4.62	4.82	5.15	5.15	5.33	5.52
Total	101.08	100.94	100.69	100.81	99.81	100.78
En	51	50	53	49	46	52
Wo	42	42	39	42	45	39
Fs	7	8	8	8	9	9

Table A 5: (continued) Microprobe analyses (in wt. %) of clinopyroxene crystals

Sample	**149-1cpx2**	**171-2cpx8**	**171-2cpx7**	**171-2cpx1**	**171-2cpx1**	**173-1cpx2**
coment	large cpx, rim	small cpx	small cpx	small cpx, rim	small cpx, rim	large cpx
NaO	0.21	0.31	0.31	0.28	0.26	0.21
MgO	17.73	15.27	15.36	16.66	16.53	17.84
Al_2O_3	2.96	5.04	4.88	3.27	2.97	1.77
SiO_2	53.34	49.26	50.09	51.79	51.80	53.36
K_2O	0.02	0.01	0.00	0.01	0.00	0.00
CaO	19.32	20.99	21.15	20.79	20.75	19.28
TiO_2	0.37	1.45	1.62	1.00	1.12	0.74
Cr_2O_3	0.49	1.10	0.34	0.45	0.31	0.13
MnO	0.14	0.10	0.18	0.17	0.19	0.18
FeOT	5.58	6.21	6.78	7.09	7.33	7.57
Total	100.16	99.75	100.73	101.50	101.27	101.07
En	51	45	45	47	46	50
Wo	40	45	44	42	42	39
Fs	9	10	11	11	12	12

Sample	**166-1 cpx2**	**190-1cpx1**	**173-1cpx7**	**171-2cpx8**	**190-1cpx2**	**166-1 cpx2**
coment	large cpx, core	small cpx, rim	large cpx	small cpx	large cpx, rim	large cpx, core
NaO	0.27	0.28	0.29	0.32	0.27	0.27
MgO	15.20	16.14	16.04	14.79	16.16	15.03
Al_2O_3	4.06	3.09	3.75	5.29	3.08	4.80
SiO_2	49.92	51.80	51.08	49.17	51.48	50.29
K_2O	0.02	0.00	0.01	0.00	0.01	0.01
CaO	19.80	21.11	20.35	21.40	20.72	20.26
TiO_2	0.96	1.11	1.24	1.90	1.13	1.54
Cr_2O_3	0.30	0.12	0.49	0.28	0.12	0.36
MnO	0.18	0.17	0.19	0.16	0.16	0.18
FeOT	7.05	7.52	7.48	7.41	7.67	7.47
Total	97.76	101.34	100.91	100.74	100.81	100.20
En	46	45	46	43	46	44
Wo	43	43	42	45	42	43
Fs	12	12	12	12	12	12

Table A 5: (continued) Microprobe analyses (in wt. %) of clinopyroxene crystals

Sample	**190-1cpx2**	**166-1 cpx1**	**190-1cpx2**	**173-1cpx2**	**191-1 cpx1**	**171-2cpx1**
coment	large cpx, core	small cpx, core	large cpx, core	large cpx	large cpx, core	small cpx, core
NaO	0.30	0.26	0.29	0.33	0.34	0.34
MgO	15.68	15.33	15.99	16.77	15.27	14.87
Al_2O_3	3.57	4.81	4.30	4.26	3.83	4.46
SiO_2	50.96	48.95	49.93	51.05	52.17	49.71
K_2O	0.01	0.01	0.00	0.01	0.00	0.01
CaO	20.91	18.89	19.86	18.78	21.08	20.89
TiO_2	1.38	1.36	1.61	1.25	1.30	1.81
Cr_2O_3	0.18	0.49	0.10	0.33	0.07	0.13
MnO	0.19	0.16	0.19	0.20	0.24	0.17
FeOT	7.75	7.53	8.11	8.41	8.56	8.57
Total	100.93	97.78	100.39	101.38	102.86	100.95
En	45	46	46	48	43	43
Wo	43	41	41	39	43	43
Fs	12	13	13	13	14	14

Sample	**190-1cpx1**	**190-1cpx1**	**191-1 cpx1**
coment	small cpx, core	small cpx, core	large cpx, rim
NaO	0.21	0.19	0.31
MgO	18.22	18.41	15.45
Al_2O_3	1.87	1.87	4.00
SiO_2	53.21	53.11	51.52
K_2O	0.01	0.01	0.01
CaO	17.57	17.15	20.47
TiO_2	0.77	0.74	1.50
Cr_2O_3	0.05	0.05	0.09
MnO	0.22	0.21	0.22
FeOT	9.24	9.40	9.23
Total	101.36	101.13	102.80
En	51	51	44
Wo	35	34	42
Fs	14	15	15

Table A 6: Microprobe analyses (in wt. %) of spinel crystals

Sample	**171-2,sp1**	**171-2,sp1**
coment	incl. in plag	incl. in plag
NaO	0.02	0.01
MgO	13.18	13.28
Al_2O_3	22.03	22.16
SiO_2	0.08	0.07
K_2O	0.01	0.00
CaO	0.16	0.10
TiO_2	1.13	1.13
Cr_2O_3	39.48	39.92
MnO	0.20	0.20
FeOT	23.82	23.72
Total	100.10	100.59

Table A 7: Microprobe analyses (in wt. %) of glassy inclusions

Sample	**156-3 plag 3-Incl.**	**156-3 plag 3-Incl.**	**156-3 plag 3-Incl.**	**156-3 plag 3-Incl.**	**156-3 plag 3-Incl.**
NaO	1.35	2.15	0.77	0.22	0.42
MgO	12.86	10.90	12.98	11.46	11.26
Al_2O_3	9.41	13.02	8.75	11.73	12.05
SiO_2	48.76	49.10	48.02	51.62	51.72
K_2O	0.07	0.19	0.09	0.16	0.22
CaO	11.40	11.14	11.34	10.54	10.43
TiO_2	1.66	1.27	1.58	1.50	1.42
Cr_2O_3	0.04	0.01	0.09	0.10	0.02
MnO	0.27	0.20	0.23	0.19	0.17
FeOT	13.78	10.99	14.61	11.32	11.10
Total	99.60	98.98	98.46	98.82	98.80

Sample	**156-3 plag 3-Incl.**	**156-3 plag 3-Incl.**	**156-3 plag 3-Incl.**	**156-3 plag 4incl**	**156-3 plag 4incl**
NaO	2.85	0.37	0.51	2.74	1.91
MgO	7.53	12.21	9.72	9.17	7.82
Al_2O_3	18.07	10.21	14.32	15.33	11.76
SiO_2	51.91	51.55	52.32	50.14	48.91
K_2O	0.06	0.30	0.22	0.05	0.15
CaO	12.14	10.14	10.87	9.62	12.45
TiO_2	1.01	1.21	0.99	0.88	1.74
Cr_2O_3	0.05	0.00	0.07	0.01	0.03
MnO	0.11	0.16	0.18	0.21	0.25
FeOT	7.35	11.73	9.56	11.77	13.36
Total	101.10	97.89	98.76	99.93	98.37

Table A 7: (continued) Microprobe analyses (in wt. %) of glassy inclusions

Sample	156-3 plag 4incl	164-1 plag 1-Incl.2	164-1 plag 1-Incl.4	164-1 plag 3-Incl.3	164-1 plag 3-Incl.5
NaO	0.47	0.32	1.56	1.29	0.32
MgO	16.48	11.01	7.24	9.40	12.07
Al_2O_3	6.05	8.73	11.21	11.58	7.55
SiO_2	47.56	52.02	52.56	51.03	49.98
K_2O	0.04	0.25	0.31	0.39	0.17
CaO	10.31	11.85	11.06	11.41	11.67
TiO_2	1.73	1.75	2.18	2.13	2.68
Cr_2O_3	0.10	0.07	0.03	0.04	0.09
MnO	0.30	0.24	0.21	0.18	0.31
FeOT	15.84	10.96	11.78	10.57	13.66
Total	98.88	97.21	98.13	98.01	98.51

Sample	164-1 plag 4-Incl.1	164-1 plag 4-Incl.3	164-1 plag 4-Incl.4	164-1 plag 5-Incl.5	164-1 plag 5-Incl.7
NaO	0.83	0.30	0.26	0.29	0.33
MgO	10.25	12.22	12.34	13.45	13.87
Al_2O_3	11.91	10.61	9.20	8.75	8.06
SiO_2	50.96	50.80	51.12	51.39	51.09
K_2O	0.37	0.26	0.18	0.18	0.09
CaO	13.07	13.16	13.04	12.18	11.82
TiO_2	1.55	1.66	1.72	0.74	1.20
Cr_2O_3	0.05	0.06	0.02	0.08	0.07
MnO	0.14	0.18	0.19	0.20	0.23
FeOT	9.50	10.35	10.85	10.39	11.99
Total	98.63	99.61	98.92	97.66	98.74

Sample	164-1 plag 5-Incl.8	164-1 plag 5-Incl.9	164-1 plag 7-Incl.1	164-1 plag 7-Incl.2	166-1 plag 1-Incl.3
NaO	0.33	0.34	0.27	0.31	1.52
MgO	14.00	15.02	11.10	11.62	12.77
Al_2O_3	7.37	6.91	7.58	7.09	9.91
SiO_2	49.45	50.26	52.88	53.44	53.10
K_2O	0.17	0.12	0.14	0.15	0.17
CaO	11.62	11.89	11.16	11.11	10.96
TiO_2	1.36	1.29	1.99	2.05	0.79
Cr_2O_3	0.10	0.09	0.01	0.03	0.06
MnO	0.17	0.18	0.21	0.22	0.24
FeOT	12.50	12.22	12.89	13.10	10.33
Total	97.05	98.33	98.23	99.12	99.86

Table A 7: (continued) Microprobe analyses (in wt. %) of glassy inclusions

Sample	166-1 plag 1-Incl.4	166-1 plag 1-Incl.5	166-1 plag 1-Incl.6	166-1 plag 1-Incl.7	166-1 plag 1-Incl.8
NaO	0.21	0.30	0.40	1.58	0.43
MgO	11.62	12.70	12.13	13.89	13.37
Al_2O_3	11.06	9.54	10.24	8.64	7.55
SiO_2	53.94	53.78	54.20	52.03	51.14
K_2O	0.17	0.15	0.30	0.24	0.18
CaO	10.42	10.80	10.15	10.96	11.14
TiO_2	0.72	1.07	0.91	0.97	1.05
Cr_2O_3	0.11	0.09	0.09	0.06	0.12
MnO	0.26	0.23	0.20	0.26	0.27
FeOT	9.48	10.58	9.99	11.18	11.78
Total	97.99	99.24	98.61	99.81	97.03

Sample	166-1 plag 1-Incl.9	166-1 plag 1-Incl.10	166-1 plag 1-Incl.11	166-1 plag 1-Incl.13	166-1 plag 4-Incl.1
NaO	1.75	0.65	0.42	2.05	0.39
MgO	11.32	10.57	10.73	11.20	11.54
Al_2O_3	10.74	11.60	8.91	10.56	9.74
SiO_2	52.52	53.71	53.19	52.10	52.71
K_2O	0.17	0.35	0.59	0.16	0.24
CaO	10.91	10.94	10.59	10.84	10.79
TiO_2	1.05	1.02	1.25	1.11	1.36
Cr_2O_3	0.07	0.09	0.04	0.10	0.10
MnO	0.23	0.21	0.31	0.24	0.26
FeOT	10.00	10.10	12.02	10.83	10.40
Total	98.78	99.24	98.05	99.18	97.52

Sample	166-1 plag 4-Incl.2	166-1 plag 4-Incl.5	176-7 plag 2-incl.	190-1plag 2 incl.	190-1plag 2 incl.
NaO	0.29	0.86	0.60	0.54	0.57
MgO	12.57	14.21	12.44	13.20	13.28
Al_2O_3	8.44	8.28	7.76	4.82	5.56
SiO_2	52.39	50.03	49.00	50.82	51.74
K_2O	0.17	0.13	0.37	0.64	0.70
CaO	11.74	11.53	11.13	11.20	11.07
TiO_2	1.18	1.41	1.93	1.60	1.45
Cr_2O_3	0.08	0.11	0.09	0.12	0.01
MnO	0.22	0.25	0.15	0.28	0.28
FeOT	11.16	12.25	13.99	14.99	14.48
Total	98.24	99.05	97.46	98.20	99.13

Table A 7: (continued) Microprobe analyses (in wt. %) of glassy inclusions

Sample	169-1 ol3incl.	169-1 ol3incl.
NaO	2.19	2.33
MgO	6.42	6.85
Al_2O_3	17.12	17.09
SiO_2	49.99	49.78
K_2O	0.10	0.10
CaO	12.99	12.96
TiO_2	1.19	1.16
Cr_2O_3	0.03	0.03
MnO	0.15	0.15
FeOT	7.75	7.56
Total	97.93	98.01

Table A 8: Microprobe analyses (in wt. %) of glass samples

Sample	119 DS-1	119 DS-2	119 DS-3	119 DS-4	119 DS-5	120 DS-1	120 DS-2	120 DS-3	120 DS-4
Na_2O	2.63	2.84	2.84	2.59	2.61	2.22	2.14	2.10	2.13
FeOT	8.99	9.30	9.22	8.99	8.99	9.73	9.69	9.14	9.34
SiO_2	49.71	50.62	50.21	49.26	49.39	47.48	46.17	47.42	46.98
CaO	11.82	11.80	11.78	11.54	11.64	11.72	11.90	11.74	11.94
K_2O	0.13	0.14	0.16	0.16	0.09	0.06	0.05	0.06	0.09
Al_2O_3	15.84	15.07	15.28	15.36	15.65	18.13	17.38	17.81	17.74
TiO_2	1.20	1.36	1.31	1.18	1.16	0.61	0.64	0.59	0.63
MgO	8.23	7.51	7.47	8.10	8.08	9.87	9.34	9.45	9.48
MnO	0.20	0.17	0.20	0.16	0.15	0.19	0.20	0.20	0.20
P_2O_5	0.26	0.29	0.28	0.26	0.24	0.23	0.18	0.17	0.18
Total	99.06	99.19	98.80	97.65	98.04	100.47	97.73	98.73	98.77

Sample	121 DS-1	121 DS-2	122 DS-1	122 DS-2	122 DS-3	122 DS-4	122 DS-5	122 DS-6	122 DS-7
Na_2O	2.89	2.83	2.87	3.01	2.98	2.94	2.89	2.84	2.97
FeOT	10.63	10.69	9.74	9.63	10.09	9.87	9.93	9.70	10.08
SiO_2	49.84	50.52	49.84	49.90	49.98	49.22	50.48	50.00	49.72
CaO	11.07	11.23	11.11	11.38	11.31	11.39	11.24	11.23	11.29
K_2O	0.16	0.15	0.20	0.17	0.14	0.16	0.17	0.18	0.15
Al_2O_3	14.60	14.94	15.51	15.51	15.51	15.29	15.70	15.55	15.45
TiO_2	1.58	1.47	1.42	1.42	1.42	1.46	1.37	1.38	1.46
MgO	6.92	7.22	7.44	7.45	7.65	7.55	7.62	7.59	7.56
MnO	0.20	0.17	0.20	0.16	0.21	0.21	0.19	0.20	0.19
P_2O_5	0.27	0.28	0.27	0.28	0.29	0.31	0.28	0.25	0.29
Total	98.23	99.56	98.70	98.99	99.86	98.68	99.96	99.00	99.45

Table A 8: (continued) Microprobe analyses (in wt. %) of glass samples

Sample	126 DS-1	126 DS-2	126 DS-3	130 DS-3	132 DS-1	132 DS-2	132 DS-5	132 DS-6	132 DS-6
Na_2O	2.43	2.49	2.48	2.53	2.47	2.43	2.33	2.43	2.45
FeOT	8.52	8.65	8.68	8.22	10.14	10.18	9.92	9.84	10.14
SiO_2	49.45	49.94	49.68	49.53	49.91	50.32	50.52	49.88	50.29
CaO	12.09	12.18	12.18	10.86	11.66	11.47	11.51	11.53	11.27
K_2O	0.05	0.05	0.04	0.04	0.17	0.15	0.19	0.19	0.16
Al_2O_3	16.40	16.47	16.48	16.68	15.00	15.10	15.16	14.85	15.35
TiO_2	0.99	1.00	1.04	0.59	1.29	1.34	1.31	1.30	1.33
MgO	8.95	8.95	8.89	9.58	8.36	8.49	8.39	8.20	8.53
MnO	0.18	0.14	0.13	0.14	0.20	0.22	0.17	0.18	0.18
P_2O_5	0.21	0.22	0.23	0.16	0.29	0.30	0.27	0.27	0.33
Total	99.32	100.14	99.89	98.56	99.81	100.32	99.83	98.78	100.31

Sample	132 DS-6	133 DS-1	133 DS-4	133 DS-7	133 DS-8	133 DS-9	136 DS-1	136 DS-3	137 DS-2
Na_2O	2.49	2.51	2.52	2.42	2.49	2.54	2.38	2.36	2.26
FeOT	9.87	9.29	9.16	9.34	9.22	9.44	9.71	9.82	9.76
SiO_2	50.13	48.69	49.05	49.81	49.53	49.63	50.14	50.58	50.47
CaO	11.67	12.18	12.45	12.23	12.35	12.17	12.04	11.81	11.95
K_2O	0.18	0.18	0.14	0.16	0.16	0.20	0.14	0.13	0.10
Al_2O_3	14.93	15.41	15.89	15.53	16.06	15.60	15.19	15.29	15.17
TiO_2	1.33	1.20	1.13	1.16	1.16	1.30	1.22	1.22	1.11
MgO	8.28	8.24	8.57	8.10	8.63	8.12	7.98	8.01	8.40
MnO	0.19	0.16	0.20	0.19	0.20	0.20	0.20	0.19	0.15
P_2O_5	0.27	0.25	0.27	0.25	0.26	0.26	0.24	0.25	0.23
Total	99.62	98.42	99.66	99.24	100.31	99.70	99.31	99.72	99.64

Sample	137 DS-3	137 DS-4	138 DS-1	138 DS-2	138 DS-3	139 DS-2	139 DS-3	140 DS-1	140 DS-2
Na_2O	2.25	2.26	2.42	2.59	2.62	2.46	2.45	2.23	2.23
FeOT	9.49	9.57	9.43	9.50	9.75	10.35	10.19	9.11	9.36
SiO_2	49.67	50.30	48.83	47.45	48.35	50.58	49.76	50.15	49.98
CaO	11.84	12.01	11.57	12.23	11.24	11.90	11.98	12.22	12.12
K_2O	0.11	0.08	0.39	0.40	0.45	0.13	0.12	0.07	0.06
Al_2O_3	15.04	15.28	15.99	15.14	16.31	14.99	14.72	16.08	16.19
TiO_2	1.09	1.09	1.66	1.83	1.85	1.32	1.32	1.03	1.04
MgO	8.14	8.35	8.06	7.63	7.72	7.96	7.79	8.97	9.11
MnO	0.15	0.17	0.16	0.18	0.18	0.22	0.20	0.18	0.19
P_2O_5	0.19	0.23	0.36	0.38	0.38	0.29	0.27	0.22	0.23
Total	98.02	99.40	98.98	97.72	98.96	100.52	99.09	100.31	100.57

Sample	141 DS-1	141 DS-2	141 DS-3	142 DS-1	142 DS-3	142 DS-4	142 DS-7	143 DS-1	143 DS-2
Na_2O	2.50	2.27	2.46	2.31	2.30	2.28	2.33	2.16	2.18
FeOT	7.64	9.15	7.51	9.64	9.46	9.57	9.28	10.50	10.64
SiO_2	52.70	50.24	52.47	50.11	49.35	50.56	50.29	48.03	48.84
CaO	10.62	12.21	10.42	11.94	11.93	11.78	11.91	12.06	12.09
K_2O	0.07	0.17	0.09	0.10	0.12	0.09	0.09	0.09	0.05
Al_2O_3	16.50	15.03	16.24	15.15	14.99	15.39	15.19	15.89	16.18
TiO_2	0.86	1.17	0.87	1.24	1.27	1.21	1.23	0.88	0.92
MgO	8.53	8.07	8.41	8.60	8.40	8.73	8.63	8.60	8.71
MnO	0.11	0.18	0.07	0.17	0.15	0.19	0.16	0.17	0.21
P_2O_5	0.21	0.24	0.17	0.24	0.25	0.26	0.26	0.15	0.23
Total	99.78	98.82	98.79	99.56	98.29	100.12	99.42	98.61	100.09

Table A 8: (continued) Microprobe analyses (in wt. %) of glass samples

Sample	**144 DS-1**	**145 DS-1**	**145 DS-1**	**145 DS-3**	**145 DS-4**	**145-DS-2**	**146 DS-1**	**146 DS-2**	**146 DS-3**
Na_2O	2.55	2.58	2.72	2.50	2.59	2.52	2.46	2.35	2.24
FeOT	10.63	10.93	11.38	10.68	11.72	10.87	9.78	9.83	9.69
SiO_2	50.91	50.66	50.74	50.94	50.78	51.11	50.40	50.76	50.42
CaO	11.69	11.48	11.61	11.35	11.05	11.56	11.95	11.84	12.04
K_2O	0.12	0.12	0.11	0.13	0.17	0.14	0.12	0.15	0.09
Al_2O_3	14.47	14.30	13.82	14.35	13.83	14.62	14.65	15.05	15.17
TiO_2	1.61	1.58	1.96	1.56	1.83	1.55	1.25	1.27	1.11
MgO	7.20	7.27	7.57	7.11	6.72	7.31	8.23	8.18	8.33
MnO	0.22	0.23	0.21	0.18	0.25	0.20	0.21	0.21	0.17
P_2O_5	0.29	0.30		0.29	0.30	0.30	0.27	0.26	0.23
Total	99.75	99.77	100.14	99.17	99.30	100.27	99.60	99.94	99.55

Sample	**147 DS-1**	**147 DS-2**	**147 DS-3**	**147 DS-4**	**148 DS-1**	**148 DS-2**	**148 DS-4**	**148 DS-4**	**149 DS-1**
Na_2O	2.52	2.75	2.78	2.23	2.40	2.38	2.82	2.65	2.87
FeOT	10.40	10.14	10.15	9.76	10.79	7.82	11.41	11.33	11.90
SiO_2	50.37	49.52	51.04	50.95	50.99	49.75	51.66	51.32	51.03
CaO	11.12	10.67	10.43	11.63	11.30	10.47	11.17	11.02	10.08
K_2O	0.16	0.06	0.04	0.24	0.20	0.01	0.23	0.23	0.35
Al_2O_3	14.00	15.99	15.60	14.68	14.51	17.08	13.58	13.75	14.03
TiO_2	1.36	1.12	1.17	1.38	1.58	0.56	2.13	1.62	2.09
MgO	6.88	7.69	8.04	7.24	6.39	9.34	6.98	6.65	5.85
MnO	0.20	0.19	0.17	0.19	0.22	0.13	0.20	0.19	0.22
P_2O_5	0.27	0.21	0.21	0.30	0.29	0.12		0.32	0.39
Total	97.34	98.59	99.85	98.69	99.01	97.70	100.19	99.45	98.92

Sample	**149 DS-2**	**149 DS-4**	**151 DS-1**	**151 DS-2**	**151 DS-3**	**152 DS-1**	**152 DS-2**	**153 DS-1**	**153 DS-3**
Na_2O	2.79	2.82	2.53	2.64	2.59	2.66	2.67	2.73	2.60
FeOT	11.91	12.08	10.08	9.88	9.06	10.18	10.34	10.83	10.52
SiO_2	50.99	51.03	51.82	51.75	51.81	50.22	48.80	50.71	51.06
CaO	10.02	10.02	10.76	10.90	10.73	11.25	11.13	10.76	11.33
K_2O	0.36	0.35	0.09	0.10	0.09	0.11	0.12	0.23	0.20
Al_2O_3	13.86	13.98	15.51	15.11	15.68	14.66	14.91	13.91	14.12
TiO_2	2.04	2.02	1.30	1.36	1.19	1.35	1.32	1.70	1.55
MgO	5.83	5.77	7.69	7.34	7.81	7.50	7.51	6.98	7.12
MnO	0.21	0.20	0.17	0.17	0.16	0.18	0.20	0.21	0.21
P_2O_5	0.37	0.40	0.23	0.24	0.22	0.25	0.24	0.30	0.29
Total	98.49	98.77	100.23	99.55	99.40	98.65	97.52	98.66	99.30

Sample	**154 DS-1**	**154 DS-3**	**155 DS-1**	**156 DS-1**	**156 DS-3**	**156 DS-4**	**157 DS-1**	**157 DS-2**	**157 DS-3**
Na_2O	2.57	2.51	2.53	2.79	2.58	2.67	2.44	2.44	2.42
FeOT	10.86	11.29	9.78	10.34	10.19	10.36	8.45	8.97	8.98
SiO_2	51.84	50.88	50.30	49.43	49.10	50.38	50.46	50.79	50.97
CaO	11.14	10.90	11.24	10.61	11.68	10.36	11.76	11.87	11.81
K_2O	0.20	0.30	0.14	0.12	0.16	0.13	0.21	0.25	0.23
Al_2O_3	14.38	14.07	15.94	15.86	15.37	16.08	15.62	15.77	15.82
TiO_2	1.74	1.75	1.10	1.24	1.17	1.24	1.46	1.50	1.49
MgO	6.98	6.41	8.10	7.90	7.84	7.84	7.97	8.09	8.15
MnO	0.25	0.22	0.19	0.19	0.18	0.18	0.16	0.15	0.15
P_2O_5	0.31	0.32	0.23	0.22	0.23	0.23	0.29	0.31	0.30
Total	100.34	98.73	99.61	98.98	98.59	99.55	98.87	100.22	100.37

Table A 8: (continued) Microprobe analyses (in wt. %) of glass samples

Sample	**158 DS-1**	**158 DS-2**	**159 DS-2**	**160 DS-1**	**160 DS-2**	**160 DS-3**	**161 DS-1**	**161 DS-2**	**161 DS-3**
Na_2O	2.70	2.74	2.93	2.76	2.74	2.70	2.56	2.56	2.48
FeOT	10.12	10.09	10.49	9.97	9.71	9.94	9.67	10.05	9.88
SiO_2	50.81	50.83	51.21	49.83	50.41	51.11	50.37	49.86	49.60
CaO	11.43	11.34	10.09	10.55	10.20	10.66	11.32	11.37	10.93
K_2O	0.25	0.30	0.12	0.07	0.06	0.19	0.10	0.13	0.10
Al_2O_3	14.27	14.34	14.75	15.96	15.15	15.34	16.09	15.99	15.68
TiO_2	1.70	1.69	1.49	1.12	1.01	1.46	1.18	1.15	1.08
MgO	7.07	7.00	7.11	8.20	7.79	7.41	8.14	8.09	7.98
MnO	0.18	0.21	0.20	0.19	0.16	0.19	0.18	0.17	0.18
P_2O_5	0.33	0.32	0.26	0.22	0.18	0.27	0.25	0.24	0.20
Total	99.21	99.24	98.93	99.06	97.64	99.56	99.91	99.70	98.17

Sample	**162 DS-1**	**162 DS-2**	**163 DS-1**	**164 DS-1**	**166 DS-1**	**166 DS-2**	**166 DS-3**	**166 DS-4**	**167 DS-1**
Na_2O	2.70	2.73	2.70	2.76	3.14	3.35	2.99	3.32	2.72
FeOT	10.69	10.86	10.25	10.79	11.53	12.32	11.51	12.39	11.63
SiO_2	51.07	50.11	50.95	50.34	50.08	49.62	49.98	50.61	48.40
CaO	11.16	11.01	10.86	10.45	10.47	10.02	10.41	9.78	11.83
K_2O	0.27	0.28	0.29	0.34	0.46	0.55	0.42	0.53	0.19
Al_2O_3	14.33	14.04	15.10	14.46	13.93	13.37	13.99	14.10	14.10
TiO_2	1.75	1.75	1.64	1.88	2.16	2.57	2.12	2.59	1.45
MgO	6.76	6.51	7.30	6.78	5.73	5.15	5.75	5.34	6.95
MnO	0.19	0.22	0.21	0.15	0.21	0.24	0.21	0.18	0.23
P_2O_5	0.29	0.29	0.34	0.34	0.42	0.46	0.37	0.45	0.29
Total	99.26	97.88	99.96	98.39	98.49	98.08	97.85	99.40	98.09

Sample	**169 DS-1**	**169 DS-2**	**170 DS-1**	**170 DS-2**	**171 DS-1**	**172 DS-1**	**172 DS-2**	**172 DS-3**	**173 DS-1**
Na_2O	2.81	2.77	2.97	3.37	3.04	3.20	3.22	3.28	3.20
FeOT	10.60	10.50	13.20	13.54	11.08	11.80	11.43	11.97	11.70
SiO_2	49.81	49.36	50.46	50.20	50.33	50.61	50.24	50.34	50.90
CaO	11.52	11.51	10.09	8.62	10.97	10.10	10.26	9.80	10.22
K_2O	0.28	0.27	0.54	0.59	0.38	0.45	0.43	0.42	0.46
Al_2O_3	14.41	14.47	11.93	13.07	14.24	14.26	14.09	14.24	14.21
TiO_2	1.69	1.67	2.70	2.89	2.03	2.36	2.35	2.38	2.41
MgO	6.74	6.81	4.52	4.32	6.35	5.86	5.62	5.80	5.75
MnO	0.17	0.19	0.26	0.21	0.22	0.23	0.23	0.24	0.21
P_2O_5	0.31	0.32	0.42	0.47	0.36	0.42	0.40	0.42	0.43
Total	98.41	97.95	98.44	97.40	99.33	99.43	98.39	99.33	99.62

Sample	**173 DS-2**	**174 DS-1**	**174 DS-2**	**174 DS-3**	**174 DS-4**	**174 DS-6**	**175 DS-1**	**175 DS-2**	**176 DS-2**
Na_2O	3.31	3.60	3.49	3.52	3.49	3.46	2.73	2.63	3.22
FeOT	12.08	11.27	10.81	11.05	11.55	10.30	9.43	9.14	9.57
SiO_2	50.46	49.75	49.94	49.98	48.97	49.34	47.33	48.67	50.38
CaO	9.93	9.91	9.99	9.98	9.94	10.73	11.30	11.36	11.69
K_2O	0.52	0.70	0.71	0.69	0.73	0.66	0.25	0.26	0.31
Al_2O_3	13.42	14.26	14.77	14.78	14.43	14.67	16.98	17.55	16.37
TiO_2	2.63	2.55	2.57	2.57	2.58	2.32	1.20	1.23	1.66
MgO	5.22	5.70	5.60	5.58	5.45	6.01	8.34	8.78	5.92
MnO	0.25	0.21	0.20	0.19	0.21	0.20	0.20	0.17	0.18
P_2O_5	0.46	0.49	0.52	0.50	0.51	0.48	0.29	0.28	0.34
Total	98.72	98.82	98.72	98.94	98.25	98.49	98.29	100.15	99.98

Table A 8: (continued) Microprobe analyses (in wt. %) of glass samples

Sample	179 DS-1	179 DS-2	179 DS-3	179 DS-4	183 DS-1	183 DS-2	183 DS-4	183 DS-5	184 DS-1
Na_2O	3.40	3.46	3.45	3.49	4.54	4.83	4.74	4.46	4.44
FeOT	12.13	11.63	11.42	11.34	10.22	10.39	10.62	11.38	11.02
SiO_2	49.13	49.39	48.84	47.97	48.40	48.95	49.31	48.30	47.06
CaO	9.83	10.08	10.09	10.23	8.40	7.30	7.23	7.99	8.66
K_2O	0.69	0.67	0.67	0.70	1.60	1.82	1.95	1.86	1.69
Al_2O_3	14.02	14.65	14.56	14.07	17.49	16.72	16.45	15.98	15.50
TiO_2	2.84	2.63	2.59	2.56	3.36	2.94	3.08	3.74	3.69
MgO	5.19	5.89	5.88	5.76	3.72	3.63	3.86	4.03	4.14
MnO	0.21	0.22	0.20	0.20	0.22	0.20	0.22	0.21	0.20
P_2O_5	0.45	0.45	0.46	0.44	0.93	1.16	1.15	1.03	0.97
Total	97.99	99.40	98.45	97.03	99.16	98.32	98.96	99.17	97.69

Sample	184 DS-2	184 DS-3	184 DS-4	184 DS-5	184 DS-6	184 DS-8	185 DS-3	186 DS-1	188 DS-1
Na_2O	4.57	4.45	4.54	4.49	4.49	4.43	6.21	3.92	3.18
FeOT	11.36	10.92	9.62	11.16	10.93	11.08	3.68	11.88	10.81
SiO_2	47.79	48.57	48.17	47.91	47.60	47.68	63.52	46.11	50.44
CaO	8.19	8.39	8.91	8.47	8.57	8.44	0.98	9.98	11.01
K_2O	1.98	1.72	1.43	1.82	1.68	1.76	5.19	1.32	0.47
Al_2O_3	15.49	16.40	17.74	15.46	16.31	15.66	17.62	15.54	14.59
TiO_2	3.82	3.63	3.17	3.79	3.66	3.69	0.42	4.10	2.19
MgO	4.02	3.95	3.57	4.01	3.90	4.24	0.35	3.86	6.22
MnO	0.21	0.18	0.19	0.21	0.22	0.22	0.21	0.24	0.18
P_2O_5	1.05	0.97	0.90	0.99	1.00	1.00	0.13	0.88	0.42
Total	98.84	99.35	98.53	98.68	98.72	98.55	98.58	98.16	99.63

Sample	188 DS-2	188 DS-3	189 DS-1	189 DS-2	190 DS-1	190 DS-2	190 DS-3	190 DS-4	191 DS-1
Na_2O	3.09	3.50	3.57	3.45	3.38	3.35	3.24	3.00	3.65
FeOT	10.41	11.49	12.21	12.02	12.50	12.67	12.25	9.96	13.63
SiO_2	50.37	49.85	49.76	50.16	50.29	50.55	50.78	50.62	50.31
CaO	11.10	9.94	9.61	9.70	9.71	9.55	10.02	11.32	9.10
K_2O	0.44	0.63	0.64	0.64	0.57	0.54	0.51	0.31	0.70
Al_2O_3	14.73	14.19	13.93	13.69	13.51	13.89	14.11	16.12	13.25
TiO_2	2.08	2.62	2.65	2.67	2.70	2.69	2.51	1.72	2.97
MgO	6.37	5.31	5.16	5.08	5.06	5.13	5.48	5.87	4.38
MnO	0.22	0.20	0.22	0.24	0.24	0.20	0.22	0.20	0.24
P_2O_5	0.39	0.46	0.51	0.49	0.47	0.46	0.42	0.34	0.48
Total	99.30	98.29	98.67	98.57	98.85	99.15	99.64	99.78	99.17

Sample	191 DS-2	191 DS-3	194 DS-1	195 DS-1	195 DS-2	196 DS-1	196 DS-2	196 DS-3	196 DS-4
Na_2O	3.65	3.40	2.57	2.45	2.47	2.85	2.85	2.87	2.89
FeOT	13.65	13.44	10.41	9.52	9.40	10.56	10.70	10.65	10.77
SiO_2	49.13	50.61	48.70	49.09	49.76	50.06	50.40	50.32	49.85
CaO	8.89	9.13	11.78	12.12	12.09	10.66	10.59	10.62	10.55
K_2O	0.68	0.71	0.17	0.10	0.10	0.35	0.37	0.36	0.37
Al_2O_3	13.24	13.45	15.39	15.56	15.09	14.39	14.47	14.49	14.76
TiO_2	2.96	3.01	1.10	1.13	1.12	1.91	1.92	1.96	1.92
MgO	4.46	4.48	7.82	8.28	8.39	6.98	7.09	6.97	7.08
MnO	0.26	0.24	0.22	0.21	0.21	0.21	0.23	0.21	0.21
P_2O_5	0.48	0.51	0.74	0.25	0.26	0.37	0.38	0.39	0.38
Total	97.83	99.46	99.23	99.00	99.18	98.66	99.35	99.19	99.10

Table A 8: (continued) Microprobe analyses (in wt. %) of glass samples

Sample	196 DS-5	197 DS-1	197 DS-2	197 DS-3	197 DS-4	197 DS-5	197 DS-6	197 DS-7	198 DS-1
Na_2O	2.89	2.87	2.93	3.01	2.83	2.98	3.00	2.96	2.19
FeOT	10.65	10.94	10.82	10.75	11.07	10.73	10.79	11.01	9.70
SiO_2	50.24	50.39	50.54	50.42	49.91	50.26	50.21	50.02	50.94
CaO	10.67	10.21	10.17	9.90	10.08	10.24	10.27	10.14	12.57
K_2O	0.37	0.41	0.44	0.43	0.46	0.44	0.43	0.43	0.12
Al_2O_3	14.47	14.09	14.12	14.14	14.31	14.03	14.11	13.96	14.35
TiO_2	1.96	2.03	2.11	2.08	2.13	2.09	2.08	2.04	1.17
MgO	7.02	6.85	6.79	6.95	6.80	6.77	6.69	6.87	7.74
MnO	0.21	0.21	0.21	0.22	0.24	0.19	0.20	0.22	0.20
P_2O_5	0.37	0.40	0.41	0.42	0.40	0.42	0.41	0.39	0.28
Total	99.17	98.78	98.90	98.68	98.59	98.52	98.56	98.38	99.53

Sample	198 DS-2	198 DS-3	198 DS-5	199 DS-1	199 DS-2	200 DS-1	200 DS-2	201 DS-2	201 DS-5
Na_2O	2.37	2.28	2.17	2.24	2.21	2.42	2.48	2.60	2.54
FeOT	9.29	10.45	10.31	8.81	9.19	10.59	8.81	10.02	9.32
SiO_2	49.68	50.25	51.29	49.98	50.57	51.16	49.69	49.67	50.33
CaO	12.68	12.23	12.25	12.61	12.61	11.90	12.20	11.18	12.35
K_2O	0.12	0.12	0.12	0.06	0.07	0.16	0.06	0.07	0.25
Al_2O_3	16.11	14.27	14.65	14.98	15.66	14.58	16.84	16.14	15.07
TiO_2	1.10	1.24	1.25	0.99	1.00	1.40	0.97	1.01	1.35
MgO	6.64	7.63	7.81	8.32	8.56	7.37	9.11	9.07	7.62
MnO	0.19	0.20	0.20	0.19	0.18	0.20	0.16	0.17	0.17
P_2O_5	0.24	0.29	0.29	0.23	0.23	0.29	0.23	0.22	0.31
Total	98.72	99.26	100.39	98.68	100.34	100.18	100.60	100.21	99.39

Sample	202 DS-1	202 DS-2	202 DS-3	202 DS-4	203 DS-1	203 DS-2	203 DS-3
Na_2O	2.65	2.68	2.33	2.29	2.32	2.22	2.31
FeOT	9.41	9.24	9.55	8.90	9.52	9.22	9.67
SiO_2	48.49	47.94	50.64	50.70	50.21	50.59	49.47
CaO	12.40	12.47	12.54	12.67	12.70	12.61	12.48
K_2O	0.05	0.06	0.13	0.13	0.11	0.09	0.10
Al_2O_3	16.59	16.32	15.05	15.17	14.38	15.13	14.98
TiO_2	0.93	0.91	1.04	1.09	1.10	1.05	1.09
MgO	9.03	8.68	8.23	8.08	7.91	8.33	8.14
MnO	0.18	0.19	0.20	0.19	0.21	0.19	0.18
P_2O_5	0.22	0.22	0.28	0.26	0.25	0.24	0.25
Total	100.20	98.98	100.25	99.53	99.00	99.72	98.96

Table A 9: Trace element concentrations (in ppm) of glass samples from ICP-MS analyses

	119 DS-3	120 DS-2	120 DS-3	121 DS-1	122 DS-5	122 DS-7	126 DS-1	126 DS-3	130 DS-1
Sc	37.36	47.87	44.16	31.13	39.84		32.05	36.63	30.38
V	255.18	191.52	176.05	220.71	274.56		216.92	260.34	150.91
Cr	201.89	194.55	192.20	145.79	259.23		242.74	304.02	375.30
Co	36.69	48.43	47.09	31.51	41.31		42.39	44.11	47.72
Cu	66.19	101.47	99.68	49.15	73.76		76.41	83.63	74.84
Zn	69.12	51.99	52.22	71.25	85.23		65.15	69.48	56.14
Ga	14.27	12.80	12.36	13.12	16.15		14.31	15.30	14.08
Rb	1.39	0.66	0.63	1.40	1.86	1.79	0.57	0.65	0.57
Sr	122.65	99.50	99.03	92.07	138.43	143.33	67.69	69.67	113.68
Y	28.40	22.71	22.82	29.80	32.34	30.68	25.71	27.08	13.84
Zr	71.73	31.96	31.62	71.20	86.30	94.65	48.58	51.48	17.30
Nb	2.21	1.20	1.08	2.30	3.32	3.52	0.50	0.58	0.57
Cs						0.02			
Mo	0.20	0.08	0.07	0.19	0.28		0.06	0.09	0.07
Ba	11.35	4.98	5.16	12.66	16.43	18.18		2.84	3.45
La	2.67	1.26	1.28	2.79	3.61	3.89	1.14	1.16	0.60
Ce	8.13	3.91	3.93	8.45	10.53	11.19	4.68	4.71	2.03
Pr	1.42	0.68	0.70	1.47	1.77	1.91	1.00	0.99	0.40
Nd	7.71	3.75	3.87	8.00	9.36	9.76	5.91	5.99	2.51
Sm	2.85	1.47	1.50	2.95	3.31	3.38	2.49	2.46	1.14
Eu	1.04	0.66	0.65	1.05	1.18	1.20	0.91	0.92	0.58
Gd	3.72	2.18	2.23	3.92	4.31	4.45	3.37	3.42	1.69
Tb	0.68	0.45	0.46	0.72	0.79	0.82	0.63	0.64	0.32
Dy	4.55	3.41	3.44	4.86	5.23	5.47	4.33	4.41	2.25
Ho	0.97	0.79	0.80	1.03	1.11	1.18	0.93	0.94	0.49
Er	2.73	2.44	2.50	2.97	3.15	3.33	2.65	2.65	1.36
Tm	0.40	0.39	0.40	0.43	0.46	0.49	0.39	0.39	0.21
Yb	2.63	2.70	2.71	2.86	3.06	3.26	2.56	2.58	1.39
Lu	0.39	0.41	0.43	0.42	0.45	0.48	0.38	0.37	0.21
Hf	2.11	1.00	1.02	2.16	2.49	2.62	1.75	1.79	0.67
Ta	0.14	0.08	0.08	0.15	0.21	0.24	0.04	0.04	0.04
Pb	0.36	0.16	0.16	0.38	0.40	0.45	0.21	0.23	0.12
Th	0.13	0.06	0.06	0.16	0.21	0.24	0.04	0.03	0.03
U	0.05	0.02	0.02	0.05	0.07	0.08	0.01	0.01	0.01

Table A 9: (continued) Trace element concentrations (in ppm) of glass samples from ICP-MS analyses

	130 DS-3	132 DS-5	133 DS-7	133 DS-9	136 DS-1	137 DS-4	138 DS-1	139 DS-1	139 DS-3
Sc		36.72				38.16	36.16		
V		273.27				256.09	320.49		
Cr		246.32				230.66	195.30		
Co		41.58				42.00	42.97		
Cu		59.38				64.93	66.34		
Zn		77.66				76.86	86.40		
Ga		15.24				15.28	17.20		
Rb	0.16	3.77	2.03	3.24	2.17	1.64	11.03	1.71	2.51
Sr	110.88	101.73	124.62	118.79	86.68	71.70	244.93	83.68	85.71
Y	10.54	31.04	18.14	25.22	23.19	29.13	24.22	26.38	24.12
Zr	12.88	64.34	36.08	67.22	41.81	47.61	104.24	57.39	42.26
Nb	0.42	6.53	3.61	6.06	3.87	2.72	18.09	3.46	4.28
Cs				0.04				0.02	
Mo		0.34				0.15	0.95		
Ba	4.13	42.26	31.53	35.75	29.54	18.40	115.85	19.51	37.54
La	0.67	5.07	3.51	4.60	3.81	2.50	12.50	3.01	4.33
Ce	1.89	12.38	8.47	11.24	9.38	6.89	27.34	8.00	10.31
Pr		1.86		1.75		1.18	3.65	1.35	
Nd	2.23	9.35	6.53	8.46	7.31	6.63	15.98	7.06	7.66
Sm	0.97	3.25	2.20	2.75	2.53	2.56	4.16	2.53	2.64
Eu	0.52	1.12	0.83	1.00	0.94	0.96	1.37	0.96	0.99
Gd	1.45	4.15	2.91	3.67	3.57	3.56	4.38	3.65	3.73
Tb	0.28	0.77	0.54	0.66	0.66	0.70	0.71	0.68	0.68
Dy	1.93	5.19	3.56	4.45	4.44	4.82	4.33	4.55	4.66
Ho	0.43	1.11	0.77	0.96	0.97	1.04	0.86	1.00	1.01
Er	1.25	3.16	2.25	2.74	2.84	2.96	2.32	2.90	2.97
Tm		0.47		0.41		0.44	0.33	0.44	
Yb	1.28	3.07	2.21	2.72	2.81	2.90	2.13	2.86	2.98
Lu	0.19	0.45	0.32	0.41	0.41	0.43	0.32	0.43	0.44
Hf	0.66	2.18	1.60	1.97	1.83	1.75	2.80	1.79	1.99
Ta	0.04	0.38	0.27	0.37	0.26	0.16	1.02	0.21	0.29
Pb	0.15	0.36	0.45	0.37	0.43	0.24	0.86	0.26	0.35
Th	0.04	0.51	0.29	0.44	0.32	0.20	1.26	0.26	0.37
U	0.02	0.15	0.09	0.13	0.09	0.06	0.40	0.08	0.11

Table A 9: (continued) Trace element concentrations (in ppm) of glass samples from ICP-MS analyses

	140 DS-1	142 DS-2	143 DS-1	144 DS-1	145 DS-1	145 DS-4	146 DS-3	147 DS-1	148 DS-4
Sc						40.94		47.65	
V						334.44		331.75	
Cr						134.85		216.20	
Co						41.95		45.27	
Cu						54.91		108.45	
Zn						97.28		87.93	
Ga						17.34		16.54	
Rb	1.18	1.90	0.44	2.43	2.59	3.64	2.16	2.67	3.46
Sr	79.98	86.57	81.73	87.00	95.03	90.31	90.10	110.09	128.76
Y	21.32	26.37	21.14	27.88	30.89	41.83	24.18	29.85	23.78
Zr	37.20	48.43	25.83	57.90	59.27	93.18	45.70	67.73	60.33
Nb	2.10	3.49	0.94	4.01	4.35	6.33	3.85	4.93	6.06
Cs									
Mo						0.35		0.29	
Ba	14.65	26.94	6.82	31.53	31.54	35.76	27.91	30.49	38.22
La	2.20	3.85	1.33	4.40	4.59	5.40	4.03	3.65	5.30
Ce	6.03	9.98	4.04	11.37	11.62	14.50	10.23	9.75	12.85
Pr						2.31		1.57	
Nd	5.50	8.00	4.13	8.99	9.46	12.12	8.13	8.16	9.35
Sm	2.05	3.02	1.58	3.13	3.32	4.32	2.76	2.93	2.96
Eu	0.79	1.03	0.68	1.07	1.11	1.42	0.99	1.04	1.10
Gd	2.88	4.10	2.56	4.20	4.38	5.61	3.65	3.76	3.86
Tb	0.56	0.76	0.51	0.79	0.82	1.03	0.68	0.70	0.68
Dy	3.78	5.23	3.77	5.27	5.44	6.85	4.51	4.73	4.43
Ho	0.83	1.13	0.87	1.17	1.19	1.48	0.99	1.01	0.92
Er	2.45	3.35	2.61	3.45	3.46	4.17	2.90	2.89	2.67
Tm						0.62		0.43	
Yb	2.48	3.30	2.79	3.38	3.43	4.07	2.93	2.86	2.66
Lu	0.36	0.50	0.42	0.50	0.52	0.60	0.43	0.43	0.38
Hf	1.58	2.27	1.25	2.50	2.40	3.08	1.94	2.10	2.23
Ta	0.15	0.24	0.08	0.26	0.27	0.38	0.24	0.29	0.39
Pb	0.44	0.38	0.21	0.53	0.41	0.49	0.48	0.35	0.48
Th	0.17	0.31	0.08	0.34	0.34	0.47	0.32	0.29	0.39
U	0.06	0.10	0.03	0.11	0.11	0.14	0.10	0.10	0.13

Table A 9: (continued) Trace element concentrations (in ppm) of glass samples from ICP-MS analyses

	148 DS-6	**149 DS-2**	**151 DS-2**	**152 DS-1**	**153 DS-3**	**154 DS-1**	**155 DS-1**	**156 DS-4**	**157 DS-3**
Sc		39.84	30.82						
V		323.84	201.96						
Cr		125.04	253.01						
Co		41.54	41.19						
Cu		63.83	93.08						
Zn		108.66	81.53						
Ga		18.00	15.74						
Rb	3.91	6.09	1.57	1.54	2.91	3.25	1.30	1.50	2.93
Sr	137.81	114.02	130.84	144.64	112.27	108.17	133.98	146.45	172.73
Y	28.94	47.42	22.73	18.22	24.83	32.87	15.65	19.20	17.73
Zr	93.41	141.34	56.96	43.35	61.91	95.98	32.49	44.11	58.06
Nb	8.30	11.58	3.23	3.47	5.92	7.49	2.63	3.23	6.59
Cs	0.05					0.04			
Mo		0.66	0.20						
Ba	42.53	55.81	14.24	19.44	35.70	33.87	17.21	20.05	42.44
La	5.69	8.54	2.36	2.87	4.99	5.03	2.27	2.96	4.89
Ce	14.14	21.54	6.54	7.35	12.18	12.97	5.72	7.15	11.79
Pr	2.22	3.33	1.13			2.11			
Nd	10.85	16.66	6.25	6.09	9.44	10.64	4.85	6.08	8.82
Sm	3.57	5.38	2.49	2.18	3.11	3.66	1.80	2.20	2.77
Eu	1.25	1.68	0.99	0.90	1.09	1.27	0.73	0.91	1.03
Gd	4.54	6.66	3.29	2.98	4.01	4.87	2.52	3.13	3.46
Tb	0.80	1.20	0.61	0.53	0.73	0.88	0.47	0.56	0.59
Dy	5.23	7.91	3.98	3.53	4.89	5.79	3.10	3.72	3.75
Ho	1.10	1.67	0.81	0.73	1.04	1.23	0.67	0.76	0.75
Er	3.12	4.69	2.23	2.10	2.97	3.52	1.94	2.18	2.13
Tm	0.46	0.69	0.32			0.53			
Yb	3.03	4.63	2.06	1.99	2.99	3.45	1.92	2.16	1.92
Lu	0.45	0.68	0.30	0.30	0.43	0.51	0.28	0.32	0.29
Hf	2.64	4.28	1.91	1.76	2.47	2.77	1.43	1.84	2.30
Ta	0.52	0.70	0.20	0.22	0.39	0.45	0.20	0.23	0.44
Pb	0.48	0.65	0.38	0.76	1.29	0.67	0.24	0.29	0.49
Th	0.51	0.76	0.16	0.19	0.36	0.41	0.14	0.19	0.35
U	0.15	0.24	0.06	0.06	0.11	0.12	0.06	0.07	0.12

Table A 9: (continued) Trace element concentrations (in ppm) of glass samples from ICP-MS analyses

	158 DS-1	159 DS-2	160 DS-3	161 DS-1	162 DS-2	163 DS-1	164 DS-1	166 DS-1	166 DS-3
Sc				40.60			40.84		40.72
V				226.49			312.30		317.17
Cr				299.81			188.71		108.95
Co				46.51			41.78		40.55
Cu				102.11			78.42		74.93
Zn				77.48			99.06		93.65
Ga				15.65			17.96		17.52
Rb	4.16	1.59	2.79	1.58	3.47	4.42	5.44	7.18	6.84
Sr	186.33	162.88	158.47	126.61	177.01	159.86	173.53	216.70	194.32
Y	24.61	19.23	20.14	23.36	22.62	26.45	34.61	30.27	34.77
Zr	75.70	53.17	59.89	54.97	67.98	85.72	129.36	103.31	130.03
Nb	8.69	4.00	5.64	3.75	7.31	8.54	11.15	12.05	12.94
Cs									
Mo				0.19			0.63		0.67
Ba	55.26	20.41	32.04	16.32	43.15	50.90	54.30	84.02	74.44
La	6.74	3.71	4.69	2.52	5.93	7.07	8.06	10.69	9.84
Ce	16.01	9.40	11.38	6.89	14.24	16.94	20.10	24.38	23.48
Pr				1.16			3.06		3.43
Nd	11.83	7.55	8.57	6.16	10.50	12.15	15.02	15.95	16.37
Sm	3.71	2.71	2.84	2.31	3.23	3.74	4.71	4.56	4.90
Eu	1.37	1.05	1.05	0.92	1.19	1.29	1.56	1.48	1.60
Gd	4.45	3.46	3.62	3.09	4.06	4.32	5.53	5.19	5.53
Tb	0.76	0.62	0.64	0.57	0.71	0.77	0.95	0.87	0.95
Dy	4.97	3.98	4.14	3.87	4.45	4.93	6.02	5.68	6.06
Ho	1.04	0.82	0.87	0.81	0.91	1.03	1.22	1.15	1.23
Er	2.79	2.29	2.40	2.28	2.64	2.88	3.36	3.22	3.37
Tm				0.34			0.49		0.50
Yb	2.70	2.17	2.27	2.23	2.46	2.80	3.15	3.10	3.23
Lu	0.41	0.31	0.33	0.33	0.35	0.41	0.46	0.46	0.47
Hf	2.95	2.15	2.37	1.76	2.67	3.11	3.76	3.55	3.75
Ta	0.59	0.28	0.39	0.23	0.46	0.54	0.57	0.76	0.80
Pb	0.53	0.57	0.39	0.29	0.67	0.66	0.62	0.89	0.76
Th	0.50	0.24	0.36	0.17	0.41	0.54	0.67	0.88	0.91
U	0.16	0.08	0.12	0.06	0.14	0.18	0.21	0.27	0.29

Table A 9: (continued) Trace element concentrations (in ppm) of glass samples from ICP-MS analyses

	169 DS-2	**170 DS-1**	**172 DS-3**	173 DS-1	**173 DS-2**	**174 DS-2**	**188 DS-1**	**189 DS-1**	**190 DS-2**
Sc	37.46			38.05		30.63			39.74
V	271.35			318.93		269.46			326.41
Cr	176.97			103.23		36.54			39.96
Co	40.27			38.14		36.26			41.17
Cu	95.48			71.04		61.96			73.60
Zn	85.28			101.45		94.17			111.27
Ga	16.68			18.64		17.19			19.55
Rb	4.09	8.43	6.73	7.79	7.96	11.08	6.69	9.00	8.36
Sr	172.18	204.22	198.94	215.97	223.19	271.30	265.37	252.50	239.55
Y	29.69	35.60	30.48	38.98	36.85	32.71	24.92	29.55	38.90
Zr	94.34	132.43	107.31	150.63	165.07	162.70	96.42	121.52	161.28
Nb	7.70	15.79	12.85	15.69	17.73	20.33	12.67	16.62	16.27
Cs					0.09				
Mo	0.42			0.85		1.08			0.89
Ba	43.72	101.58	86.98	86.52	90.63	127.52	91.08	119.13	92.28
La	6.45	13.56	11.44	11.48	11.95	14.93	10.78	13.70	11.70
Ce	15.92	31.29	26.14	27.95	28.15	34.36	24.28	31.92	28.48
Pr	2.41			4.10	4.16	4.82			4.20
Nd	11.74	20.56	17.47	19.36	19.22	21.73	16.09	20.26	19.80
Sm	3.73	5.81	5.10	5.81	5.62	5.87	4.60	5.57	5.90
Eu	1.34	1.96	1.67	1.89	1.90	1.90	1.53	1.89	1.96
Gd	4.48	7.01	5.80	6.47	6.56	6.23	4.99	6.33	6.57
Tb	0.78	1.17	0.99	1.11	1.10	1.01	0.83	1.04	1.10
Dy	5.03	7.33	6.31	6.96	6.87	6.17	5.07	6.31	6.85
Ho	1.03	1.49	1.30	1.40	1.41	1.20	1.02	1.27	1.36
Er	2.87	4.21	3.68	3.83	3.86	3.20	2.79	3.51	3.71
Tm	0.42			0.55	0.56	0.46			0.53
Yb	2.73	4.00	3.45	3.58	3.62	2.93	2.61	3.31	3.44
Lu	0.40	0.59	0.51	0.52	0.52	0.43	0.37	0.48	0.50
Hf	2.79	4.92	4.16	4.49	4.44	4.65	3.54	4.59	4.51
Ta	0.48	1.12	0.88	1.00	1.10	1.24	0.81	1.14	1.01
Pb	0.51	1.10	0.84	0.93	1.90	1.21	0.99	1.69	1.16
Th	0.53	1.11	0.98	1.09	1.15	1.48	0.89	1.23	1.07
U	0.17	0.41	0.29	0.34	0.33	0.46	0.28	0.38	0.34

Table A 9: (continued) Trace element concentrations (in ppm) of glass samples from ICP-MS analyses

	191 DS-3	175 DS-1	175 DS-2	176 DS-2	179 DS-2	179 DS-4	183 DS-3	183 DS-5	184 DS-3
Sc		36.54			31.86	32.83		17.31	
V		181.05			276.63	274.49		186.01	
Cr		297.37			67.95	71.69		23.99	
Co		44.00			47.15	42.77		30.77	
Cu		80.91			66.84	65.19		25.08	
Zn		58.82			108.52	111.85		116.70	
Ga		14.17			19.87	19.35		19.73	
Rb	9.03	4.08	3.48	4.89	10.77	10.13	32.70	28.77	30.82
Sr	239.54	229.55	223.93	234.45	390.55	379.15	783.73	764.00	888.33
Y	31.08	21.42	18.31	22.91	29.96	28.95	37.12	40.99	36.66
Zr	122.55	73.41	71.34		162.80	161.07	253.23	297.72	260.73
Nb	16.45	7.85	7.45	9.64	16.92	18.17	54.30	53.69	52.93
Cs			0.04						
Mo		0.43			1.07	1.11		2.37	
Ba	112.25	53.69	45.25	64.24	128.09	128.45	464.95	376.91	414.59
La	13.16	5.56	5.34	8.31	14.55	14.77	44.89	38.13	42.15
Ce	29.84	13.57	12.68	19.87	33.69	34.33	95.04	83.72	88.90
Pr		2.00	1.88		4.74	4.85		11.28	
Nd	19.32	9.46	8.73	13.14	21.41	22.10	49.70	47.78	46.99
Sm	5.45	2.87	2.51	3.87	5.86	5.93	10.88	11.17	10.48
Eu	1.85	1.05	0.98	1.40	1.99	1.99	3.64	3.42	3.42
Gd	6.18	3.21	3.04	4.56	6.00	5.95	10.57	10.15	10.05
Tb	1.02	0.57	0.52	0.76	0.95	0.96	1.55	1.49	1.45
Dy	6.47	3.69	3.33	4.76	5.58	5.67	8.52	8.28	8.08
Ho	1.29	0.75	0.71	0.98	1.04	1.07	1.59	1.52	1.51
Er	3.58	2.11	1.99	2.73	2.83	2.78	4.25	3.89	3.92
Tm		0.31	0.30		0.38	0.38		0.53	
Yb	3.40	2.06	1.95	2.71	2.42	2.39	3.54	3.31	3.41
Lu	0.49	0.31	0.29	0.41	0.35	0.34	0.51	0.47	0.49
Hf	4.50	2.04	1.87		4.55	4.54	8.29	8.16	8.34
Ta	1.08	0.50	0.47	0.67			3.42	3.33	3.28
Pb	1.97	0.97	0.55	0.99	1.99		3.18	2.36	2.67
Th	1.14	0.50	0.47	0.77	1.58	1.43	3.80	3.41	3.35
U	0.34	0.16	0.15		0.51	0.45	1.09	1.05	0.97

Table A 9: (continued) Trace element concentrations (in ppm) of glass samples from ICP-MS analyses

	184 DS-4	**186 DS-1**	**194 DS-1**	**195 DS-1**	**195 DS-2**	**196 DS-3**	**197 DS-1**	**197 DS-3**	**198 DS-1**
Sc	19.82								
V	215.16								
Cr	80.95								
Co	34.96								
Cu	27.49								
Zn	115.62								
Ga	19.35								
Rb	27.54	19.01	2.00	1.55	1.59	5.81	9.15	7.74	1.74
Sr	712.19		96.00	94.53	92.41	137.37	162.31	152.23	68.59
Y	38.42	27.67	19.82	24.53	21.84	30.12	34.31	36.57	22.92
Zr	298.62	168.80	46.02	59.66	42.86	91.63		154.51	37.82
Nb	46.27	33.46	3.86	2.86	2.39	10.00	13.17	15.40	2.57
Cs				0.02				0.09	
Mo	2.38				0.00				
Ba	349.27	250.97	25.58	17.41	19.04	70.74		81.10	22.66
La	36.86	26.02	3.84	2.65	2.75	8.81	11.22	10.51	2.65
Ce	80.28	54.23	9.60	7.38	7.44	20.32	25.99	24.82	6.82
Pr	10.75			1.28	0.00			3.71	
Nd	45.39	30.51	6.83	6.64	6.32	13.71	16.76	17.22	6.15
Sm	10.58	7.15	2.25	2.49	2.28	4.21	4.74	5.09	2.30
Eu	3.27	2.36	0.82	0.91	0.87	1.42	1.57	1.65	0.88
Gd	9.55	7.22	2.93	3.44	3.16	5.04	5.85	6.16	3.23
Tb	1.41	1.04	0.55	0.64	0.61	0.90	1.02	1.05	0.61
Dy	7.80	5.76	3.85	4.32	4.17	5.88	6.42	6.71	4.17
Ho	1.45	1.07	0.85	0.94	0.90	1.23	1.36	1.40	0.92
Er	3.72	2.85	2.50	2.72	2.64	3.55	3.98	3.91	2.80
Tm	0.51			0.40	0.00			0.56	
Yb	3.17	2.49	2.59	2.68	2.60	3.45	3.97	3.72	2.79
Lu	0.45	0.34	0.38	0.40	0.39	0.50	0.59	0.54	0.41
Hf	8.09	5.31	1.75	1.80	1.71	3.45		4.13	1.66
Ta	2.52	2.04	0.28	0.19	0.15	0.66	0.84	0.95	0.18
Pb	3.19	2.31	0.84	0.45	0.94	1.10		1.86	0.57
Th	3.52	1.95	0.31	0.21	0.19	0.76	1.29	1.06	0.20
U	1.08	0.60	0.10	0.06	0.06	0.22		0.30	0.07

Table A 9: (continued) Trace element concentrations (in ppm) of glass samples from ICP-MS analyses

	199 DS-2	200 DS-1	201 DS-5	202 DS-3	203 DS-1	203 DS-2
Sc			40.14		43.65	41.22
V			261.92		292.47	267.78
Cr			232.25		351.73	331.20
Co			39.07		43.38	41.87
Cu			66.32		76.74	70.81
Zn			71.58		74.10	71.46
Ga			14.85		15.02	14.76
Rb	0.66	2.37	5.14	2.28	1.76	1.63
Sr	71.70	89.70	142.75	91.60	83.50	82.62
Y	19.35	25.75	27.90	20.30	27.37	26.36
Zr	32.71	66.76	71.70	38.57	51.28	49.14
Nb	1.25	3.66	7.18	3.30	2.44	2.40
Cs						
Mo			0.37		0.17	0.17
Ba	9.59	28.51	59.75	27.41	15.87	14.78
La	1.83	3.93	5.74	3.33	2.36	2.24
Ce	5.25	9.88	13.62	7.98	6.71	6.40
Pr			2.01		1.15	1.11
Nd	5.15	7.96	9.45	6.14	6.29	6.15
Sm	1.97	2.82	3.05	2.17	2.44	2.39
Eu	0.77	1.02	1.08	0.82	0.90	0.87
Gd	2.85	3.95	3.87	3.00	3.35	3.18
Tb	0.55	0.72	0.70	0.57	0.64	0.63
Dy	3.79	5.01	4.68	3.93	4.38	4.26
Ho	0.83	1.08	0.99	0.86	0.95	0.92
Er	2.42	3.17	2.80	2.49	2.71	2.63
Tm			0.41		0.40	0.39
Yb	2.47	3.20	2.75	2.52	2.70	2.60
Lu	0.37	0.49	0.41	0.37	0.40	0.39
Hf	1.45	2.74	2.18	1.67	1.70	1.67
Ta	0.10	0.26	0.43	0.22	0.15	0.15
Pb	0.48	0.51	0.69	1.31	0.70	0.53
Th	0.10	0.33	0.58	0.30	0.18	0.18
U	0.04	0.12	0.17	0.09	0.06	0.05

Table A 10: Pb isotope ratios of glass samples

Samplel	206/204	207/204	208/204	6/4 err	7/4 err	8/4 err
122 DS-5	17.71666	15.43990	37.20492	0.0028	0.0022	0.0061
126 DS-1	17.85379	15.44781	37.36473	0.0007	0.0008	0.0025
130 DS-3	17.92062	15.46899	37.48811	0.0015	0.0016	0.0044
132 DS-5	18.84635	15.55021	38.38072	0.0011	0.0011	0.0031
142 DS-2	18.39464	15.50284	37.91472	0.0011	0.0011	0.0032
144 DS-1	18.33247	15.49394	37.86669	0.0010	0.0010	0.0027
149 DS-2	18.79171	15.55187	38.36565	0.0021	0.0018	0.0047
151 DS-2	18.84737	15.55056	38.29475	0.0023	0.0022	0.0062
154 DS-1	18.60238	15.53540	38.14436	0.0023	0.0024	0.0074
158 DS-1	18.98245	15.56960	38.52359	0.0011	0.0011	0.0035
164 DS-1	19.10166	15.57987	38.68458	0.0019	0.0018	0.0053
166 DS-3	19.14944	15.59334	38.90769	0.0025	0.0022	0.0059
166 DS-3	19.14856	15.59441	38.90226	0.0011	0.0012	0.0038
169 DS-2	19.18189	15.60002	38.96113	0.0020	0.0017	0.0047
173 DS-1	19.18548	15.59587	38.91523	0.0013	0.0012	0.0032
174 DS-2	19.20672	15.59497	38.90330	0.0011	0.0010	0.0031
175 DS-2	19.04715	15.57946	38.72468	0.0013	0.0012	0.0035
179 DS-2	19.42051	15.60880	39.18495	0.0009	0.0009	0.0029
183 DS-5	19.23084	15.58885	38.86353	0.0017	0.0014	0.0041
188 DS-1	19.17958	15.59443	38.92102	0.0036	0.0031	0.0084
190 DS-2	19.13579	15.59385	38.90936	0.0014	0.0015	0.0046
195 DS-1	18.43116	15.51284	38.04179	0.0010	0.0012	0.0038
201 DS-5	19.05484	15.59061	38.58845	0.0009	0.0009	0.0026

Table A 11: Sr isotope ratios of glass samples

Sample	Coment	87/86 Sr	2 sig.
120 DS-3	MZ	0.702239	0.000010
122 DS-5	MZ	0.702176	0.000007
122 DS-7	MUE	0.702202	0.000009
126 DS-1	MZ	0.702284	0.000042
130 DS-3	MZ	0.702369	0.000021
132 DS-5	MZ, MW	0.702473	0.000010
133 DS-9	MUE	0.702433	0.000010
138 DS-1	MUE	0.702670	0.000010
139 DS-1	MUE	0.702338	
142 DS-2	MZ	0.702299	0.000015
144 DS-1	MZ	0.702079	0.000096
148 DS-6	MUE	0.702538	0.000011
149 DS-2	MZ	0.702412	0.000009
151 DS-2	MZ	0.702348	0.000011
154 DS-1	MUE	0.702442	0.000011
158 DS-1	MZ	0.702468	0.000014
164 DS-1	MUE	0.702550	0.000010
166 DS-3	MZ	0.702683	0.000011
169 DS-2	MUE	0.702768	
173 DS-1	MZ	0.702658	0.000009
173 DS-2	MUE	0.702703	0.000008
174 DS-2	MZ	0.702663	0.000014
	MUE	0.702753	0.000018
175 DS-2	MZ, MW	0.702530	0.000023
	MUE	0.702485	
179 DS-2	MZ	0.702608	0.000014
	MUE	0.702656	0.000013
183 DS-5	MZ	0.702610	0.000011
184 DS-4	MZ	0.702626	0.000011
188 DS-1	MZ	0.702664	0.000015
190 DS-2	MZ	0.702668	0.000021
	MUE	0.702716	
195 DS-1	MZ	0.702371	0.000021
	MUE	0.702476	0.000013
197 DS-3	MUE	0.702675	0.000009
201 DS-5	MZ	0.702543	0.000009
203 DS-2	MUE	0.702435	0.000015

Source calculations:

Calculations were done following (Niu et al., 2001). In contrast to (Niu et al., 2001) who took Ba/element ratios, Rb/element ratios were taken here. Analytical problems are probably the cause for the calculation problems with Ba. As Rb is comparable to Ba in terms of incompatibility the calculations should not be affected.

Formula:

In concordance to Ba, Rb is assumed to have a bulk partition coefficient $D^{Rb} = 0$. Following (Niu et al., 2001) C^{Rb}/C^{i} against C^{Rb} can be plotted. This gives the linear equation: $C^{Rb}/C^{i} = S^{i}C^{Rb}+I^{i}$ for each element i considered for Seg.2,3 (depleted samples) and Seg. 5 (enriched samples) whereby C^{Rb}: concentration of Rb in the sample, C^{i} concentration of element i in the sample. The slopes S^{i} and intercepts I^{i} are obtained by linear regression. The slope is defined by: $S^{i} = D^{i}_{o}/C^{i}_{o}$, I^{i} is defined by $I^{i} = C_{o}^{Rb}/C_{o}(1-P^{i})$, whereby: D^{i}_{o} = bulk partition coefficient of element i, C^{i}_{o}, concentration of element i in the source, C_{o}^{Rb}: concentration of Rb in the source and P^{i} is the effective bulk partition coefficient of element i depending on mineral melting modes. D^{i}_{o} is assumd to be the same for depleted and enriched MAR segments, but not $P^{i.}$ If D^{i}_{o} is the same for both areas then: $C^{i}_{o}{}^{enr}/ C^{i}_{o}{}^{depl}$. $= S^{i\ enr.}/S^{i\ depl.}$ ($C^{i}_{o}{}^{enr.}$: conc. of element i in enriched source, $C^{i}_{o}{}^{depl}$. conc. of element i in depleted source, = $S^{i\ enr.}$: slope of element i of enriched source, /$S^{i\ depl.}$: slope of element i of depleted source. By resolving this equation $C^{i}_{o}{}^{enr.}$can be calculated. Depleted source composition is calculated by $C^{i}_{o}= D^{i}_{o}/S^{i}$. The extend of melting in both sources is calculated using: $F = (C^{i}_{o}/C^{i}-D^{i}_{o})(1-P^{i})$.

Partition coefficients:

Following partition coefficients were used: Cpx: (Hart and Dunn, 1993), Opx and Ol: (Kennedy et al., 1993), Spl: Compilation of (Niu and Hékinian, 1997). Bulk partition coefficients were calculated assuming melting in the spinel lherzolite field with 55 % Ol, 30 % Opx 13 % Cpx and 2 % Spl. $P^{i} = 0{,}466Cpx+0{,}681Opx+0{,}048Spl = 0{,}193Ol+1melt$.

Table A 12: Slopes, calculated element abundances and calculated degree of partial melting of the depleted source

depleted source	**S depl.**	**Co depl.**	**F**
La	0.11	0.27	0.04
Ce	0.05	0.73	0.04
Nd	0.06	0.74	0.05
Sm	0.19	0.33	0.06
Eu	0.53	0.13	0.07
Gd	0.16	0.47	0.05
Tb	0.88	0.09	0.05
Dy	0.14	0.63	0.05
Ho	0.64	0.13	0.04
Er	0.23	0.37	0.04
Yb	0.24	0.43	0.04
Lu	1.62	0.07	0.04
		mean	0.05
		stand. dev.	0.01
	H_2O MAX	0.00024	136.3
H_2O	H_2O MIN	0.00024	45.8
	H_2O mean	0.00024	91.0

Table A 12: Slopes, calculated element abundances and calculated degree of partial melting of the enriched source

enriched source	**Co depl.**	**S depl.**	**S enr.**	**Co enr.**	**F**
La	0.27	0.11	0.02	1.47	0.11
Ce	0.73	0.05	0.01	3.40	0.10
Nd	0.74	0.06	0.02	2.20	0.09
Sm	0.33	0.19	0.10	0.65	0.08
Eu	0.13	0.53	0.33	0.21	0.07
Gd	0.47	0.16	0.10	0.73	0.07
Tb	0.09	0.88	0.67	0.12	0.06
Dy	0.63	0.14	0.11	0.75	0.05
Ho	0.13	0.64	0.61	0.14	0.03
Er	0.37	0.23	0.24	0.36	0.03
Yb	0.43	0.24	0.26	0.39	0.03
Lu	0.07	1.62	1.82	0.06	0.03
				mean	0.06
				stand. dev.	0.03
	H_2O MAX	0.0002	0.00004	681.32	
H_2O	H_2O MIN	0.0002	0.00004	229.09	
	H_2O mean	0.0002	0.00004	455.21	

Table A 13a: Sr-Standard NBS 987 measurements, Münster

Sample	Date	87/86 meas
NBS 987	06.08.99	0.710313
NBS 987	09.08.99	0.710309
NBS 987	10.08.99	0.710310
NBS 987	12.08.99	0.710308
NBS 987	13.08.99	0.710329
NBS 987	27.08.99	0.710335
NBS 987	30.08.99	0.710346
NBS 987	30.08.99	0.710330
NBS 987	02.09.99	0.710336
NBS 987	20.09.99	0.710339
NBS 987	21.09.99	0.710318
NBS 987	22.09.99	0.710325
NBS 987	19.11.99	0.710337
NBS 987	19.11.99	0.710353
NBS 987 mean		**0.710328**
2 sig. mean		**0.000029**
True value		0.710240

Table A 13b: Sr-Standard NBS 987 measurements, Mainz

Sample	Date	87/86Sr	2 sig.
NBS 987-1	**12.02.00**	0.7102243	0.0000075
NBS 987-2	**12.02.00**	0.7102311	0.0000115
NBS 987-4	**13.02.00**	0.7102545	0.0000124
NBS 987-3	**13.02.00**	0.7102400	0.0000146
NBS 987-1	**02.03.00**	0.7102185	0.0000128
NBS 987-2	**02.03.00**	0.7102249	0.0000134
NBS 987-1	**12.02.00**	0.7102243	0.0000075
NBS 987-2	**12.02.00**	0.7102311	0.0000115
NBS 987-4	**13.02.00**	0.7102545	0.0000124
NBS 987-3	**13.02.00**	0.7102400	0.0000146
NBS 987-1	**02.03.00**	0.7102185	0.0000128
NBS 987-2	**02.03.00**	0.7102249	0.0000134
NBS 987 MW		0.7102322	0.0000120
NBS 987 mean		0.7102322	
2 sig. mean		0.0000120	
True value		0.710240	
Corr. factor		1.000011	

Table A 13b: Sr-Standard NBS 987 measurements, Mainz, continued

Sample	Date	87/86Sr	2 sig.
NBS 987	**26.03.00**	0.710239	0.000008
NBS 987	**26.03.00**	0.710211	0.000008
NBS 987	**26.03.00**	0.710218	0.000008
NBS 987	**13.04.00**	0.710229	0.000008
NBS 987	**14.04.00**	0.710112	0.000012
NBS 987	**28.04.00**	0.710181	0.000007
NBS 987	**28.04.00**	0.710188	0.000008
NBS 987	**29.04.00**	0.710207	0.000012
NBS 987 mean		0.710210	
2 sig. mean		0.000006	
True value		0.710240	
Corr. factor		1.000042	

Table A 14: Pb-Standard NBS 981 measurements, Mainz

Std	Date	206/204	207/204	208/204	6/4 err	7/4 err	8/4 err
NBS981-ic1	23.10.96	16.939529	15.496456	36.719776	0.001208	0.001219	0.003206
NBS981-ic2	23.10.96	16.941450	15.497552	36.723886	0.000928	0.001014	0.002736
NBS981-ic3	30.10.96	16.940187	15.497317	36.721312	0.000694	0.000797	0.002390
NBS981-ic4	30.10.96	16.941934	15.499024	36.725191	0.000820	0.000927	0.002571
NBS981-ic5	06.11.96	16.939628	15.495858	36.720381	0.001263	0.001459	0.004264
NBS981-ic6	09.11.96	16.941438	15.497994	36.724421	0.001216	0.001417	0.004198
NBS981-ic7	13.11.96	16.941775	15.499489	36.727042	0.000918	0.001012	0.002694
NBS981-ic8	23.11.96	16.941332	15.497434	36.726049	0.001839	0.001740	0.004380
NBS981-ic9	23.11.96	16.938995	15.496299	36.720854	0.001209	0.001221	0.003185
NBS981-ic10	27.11.96	16.941314	15.498905	36.728679	0.000915	0.001014	0.002922
NBS981-ic11	28.11.96	16.943011	15.500403	36.732321	0.000984	0.001088	0.003024
NBS981-ic12	04.12.96	16.941740	15.498148	36.728306	0.000816	0.000896	0.002538
NBS981-ic13	12.12.96	16.941118	15.497423	36.726967	0.001489	0.001408	0.003708
NBS981-ic14	18.05.97	16.937829	15.495392	36.713607	0.001243	0.001250	0.003271
NBS981-ic15	19.05.97	16.942258	15.499189	36.723215	0.001036	0.001189	0.002915
NBS981-ic16	19.05.97	16.942347	15.498974	36.723263	0.000990	0.001050	0.002834
NBS981-ic17	19.05.97	16.944723	15.500315	36.728315	0.001501	0.001476	0.003739
mean		16.941212	15.498010	36.724329	0.001122	0.001187	0.003210